Photoproduction and Vector Dominance

by

David W. G. S. Leith

Lectures presented to

Scottish Universities Summer School in Physics

July 26 - August 15 1970

- - - - - - - - - - - - - - - - -

Part A - Photoproduction of Vector Mesons and the Vector Dominance Model

Part B - Review of Photoproduction Experiments

PART A. Photoproduction of Vector Mesons and the Vector Dominance Model

CHAPTER I. Introduction

In these lectures we will discuss photoproduction processes and compare them to the predictions of the vector dominance model (VDM). In particular, we will examine the data on the photoproduction of vector mesons on protons, deuterons and complex nuclear targets; compton scattering, total photo-absorption cross sections and the question of the existence of higher mass vector mesons; all these topics may be related through the VDM theory, which supposes that the hadronic interaction of the photon is mediated by its coupling to the vector mesons. Good review papers on these topics have been given by S. Ting[1], E. Lohrman[2], R. Diebold[3] and A. Silverman[4].

I. 1. Diffraction Scattering

We are familiar with diffraction scattering as an optical phenomena, leading to sharp forward peaking in light scattering. However, in high energy physics, the diffraction process also contributes strongly to the forward scattering from an absorptive target[5]. The details of the scattering will depend upon the "wavelength" of the incident beam, the size of the scatterer, and on how "black", or absorptive, the scatterer appears to the incoming beam. Although the diffraction scattering process involves no change of quantum numbers, it does proceed when angular momentum is picked up in the scattering. Thus, the spin-parity of the diffracted system may be changed in the series $0^- \rightarrow 0^-$, 1^+, 2^- . . or $1^- \rightarrow 1^-$, 2^+, . . . In the case of complex nuclear targets, the diffractive phenomena implies the coherent production from each of the individual nucleons within the nucleus.

The diffraction scattering process need not be elastic, in the sense that

the outgoing particle may have a different mass than the incoming particle. For example, $\pi p \rightarrow \pi p$ and $\gamma p \rightarrow \gamma p$ are examples of elastic diffraction scattering while $\pi p \rightarrow A_1 p$ and $\gamma p \rightarrow \rho p$ are examples of diffraction processes involving a change in mass of the diffracted system. In these latter cases, the longitudinal momentum transfer required to make up the mass difference must be small compared to the "form factor" of the target -- this is especially important in complex nuclear targets where the momentum transfer may cause the target to "break-up" into its constituent parts and destroy the coherence effect. For the photoproduction of mesons, this longitudinal momentum transfer, t_{min}, is given by $\frac{(M^2_{meson})}{2k}$ where M_{meson} is the mass of the meson system in the final state, and k is the photon energy. It should also be noted, that for these reactions, the forward production (i.e. at $\theta=0^\circ$) will be at finite momentum transfer, t_{min}, and that the difference between the $t = 0$ and $t = t_{min}$ cross section is also strongly momentum and nucleus dependent. For example, for photon energies of 2.7, 4.5, and 9 BeV the extrapolation factors on Pb are 19, 2.7, and 1.3, while for Be they are 2, 1.3, 1.1, respectively.

A list of reactions which could proceed coherently is given below, and includes examples involving mass changes and excitation of the spin-parity series:

(a) elastic scattering at small momentum transfers:-

$$\pi + T \rightarrow \pi + T$$

$$K + T \rightarrow K + T$$

$$N + T \rightarrow N + T$$

$$\gamma + T \rightarrow \gamma + T$$

where T represents the target particle.

(b) diffraction dissociation,

$$p + T \rightarrow N_{1400} + T$$

where N_{1400} is a $J^P = 1/2^+$ nuclear isobar,

$$\pi + T \rightarrow A_1 + T$$

where A_1 is a 3 mesonic state of mass 1080 MeV
with $J^P = 1^+$,

$$K + T \rightarrow K^*_{1300} + T$$

where K_{1300} is a K meson of mass 1300 MeV, and
with $J^P = 1^+$,

$$\gamma + T \rightarrow \rho + T$$

where ρ is the 750 MeV dipion meson resonance
with $J^P = 1^-$.

The characteristics of diffraction scattering are (a) a sharp forward peak in the scattering process that can be approximated by an expotential for momentum transfers smaller than the first diffraction minimum (i.e. e^{-8t}), (b) the forward cross section, $d\sigma/dt$, should be constant, and (c) the total cross section should be a constant. Also for these reactions involving particles with spin, the alignment has to be such as to take care of angular momentum balance without disturbing the target particle. For example, a $\pi p \rightarrow A_1 p$ reaction will require the A_1 to be aligned such that $m = 0$, and for $\gamma p \rightarrow \rho p$, the rho will have to be transversely polarized with $m = \pm 1$, since the photon cannot populate the $m = 0$ state. It should also be noted that by studying the above type of reactions, on a complex nuclear target, the diffraction phenomena provides a filter for the isolation of these reactions in preference to reactions involving meson exchange, spin-flip, I-spin exchange, etc.

One final comment before leaving the diffraction process. In high energy theory terms, where one imagines the interactions proceeding via exchanges of particles, or even whole Regge trajectories, the diffraction scattering is thought of in terms of the exchange of a Pomeron. Thus we might write down some of the above processes in terms of the graphs shown in Fig. 1.

I. 2. Absorption

A second phenomenon that will be encountered is the use of complex nuclear targets to measure the absorption, or attenuation, by nuclear matter of the outgoing secondary particles. If the outgoing particles live long enough to traverse the nucleus, then by varying the path length in nuclear matter, (which we do by varying the size of the nucleus - see Fig. 2.), and observing the relative yield, we can deduce the total cross section. Since we have a whole menagerie of unstable particles in our high energy physics "zoo", with lifetimes so short, (i.e. $< 10^{-10}$ secs), that we have no way of applying classical methods of determining their total cross section, this is a useful technique. The idea was originally used by Drell and Trefil[6] to show that the total cross section for protons on protons, derived from an experiment measuring p-A scattering[7] was in good agreement with observed p-p data. The technique is currently being used to determine A_1-p[8] and K_{1300}-p[9] total cross sections in addition to the experiments on the absorption of photoproduced rho mesons to be discussed below.

These studies of the attenuation of short-lived particles were initially assumed to be independent of the details of the nuclear models, or indeed of the details of the interactions within the nucleus. It was hope to treat the nucleus as a black box which was the variable-thickness absorber in a classical experiment to measure the total cross section by attenuation. However, it turned out that these were naive hopes and that the nucleus had to be treated with more care. Some of these effects will receive detailed attention in the lectures of Professor Yennie[10] and we discuss them only qualitatively so that we will be able to deal with the analysis of the experimental data.

(i) Two-Body Correlations

The existence of two-body correlations in nuclear matter has long been recognized, but the effects had been assumed to be small and the independent particle model of the nucleus had been taken to be an adequate description of

the nuclear interaction. However, a more careful and detailed analysis of the impact of these correlations on calculations of particle absorption in nuclear matter showed that the effect was substantial and should not be neglected.[11,12] The two-body correlation function was evaluated using a "hard-core" repulsive potential together with a short range attractive force determined from the fitting to the low energy nucleon-nucleon scattering data. This implies that within nuclear matter the particle under study sees effectively "larger nucleons" than in the free particle scattering case, leading to an overestimate of the attenuation cross section. For a total cross section of ~ 30 mb, this is about a 10% effect. (i.e. a 33 mb total cross section evaluated ignoring the two-body correlations, would be reduced to give 30 mb as the "free" particle total cross section.)

(ii) Incoherent Background

The question of how to subtract the "incoherent" reactions from the coherent, or diffractive, events where the nucleus remains undisturbed in its ground state, has received a great deal of attention recently. The incoherent reactions can be thought of as processes in which (a) there is a quasi-elastic reaction in which the nucleus is excited (change of quantum numbers) but does not break up, or (b) where one or more nucleons or fragments are ejected from the nucleus. Standard procedure has been to fit the large momentum transfer region to

$$\frac{d\sigma}{dt} = Ae^{-Bt} \qquad [I\text{-}1]$$

assuming that it is dominated by single nuclear processes. This curve is then extrapolated in under the forward diffraction peak to give the incoherent contribution, (see Fig. 3). This is clearly wrong, in that as the momentum transfer goes to zero the chance of exciting the nucleus, or ejecting a particle from the nucleus becomes very small. Rather detailed calculations, with a recipe for extracting the incoherent contribution from the total scattering have been performed by Kolbig and Margolis[13] and Trefil.[14] These considerations are not important

for the rho photo-production data, but become sizeable corrections when studying the ω and ϕ experiments.

(iii) Nuclear-Density Distributions

The four common density distributions used in these studies are:

Hard sphere: $\rho(r) = \text{const}, \; r < R$

$0 \quad , \; r > R$ [I - 2]

Wood-Saxon: $\rho(r) = \rho_0 \, (1 + e^{(r-c)/R})^{-1}$ [I - 3]

Trefil: $\rho = \sum_{j=1}^{A} e^{-(r_a/R)^2}$ [I - 4]

Harmonic Oscillator: $\rho(r) = \rho_0 (1 + \alpha \frac{r^2}{a_o^2}) \, e^{-r^2/a_o^2}$ [I - 5]

Model (d) is often used for low A nucleii, as recommended by electron scattering experiments.[15] Models (a), and (b) claim to be good for large A, while (c) claims to be good for all A. The question of which value of radius to use has been difficult. Most analyses have used two radii and suggested that the answer lies somewhere between the two -- the electron scattering radii[15] and the "strong" radii obtained from fitting the total cross section as a function of A for π, K, p, n scattering.[16]

Recently the DESY-MIT[17] group were able to determine the nuclear radius as a function of A, for the photoproduction of rho mesons. (See Fig. 4) They found:

$$R(A) = (1.12 \pm 0.02) \, A^{1/3} \, f$$

(iv) Finite Width of the Rho

The question of the effect of the finite width of the rho meson has been investigated in detail by Gottfried and Julius.[18] The full $\pi\pi$-production amplitude is a coherent sum of two parts: a term that describes ρ-decay outside the nucleus, and another wherein the ρ decays inside the nucleus. The former dominates at high energy ($\gtrsim 5$ GeV) in even the heaviest nuclei. The interior decay amplitude has a $\pi\pi$-mass spectrum that differs very markedly from that of ρ-decay in vacuum because of a process closely akin to ordinary collision

broadening. The exterior amplitude has a mass spectrum that differs somewhat from that of vacuum decay because the minimum momentum transfer, t_{min}, increases with $\pi\pi$-mass, and the decrease of the nuclear form factor with t_{min} therefore skews the mass distribution towards low masses, (see Fig. 5).

Aside from these modifications of the mass spectrum, there is also some effect on the magnitude of the differential cross section for ρ production arising from the difference in nuclear mean free path between the ρ and its decay products; that is, the $\pi\pi$-state has greater difficulty in escaping the nucleus than does the ρ itself. Their calculations showed that for energies $\gtrsim 5$ GeV, such effects may be safely ignored.

(v) Real Part of the Forward Scattering Amplitude

In all of the early analysis of vector meson photoproduction, it had been assumed that the forward scattering amplitude was purely imaginary down to photon energies of ~ 4 GeV. The importance of taking into account the presence of a real part in ρ-nucleon scattering was emphasized by Talman and Schwartz,[19] who showed that the inclusion of this amplitude would substantially alter the results of the analysis of rho photoproduction. Let us look at how this really affects the analysis.[20]

In the analysis of the experiments we relate the forward elastic scattering of rho mesons to the square of the total rho nucleon cross section, by the optical theorem:

$$\left.\frac{d\sigma}{dt}\right|_{o}^{+} (\rho p \rightarrow \rho p) \; \alpha \; \sigma^{2}_{TOT}(\rho p) \qquad [I - 6]$$

This equation assumes that the ratio of real to imaginary parts of the scattering amplitude in rho-nuclear scattering, $\alpha_{\rho N}$, is zero, which introduces an error, proportional to $\alpha^{2}_{\rho N}$, which is quite negligible.

However, the cross section appearing on the left hand side of equation [I-6] is, unfortunately, not directly measurable. By using the vector dominance model we may relate this reaction to the photoproduction process:

$$\left.\frac{d\sigma}{dt}\right|_o (\rho p \rightarrow \rho p) \alpha \left.\frac{d\sigma}{dt}\right|_o (\gamma p \rightarrow \rho p) \qquad [I - 7]$$

However, because of the mass change in the photo-induced reaction, $\gamma \rightarrow \rho$, we can never physically study zero momentum transfer collisions since there will be a minimum momentum transfer, t_{min}, which goes into making up the mass difference. Thus, the theory is required to calculate the t = 0 cross sections from those measured in the physical region. This done by the following optical model formula:

$$\left.\frac{d\sigma}{dt}\right|_{\theta=0} (\gamma A \rightarrow \rho A) = \left|A_{\gamma\rho}\right|^2 \qquad [I - 8]$$

where $A_{\gamma\rho} = A_o \int d^2b \int dz\ \rho(b,z)\ e^{iq_{11}z}\ e^{-\sigma_{\rho N}(1-i\alpha_{\rho N})T(b,z)/2}$

where $T(b,x) = \int_z^\infty \rho(b,z')\ dz'$, and A_o is the single nucleon production amplitude.

The importance of $\alpha_{\rho N}$ in this equation can be understood qualitatively. The term involving $\alpha_{\rho N}$ introduces a phase factor similar to $e^{iq_{11}z}$. If $\alpha_{\rho N} \neq 0$ the optical potential is complex corresponding to an index of refraction for the medium. The factor $e^{iq_{11}z}$ results in lengthening the wavelength of the vector meson relative to the photon. The index of refraction either enhances or suppresses this effect depending on the sign of $\alpha_{\rho N}$.

A useful approximate expression relating the forward to the extrapolated cross section is, (following Silverman[15]),

$$\left.\frac{d\sigma}{dt}\right|_{t=0} \sim \left.\frac{d\sigma}{dt}\right|_{\theta=0} e^{a(q_{11}^2 - q_{11}\alpha_{\rho N}\sigma_{\rho N}\bar{\rho})\langle R^2\rangle} \qquad [I - 9]$$

where a is a constant very nearly equal to 1/3, $\langle R^2 \rangle$ is the mean squared radius of the nucleus, and $\bar{\rho}$ is roughly the mean nuclear density.

From this equation we see that if $\alpha_{\rho N}$ is negative, the t = 0 cross section is enhanced relative to the $\theta = 0$. The effect is linear in $q_{11}\alpha_{\rho N}$ and therefore is more important at low energies. It is also A-dependent through the factor $\langle R^2 \rangle$.

We have now established that some allowance for the existence of a real part in rho-nuclear scattering must be included in the analysis. However, we must now determine what size we might expect $\alpha_{\rho N}$ to be.

In Fig. 6, the total photon cross section is plotted as a function of energy.[21] The solid line is 1/200 of the average of the $\pi^+ p$ and $\pi^- p$ total cross sections. A best fit to the photon data above the resonance region (i.e., above 2 GeV), is found to be:

$$\sigma_{TOT}(\gamma p) = (96.4 + \frac{70}{\sqrt{R}}) \ \mu b \qquad [I - 10]$$

where k is the photon energy.

The agreement in magnitude and energy dependence between the photon and hadron cross sections is surprisingly good, both showing a slow fall-off in cross sections in the high energy region. Such an observation might lead one to expect that the real parts involved in the two processes should be comparable

$$(\text{i.e. } \alpha_{\gamma N} \sim \alpha_{\rho N} \sim \alpha_{\pi N} \sim -0.2 \text{ at } 5 \text{ GeV/c})$$

Another more quantitative estimate for the real part, $\alpha_{\rho N}$, may be obtained from dispersion relation fits to the high energy total cross section data, shown in Fig. 6. Damashek and Gilman[22] have used the dispersion calculation to estimate the real part in Compton scattering. The ratio of the real to the imaginary part of the forward Compton scattering amplitude from these calculations is shown in Fig. 7. Again this would indicate an $\alpha_{\rho N}$ in γn, and hence from VDM in ρp scattering, of ~ -0.2 at 5 GeV/c, falling to ~ -0.1 at 20 GeV/c.

A more detailed account of this question and a discussion of the possible existence of an "anomalous" real part in ρN scattering, are given by Professor Yennie.[10] In the following we shall assume:-

$$\alpha_{\rho N} \sim \alpha_{\gamma N} \sim \begin{cases} -0.2 \text{ at } 5 \text{ GeV.} \\ -0.1 \text{ at } 20 \text{ GeV.} \end{cases}$$

I. 3. Vector Dominance Model

The origin of the vector dominance model dates back to the early 1960's, when Frazer and Fulco[23] and Nambu[24] suggested that the isovector nucleon form factor could be understood only in terms of a strong π-π resonance, (to be later identified as the rho meson), and when Sakurai[25] suggested that as the electromagnetic current had associated with it a photon, so the isospin current and baryon current and hypercharge current had associated vector mesons and that there would be strong coupling between the "current-associated" particles. For excellent reviews of the vector dominance model, see Joos[26] and Schildknecht.[27]

Basically, the electromagnetic interaction of hadrons is described by the coupling of the electromagnetic field to the hadronic electromagnetic current --

$$j_\mu^{em}(x) = j_\mu^{I}(x) + \frac{1}{2} j_\mu^{Y}(x) \qquad [I - 11]$$

where $j_\mu^I(x)$ and $j_\mu^Y(x)$ are the zero components of the isospin current and hypercharge current respectively. The smallness of the coupling constant, $\alpha = e^2/4\pi$, allows one, in most cases, to treat photoproduction in lowest order of the electromagnetic interactions.

The vector dominance model then connects the hadronic electromagnetic current with the fields of the vector mesons ρ^o, ω, ϕ which have the same quantum numbers as the electromagnetic current, namely $J = 1$, $P = -1$, $C = -1$, $Y = 0$. This connection can be made via the current field identity --

$$j_\mu^{em}(x) = -\left[\frac{m_\rho^2}{2\gamma_\rho}\cdot\rho_\mu^o(x) + \frac{m_\omega^2}{2\gamma_\omega}\cdot\omega_\mu(x) + \frac{m_\phi^2}{2\gamma_\phi}\cdot\phi_\mu(x)\right] \equiv -\sum_V \frac{m_V^2}{2\gamma_r}\cdot V_\mu(x) \quad [I - 11]$$

where γ_ρ, γ_ω, γ_ϕ are the coupling constants of the electromagnetic current to the vector meson fields $\rho_\mu^o(x)$, $\omega_\mu(x)$, $\phi_\mu(x)$ respectively. m_ρ, m_ω, m_ϕ are the masses of the vector mesons.

The assumption which is being made here is that the vector mesons ρ, ω, ϕ completely satisfy this summation. That is, the contribution from the three known hypercharge zero vector mesons completely saturates the electromagnetic current. This is a very strong statement and I wish to return to it in Chapter VII.

Now, according to the field-current identity, any amplitude involving real or virtual photons is a linear combination of vector meson amplitudes, each multiplied by a vector meson propagator. The assumption is then made that the invariant vector meson amplitudes are slowly varying functions of the vector mass, m_v -- i.e., any energy dependence comes from the propagators and not the coupling constants.

Kroll, Lee and Zumino[28] have given a very general treatment of the vector meson dominance model in which they discuss the field theoretic nature of the assumptions. They showed that the model is rather general and has support in Lagrangian field theory.

We may obtain relations between the strength of these coupling constants if we assume,

(a) the photon is the U-spin singlet of an SU3 octet,

(b) ω and ϕ are mixed octet-singlet states with a mixing angle aroung 40° as given by the Gell-Mann-Okubo mass formula,

(That is, the physical states ω, ϕ are mixtures of the pure singlet $|1>$ and pure octet $|8>$ states:

$$|\omega> = \cos\theta|1> - \sin\theta|8>$$

$$|\phi> = \sin\theta|1> + \cos\theta|8>$$

The mixing angle is given by

$$\sin^2\theta = \frac{\omega^2 - M_8^2}{\omega^2 - \phi^2}$$

and

$$M_8^2 = 1/3\ (4K^2 - \pi^2)$$

where the square of the mass of the meson state is always used in these formula.)

(c) the process $\gamma p \rightarrow Vp$ proceeds at high energies, predominantly by the exchange of an SU3 singlet. (A similar assumption for pseudoscalar meson-baryon elastic scattering would yield $\sigma_{el}(\pi p) = \sigma_{el}(Kp)$ at high

energies, which seems to be correct within 20 percent.)

From these assumptions alone, (i.e. nothing to do with SU6, quark model or even VDM), we find

$$\sigma(\gamma p \rightarrow \rho p): \sigma(\gamma p \rightarrow \omega p) : \sigma(\gamma p \rightarrow \phi p) = 9:1:2$$

and therefore

$$\gamma_\rho : \gamma_\omega : \gamma_\phi = 1 : 3 : \frac{3}{\sqrt{2}}$$

Historically, one of the first applications of the idea of vector meson dominance was to an understanding of the pion form factor. The vector meson dominance diagram for the pion form factor is shown below. A single calculation gives

$$F_\pi(a^2) = \frac{m_\rho^2}{m_\rho^2 - q^2} \cdot \frac{1}{2\gamma_\rho} g_{\rho\pi\pi} \qquad [I - 13]$$

For $q^2 = 0$ this equation gives

$$\gamma_\rho = \frac{g_{\rho\pi\pi}}{2} .$$

This relationship can be used to determine γ_ρ from $g_{\rho\pi\pi}$. The decay width for the ρ decay into 2 pions is given by the expression:

$$\Gamma(\rho \rightarrow \pi^+ + \pi^-) = \frac{(g_{\rho\pi\pi})^2}{4\pi} \cdot \frac{m_\rho}{12} \left[1 - \left(\frac{2m_\pi}{m_\rho}\right)^2\right]^{3/2}$$

From the measurements of this process, (see Fig. 8), with electron-positron storage rings, we can determine $\gamma_\rho^2/4\pi$. Professor Gourdin[29] deals with the overall situation with respect to VDM and colliding beam experiments. We will use the value of the coupling constants from these experiments as standards for the photoproduction experiments. The best measurements for the rho width, $\Gamma_{\rho\pi\pi}$, is found to be (111 $\pm$ 6) MeV giving $\gamma_\rho^2/4\pi$ as 0.50 $\pm$ 0.03.

The vector dominance model can also be used to analyze the nucleon form factors One would expect the isovector form factor to be dominated by the rho meson and to be given by an expression of the form:

$$\frac{1}{\left(1 - \frac{q^2}{m_\rho^2}\right)} \qquad [I - 14]$$

However, the experimental data is not explained by the vector dominance model, and no simple explanation is known for its behaviour.

Yet another application of the vector meson dominance model is in the branching ratio in ω decays[30]:

$$\omega \rightarrow \pi^+ + \pi^- + \pi^o$$

$$\omega \rightarrow \pi^o + \gamma$$

The ω decay may be thought of in terms of the diagrams shown in Fig. 9.

The widths for these decays are given by

$$\Gamma(\omega \rightarrow 3\pi) = (0.69)\, m_\omega m_\pi^2 \frac{(m_\omega - m_\pi)^4}{(m_\rho^2 - 4m_\pi^2)} \left(\frac{g_{\rho\pi\pi}^2}{16\pi}\right) \left(\frac{g_{\rho\omega\pi}^2}{4\pi}\right)$$

$$\Gamma(\omega \rightarrow \pi^o\gamma) = \frac{\alpha}{96} \cdot \frac{(m_\omega^2 - m_\pi^2)}{m_\omega^3} \cdot \left(\frac{g_{\rho\omega\pi}^2}{4\pi}\right) \left(\frac{4\pi}{\gamma_\rho^2}\right) \qquad [I - 15]$$

Taking the ratio of the above expressions and the measured branching ratio[31], 0.108 ± 0.008, we can determine the coupling of the photon to the rho, $\gamma_\rho^2/4\pi$.

$\gamma_\rho^2/4\pi$ is found to be $0.95 \pm .1$, in marked disagreement with the value obtained from the colliding beam experiments. However, it should be noted that in the e^+e^- experiments we are dealing with virtual photons on the vector meson mass shell, whereas in this decay we are dealing with real photons. This question will be dealt with in more detail in subsequent chapters.

More generally, the vector dominance model is used to explain the coupling of photons to vector mesons, (ρ, ω, ϕ). Such processes, see Fig. 10, may be studied in three regions of q^2, the momentum transfer between the photon and the rho: $q^2 = 0$, which may be studied in photoproduction reactions, and $q^2 > 0$, which may be studied in inelastic electron scattering.

The assumption implicit in the vector dominance theory is that the same coupling constant $\gamma_v^2/4\pi$ will hold in all processes independent of the reaction and independent of the mass of the photon (i.e., independent of q^2 at the γ-v vertex)

The values of $\gamma_v^2/4\pi$ obtained from storage ring studies[29] (i.e., where the photon is on the vector meson mass shell i.e., $q^2 = m_v^2$), are given in Table I.

The values of the coupling constants obtained in photoproduction processes are the subject of the following chapters.

CHAPTER II. Experimental Situation for $\gamma A \rightarrow \rho A$.

The cross-section for the photoproduction of rho mesons from nuclear targets was measured originally by Lanzerotti et al.[32], and then at DESY[33,34] (at 2.7-4.5 BeV), at Cornell[35] (at 6.2 BeV) and at SLAC[36] (at 8.8 BeV). There was substantial disagreement between these experiments, but a detailed comparison of them is hard due to the difficulty in obtaining raw data and to the difference in the nuclear models used in the analyses. Recently the three latter groups have taken new data and reanalysed their old data; in addition, a new experiment has been performed by a Rochester group (at 8.8 BeV). We shall review these new experiments one by one, and then try to summarize the present status of rho meson photoproduction from complex nucleii.

II. 1. The SLAC Experiment.

The SLAC experiment has measured the photoproduction of rho mesons from hydrogen, deuterium and six complex nuclear targets (Be, C, Al, Cu, Ag, Pb) at photon energies from 5 GeV to 16 GeV. The scope of the experiment is shown in Table II.

The data up to 10 BeV has been obtained using a monochromatic photon beam which has been described previously[37]. The beam is obtained from two-photon annihilation in flight of 12 GeV positrons on the orbital electrons in a liquid hydrogen target. The beam delivered ~ 300 monochromatic photons per pulse, with an energy resolution of $\sim \pm 1.5\%$. The energy spectrum of the photon beam is shown in Fig. 11a.

The data above 10 BeV was obtained using a conventional thin target bremsstrahlung beam at 10, 13, and 16 eV. The energy spectrum at 16 GeV is shown in Fig. 11(b). The exposures were made in such a way that one is able to

test for inelastic contributions as one moves away from the endpoint of the bremsstrahlung spectrum by comparison of the cross sections for several energy cuts (see Fig. 11(c)). This is an especially important point here.

The apparatus used in this experiment is shown schematically in Fig. 12. The wire spark chamber spectrometer and the online IBM 1800 computer system have been described in detail elsewhere.[38] The photon flux is measured, pulse-by-pulse, by a simple e^+e^- pair spectrometer installed in the last sweeping magnet. To calibrate the absolute photon flux, the spark chamber system was periodically used as a pair spectrometer. The properties of the system are: (a) a large mass acceptance of ~ 1000 MeV per setting, with a maximum detectable mass of ~ 3000 MeV, (b) good mass resolution, ~ $\pm$ 8 MeV, (c) large decay angular acceptance, (d) momentum transfer acceptance from 0 to 0.25 $(GeV/c)^2$, with a resolution of 0.0005 $(GeV/c)^2$ for small t, increasing to 0.002 $(GeV/c)^2$ for large t. It is important to note that this apparatus records events over the whole range of dipion mass, decay angle and momentum transfer at the one setting.

The large decay angular acceptance allows us to verify that the rho mesons are indeed transversely polarized, normally an assumption in the other experiments measuring rho photoproduction. The decay distribution, evaluated in the helicity system, for rho mesons produced at 9 BeV from a Be target is shown in Fig. 13. The solid curve is the result of a fit to the distribution, evaluating the spin density matrix elements using:

$$W(\cos\theta, \phi) = \frac{3}{4\pi}\left[0.5\ (1-\cos^2\theta) + \rho_{00}(3/2\ \cos^2\theta - 1/2)\right.$$
$$\left. -\rho_{1-1}\ \sin^2\theta\cos^2\phi - 2\ \mathrm{Re}\ \rho_{10}\ \sin 2\theta\ \cos\phi\right] \qquad \text{[II - 1]}$$

assuming

$$\rho_{00} + 2\rho_{11} = 1$$

The fit, which takes into account the geometrical acceptance of the system, resulted in:

$$\rho_{00} = 0.0 \pm 0.1$$

$$\rho_{1-1} = -0.03 \pm 0.05$$

$$\mathrm{Re}\rho_{10} = 0.03 \pm 0.03$$

Clearly the rho mesons are produced with an essentially complete transverse alignment.

The effective mass distribution of the dipion paris is measured for each target at each energy. Figure 14 shows a representative mass spectrum. The solid line is the result of a fit to the model described in Fig. 15.

$$\frac{dN}{dM_{\pi\pi}} = C_0 M_\rho \left[\frac{M_{\pi\pi}\Gamma}{(M_\rho^2 - M_{\pi\pi}^2)^2 + M_\rho^2\Gamma^2} + C_1 \frac{M_\rho^2 - M_{\pi\pi}^2}{(M_\rho^2 - M_{\pi\pi}^2)^2 + M_\rho^2\Gamma^2} + C_2 \right]$$

where

$$\Gamma = \Gamma_\rho \frac{M_\rho}{M_{\pi\pi}} \left(\frac{M_{\pi\pi}^2 - 4\mu^2}{M_\rho^2 - 4\mu^2} \right)^{3/2} \qquad [\mathrm{II} - 2]$$

and C_0, C_1, C_2, M_ρ, Γ_ρ are free parameters, the last two being the mass and width of the rho. This model assumes that the rho meson production amplitude is given by the Breit-Wigner form, and that it interferes coherently with an imaginary amplitude describing the diffractive $\pi\pi$ scattering. This formalism is due to Söding.[39] The SLAC group find the measured mass and width of the rho meson do not vary as a function of the photon energy, k, or the atomic number, A, and the mean values are found to be;

$$M_\rho \sim 765 \pm 10 \text{ MeV}$$

$$\Gamma_\rho \sim 145 \pm 10 \text{ MeV}$$

The background is A dependent, varying about a factor of two from Be to Pb, and also k dependent, varying ~ 20% from 5 GeV to 16 GeV.

The SLAC group also fit the data using other forms of the Söding model which include a) a different t-dependence for the Söding amplitude than for the ρ amplitude, and b) an "anti-resonance" factor in the p-wave background term to avoid "double counting"[40]. These effects have been investigated in detail by

the SLAC HBC group[41] and their results are discussed below in Part B. The form a) had effect only on the hydrogen and deuterium data, while b) introduces a 12% correction to the cross-sections if it is included. However, I am far from being happy about the question as to the "correct" mass dependence to use in fitting the rho shape.

The mass spectra for the hydrogen data is shown in Fig. 16. The solid line represents the best fit using the model described above. The mass and width of the rho are found to be:

$$\left.\begin{aligned} M_\rho &= 760 \pm 10 \text{ MeV} \\ \Gamma_\rho &= 135 \pm 10 \text{ MeV} \end{aligned}\right\} \quad \text{Hydrogen, 9 GeV.}$$

$$\left.\begin{aligned} M_\rho &= 765 \pm 10 \\ \Gamma_\rho &= 152 \pm 10 \end{aligned}\right\} \quad \text{Deuterium, 9 GeV.}$$

The decay distribution of rho mesons produced on hydrogen at 9 GeV, was fitted by Equation [II-1], and the resulting density matrix elements are shown in Fig. 17 (a) for the helicity system[42] and Fig. 17 (b) for the Jackson system.[43] We see that the dynamics of the production are such that the rho meson is transversely polarized in the helicity frame, and not in the Jackson system, (this will be discussed more fully in Part B). Density matrix elements from HBC experiments[44] at 4.3 and 5 GeV are shown for comparison.

The differential cross section for rho production for both hydrogen and deuterium[45] is shown in Fig. 18 (a). The forward cross sections are found to be:

$$\frac{d\sigma}{dt}(\gamma p \to \rho p) = (104 \pm 11) \quad \mu b/GeV/c^2$$

$$\frac{d\sigma}{dt}(\gamma d \to \rho d) = (360 \pm 26) \quad \mu b/GeV/c^2$$

$$\text{and} \qquad R = \left.\frac{d\sigma/dt\ (d)}{d\sigma/dt\ (p)}\right|_{t=0} = 3.5 \pm 0.3$$

The value of R expected, after taking into account the Glauber correction, is 3.65, while the Cornell group have measured R, at 6.2 GeV, to be $(3.2 \pm .2)$.[46]

Our measurement is in agreement with the expected value of R for the case of pure diffraction, but also agrees, within errors, with the Cornell determination. In addition, we see no differences in the spin-density matrix elements in the forward direction for the hydrogen and deuterium experiments. We therefore conclude that the rho production on hydrogen is predominantly diffractive and use the hydrogen data in an analysis of the A-dependence.

The differential cross section is then found by integrating over all decay angles, and all masses around the rho. A study of the differential cross section may then be used to find the total rho-nucleon cross section, $\sigma(\rho N)$, and the vector dominance coupling constant,[47] $\gamma_\rho^2/4\pi$. The equations used in this analysis[48] are given below, and the process shown schematically in Fig. 19.

$$\left.\frac{d\sigma}{dt}\right|_{t_{min}} (\gamma A \rightarrow \rho A) = \left.\frac{d\sigma}{dt}\right|_{t_{min}} (\gamma N \rightarrow \rho N)\, N_{eff}^2\, (\sigma_{\rho N},\, A,\, \alpha,\, k,\, M_{\pi\pi}) \qquad [II - 3]$$

where t_{min} = the minimum four-momentum transfer $\sim -\frac{M_\rho^4}{4k^2}$

and

$$N_{eff} = \left| -2\pi \int_o^\infty \int_{-\infty}^\infty \underbrace{bdbdz\, J_o(q\, b)\, \rho(b,z)}_{\text{Nuclear shape}}\, \underbrace{e^{i\sqrt{-t_{min}}\, z}}_{\text{Mass dependence}}\, \underbrace{-\frac{\sigma_{\rho N}}{2}(1-i\alpha)\int_z^\infty \rho(b,z')dz'}_{\text{Attenuation of Rho}} \right| \qquad [II - 4]$$

Now the A-dependence of $\left.(d\sigma/dt)\right|_{t_{min}} (\gamma A \rightarrow \rho^o A)$ can be used to determine $\sigma_{\rho N}$.

Further, assuming vector dominance and an imaginary forward amplitude, we can write,

$$\left.\frac{d\sigma}{dt}\right|_{t_{min}} (\gamma A \rightarrow \rho^o A) = \frac{\alpha}{\gamma_\rho^2}\, \frac{\sigma_{\rho N}^2}{16}\, f(\sigma_{\rho N}, \rho(r), t_{min}) \qquad [II - 5]$$

Thus, the measurements of the relative A dependence of the forward rho photoproduction cross-section may be used to determine the total rho-nucleon cross-section, $\sigma(\rho N)$. Having determined $\sigma(\rho N)$, the absolute value of the photo-rho- cross-section may be used to determine the photo-rho coupling constant, $\gamma_\rho^2/4\pi$.

The nuclear density distributions used in these calculations were: a) for $A \geq 27$, the Wood-Saxon distribution (equation [I - 3]), with $C = C_o A^{1/3}$ fermi,

and R = 0.535 fermi. Two values of C_o were used - one taken from electron-nucleus scattering[15] as $C_o = 1.08$, and the other derived from nucleon-nucleus scattering[16] where $C_o = 1.18$.

b) for Be and C, the harmonic oscillator distribution (equation [I - 5]) was used with $\rho_o = (A/\pi^{3/2})\ a_o^3(1 + {}^3/_{2\alpha})$ and $\alpha = (A-4)/6$, (a_o is a shape parameter).

Typical differential cross-sections for several targets, at $E_\gamma = 9$ GeV, are shown in Fig. 17b. The experimental slope of the cross-sections changes from ~ 8 on hydrogen, to ~ 400 on Pb.

Some preliminary results of the data are shown in Fig. 20 and Fig. 21. The forward cross-section for several targets, as a function of the photon energy, k, is shown in Fig. 20, where the solid curve is the prediction of the Drell-Trefil[49] formalism, normalized to the highest energy data points. The measured energy dependence shows good agreement with the model. The extrapolated t=0 differential cross-section is shown in Fig. 21 for several targets, and the data is certainly in agreement with an energy independent cross-section, as would be expected for a diffractive process. However, perhaps more important, the SLAC experiments at different energies (5, 7, 9 and 16 GeV) agree rather well on the k-dependence and A-dependence and seem to represent a self-consistent set of data.

The current status of the analysis gives

$$\sigma(\rho_N) = (29 \pm 2.3)\ \text{mb}$$

$$\gamma^2_{\rho/4\pi} \sim 0.85 \pm .11$$

where the real to imaginary ratio in ρ-N scattering was taken from Fig. 7.

II. 2. <u>The Cornell Experiment</u>.

The group at Cornell[50] have presented results on the photoproduction of rho mesons from 10 targets, (H_2, D_2, Be, C, Mg, Cu, Ag, In, Au, Pb), at average photon energies ranging from 4 GeV to 9 GeV. Some of the data had been published earlier, but has been reanalysed and included with the new data for completeness and consistency.

Their experimental arrangement is shown in Fig. 22. The bremsstrahlung beam, which was monitored by a thin ion chamber upstream, passes through the target mounted in front of the first magnet, and into a uranium beam stop. Photoproduced ρ's decay into $\pi^+\pi^-$ pairs; the $\pi^+\pi^-$ go through separate "arms" of the magnet system. A six-fold coincidence in the scintillation counters trigger the optical spark chambers. The entire magnet system is mounted on a platform which rotates vertically to $\sim 7^\circ$ above the target, thus varying the production angle. The spark chamber pictures are used for high resolution analysis of the data taken on heavy nucleii.

They studied the dependence on incident photon energy and on the mass of the dipion system. The dipion mass dependence is obtained by varying the magnetic fields in the two magnets with their ratio fixed. The photon momentum is varied by moving the target along the beam direction and changing the magnetic field (i.e. target moves closer to magnet for lower energy photons, and further away for the highest energies).

The apparatus detects rho mesons which decay approximately transverse to the rho direction, and the assumption is made that the ρ decay distribution is given as $\sin^2\theta$, where θ is the center of mass polar angle relative to the ρ direction of flight. The acceptance in mass is typically $\frac{\Delta M_{\pi\pi}}{M_{\pi\pi}} \sim \pm 4\%$, and in momentum, $\frac{\Delta p_\rho}{p_\rho} \sim \pm 7\%$ (except for the hydrogen and deuterium measurement at 6.1 GeV and 6.5 GeV, where the acceptance was increased to + 20%.

Complete mass spectra were taken only at several energies and targets. The fitting procedure applied to the mass plot (described below), was then used for all targets at a given energy.

The mass spectra are fit by assuming that the Söding mechanism (described above) describes the reaction mechanism. Their treatment of the line shape includes two refinements over that normally used;

a) the two pions from the ρ decay are allowed to rescatter from the nucleus, and

b) they include an "anti-resonance" term in the Drell amplitude to avoid

"double counting". The treatment of these effects is dealt with more fully by Bauer[51], D. Yennie[40] and J. Pumplin[40]. A typical distribution is shown for copper in Fig. 23.

The data from hydrogen and deuterium was taken at ten momenta between 4 and 9 GeV. A typical differential cross-section is shown in Fig. 24. The coherent peak for deuterium is clearly seen for $|t| < 0.05$ GeV/c^2. For large momentum transfers, the fall-off is seen to be the same as for hydrogen. These shapes are measured by fitting the cross-section to:

$$\frac{d\sigma}{dt} = A\ e^{-bt}$$

and b was found to be (8.5 ± 0.6) $(\text{GeV}/c)^{-2}$ at 7.3 GeV.

The ratio of the forward cross-sections for both targets is shown as a function of energy in Fig. 25. At energies below 6 GeV the ratio is significantly lower than the prediction of the Glauber theory (straight line in Fig. 23), but is quite consistent with the prediction above 6 GeV. (Note that constant value of $\sigma_{\rho N} = 29$ mb was used in calculating the Glauber multiple scattering correction). The discrepancy from the predicted value can be used to indicate the presence of I = 1 isospin exchange in the nuclear amplitude. The energy dependence of the discrepancy is consistent with an s^{-1} form as shown by the dashed curve in Fig. 25.

If ρ photoproduction were proceeding entirely through diffraction, the Glauber corrected ratio of 3.64 would be the expected ratio in the forward direction. The fact that the measured ratio is less than the calculated value, implies that some fraction of the free nuclear amplitude is non-diffractive, and involves exchange of some quantum numbers in the t-channel - either spin or isospin. The "coherent amplification" of the deuteron then picks out only the diffractive part of the hydrogen cross-section leading to the lower ratio. These data imply that at lower energies, the diffractive part of rho photoproduction on hydrogen is not accounting for all of the observed cross-section.

The yield of rho mesons from the complex nuclear targets was measured at four photon energies 4.4, 6.1, 6.5 and 8.8 GeV. For many of the measurements,

only the yield at $M_{\pi\pi}$ = 760 MeV was measured and the mass fitting function described above used to give the total cross-section. The data was treated by an optical model which describes the coherent cross-section at $\theta = 0$, as the single nucleon cross-section f_o^2, times the square of the "effective number of nucleons". The model took into account the real part in ρ-N scattering, which was set equal to that for γ-N scattering as derived from dispersion relation calculations using the total (γ-p) cross-sections.[52] The effect of two particle correlations within the nucleus were also included.

The incoherent contribution at θ=0 was estimated as outlined by Trefil[14], and found to be negligible for all the nuclear targets at these energies.

The optical model used a Wood-Saxon nuclear density distribution for all nucleii with $t \geq 27$, (see equation I-3), while for Be and C targets the harmonic oscillator shell model distribution was used (see equation I-5) with $\alpha = 4/3$ for C and $\alpha = 5/6$ for Be.

The analysis involved using two nuclear models, or at least two estimates of the nuclear radius as a function of A. One model used the nuclear radii as determined from the electron scattering data[15] and are labelled E-S. The second model, called the "Best Fit", took radii obtained from fits to the measured neutron-nucleus and proton nucleus total cross-sections, using a similar optical model to that used in the analysis of the photoproduction data. By using a consistent optical model for both ρ^o-photoproduction and the nucleon-nucleus scattering they hoped that uncertainties due to nuclear parameters would be minimized.

The results of the A-dependence fits to their data are given in Table III for each energy. Also shown are the predicted forward hydrogen cross-sections from their optical model fit to the complex nuclear targets. These are also plotted in Fig. 26, where the agreement with measured data is seen to be very good. The coupling constant is found to be somewhat less than the original Cornell publication[35], due to the inclusion of the real part in the ρ-N

scattering and the two-body correlations in the nuclear absorption calculation. Average values for the $\gamma_\rho^2/4\pi$ and $\sigma_{\rho N}$ are 0.68 ± 0.03, and $\sim 28 \pm 1$ mb. The value of the VDM coupling constant is not in good agreement with the measurement or the rho mass shell, from the storage rings, while no systematic energy dependence is observed for $\sigma_{\rho N}$.

II. 3. DESY-MIT Experiment.

Let us now deal with the new DESY-MIT experiment. They have measured the reaction

$$\gamma + A \rightarrow \rho^o + A$$
$$\rho^o \rightarrow \pi^+ + \pi^-$$

on fourteen[53] targets (H_2, Be, C, Al, Ti, Cu, Ag, Cd, In, Ta, W, Au, Pb, U), at energies (2.6 - 6.8) GeV. They have analyzed 10^5 events on hydrogen, and 10^6 events on the 13 complex nuclear targets.

Their experimental set-up is shown in Fig. 27. A bremsstrahlung beam is brought onto the target, and the pions (from ρ decay), pass through the two armed magnetic spectrometer, where they are detected by scintillation counter hodoscopes and Cerenkov counters. The momentum and angle for each pion is recorded. The data is then corrected for systematic effects like beam attenuation in the target, target-out background, absorption of pion in the target and the counter, dead time, and accidentals. The geometrical acceptance was calculated by a Monte Carlo method.

The experimental data for hydrogen and the complex targets are shown in Fig. 28 and 29. Data was taken at twenty intervals in the dipion mass region 400-1000 MeV, six intervals in the dipion momentum from 4.8 to 7.2 GeV/c, and twenty intervals in the transverse momentum transfer to the nucleus from 0.0 to -0.04 GeV/c^2. At a given spectrometer setting the acceptance of the spectrometer was $\Delta p/p \sim \pm 18\%$, $\frac{\Delta\theta}{\theta} \sim \pm 14\%$ and $\frac{\Delta M}{M} \sim \pm 10\%$, with typical resolution for a given event of $\delta M \sim \pm 15$ MeV, $\delta p \sim \pm$ MeV/c and $\delta t_1 \sim 0.001$ (GeV/c)^2. Great care was

taken to monitor the beam, the spectrometer, and the counters during the experiment and many checks were performed to make sure the apparatus was well understood.

Their analysis of this large volume of data involved calculating cross-sections as a function of A, M, p and t_1 (i.e. in a 13 x 20 x 6 x 20 space, or 31200 different cross-sections).

The DESY experiment analysed their mass spectra in terms of a Ross-Stodolsky[54] type fit -- where the normal resonance formula is modified by a term, $\left(\frac{M_\rho}{M_{\pi\pi}}\right)^4$, - and also by parameterizing the background as a Drell type diffraction amplitude, as suggested by Söding.[39] They find no appreciable difference between these two fits.

However, in the light of the results for the SLAC HBC experiment discussed above,[41] where a detailed study of several models of the rho line shape showed the "rho cross-section" to be uncertain to 30-40%, we must treat this comment with great care. I think that no experiment can really claim to measure the rho cross-section precisely, or in a model independent way.

The data was fit by a theoretical form

$$\frac{d\sigma}{d\Omega dm}(A, M, p, t_1) = \underbrace{\frac{1}{\pi} p^2 \, 2M \, R_n(M) \, (f_c + f_{inc})}_{\text{p contribution}} + \underbrace{BG\,(A, M, p, t)}_{\text{non-resonant background}}$$

$$f_c = \left(\frac{\sigma'}{\sigma}\right)^2 \left| 2\pi f_o \int_o^\infty b\,db \int_{-\infty}^\infty dz \; J_o\left(b\sqrt{t}\right) e^{iz/t_{11}} \, p(z,b) e^{\left(-1/2\sigma'(1-i\alpha)\int_z^\infty \rho(z',b)dz'\right)} \right|^2 \qquad [II - 6]$$

where $\sigma' = \sigma(1 - z\xi\sigma)$,

$$\xi = \frac{1}{16\pi a} \int \exp\left(-\frac{b^2}{4a}\right) g(z,b) \, d^2b\,dz,$$

$$z = \frac{\int e^{-\frac{\sigma}{2} T(b)} Q(b) d^2b}{\int e^{-\frac{\sigma}{2} T(b)} T(b) d^2b},$$

$$Q(b) = \int_{-\infty}^\infty \rho^2(z,b)dz,$$

$$T(b) = \int_{-\infty}^\infty \rho(z,b)dx,$$

ξ is the correlation length, g the correlation wave function, and $B = \frac{ReA}{ImA}$.

This nuclear model was suggested by Von Bochman et al.[12] and includes the effects of a real part to the ρ-N scattering, and also the two-body nuclear correlations. They find that the incoherent contributions, f_{inc}, is of order 10% for low A nucleii, but falls quickly being negligible for A > 100. The background amplitude, BG was parameterized as a general polynomial in (A, M, p, t_1) space, and was ~ 20% for small A nucleii, falling to ~ 5% for the large A nucleii.

As discussed in Chapter 1, this experiment was able to determine the nuclear radiis in photo rho process from analysis of their own data and those values were used in their optical model. They also set the ratio of the real to imaginary part equal to -0.2, in agreement with the dispersion calculations from the total photon cross-section. Having set these quantities the measured cross-sections were compared with the optical model cross section, calculated as described above, and $\sigma_{\rho N}$, $|f_o|^2$ and $\gamma_\rho^2/4\pi$ determined. The results of these fits are shown in Table IV for the Ross-Stodolsky type fit -- called Fit 1, and for the coherent imaginary (in Soding-type) fit -- called Fit 2. They find $\sigma_{\rho N} = 27.7 \pm 1.7$ mb, and $\gamma_\rho^2/4\pi = 0.59 \pm 0.08$, while the forward hydrogen cross-section is predicted to be

$$|f_o|^2 = \left.\frac{d\sigma}{dt}\right|_o (\gamma p \rightarrow \rho p) = (120 \pm 7)\ \mu b/(GeV/c)^2$$

This is by far the most systematic work on the A dependence of rho photoproduction both in terms of the high statistics and also in terms of the number of targets studied. However, the uncertainties in the nuclear physics and more seriously, in the model for the rho line shape, makes it impossible for the full weight of the experiment to bear on the vector dominance questions.

II. 4. The Rochester Experiment.

The Rochester group[55] have measured rho photoproduction at 8 GeV from 7 targets - (Be, C, Al, Cu, St, W, Pb) - using a wire spark chamber spectrometer. (This experimental set-up was a sub-set of that used by the same group to investigate ω-photoproduction, and which is described in some detail in Chapter III).

They used a 9.15 GeV bremsstrahlung beam incident on these targets (varying from 2% to 8% of a radiation length thick), located just upstream of a large aperture magnet. (100 x 25 cm gap). Charged particles emerging from the target were bent by the magnetic field and their tracks were recorded in a magnostrictive wire spark chamber away behind the magnet extending over 85 cm in the beam direction. Six spark chambers of 1 m^2 area were used, each capable of measuring both coordinates with an accuracy of $\pm$ 0.5 mm. In the first two chambers, one of the wire directions was tilted by 15° in order to separate the coordinates of multiple tracks. The events were fed into an IBM 1800 computer which wrote them onto magnetic tape and performed on-line stability checks of the apparatus. One vertical plane of scintillation counters in front of the chambers and two in back served for triggering. Each plane was divided into four separate counters in order to trigger selectively.

The primary photon beam, which was typically 10^6 effective quanta per second, was monitored by a quantameter.

The detection efficiency was calculated using a Monte Carlo program, as a function of mass, decay angles, production angles and energies of the pion pairs. The computation took into account multiple scattering, finite size of the target, and finite accuracy of determining the track-coordinates. The detection efficiency for a forward produced 8 GeV ρ meson decaying symmetrically was typically 50% averaged over the azimuthal decay angle.

An off-line program reconstructed the event configuration from the tracks and determined the kinematical variables. The photon energy was determined to 150 MeV, the momentum transfers to 0.002 $(GeV/c)^2$, and masses to 20 MeV.

The final data was corrected for geometrical losses, absorption and decay of pions, absorption of the photon beam and inefficiencies of the chambers and counters. Care was taken to check out the spectrometer for systematic effects. Normalization was done using the quantameter data.

The mass distribution of pion pairs, integrated over all momentum transfers less than 0.1 $(Gev/c)^2$ is shown in Fig. 30a. They fit this spectrum with the two models described above:- the Ross-Stodolsky model and the Drell-Söding model. In both fits they added an arbitrary incoherent background amplitude. Both of these descriptions fit the data equally well. The Ross-Stodolsky fit gave $M_\rho = 760 \pm 10$ MeV, $\Gamma_\rho = 144 \pm 10$ MeV, while the Söding-type yielded $M_\rho = 770 \pm 10$ MeV and almost the same width. They point out that the derived rho cross-sections are somewhat lower when the Söding fit is used, (by about 5%), but they used the Ross-Stodolsky cross-sections for the remainder of their analysis.

We must remember again that the SLAC HBC experiment[41] found quite drastic changes to their rho cross-sections when they use the "correct" form of the Söding amplitude (i.e. when they allow the diffraction pion scattering to have its own t-dependence, different from that of the ρ mesons). We might then expect even lower cross-sections when we include this form of the dipion spectrum.

An example of the measured diffracted cross-section is shown in Fig. 30b. These distributions were analysed to obtain the forward and extrapolated (t=0) rho cross-sections using an optical model given by:

$$A_{\gamma\to\rho} = A_o \int_0^\infty d^2b \int_{-\infty}^{\infty} dz\ \rho(b,z) e^{iq_{11} z}\, e^{i\bar{q}\cdot\bar{b}}\, e^{-\frac{\sigma}{2}(1-i\alpha_{\rho N})\int_z^\infty \rho(b,z')dz'} \qquad [II - 7]$$

where A_o is the production amplitude of a ρ-meson from a single nucleon, b is the impact parameter, z the coordinate in the forward direction, $q_{11} = \frac{M_\rho^2}{2E_\gamma}$, $\rho(b,z)$ the nuclear density distribution, σ the ρ-N total cross-section and $\alpha_{\rho N}$ the ratio of the real to imaginary part of the rho-nucleon scattering amplitude.

The nuclear density distribution was taken as Wood-Saxon for elements with $A \geq 27$, (see equation [I - 3]), while for carbon and berylium the harmonic well density distribution (see equation [I - 5]) was used.

The radius in the Wood-Saxon case was taken as, $R. = 1.12A^{1/3}$ as determined by Alvensleben et al.[17], while for the harmonic oscillator the radius was taken as R = 2.55f and 2.15f for C and Be respectively. These models allowed a good fit

to the data.

Using this optical model, and setting $\alpha_{\rho N} = -0.2$, as suggested from an analysis of the total photon cross-section[22], the cross-section at $\theta = 0$, (i.e. $t = t_{min}$), was fitted taking $|A_o|^2$ and $\sigma_{\rho N}$ as free parameters. They found

$$|A_o|^2 = 117 \pm 8 \ \mu b/GeV^2$$

$$\sigma_{\rho N} = 29.2 \pm 2.5 \text{ mb}.$$

They then renormalised to the forward cross-sections as measured by the DESY group[53] which were ~ 10% lower, and proceeded to give another value for the total rho-nuclear cross-section:

$$\sigma(\rho N) = 26.8 \pm 2.4 \text{ mb}.$$

Using this value they determine the photon rho coupling to be $\gamma_\rho^2/4\pi = 0.62 \pm 0.12$.

I think they are only confusing the issue by renormalising to the DESY data. While there is a problem between the various determinations of the quantities $\sigma(\rho N)$ and $\gamma_\rho^2/4\pi$, the most valuable contribution the Rochester people can make is to provide an independent measure of these quantities.

Thus we take their results to be (using their Söding cross-sections)

$$\sigma(\rho N) = 29.2 \pm 2.5 \text{ mb}$$

$$\gamma_\rho^2/4\pi = 0.71 \pm 0.12$$

II-5 Summary

I have summarized the situation with respect to the determination of $\gamma_\rho^2/4\pi$ and $\sigma(\rho N)$ in Table V. The total picture is not very precise but has firmed up to the point that we could estimate $\gamma_\rho^2/4\pi \sim 0.7$ and $\sigma(\rho N) \sim 29$ mb without violating anyone badly. (See Fig. 31).

CHAPTER III. The A-Dependence in Photoproduction of ω and ϕ Mesons

There are not as many experiments measuring the A-dependence for the isoscalar vector mesons as have been described above for the rho. These experiments are more

difficult in that we are dealing with a much smaller cross section, and that the decay modes are more difficult to isolate. In the case of the ω^o experiments, the experiment must detect a three-body decay involving one neutral particle, while for the ϕ, the K^+K^- pairs have to be detected in a fierce background of pion and electron-positron pairs. Let us now review those few experiments which have tried to make these interesting measurements.

III. 1. Photoproduction of ω:

This process has been measured only once from nuclear targets -- by the Rochester group[56] at 6.8 GeV from Be, C, A, Cu and Pb targets -- although several measurements exist on hydrogen.[57]

The experimental set up is shown in Fig. 32. A 9.2 GeV bremmstrahlung beam, produced on an internal target of the 10 GeV Cornell electron synchrotron, was hardened by a 1-meter long LiH hardener, and collimated to a size of 0.5 cm x 1.0 cm at the target. The target was mounted inside a dipole magnet.

The photoproduced ω mesons were detected through the dominant decay mode, $\omega \rightarrow \pi^+\pi^-\pi^o$. The charged pions were measured in a wire chamber array, SP1, located downstream of the magnet. The x-coordinate wires of the first two chambers were rotated by 15^o from the vertical, thus enabling a correlation of the two views of each track. All chambers had a dead region in the median plane so that the γ-beam and electron pairs produced in the target did not pass through their sensitive region. Aluminum absorbers above and below the beam between the chambers reduced low energy background. Four trigger counters F in symmetric quadrants in front of the spark chamber array, and four pairs of counters B_1, B_2 in back registered the presence of charged pions.

The γ-rays from the π^o decay passed through the charged pion detecting apparatus and an array of anti-counters A, and were then converted in 1.5 radiation lengths of lead. The position of the converted γ's was recorded by spark chamber SP2, and the energy by the shower counter. An on-line computer recorded data on

magnetic tape and performed checks on chamber efficiencies and the consistency of the data.

The geometric efficiency of the experimental set up was determined by a detailed Monte Carlo study. The detection efficiency varied typically from 0.05% for 5 GeV ω mesons, to 0.25% for 8 GeV/c mesons.

The analysis was performed as follows: - first the π^o mass was reconstructed from the γ-ray energies and directions, (see Fig. 33a), and then selecting those events in the π^o peak the π^o momentum was determined. The charged pion momenta were determined by reconstructing their tracks in the chamber array SP1 and tracing their path back to the target. From the pion momenta, the ω-mass, momentum and decay parameters were determined. The 3π invariant mass spectrum in Fig. 33b shows clearly a peak at the ω mass and a background which consists mainly of non-resonant $\pi^+\pi^-\pi^o$ events.

The data was corrected for γ-conversion efficiency, the effective solid-angle of the system, photon and pion absorption, the ω-branching ratio, counter inefficiencies and dead times, pion decays and losses due to kinematic cuts (e.g., mass or angle cuts). The background under the ω peak, (see Fig. 33b), was subtracted by assuming that the t distribution of these events was the same as for those in the wings.

The differential cross sections $d\sigma/dt$ for Be and Cu are shown in Fig. 34. They show a clear diffraction-type forward peak, but there is also a very substantial non-diffractive background, as to be expected since the one-pion exchange (O.P.E.) process is much more important in ω-photoproduction than for ρ photo production. ω-photoproduction shows clear indications of non-diffractive contributions. This can be easily understood if we note that SU(3) (including ω-ϕ mixing) predicts that the OPE contribution to $\gamma p \rightarrow \omega p$ is nine times larger than in $\gamma p \rightarrow \rho^o p$ while if the Pomeranchon is an SU(3) singlet, its contribution to ρ^o photoproduction is nine times larger than to ω. We have:

$$\frac{\sigma_{DIFF}(\rho^o)}{\sigma_{DIFF}(\omega)} = 9 \qquad \frac{\sigma_{OPE}(\rho^o)}{\sigma_{OPE}(\omega)} = \frac{1}{9} \qquad [III - 1]$$

Since σ_{OPE} is proportional to $1/s^2$ (both for Reggerized and single pions) and σ_{DIFF} is constant, we expect that as $s \to \infty$, the ρ:ω photoproduction ratio will approach 9. wever, at lower energies, $\gamma p \to \omega p$ may still have substantial contributions of OPE. For example, if at a given energy 99% of the ρ^o cross section is contributed by diffraction or Pomeranchon exchange and 1% by OPE (or exchange of the A_2 trajectory which has the same SU(3) quantum numbers), the ω cross section at the same energy will include approximately equal contributions of diffraction and OPE.

The contribution of inelastic and incoherent events was calculated using the following expression:

$$\frac{d\sigma}{dt}^{OPE} = A_{eff} \left[\left(\frac{d\sigma}{dt^*}\right)_{\omega N^*} + G(t) \left(\frac{d\sigma}{dt}\right)_{\omega N} \right] \qquad [III - 2]$$

Here A_{eff} is the effective number of nucleons contributing to incoherent photoproduction; its value was taken as obtained from large angle ρ^o photoproduction[58] and π^+ photoproduction[59] in complex nuclei. $(d\sigma/dt^*)_{\omega N^*}$ and $(d\sigma/dt)_{\omega N}$ are cross sections for the processes $\gamma N \to \omega N^*(1236)$ and $\gamma N \to \omega N$ calculated by G. Wolf using an OPE model.[60] The cross section for $\gamma N \to \omega N^*$ was taken at a different value $t \to$ to take into account that in this experiment the momentum transfer was reconstructed assuming elastic photoproduction. Finally, $G(t)$ is a correction factor calculated by von Bochmann, Margolis and Tang[12] to take into account the suppression of incoherent processes at small t because of nuclear correlations. The dashed and the dotted lines in Fig. 34 indicate the relative importance of the inelastic and the incoherent contribution to $d\sigma/dt^{OPE}$.

The solid lines in Fig. 34 are obtained by fitting

$$\left(\frac{d\sigma}{dt}\right)_{\omega A} = \left(\frac{d\sigma}{dt}\right)^{DIFF}_{\omega A} + \left(\frac{d\sigma}{dt}\right)^{OPE} = \frac{1}{\eta(A)} \left(\frac{d\sigma}{dt}\right)_{\rho A} + \left(\frac{d\sigma}{dt}\right)^{OPE} \qquad [III - 3]$$

where $d\sigma/dt^{OPE}$ is taken from Eq. III - 2, $(d\sigma/dt)_{\rho A}$ is the measured photoproduction

cross section of ρ^o mesons on the same nucleus and $\eta(A)$ is a fitting parameter which gives the ratio between diffractive ρ^o and ω photoproduction cross sections.

The diffractive contribution to ω photoproduction can be expressed at small angles, where coherent production dominates, as

$$\left(\frac{d\sigma}{dt}\right)^{DIFF}_{\omega A} = \left(\frac{d\sigma}{dt}\right)_{\omega N} \cdot f\,(R_A, \sigma_{\omega N}, \alpha_{\omega N}, t) \qquad [III - 4]$$

where $(d\sigma/dt)_{\omega N}$ is the diffractive photoproduction cross-section on hydrogen, and where $f\,(R, \sigma, \alpha, t)$ is a function of the nuclear radius R_A, the ω nucleon total cross-section $\sigma_{\omega N}$ and of $\alpha_{\omega N}$, the ratio of the real to the imaginary part of the ω-nucleon forward scattering amplitude. The data was analysed assuming $\alpha_{\omega N}=\alpha_{\rho N}=-0.2$, and searching for $\sigma_{\omega N}$ and $(d\sigma/dt)_{\omega N}$. The result is:

$$\sigma_{\omega N} = 33.5 \pm 5.5 \text{ mb}, \quad \left(\frac{d\sigma}{dt}\right)_{\omega N} = 11.4 \pm 1.9 \ \mu b/GeV/c^2$$

Applying vector meson dominance we find a value of the γ-ω coupling constant $\gamma^2_\omega/4\pi = 9.5 \pm 2.1$.

They then re-evaluate the $(d\sigma/dt)_{\omega N}$ and $\gamma^2_\omega/4\pi$ by taking $\sigma_{\omega N}=\sigma_{\rho N}= 27 \pm 2$ mb. However, since neither the correctness of this equality nor the absolute value of $\sigma_{\rho N}$ is well established, again, I feel that the most useful contribution the Rochester group can make is to provide us with their own measurement of these parameters.

It should be noted that this value of the γ-ω coupling constant is substantially larger than that obtained from the colliding beam investigations[29] (i.e. $\gamma^2_\omega/4\pi = 3.7 \pm 0.7$). It should be further noted that this very model dependent separation gives $\left(\frac{d\sigma}{dt}\right)^{DIFF}_{\omega N}$ in good agreement with the data from polarised photon experiments. This will be discussed further in Part B.

III. 2. Photoproduction of ϕ.

Here there are two experiments - one from the DESY group[61] and one from Cornell[62]. Both of these experiments use the same experimental set-up described in some detail in Chapter II, except that gas threshold Cerenkov counters are

added to identify the K^+K^- mesons from the large background of $\pi^+\pi^-$ pairs.

The Cornell experiment measured the ϕ production at 6.2 and 8.25 GeV on the following nuclear targets: H_2, D, C, Mg, Cu, Ag, Pb. They analyzed the differential cross-sections in terms of an optical model as discussed in Chapter II. Again they used nuclear radii determined from a best fit to the n-A and p-A scattering data and a second analysis with the radius set equal to the electron scattering radius. The difference between the two results is ~ 10%.

The data were fit to the optical model to determine the total ϕ-N cross-section, $\sigma(\phi N)$, the γ-ϕ coupling constant, $\gamma_\phi^2/4\pi$, and the ratio of real to imaginary parts in ϕ-N scattering, $\alpha_{\phi N}$.

The results of a fit with $\alpha_{\phi N} = 0$, give:

$$\sigma(\phi N) = (20 \pm 3) \text{ mb}$$

and

$$\gamma_\phi^2/4\pi = 8.5 \pm 0.3$$

This is in serious disagreement with the value of the coupling constant determined from the colliding beam experiments,[29] (i.e. $\gamma_\phi^2/4\pi = 2.9 \pm .2$).

The quantity $\alpha_{\phi N}$ was varied to attempt to find a better agreement between the storage ring and the photoproduction determination of the coupling constant. For $\alpha_{\phi N} = -0.35$, $\sigma(\phi N)$ was found to be ~ 12 mb, and $\gamma_\phi^2/4\pi \sim 3.4$, in good agreement with the expected quark model cross section and the storage ring coupling constant. However, it is highly unlikely that $\alpha_{\phi N}$ is large, since the ϕ meson does not seem to couple to other particles very strongly, and all exchanges, other than the pomeron, which would be giving rise to any real part of the ϕ-N scattering, are expected to be suppressed. Therefore, the real part is expected to be small, and it is almost certainly < 0.1. If we use the rather poor high energy $K^{\pm}p$ scattering data, (together with the quark model), to determine the possible real part in ϕN scattering, the data is unable to rule out $\alpha_{\phi N}$ as great as -0.2. In these circumstances $\sigma(\phi N)$ would be reduced to ~ 15 mb and $\gamma_\phi^2/4\pi \sim 6$.

The DESY experiment[61] measured the photoproduction of ϕ mesons from Be, C, Al, Cu, Ag, Ta, and Pb targets at 5.2 GeV. The kaon pairs were detected in the double arm spectrometer described in Chapter II above. The separation of K^+K^- from the background of $\pi^+\pi^-$ and e^+e^- was accomplished by four large aperture threshold Cerenkov counters and two lead lucite shower counters; protons were rejected by time-of-flight techniques. The contamination of π, p, e, in the final $\phi \rightarrow K^+K^-$ events was $\sim 1.5\%$.

The geometrical acceptance of the apparatus was calculated by a Monte Carlo method. The usual corrections described in Chapter II above were applied to the data.

A total of 20,000 K^+K^- events were observed and from an optical model fit to the data they claim to measure the total ϕ-N cross section to be

$$\sigma(\phi N) = 12 \pm 4 \text{ mb}.$$

This is from their presentation to the 1968 Vienna Conference. No further data or analysis has been presented.

III. 3. Summary:

The measured coupling constants are listed in Table I for the ρ, ω, and ϕ mesons together with the colliding beam measurements of the various models. The coupling constants are substantially larger, as measured in photoproduction, than those measured on the vector meson mass shell, but the ratio of the coupling constants is compatible with being the same, see Table VI.

CHAPTER IV. Coherent Rho Photoproduction from Deuterium

A new experiment has just been completed at SLAC by the Ritson group[65] measuring the photoproduction of rho mesons from deuterium. This is an interesting new way to determine the quantities $\sigma(\rho N)$ and $\gamma_\rho^2/4\pi$ without getting embroiled in questions of nuclear size and real parts. The idea is that at large momentum transfers, (i.e. $|t| > 0.6(\mathrm{GeV/c})^2$), the requirement that the deuteron remain bound causes the process to be dominated by a two-step process in which the rho is produced on one nucleon and scatters on the others, giving approximately equal recoil to both nucleons.

The single scattering, or impulse approximation is a good description for the small momentum transfer production. Here the photon interacts with only one of the nucleons, which then must scatter and transfer half of its momentum to the spectator nucleon in order for the deuteron to stay bound. Hence this term is proportional to the deuteron form factor. Since the deuteron is an isoscalar, only the isovector part of the photon can contribute to the reaction, and using the Vector Dominance Model, the leading term in the cross section at high energy for small values of $|t|$ is given by:

$$\frac{d\sigma}{dt} \simeq \alpha\left(\frac{4\pi}{\gamma_\rho^2}\right) \cdot \frac{d\sigma}{dt_{\rho N}}(t) \left[S_0^2(t/4) + S_2^2(t/4)\right] \quad + - - - - \text{[IV - 1]}$$

Here, $\gamma_\rho^2/4\pi$ is the γ-ρ coupling constant, $\frac{d\sigma}{dt_{\rho N}}(t)$ is the ρN scattering cross section and $S_0(t/4)$ and $S_2(t/4)$ are quantities proportional to the deuteron charge and quadrupole form factor respectively. Therefore, using the optical theorem, the magnitude of the cross section is determined by $\sigma_{\rho N}^2/\gamma_\rho^2$ where $\sigma_{\rho N}$ is the total rho-nucleon cross section. Since the single scattering term is proportional to the deuteron form factor, it decreases rapidly with increasing $|t|$ and the cross section for large $|t|$- values (i.e. $|t| \geq .7\ (\mathrm{GeV/c})^2$)) is dominated by the double scattering term in the Glauber expansion. Here the ρ is produced on one then re-scatters on the other nucleon in such a way that the two nucleon

average have the same final momentum. This term is given by:

$$\frac{d\sigma}{dt}(t) = \frac{\alpha}{4} \cdot \left(\frac{4\pi}{\gamma_\rho^2}\right) \cdot \left(\frac{K^2}{4\pi^3}\right) \cdot \left[\frac{d\sigma}{dt}_{\rho N}(t/4)\right]^2 \qquad [IV - 2]$$

where K is an integral defined below over the well known wave functions for the ground state of the deuteron. The magnitude of the double scattering term is therefore determined by $\sigma_{\rho N}^4/\gamma_\rho^2$ and will decrease as exp(At/2) if exp(At) is the t-dependence of the single scattering amplitude. Since the cross-section depends differently on $\sigma(\rho N)$ in these two separate regions of momentum transfer, a good measurement of the coherent production over a wide range in $|t|$ may determine $\sigma(\rho N)$ and hence $\gamma_\rho^2/4\pi$ without being dependent of the ratio of the real to the imaginary part in the scattering amplitude or the value of nuclear radii. The nuclear physics of the deuteron is well understood and the real to imaginary ratio is relatively unimportant.

The layout of the experiment is shown in Fig. 35. The electron beam was specially prepared to provide 5 nsec wide bunches spaced typically 50 nsec apart within the 1.6 μsec long SLAC beam pulse. The momentum analysed electron beam passed through several collimators and sweeping magnets before impinging on the hydrogen target, and was finally stopped in a Secondary Emission Quantameter which served as the primary beam monitor. In addition the intensity of the photon beam was also measured by a Cerenkov monitor located in front of the target.

For momentum transfers larger than $t = 0.4(GeV/c)^2$ a conventional liquid deuterium target was used, (38 cm long), while the small momentum transfer data was taken with a high pressure gas target. The angle and momentum of the recoil deuteron was determined by the SLAC 1.6 GeV/c spectrometer[66]. One essential difference between this experiment and the previous experiments measuring the photo rho production on deuterium is that the deuteron is detected and identified.

The arrangement of the counters is shown in more detail in the insert to

Fig. 35. It consisted of a range telescope, a lucite threshhold Cerenkov counter to veto π's, eight hodoscope counters. The ratio of protons to deuterons incident on the counters was typically 1000 to 1, making it difficult to achieve a clean separation by using pulse height and range only. However, since the photons arrive in well defined time bunches at the target, particles with the same mass arrive simultaneously at the top of the spectrometer. Fig. 36 shows such a time-of-flight spectrum for 6 GeV and $t = -1.2(\text{GeV/c})^2$ gated with deuteron biases in the counters. There is a clean separation between deuterons and protons. Since the measurement consisted of determining a step height on a smooth background a small residue of protons will not affect the result.

The spectrometer focuses p and θ onto a single focal plane normal to the particle trajectory. For a fixed photon energy particles of a given missing mass will fall along a straight line over the small p-θ acceptance of the spectrometer. Data were collected by aligning the hodoscope along the corresponding line and measuring the yield of deuterons for fixed p varying θ. This allows us to see a step in the yield curve corresponding to ρ-photoproduction. The method is well described in the literature[67]. Fig. 37 shows such an yield curve for an incident photon energy of 12 GeV and $t = -.3(\text{GeV/c})^2$. The ρ-step is clearly visible.

The solid line through the data points is the result of a least squares fit to the data assuming a ρ-step in addition to a polynomial representing the background. The polynomial used in this fit consisted of a linear and a quadratic term where the quadratic term started at π threshhold. The shape of the dipion spectrum was assumed to be given by an interference between the Söding diagrams and the ρ resonance as described recently by the SLAC HBC group[41].

The extracted step heights were corrected for counter inefficiencies, loss of deuterons in the target or in the counters due to breakup of the deuteron as well as the change in the $\Delta p/p$ acceptance caused by the energy loss of the deuterons in traversing the target. These corrections were typically 15%. In addition to the momentum dependent errors they had a 3% correction due to photons converting

before the target. In addition a 3% uncertainty was assigned to the acceptance of the spectrometer as well as a 2% uncertainty in the calibration of the beam monitors. The largest systematic uncertainty is due to ambiguity in extracting the ρ-step height from the data as previously mentioned.

The measured cross sections are plotted in Fig. 38 versus $|t|$ for 6, 12, and 18 GeV. The observed t-dependence is the characteristic one for a coherent process on deuterium. It consists of a single scattering region where the cross section decreases rapidly with increasing $|t|$, a flattening out around $t = -.5(\text{GeV/c})^2$, where the interference terms and the contributions from the D-state in deuterium are important, and then finally for $|t| \geq .7\ (\text{GeV/c})^2$, a region where the cross section is dominated by double scattering terms.

In the Glauber theory[68], using the V.D.M. the cross section is given by:

$$\frac{d\sigma}{dt}(t) = 4 \cdot \frac{d\sigma}{dt}_{\gamma\rho}(t) \cdot \left[S_0^2(t/4) + S_2^2(t/4)\right]$$

$$- \frac{2}{\pi^{3/2}\sqrt{1+\alpha_{\rho N}^2}} \left[K_0 S_0(t/4) + 1/4\ K_2 S_2(t/4)\right] \cdot \frac{d\sigma}{dt}_{\gamma\rho}(t/4) \left[\frac{d\sigma}{dt}_{\rho N}(t)\right]^{1/2}$$

$$+ \frac{1}{4\pi^3}(K_0^2 + 1/4\ K_2^2) \cdot \frac{d\sigma}{dt}_{\gamma\rho}(t/4) \cdot \frac{d\sigma}{dt}_{\rho N}(t/4) \qquad \text{[IV - 3]}$$

where

$$S_0(\underset{\sim}{q}) = \int_0^\infty dr \left[u^2(r) + w^2(r)\right] J_0(qr)$$

$$S_2(\underset{\sim}{q}) = \int_0^\infty dr\ 2w(r) \left[u(r) - \frac{w(r)}{\sqrt{8}}\right] J_2(qr)$$

Here u(r) and w(r) are the radial wave functions associated with the deuteron's S and D-state respectively, and $\alpha_{\rho N}$ is the ratio of $\frac{\text{Re}f_{\rho N}}{\text{Im}t_{\rho N}}$, which was taken to be -.2, -.18, -.15 at 6, 12, and 18 GeV respectively. $\frac{d\sigma}{dt}_{\gamma p}(t)$ is the isovector part of the cross section for the reaction $\gamma + p \rightarrow \rho^o + p$. Recent experiments at Cornell[69] have shown that by 8 GeV, and presumably higher, the isoscalar part of the amplitude is consistent with zero for small t-values. They therefore

proceded to analyse using the previously published cross-sections for $\gamma + p \rightarrow \rho + p$ from this group.[67]

They used the wave functions computed by Partovi[70] and by Lassila, et al.[71]. Both these sets of wave functions reproduce the static properties of the deuteron and the electric form factor in elastic e-d scattering. It is important to know that we only need to know the form factor out to about $t = -.7(\text{GeV/c})^2$. In this range these wave functions essentially give the same results. If we call the single scattering amplitude $f(q^o)$ then K_0 and K_2 are defined by:

$$K_0 \cdot f^2(1/2\underset{\sim}{q}) = \int_{m_\rho^2/2k}^{2k} d^2\underset{\sim}{q}' S_2(\underset{\sim}{q}') f(-\underset{\sim}{q}' + 1/2\underset{\sim}{q}) f(\underset{\sim}{q}' + 1/2\underset{\sim}{q}) \qquad [IV - 4]$$

$$K_2 \, f^2(1/2\underset{\sim}{q}) = \int_{m_\rho^2/2k}^{2k} d^2\underset{\sim}{q}' S_2(\underset{\sim}{q}') f(-\underset{\sim}{q}' + 1/2\underset{\sim}{q}) f(+\underset{\sim}{q}' + 1/2\underset{\sim}{q}) \qquad [IV - 5]$$

$\frac{d\sigma}{dt}_{\rho N}(t)$ is the elastic rho nucleon scattering cross section:

$$\frac{d\sigma}{dt}_{\rho N}(t) = (\sigma_{\rho N}^2/16\pi) \cdot (1 + \alpha_{\rho N}^2) e^{8.5t + 2.1\, t^2} \qquad [IV - 6]$$

This is the t-dependence observed in ρ-photoproduction on the proton.

In the actual fit, only data in the double scattering region from $-.7(\text{GeV/c})^2$ to $-1.4(\text{GeV/c})^2$ was used. At t=0 the proton data were used. This avoids the use of the data at small t-values, which at present has relatively large uncertainties, as well as the data between $-.3(\text{GeV/c})^2$ and $-.6(\text{GeV/c})^2$ where interference terms between the single and double scattering as well as contributions from the deuteron D-state are important.

Each energy was fit independently and the results are shown as the solid lines in Fig. 38 and the preliminary values for $\gamma_\rho^2/4\pi$ and $\sigma_{\rho N}$ are listed in Table VIII as well as the forward proton cross sections used.

It should be noted that although they used only data for $|t| \geq .7(\text{GeV/c})^2$ in the fit, the curve is in good agreement with the data points at smaller values

of $|t|$. This shows that including these points in the fit would not have changed the quoted results. Also note that the assumed t-dependence for $\frac{d\sigma}{dt}_{\rho N}(t)$ is in excellent agreement with the measured slope.

The fit is consistent with an energy independent value for $(\gamma_\rho^2/4\pi)$ around .7, whereas the total cross section tends to decrease slowly with increasing photon energy, being around 30 mb at about 6 GeV and dropping to 28 mb at 18 GeV.

CHAPTER V. Total Photon Cross Sections on Nucleii

There have been two rather detailed studies of the A-dependence of the total photon cross section, one covering the low energy region by a DESY group[72] while the other was done by a Santa Barbara Group[73] at SLAC, covering the high energy region.

The DESY experiment measured the cross section of 6 complex nuclear targets (D_2, Be, C, Al, Ti, and Cu) at photon energies between 1.5 and 6.3 GeV. The experiment used a tagged photon beam and a detection system of scintillation counters surrounding the target. Typical beam intensity was of the order 5.10^3 tagged photons/second, with a photon energy resolution of $\pm$ 50 MeV. A schematic layout of the detection system is shown in Fig. 39. The electromagnetic reactions are confined to the very forward angles, and are vetoed out by the shower counter. A hadronic event is defined by a signal from the tagging system, a count from the hadron detectors (which have a hole in the forward direction to let through the electromagnetic secondaries), and anticoincidence from the shower counter.

They measured the A-dependence of the cross section at 5.5 GeV and the energy dependence for Be and C targets from 1.5 through 6 GeV.

The Santa Barbara experiment measured the photo absorption at 8, 13.6 and 16.4 GeV on D_2, C, Cu, and Pb targets. This experiment also used a tagged photon beam, with $\pm$ 2.5% energy resolution, and is schematically represented in Fig. 37. The great problem in these experiments is to avoid counting electron pairs as hadronic final states. Since pairs range from 200 times the hadrons in hydrogen

to 5000 times the hadrons in lead, the danger of an A-dependent background is obvious. Both the Santa Barbara and DESY experiment take great precautions and perform many checks to be sure the electromagnetic background is small and understood.

The A-dependence of the total photon cross section is of interest, in that if the photon interacts with matter as a classical photon, then we expect matter to be essentially transparent to it. In fact, the total cross section on hydrogen implies a mean free path in nuclear matter of ~ 800 fermis. Under these circumstances the total cross section should be linearly dependent on A, the number of nucleons in the target. However, if the photon mainly interacts via the ρ meson, as implied by VDM, then the attenuation of the photon in nuclear matter will be strong, (the corresponding mean free path would be ~ 3 fermis), and consequently the surface nucleons will shadow the rest. If the mean free path were zero, the shadowing would be complete and the cross section would be proportional to the nuclear surface area. These studies therefore allow some insight on the interaction of the photon with matter.

The detailed theoretical treatment of the absorption of photons will be given in Professor Yennie's lectures,[10] and may be found in the literature.[76] Let us look at it rather simply for the moment.

The total cross section can be understood, via the optical theorem, from the behavior of the forward elastic scattering amplitude. In fact, the total cross section may be simply expressed in terms of the following processes: (see Fig. 40).

In process (a), the Compton scattering proceeds through the single step or direct interaction with one of the nucleons, whereas in (b) there is an intermediate state of the rho meson -- a two-step process. At low energies, the phase difference between these two diagrams is rather large, being given by $\left|\exp\left[(m_{\pi\pi}^2/2k)\cdot R\right]\right|$, and therefore only the left-hand process contributes. This means that the photon is very weakly absorbed and the A-dependence will go as A.

At high energies, the phase difference becomes negligible, but the diagrams are 180° out of phase, and so there is complete cancellation. This results in an A-dependence characteristic of the absorption cross section of the strongly interacting particle in the intermediate state of process (b). The A-dependence of the cross section would then be expected to go as $\sim A^{0.8}$ at the energies of these experiments. The transition between the 1-step and 2-step domain, or between the cross section varying as A and $A^{0.8}$, is predicted to be in the region 4-8 BeV. The A dependence is shown in Fig. 41, for both experiments. The DESY experiment gives the A-dependence as $A^{0.95 \pm 0.02}$, while UCSB say it is of order $A^{0.9}$. Both experiments yield a value which is neither in one domain nor the other. There is also no observed change in slope as a function of energy. In Fig. 42, we show the energy dependence of the total cross section for several nucleii normalized to hydrogen; the black dots refer to the Santa Barbara experiment while the open circles represent the data from DESY. The consistency between the two experiments is very evident.

The curves show the energy dependence as calculated in the model of Brodsky and Pumplin for various values of the rho-nucleon cross section. The data clearly agree with a cross section of 19 mb or less, and disagree with the 30 mb cross section that would be expected from the SLAC-Cornell determination of $\sigma(\rho N)$. In addition it should be noted that the data do not agree with the 26 mb that is predicted by DESY/MIT experiment. The ratio of real to imaginary parts in the forward scattering amplitude have been taken from Fig. 7.

In Fig. 41, the A-dependence of the total cross sections, normalized to hydrogen, is plotted for energies between 5 and 18 BeV. The upper and lower lines reference the case of zero absorption and complete absorption respectively. The total cross section data agree very well between experiments, and for different energies, on a slope just a little less than the zero absorption limit. The other data points on the plot are the square root of the rho photoproduction cross sections normlized to hydrogen, from the SLAC and Cornell experiments.

From the optical theorem and rho dominance, it can be shown:

$$\frac{\sigma_T(\gamma A)}{\sigma_T(\gamma p)} = \sqrt{\left.\frac{\frac{d\sigma}{dt}(\gamma A \to \rho^o A)}{\frac{d\sigma}{dt}(\gamma p \to \rho^o p)}\right|_{t=0}} \qquad [V - 1]$$

This comparison of ratios is independent of nuclear physics and the absolute values of the vector dominance parameters -- both sides of the equation can be experimentally measured. The equality of Eq. [V - 1] is badly violated, as clearly shown in Fig. 41, where for lead the left-hand side is measured as ~ 140, while the right-hand side gives ~ 70, and for copper where it is 65 as against 30. This discrepancy has serious implications for vector dominance.

From a comparison with the experiments measuring the rho photoproduction on complex nucleii and from the rho cross section on protons, one can extract the value of thephoton-rho coupling constant using the A-dependence of the total cross section. Such a study gives $\gamma_\rho^2/4\pi \sim 0.35$.

[One comment should be made at this stage on the spectral functions used in the above detailed calculation.[74] The evaluations of the A-dependence of the total photon cross sections have been made using a symmetric, 110 MeV wide mass distribution for the rho, as seen by the storage rings.[29] Now clearly the dipion mass spectrum, as seen in photoproduction, is a very different shape, showing a large shoulder at low $\pi\pi$ masses. These 300-400 MeV dipions will be coherently produced and thereby cause appreciable shadowing at very low photon momenta. Therefore, the transition region calculated by these models will in fact be much more gradual than has been presented to data, although at high energies the results will be unchanged.]

We shall leave the total cross-section discussion for the moment, and return to it after reviewing the overall vector dominance model situation.

CHAPTER VI. Status of Photoproduction Experiments on Hydrogen.

We will quickly review the status of several photoproduction processes on protons, and then incorporate this data into the final picture of where we are with VDM

VI. 1. Compton Scattering at High Energies

Let us first look at some new data on Compton scattering at high energies. The experiment was performed at SLAC by the Ritson group[75], measuring proton compton scattering at energies of 5.5, 8.5, 11.5 and 17 GeV, in the momentum transfer range from 0.06 to 1.1 $(GeV/c)^2$.

The data was obtained by performing a coincidence between the SLAC 1.6 GeV/c spectrometer and a lucite shower counter to measure the scattered γ-rays. The angle and momentum of the recoil proton were determined using the spectrometer. Photoproduced π^o's were the main source of background in the experiment; however, since the solid angle of the shower counter matched to the spectrometer was small compared to the decay cone of the π^o(i.e. $\theta \sim M\pi/E_\pi$), the π^o contamination was strongly suppressed by using the shower counter. The remaining π^o contribution was measured directly by moving the shower counter out of the Compton plane. The main event selection was made by the spectrometer. The shower counter simply provided an additional kinematic constraint, largely geometric in nature and not strongly dependent on the energy resolution of the counter. This was important, since the high instantaneous rates at SLAC made a good energy measurement of the photon very difficult without severely limiting the rate.

The layout of the experiment is shown schematically in Fig. 43.

The acceptance of the system was well defined. The spectrometer determined the t-value, the t-acceptance and the effective target length. The acceptance in photon energy $\Delta k/k$ and the azimuthal angle Δp was determined by the vertical and horizontal slits in front of the shower counter. During the experiment Δt varied from .004 GeV/c^2 at the lowest t-values to .04 $(GeV/c)^2$ at 1.1 $(GeV/c)^2$,

$\Delta k/k$ was typically 10%, and $\Delta\phi$ varied from .6 mrad to 7 mrad depending upon the kinematics. $\Delta\phi$ was always small compared to $m_\pi E_\pi$.

As a check on the acceptance as well as the overall alignment of the system, cross sections for elastic e-p scattering were measured detecting the recoil proton in coincidence with the scattered electron. Elastic e-p scattering has the same kinematics as Compton scattering at high energy. The response of the shower counter to electron and photon beams is very nearly the same and the cross sections are well known for the momentum transfers of our experiment. The data was corrected for counter efficiencies, losses due to multiple scattering, and for radiative effects according to Meister and Yennie.[76] The agreement between the 18 GeV electron scattering data and other published data[77] is good. However, at lower energies the data from this experiment is systematically low and the agreement is only at about the 10% level. The authors claim that the discrepancy is still being studied because of its possible effect on the overall normalization.

Fig. 44 shows a γ-p coincidence peak for an incident photon energy of 12 GeV and $-t = .5\ (\mathrm{GeV/c})^2$. Plotted is the coincidence yield versus missing mass for the shower counter in and out of the Compton plane. The width of the peak is mainly due to multiple scattering of the recoil proton. The contribution from π^o photoproduction measured with the shower counter out of the Compton plane is small although the π^o cross section is comparable to the Compton cross section for this t-value and energy. This is because the solid angle of the shower counter is small compared to the π^o decay cone. Fig. 44 shows the result of subtracting the out-of-plane yield from the in-plane yield. The resultant curve is the experimental Compton yield. The yield goes to zero on both sides of the peak indicating that the accidental counts are properly subtracted and background from many-body processes is negligible. Since the π^o detection efficiency in the Compton plane (C) is slightly greater than the π^o detection efficiency (C') out of the Compton plane, a small residual π^o signal still remains in the Compton peak. This residual

π^o signal is given by (1-C'/C) x the measured π^o rate, and is generally small. For the yields of Fig. 44 it is less than a 1% correction. The largest correction was at 18 GeV and t = -1.1 GeV^2 where it was about 8%. Corrections for these residual π^o signals were determined by computing C'/C. We have checked the computation by moving the counter different distances out of the plane and by computing π^o cross sections using the computed values of C'/C and the π^o yields. The π^o cross sections determined in this way are in good agreement with earlier measurements on π^o photoproduction by the same group.(67)

The Compton data was corrected for counter efficiencies, loss from pair production of the scattered photon before the sweeping magnet, loss of incident photons before the SEQ, and the change in the Δt acceptance of the spectrometer due to energy loss of the proton in the target. The total corrections were about 30% and were largely determined experimentally. The total uncertainty introduced by these corrections, uncertainty in the acceptance and the uncertainty in the target density is estimated to be about 6%.

The corrected cross sections are shown in Fig. 45. The differential cross sections ($d\sigma/dt$) are plotted versus t for incident photon energies of 5.5, 8.5, 11.5, and 17 GeV. The solid lines through the data are least squares fits of the form $Ae^{Bt + Ct^2}$. The slope is essentially independent of energy and the average values of B and C are 6.2 $(GeV/c)^{-2}$ and .5 $(GeV/c)^{-4}$ respectively. The cross sections decrease slowly with increasing photon energy. In the range from -.1 $(GeV/c)^2$ to -1.1 $(GeV/c)^2$ we cannot fit our data to a single exponential. Fits to the data for $t \leq 0.6$ $(GeV/c)^2$ are consistent with a slope of 6$(GeV/c)^{-2}$. We conclude from this lack of shrinkage that the scattering is predominantly diffractive out to t of 0.6 $(GeV/c)^2$. The optical points at t=0 are computed from the measurements by Caldwell, et al.(73) of the total photoabsorption cross section using the optical theorem and from the dispersion relation results for $Re(f_1)$ of reference (22). The t=0 intercepts of the fits to our data are in fair agreement with these optical points, although on the average they are low.

The vector dominance model relates the amplitude for Compton scattering to the amplitude for photoproduction of transverse rho mesons, thus providing the following relation:

$$\frac{d\sigma}{dt}(\gamma p \rightarrow \gamma p) = \sum_{\rho,\omega,\phi} \frac{\alpha_\pi}{\gamma_V^2} \frac{d\sigma}{dt}(\gamma p \rightarrow V p) \qquad [VI - 1]$$

where the sum is over the known vector mesons, and $\gamma_V^2/4\pi$ is the photo-vector meson coupling constant. They evaluated this equation as follows:

(a) the coupling constant $g_{\gamma V}$ were taken from the Orsay storage ring measurements.

(b) the differential cross sections for ρ and ϕ photoproduction were taken from our earlier measurements.[67]

(c) the ω cross sections were assumed to be 1/9 of the ρ cross section. The fits do not depend strongly upon this assumption.

The results are shown in Fig. 45 as the dashed lines. They are systematically lower and the slope is steeper than the Compton scattering data. Evaluation using the recent results of Ballam, et al.,[41] for ρ and ω photoproduction gives a slope that is in better agreement with the data, but the absolute discrepancy is worse. The agreement is not improved by using the values of $g_{\gamma V}^2$ measured on the photon mass shell instead of the storage ring values, but require a value more in the neighbourhood of 0.3.

VI. 2. Forward Rho Production and Total Photon Cross Section:

We may derive VDM relationships between the forward rho cross section on protons, and the total γp hadronic cross section:

$$\frac{d\sigma}{dt}(\gamma p \rightarrow \rho p) = \frac{\gamma_\rho^2}{\alpha_\pi} \frac{d\sigma}{dt}(\gamma p \rightarrow \gamma p) \qquad \text{from VDM.}$$

Now from the optical theorem we may relate the forward elastic scattering amplitude to the total cross section;

$$\frac{d\sigma}{dt}(\gamma p \rightarrow \gamma p) = \frac{1}{16\pi} \sigma_{tot}^2 (\gamma p)$$

Thus,

$$\frac{d\sigma}{dt}(\gamma p \rightarrow \rho p) = \frac{\gamma_\rho^2}{16\pi^2\alpha} \sigma_{tot}^2(\gamma p) \qquad [VI - 2]$$

assuming the ρ production to be purely imaginary. For a real to imaginary ratio, $\alpha_{\rho N}$, in the forward scattering amplitude this becomes:

$$\frac{d\sigma}{dt}(\gamma p \to \rho p) = \frac{\gamma_\rho^2}{16\pi^2\alpha}\,\sigma_{tot}(\gamma p)\,(1+\alpha_{\rho N}^2) \quad \ldots \quad [VI-3]$$

This same forward rho production cross section is related to the total ρ-N cross section via similar arguments:

$$\frac{d\sigma}{dt}(\gamma p \to \rho p) = \frac{\alpha\pi}{\gamma_\rho^2}\cdot\frac{d\sigma}{dt}(\rho p \to \rho p) \qquad \text{by VDM}$$

$$= \frac{\alpha}{16\gamma_\rho^2}\,\sigma_{tot}^2(\rho p) \qquad \text{by Optical Theorem} \quad [VI-4]$$

or

$$= \frac{\alpha}{16\gamma_\rho^2}\cdot\sigma_{tot}^2(\rho p)(1+\alpha_{\rho N}^2) \text{ for some real} \quad [VI-5]$$

part in the ρ-N scattering amplitude. Therefore we have:

$$\frac{\gamma_\rho^2}{16\pi^2}\,\sigma_{tot}^2(\gamma p) = \frac{d\sigma}{dt}(\gamma p \to \rho p) = \frac{\alpha}{16\gamma_\rho^2}\,\sigma_{tot}^2(\rho p) \qquad [VI-6]$$

We will not review the individual experiments on the total photon cross-sections on hydrogen, or the forward rho photoproduction on protons, but merely summarize the situation. In Fig. 6, the world summary of total cross-section data as a function of energy is shown, and in Fig. 46, the published data on forward rho cross-sections. Around 8 GeV the isovector contribution to the total cross-section is about 100 μb, while the forward cross-section from Fig. 44 would be around 125 $\mu b/(GeV/c)^2$. However, we will discuss in detail in Part B some new experimental evidence that the Söding model gives a correct explanation of the dipion mass spectrum and that when applied in its general form, it leads to a reduction in the rho cross section of ~ 30%. This is also confirmed by the SLAC wire chamber measurement. Therefore, I would take 100 $\mu b/(GeV/c)^2$ as a better estimate of the forward photo-rho cross-section. If we then try to satisfy equation [VI - 6], we

find: $\gamma_\rho^2/4\pi$ must be ~ 0.34

and $\sigma(\rho N)$ must be ~ 20 mb .

This is in surprising agreement with the total photon absorption in complex nucleii and not at all in agreement with either the colliding beam experiments[29] or rho photoproduction in complex nucleii described in Chapter II.

In addition, it is interesting to note that the solid line in Fig. 46 is 1/200 of the average of the π^+p and π^-p total cross-sections.

By combining quark model and VDM predictions the following relationship may be obtained:

$$\sigma_\tau(\gamma p) = \frac{\alpha}{4} \cdot \left(\frac{4\pi}{\gamma_\rho^2}\right) \cdot \frac{1}{2} \left[\sigma_\tau(\pi^+ p) + \sigma_\tau(\pi^- p)\right] . \qquad [VI - 6]$$

This relationship is satisfied for $\gamma_\rho^2/4\pi \sim (0.35 - 0.4)$

VI. 3. Quark Model Predictions:

We may also use the quark model sum rule

$$\sigma_\tau(\rho p) = \sigma_\tau(\omega p) = \frac{1}{2}\left[\sigma_\tau(\pi^+ p) + \sigma_\tau(\pi^- p)\right] = \sigma_\tau(\pi^o p)$$

to help derive the vector dominance coupling constant.

Using the optical theorem we may rewrite the above equation as:

$$\frac{d\sigma}{dt}(\rho p \to \rho p) = \left[\frac{1}{2}\sqrt{\frac{d\sigma}{dt}(\pi^+ p)} + \frac{1}{2}\sqrt{\frac{d\sigma}{dt}(\pi^- p)}\right]^2 \qquad [VI - 7]$$

Now from VDM we may write

$$\frac{d\sigma}{dt}(\gamma p \to \rho p) = \frac{\alpha}{4} \cdot \left(\frac{4\pi}{\gamma_\rho^2}\right) \frac{d\sigma}{dt}(\rho p \to \rho p)$$

Thus a comparison of the forward rho photoproduction cross section with the forward elastic $\pi^{\pm}p$ scattering cross sections will allow a determination of $\gamma_\rho^2/4\pi$. Taking the value to be $\sim 100\ \mu b(GeV/c)^2$ around 8 GeV, this leads to $\gamma_\rho^2/4\pi \sim 0.8$.

VI. 4. Single Pion Photoproduction:

There is considerable amount of data on the single pion photoproduction processes, from (1-16) GeV.[78]

$\gamma N \rightarrow \pi N$

The vector dominance model relates this reaction to rho production by pions, via

$$\gamma N \rightarrow \pi N = \rho_{\perp}^{o} N \rightarrow \pi N \quad \text{by VDM},$$

where the $\rho_{\perp}^{o}$ represents transversely polarized rho mesons. Since the rho meson can have any of its three polarization states occupied (while the real zero mass photon can only be transversely polarized), we have to project out the transversely polarized component in making comparison with the photon processes.

Using time reversal invariance in the strong interactions, the above relationship can be extended:

$$\gamma N \rightarrow \pi N = \rho_{\perp}^{o} N \rightarrow \pi N \equiv \rho_{\perp}^{o} N.$$

An interesting test of VDM is to check out this relationship using photoproduction data on the one hand, and strong interaction data on the rho production on the other hand.

There are two single pion production photon reactions:

$$\gamma p \rightarrow \pi^{+} n$$

$$\gamma n \rightarrow \pi^{-} p$$

These reactions are charge symmetric and if the photon had definite isospin the cross sections would be equal. The realative sign of the isoscalar and isovector photon amplitudes is difficult in π^{+} and π^{-} production, thus any interference between the two types of amplitudes will appear with opposite signs in the two reactions. Experimentally, the ratio $(\frac{\pi^{+}}{\pi^{-}})$ is far from unity (see Fig. 47) implying interference between isovector (or ρ-like) and isoscalar (or ω, ϕ-like) photons. We shall ignore the ϕ contribution, since the coupling is experimentally small.

In analysing these reactions, the effects of the interference is removed by considering the sum of π^{+} and π^{-} cross sections:

$$\frac{1}{2}\left[\frac{d\sigma}{dt}(\gamma n \rightarrow \pi^{-} p) + \frac{d\sigma}{dt}(\gamma p \rightarrow \pi^{+} n)\right] = \frac{\pi\alpha}{\gamma_{\rho}^{2}} \cdot \rho_{11} \frac{d\sigma}{dt}(\pi^{-} p \rightarrow \rho^{o} n) + \frac{\pi\alpha}{\gamma_{\omega}^{2}} \cdot \rho_{11} \frac{d\sigma}{dt}(\pi^{+} n \rightarrow \omega p)$$

[VI - 8]

where the density matrix element ρ_{11} is evaluated in the helicity frame and projects out the transversely polarized ρ, ω's. The results of a typical analysis[79] are shown in Fig. 48, where $\gamma_\rho^2/4\pi$ was found to be ~ 0.4.

The single pion reactions show very strong forward peaking at very small momentum transfers. The cross section increases by a factor of 2 from $t \sim m_\pi^2$ to $t \sim 0$, (see Fig. 49). To date no hadronic experiments have had sufficient momentum transfer resolution or sufficient statistics to see this sharp forward spike in rho production by pions. Preliminary results from an experiment at SLAC should be available later this year.

These tests can be extended by using polarized photons. The difference between π^+ and π^- photoproduction cross sections for photon polarization perpendicular to the production plane can be related to the ρ alignment via

$$1/2\ (\sigma_\perp^+ + \sigma_\perp^-) = \frac{\pi\alpha}{\gamma_\rho^2}\left[(\rho_{11} + \rho_{1-1})\ \frac{d\sigma}{dt}\right]_{\pi^- p \to \rho^o n} \qquad \text{[VI - 9]}$$

Fig. 50 shows a comparison of the data for $\gamma_\rho^2/4\pi$ taken to be 0.52 (i.e., the colliding beam value). Clearly agreement could only be obtained with a value of $\gamma_\rho^2/4\pi \sim 0.3$.

Notice that whenever we observe the photon going explicitly into a rho meson, we find $\gamma_\rho^2/4\pi \sim 0.7$ to 0.8, while for processes involving hadrons in general, the coupling constant is coming out ~ 0.3 to 0.4.

CHAPTER VII. Summary of VDM Problems and Description of a Simple Model:

In the preceding chapters we have reviewed the experimental situation with regard to photoproduction and the vector dominance model. The main features which we have discussed are:

1. The rho photoproduction A dependence gives a total rho-nuclear cross-section of $\sim$ 29 mb, and a photon-rho coupling constant of $\sim$ 0.7.

2. The photon-vector meson coupling constant, as measured with real photons ($q^2 = 0$), are larger than the coupling constants measured with the photon on the

vector meson mass shell, ($q^2 \simeq m_v^2$).

3. The total photon-hadron cross section has an A-dependence which is less than A (i.e. not infinite mean free path), but greater than $A^{0.8}$ - which would be expected from rho dominance. In fact a detailed examination of those experiments yields a determination of the photon-rho coupling constant equal to ~ 0.3.

4. The data on hydrogen are no less confusing, yielding $\gamma_\rho^2/4\pi \sim 0.3$ for compton scattering analysis and the relationship between the forward rho cross section and the total photon cross section, and $\gamma_\rho^2/4\pi = 0.7$ for comparison of the forward rho cross section with the $\pi^{\pm}p$ cross section through the quark model.

5. The values of the coupling constants discussed above are in disagreement with those obtained in the colliding beam experiments.

This makes for a disquieting kind of summary. We may accept the factor of two discrepancies as the limits of applicability of VDM and be content that it is such a useful model, i.e. that the photon behaves so much like a rho meson in its hadronic interaction. On the other hand we might look for clues as to how to improve the agreement. The differences between the $\gamma_\rho^2/4\pi$ deduced from processes where the photon couples to a rho, and processes where the photon couples to other hadrons, and the fact that the shadowing observed in the total cross-section measurements is finite but not as much as would be expected from rho dominance, leads naturally to a simple model.

The simple model violates rho dominance but not the spirit of vector dominance, and it allows a simple description of the above phenomena. Let us examine once more the current field identity, (equation [I - 12]),

$$j_\mu^{\rho m}(x) = -\Sigma\, M_v^2/2\gamma_v$$

and rather than making the assumption that the rho meson saturates the electromagnetic current, we postulate a series of additional vector mesons of higher mass, or a continuum of p-wave pion pairs, which also couple to the photon. We parameterize these additional contributions as an "equivalent meson", ρ' such that:

$$\rho' = \Sigma_{V'} \quad , \quad M_{\rho'} = \overline{M}_{V'}$$

$$\text{and} \qquad \gamma^2_{\rho'} = \Sigma \gamma^2_{V'}$$

Where ρ' represents the sum over the other P-wave states, $M_{\rho'}$ is the "average" mass of the additional states, and $\gamma^2_{\rho'}$ is the "average" coupling of the photon to these new states.

In this picture the hadronic interaction of the photon is mediated by both the ρ and the ρ' (see Fig. 51), the relative amounts being given by the coupling constants[43] $\gamma^2_\rho/4\pi$ and $\gamma^2_{\rho'}/4\pi$. The absorption of the photon will depend on the masses of the ρ and ρ' (i.e. we only have "strong" absorption when the phase difference exp. $[(M^2_V/2k) \cdot R]$ is small), a d their total cross sections $\sigma(\rho N)$ and $\sigma(\rho' N)$.

It should be emphasized that we only picture this additional photon coupling as being a single particle -- it may be many resonances or, indeed, it may be just a strong coupling to a continuum of hadron states extending to high masses.

If the mean mass of the ρ' is greater than 2 BeV, then at present energies, the contribution from the other states will not give rise to a coherent amplitude in photoabsorption. This means that the photon absorption will have a contribution which has essentially zero absorption (the ρ' amplitude) and a contribution which has strong absorption (the ρ amplitude). The A-dependence, and the k-dependence of the total photon cross section may be used to determine the relative amounts of the ρ and ρ' amplitudes, and also the minimum mass of the ρ'. Measurement of the coherent rho photo-production cross section may be used to fix the parameters of the ρ amplitude, since even if $\rho' \rightarrow \rho$ coupling is substantial, the ρ' amplitude is not coherent at these energies and does not contribute.

Quantitatively, the coherent rho experiment gives $\sigma(\rho N) \sim 29$ mb, and $\gamma^2_\rho/4\pi \sim 0.7$. The fit to the total cross section data implies the ρ and ρ' amplitudes are roughly equal and that the effective mass of the ρ' be greater than 3000 MeV. Figures 52 and 53 show the A-dependence and k-dependence respectively, as calculated from this model. They are in good agreement with the data.

We return now to the discrepancy, between Eq. [V - 1] and the measured data, discussed above. The equation should now be rewritten as:

$$\frac{\sigma_{tot}(\gamma A)}{\sigma_{tot}(\gamma p)} = \frac{\left[\frac{1}{\gamma_\rho^2}\frac{d\sigma}{dt}(\gamma A \to \rho^o A)\right]^{1/2} + \left[\frac{1}{\gamma_{\rho'}^2}\frac{d\sigma}{dt}(\gamma A \to \rho' A)\right]^{1/2}}{\left[\frac{1}{\gamma_\rho^2}\frac{d\sigma}{dt}(\gamma p \to \rho^o p)\right]^{1/2} + \left[\frac{1}{\gamma_{\rho'}^2}\frac{d\sigma}{dt}(\gamma p \to \rho' p)\right]^{1/2}}$$

The RHS of this equation is $(70 + 208)/(1 + 1) = 139$, for the lead case. The denominator has equal contributions from the ρ and ρ' amplitudes as required by the model fits discussed above, while in the numerator the 70 comes from the measured ρ cross section on lead, and the 208 is the ρ' amplitude contribution with no absorption or shadowing (i.e., the heavy mass ρ' has essentially zero absorption and consequently $\sigma(A) \propto A$). We see, then, that the new form of the equation is satisfied.

To show that this model also works for hydrogen data, consider the relationship (omitting the ρ' amplitude, for the moment),

$$\sigma_{tot}(\gamma p) \propto \left[\frac{1}{\gamma_\rho^2}\frac{d\sigma}{dt}(\gamma p \to \rho p)\right]^{1/2} + [\text{term for } \omega \text{ and } \phi]^{1/2}$$

Here the total photon cross section on hydrogen is related to the forward Compton amplitude, by the optical theorem, which in turn is related to the forward vector meson cross sections by VDM. This relationship has been shown to work well for $\gamma_\rho^2/4\pi \sim 0.3$ to 0.4. Within our simple model, we now rewrite this equation as:

$$\sigma_{tot}(\gamma p) \propto \left[\frac{1}{\gamma_\rho^2}\frac{d\sigma}{dt}(\gamma p \to \rho p)\right]^{1/2} + [\text{term for } \omega \text{ and } \phi]^{1/2} + \left[\frac{1}{\gamma_{\rho'}^2}\frac{d\sigma}{dt}(\gamma p \to \rho' p)\right]^{1/2}$$

This relationship is also well satisfied for $\gamma_\rho^2/4\pi \sim 0.8$ and roughly equal ρ and ρ' amplitudes.

We have shown that with a simple model which assumes there are contributions to the hadronic interaction of the photon in addition to the ρ meson, that the

new data on total photon cross sections can be explained and made compatible with the coherent rho production data. In addition, we have shown that this model is consistent with the hydrogen photoproduction data.

We shall learn in the next chapter, that there is no evidence for any additional vector mesons up to masses of ~ 2000 MeV. This implies that the additional coupling of the photon, which we are discussing here, must be due either to the continuum of P-wave states or that the additional mesons be higher in mass.

Recent experiments at ADONE indicate a possible strong coupling of the photon to hadronic final states, (non-resonant), in the 2 GeV region. These preliminary results may be evidence for the existence of the additional photon couplings discussed above.

CHAPTER VIII. Search for High Mass Vector Mesons

Several groups have searched for evidence of the photoproduction of high mass vector mesons. The existence of such particles would have a great impact on the vector dominance model. It is of general interest, beyond the VDM, to search for such particles since the quark model and the Veneziano model predict the existence of states at masses of ~ 1250 MeV and between 1500-1600 MeV.

The experiments fall into three main classes -- 1) looking at a particular hadronic final state and studying the mass spectra[80-83]; 2) using a missing mass spectrometer and averaging over all decay modes[84]; 3) looking in lepton pair mass spectra.[85,86] I would like to describe our experiment at SLAC and then try to summarize the field.

The SLAC experiment[80] studied the dipion mass spectrum produced from a Be target by 16 GeV bremsstrahlung beam. The apparatus was the same as that discussed in Chapter II above. The geometry of the system was arranged so that the dipion mass acceptance (for energies $\geq$ 14 GeV) extended from 0.7 to 2.5 GeV, and did not vary much between 1000 and 2000 MeV.

As the incident photon and target recoil were not observed, each event was analyzed assuming the reaction was of the form $\gamma + A \rightarrow A + \pi^+ + \pi^-$. A comparison of the energy spectra of the dipions and the incident photon beam reveals that for $E_{\pi\pi} \geq 14$ BeV, the upper limit on the inelastic contamination is 10% for $M_{\pi\pi} \leq 1.0$ BeV and 25% for $1.0 \leq M_{\pi\pi} \leq 2.0$ BeV.

The spectrometer acceptance was unfolded from the observed spectra with the assumption that the cross section was azimuthally uniform in the helicity system.

We observed a total of 620 events in the intervals $E_{\pi\pi} \geq 14$ BeV, $t\text{-}t_m \leq 0.3$ BeV/c^2, $0.9 \leq M_{\pi\pi} \leq 2.0$ and $-0.6 \leq \cos\theta_{\pi\pi} \leq 0.6$. The distribution of weighted events versus polar decay angle $\theta_{\pi\pi}$ evaluated in the helicity system is shown in Fig. 54. The cutoff at $\cos\theta_{\pi\pi} = 0.6$ is imposed by the acceptance. The data are consistent with p-wave dominated dipions following a $\sin^2\theta_{\pi\pi}$ distribution indicated by the smooth curve.

The momentum transfer distribution is shown for two mass regions in Fig. 55. It is clear from the data that this distribution changes significantly as the dipion mass is varied. This change can not be explained by the nuclear form factor. In Fig. 56 we plot versus $M_{\pi\pi}$ the ratio of the forward ($t = t_{min} = -(M_{\pi\pi}^2/2E_{\pi\pi})^2$) cross section to the cross section at $t\text{-}t_{min} = -0.12$(BeV/c). The curves are calculations of the expected ratio assuming (a) that the effect is due solely to the variation of the nuclear form factor with t_{min}, ($e^{45t_{min}}$), and (b) through (d) that, in addition to (a), there is a Drell-type dipion production that interferes with the rho production.[87] The separate curves refer to different parameterisation of the rho meson width.[88] The model predicts that the t-slope of the elementary process $\gamma + p \rightarrow p + \pi^+ + \pi^-$ depends upon $M_{\pi\pi}$ and is supported, for $M_{\pi\pi} \leq 1.4$ BeV/c^2, by experiment.[89]

In Fig. 57 we show the weighted yield (for $t\text{-}t_{min} \leq 0.046$ (BeV/c)^2) versus $M_{\pi\pi}$ and the expectations (normalized to the rho peak) based on the model of rho production plus interfering Drell-type dipions.[87,88] This small t region, where

coherence dominates would most sensitively reveal the presence of any high mass vector mesons.

There is no agreement between the data and the model dependent calculations as displayed in Figs. 56 and 57. Although the precise manner in which the rho tail disappears is unknown we believe that the widths Γ_b and Γ_d represent the extremes and that the truth is intermediate to these. An upper limit for any dipion production in excess of rho and Drell-type production can be deduced from the difference of the data and curve d, Fig. 57. Assuming that all dipions have a $\sin^2\theta_{\pi\pi}$ distribution we deduce, for example, that at $M_{\pi\pi} = 1.4\text{-}1.6$ BeV/c^2 the upper limit $10^{-2} \frac{d\sigma}{dM_{\pi\pi}} (M_{\pi\pi} = M_\rho)$.

Two other experiments (at CEA[82] and at Cornell[81]) have measured the 2π mass spectra from nuclear targets, but only for forward angles and at photon energies below 9 GeV. The Cornell mass plot is shown in Fig. 58. In addition, the HBC experiments[83] have information on the 2π mass spectrum produced from protons. A histogram summing over all experiments is shown in Fig. 59. (The DESY-MIT group have finished an experiment studying this question, but at present no results are available.)

The missing mass survey was performed by the Ritson group at SLAC using the SLAC 1.6 GeV/c spectrometer.[84] They searched for the production of resonances with masses between 1.3 GeV and 2 GeV at a momentum transfer, $t = -0.2$ $(\text{GeV}/c)^2$, and ~ 17 GeV photon energy. The low t value and high energy should be specially suitable for singling out states that could be diffractively produced. In particular, they should have been sensitive to any new vector mesons in this mass range.

A single integral yield curve shows structure arising from both the high energy photoproduction of high mass states and from lower energy photon production of single pion states or other low mass states. Therefore, they used a subtraction of two sweeps taken at 17.8 GeV and 16 GeV peak energies. Fig. 60 shows both the unsubtracted and subtracted yields. The integral yield curves represent on the order of 2.10^7 counts each. Any produced particle would show up as a peak in

the subtracted yield curve. No such peak can be seen in the data.

This observation is important since it searches for the effect in all decay modes and does not require a large branching ratio into a specific mode (like the 2π mode, discussed above). The results are summarized in Table XV.

There have been two experiments[85,86] measuring $\mu^+\mu^-$ mass spectra up to 2000 MeV. One such spectrum is shown in Fig. 61, or rather the ratio between the observed spectrum and that expected from Bethe-Heitler production. The results of these experiments are also summarized in Table IX.

In summary, there is no evidence of any sharp structure (i.e., width $\sim$ 100-200 MeV) in the high mass photoproduction surveys.

CHAPTER IX. Conclusions

We have reviewed the experimental situation in vector meson photoproduction and total photon absorption measurements and have shown that vector dominance is qualitatively in good shape. There are quantitative problems, but a simple model has been proposed to explain these discrepancies. We require some other strong coupling to the photon (other than the ρ, ω, ϕ) and the acceptance of some q^2 dependence at the γ-v vertex (to explain the difference between the colliding beam value of 0.5 and the model value of 0.7) and then the model would be in satisfactory shape. Searches for higher vector meson to satisfy the first of these criteria have yielded negative results, although a hint of some confirmation of such an effect is coming from ADONE these days. The A-dependence of the total photoabsorption cross-section being $A^{0.9}$ is already a strong hint that such coupling to heavy objects does exist -- however, we will see. Finally, the q^2 dependence of the γ-v vertex can not be judged, yea or nay, from present experiments - but it is certainly not unreasonable.

In conclusion, I think that we should not be surprised or disappointed at the detailed troubles and "fixing-up" of VDM, but that rather we should be surprised that such a simple model so successfully ties together so many different processes.

References and Footnotes

1. S. Ting, Int. Conf. on High Energy Physics, Vienna, 1968.
2. E. Lohrman, Int. Conf. on High Energy Physics, Lund, 1969.
3. R. Diebold, Boulder Conference on High Energy Physics, 1969.
4. A. Silverman, Int. Symp. on Electron and Photon Interaction, Liverpool, 1969.
5. M. L. Good and W. D. Walker, Phys. Rev. 120, 1859 (1969); A. S. Goldhaber and M. Goldhaber, Preludes in Theoretical Physics (North Holland, Amsterdam, 1966).
6. S. D. Drell and J. S. Trefil, Phys. Rev. Letters 16, 552 (1966).
7. G. Bellettini, Nuclear Physics 79, 609 (1966).
8. A. S. Goldhaber, Phys. Rev. Letters 15, 802 (1969).
9. Berkeley-BNL-Orsay-Milan Collaboration, private communication (H. H. Bingham).
10. Yennie, These Procedings.
11. E. J. Moniz, G. D. Nixon and J. D. Walecka, Paper presented to the Third Int. Conf. on High Energy Physics and Nuclear Structure, Columbia, New York (1969).
12. G. Van Bochmann, B. Margolis and C. L. Tang, P.L. 30B, 254, (1969).
13. K. S. Kolbig and B. Margolis, N.P. B6, 85 (1968).
14. J. S. Trefil, N.P. B11, 330 (1969); P.R. 180, 1379 (1969).
15. R. Hofstadter, Ann. Rev. Nucl. Sci. 7, 231 (1957); H. R. Collard, L. R. B. Elton, R. Hoffstadter, and H. Schoper, in Landolt-Börnstein Numerical Data and Functional Relationships in Science and Technology, edited by K.-H. Hellwege (Springer-Verlag, Berlin, 1967), New Series Group I, Vol. 2.
16. See for example;
    R. G. Glauber and G. Matthiae, Istitute Superiore di Sanita, Rome, Italy, Report No. ISS 67/16, 1967 (unpublished).
    A. Silverman, Cornell University Report No. CLNS-73 (1969).
17. H. Alvensleben, DESY 70/6 and PRL.
18. K. Gottfried and D. I. Julius, Cornell Preprint CLNS-66 (1969).
19. J. Swartz and R. Talman, Cornell University Report No. CLNS-79, (1969).

20. See for example, A. Silverman, p. 71, Int. Symposium on Electron and Photon Interactions, Liverpool, Sept. 1969.

21. Taken from D. W. G. S. Leith, Invited talk presented at Third Int. Conf. on High Energy Physics and Nuclear Structure, Columbia University, September 1969.

22. M. Damashek and F. J. Gilman, Stanford Linear Accelerator Center Report to be published.

23. W. R. Frazer and J. R. Fulco, Phys. Rev. 117, 1603 (1960).

24. Y. Nambu, Phys. Rev. 106, 1366 (1957).

25. J. J. Sakurai, p. 41, Proceedings of the International School of Physics for 1963. (Academic Press, New York and London, 1963).
Y. Nambu and J. J. Sakurai, PRL 8, 79 (1962).
J. J. Sakurai, Ann. Phys. (N.Y.) 11, 1 (1960).

26. H. Joos, Schladming Lectures (1967), Acta Physica Austriaca, Suppl. IV (1967).

27. D. Schildknecht, DESY Reports 69/10 (1969).

28. N. M. Kroll, T. D. Lee and B. Zumino, Phys. Rev. 157, 1376 (1967).

29. Gourdin, These Procedings.

30. M. Gell-Marn, D. Sharp and W. G. Wagner, PRL 8, 261 (1962).

31. A. Barbaro-Galtieri, "Review of Particle Properties" - Rev. Modern Physics 42, 87 (1970).

32. L. J. Lanzerotti, P.R. 166, 1365 (1968).

33. J. G. Asburg, Phys. Rev. Letters 19, 865 (1967); Phys. Rev. Letters 20, 227 (1968).

34. H. Blechschmidt, Nuovo Cimento 52A, 1348 (1967).

35. G. McClellan, Phys. Rev. Letters 22, 377 (1969).

36. F. Bulos, Phys. Rev. Letters 22, 490 (1969).

37. J. Ballam, Stanford Linear Accelerator Center Report No. SLAC-PUB-530 (1968), Nucl. Instr. and Methods.

38. F. Bulos, "Photoproduction of Rho Mesons at 9 BeV," in Proc. of the Fourteenth Int. Conf. on High Energy Physics, Vienna, Austria (1968);
M. Beniston, "On Line Analysis of Wire Spark Chamber Data," in Fifteenth IEEE Nuclear Science Symposium, Montreal, Canada (1968), to be published;

R. Russell, "On-Line Wire Spark Chamber Data Acquisition System," in Fifteenth IEEE Nuclear Science Symposium, Montreal, Canada (1968), to be published; F. Bulos, in Proceedings of the Int. Symposium on Nuclear Electronics and Institute for High Energy Physics, Versailles, France (1968), to be published and S. H. Williams et al. SLAC-PUB 547.

39. P. Söding, Phys. Rev. Letters 19, 702 (1966).

40. D. Yennie - See G. McClellan, Paper presented to Int. Conf. on High Energy Physics, Kiev, Sept. 1970.
Jon Pumplin, SLAC-PUB.

41. J. Ballam, SLAC-PUB and PRL.

42. The coordinate system is defined with z-axis as the line-of-flight of the rho in the rho center-of-mass.

43. The coordinate system is defined with the z-axis as the line-of-flight of beam particle in the rho center-of-mass.

44. J. Ballam, Stanford Linear Accelerator Center Report, to be published; Y. Eisenberg, Phys. Rev. Letters 22, 669 (1969).

45. F. Bulos, p. 462, Contribution to the APS Boulder Conference on Particles and Fields (1969).

46. G. McClellan, Phys. Rev. Letters 22, 374 (1969).

47. We define the photon-rho coupling constant to be $em_\rho^2/2\gamma_\rho$ but, by convention, will deal with the quantity $\gamma_\rho^2/4\pi$.

48. The optical model analysis has been discussed in detail by: R. Glauber, Lectures in Theoretical Physics (Interscience, N.Y.), Vol I(1959); S. D. Drell and J. S. Trefil, Phys. Rev. Letters 16, 552 (1966); K. S. Kölbig and Margolis, Nuclear Physics B6, 85 (1968).

49.

50. G. McClellan, Contribution to International Conference on High Energy Physics, Kiev, Sept. 1970.

51. T. Bauer, Ph.D. Thesis, Cornell University, 1970.

52. E. D. Bloom et al., Stanford Linear Accelerator Center Report No. SLAC-PUB 53 (1969); D. O. Caldwell et al., Paper submitted to the 1969 Int. Symposium on Electron and Photon Interactions at High Energies, Liverpool, England (1969); M. Meyer et al., Paper submitted to the 1969 Int. Symposium on Electron and Photon Interactions at High Energies, Liverpool, England (1969); J. Ballam et al., Paper submitted to the 1969 Int. Symposium on Electron and Photon Interactions at High Energies, Liverpool, England (1969); J. Ballam et al., Phys. Rev. Letters 21, 1541 (1968).

53. H. Alvensleben et al., N. P. B18, 333 (1970).

54. M. Ross, L. Stodolsky, Phys. Rev. 149, 1172 (1966).

55. H. J. Behrend et al., P. R. L.

56. H. J. Behrend et al., P. R. L.

57. DESY HBC Collaboration, P. R. 175, 1669 (1968).
Cambridge HBC Collaboration, P. R. 155, 1468 (1967).
J. Ballam et al., SLAC-PUB-729 (1970).

58. G. McClellan et al., P.R.L. 24, 554 (1969).

59. A. M. Boyarski et al., P.R.L. 24, 1343 (1969).

60. G. Wolf, Phys. Rev. 182, 1588 (1969).

61. U. Becker et al., Contribution to the Int. Conf. on High Energy Physics, Vienna, Sept. 1968.

62. G. McClellan et al., Cornell Preprint, CLNS-70.

63. T. Das, V. S. Mathur and S. Okubo, P.R.L. 19, 470 (1967).

64. R. J. Oakes and J. J. Sakurae, P.R.L. 19, 1266 (1967).

65. R. L. Anderson et al., Contribution to the International Conference on High Energy Physics, Kiev, Sept. 1970.

66. R. L. Anderson, et al., Nuclear Instruments and Methods 66, 328 (1968).

67. See for example, R. L. Anderson, et al., Phys. Rev. D1, 27 (1970).

68. R. J. Glauber, Lectures in Theoretical Physics, Interscience Publishers, Inc., Vol, 315 (1959).
V. Franco and R. J. Glauber, Phys. Rev. 142, 1195 (1966).
V. Franco and E. Coleman, Phys. Rev. Letters 17, 827 (1968).
D. Harrington, Phys. Rev. Letters 21, 1496 (1968).

69. Harold Ogren, thesis, Cornell Univ., 1970 (unpublished).

70. F. Partovi, Ann. Phys. 27, 79 (1964).

71. K. Lassila, et al., Phys. Rev. 126, 881 (1962).

72. M. Meyer et al., Paper submitted to 1969 Int. Symposium on Electron Photon Physics at High Energies, Liverpool, England.

73. D. O. Caldwell et al., Paper submitted to the Third Int. Conf. on High Energy Physics and Nuclear Structure, Columbia, New York (1969).

74. K. Gottfried and D. R. Yennie, Cornell University Report No. CLNS-51; S. J. Bordsky and J. Pumplin, Stanford Linear Accelerator Center Report No. SLAC-PUB-554 (1969); B. Margolis and C. L. Tang, Nucl. Phys. B10, 329 (1969); M. Nauenberg, Phys. Rev. Letters 22, 556 (1969).

75. R. L. Anderson et al., Contribution to Int. Conf. on High Energy Physics, Kiev, Sept. 1970.

76. N. Meister and D. Yennie, P.R. 130, 1210 (1963).

77. T. Gaussens et al., P.R. 142, 922 (1966).

78. P. Heide et al., P.R.L. 21, 248 (1968).
A. M. Boyarski et al., P.R.L. 20, 300 (1968).

79. R. Diebold and T. A. Poirier, P.R.L. 20, 1532 (1968).
A. Bialas and K. Zalewski, P.L. 28B, 436 (1969).
J. T. Donohue and H. Hogaasen, P.L. 25B, 554 (1967).
M. Krammer and D. Schildknecht, N.P. B7, 583 (1968).

80. F. Bulos et al., Submitted to Meson Spectroscopy Meeting, Philadelphia, May 1970; SLAC-PUB 751 (submitted to P.R.L.).

81. G. McClellan et al., P.R.L. 23, 718 (1969).

82. N. Hicks et al., P.L. 29B, 602 (1969).

83. J. Ballam et al., Contribution to Int. Symp. on Electron and Photon Interactions at High Energy, Liverpool, 1969.

84. R. Anderson et al., SLAC-PUB 644.

85. P. Rothwell et al., P.R.L. 23, 1521 (1969).

86. S. Hayes et al., P.R.L. 24, 1369 (1970).

87. P. Söding, Phys. Letters 19, 702 (1966).

88. In Figs. 3 and 4, curves (b)-(d) assume different functions for the rho width:

$$\Gamma_b = \Gamma_\rho \frac{M_\rho}{M_{\pi\pi}} \frac{q^3}{q_\rho^3}$$

$$\Gamma_c = \Gamma_b \frac{1 + R^2 q_\rho^2}{1 + R^2 q^2}$$

$$\Gamma_d = \Gamma_\rho \text{ for } M_{\pi\pi} \geq M_\rho$$

with q the pion momentum in the π-π c.m., $M_\rho = 0.765$ GeV/c^2, $\Gamma_\rho = 0.140$ BeV, and $R^2 = 2.3$ (GeV/c)$^{-2}$.

89. H. Bingham et al., P.R.L. 24, 955 (1970).

FIGURE CAPTIONS

Fig. 1. Feynman graphs for a) diffractive elastic scattering of pions on a nucleon and b) diffractive photoproduction of rho mesons on a nucleon.

Fig. 2 Schematically showing the use of different sized nucleii to measure the nuclear absorption of the short-lived rho particle.

Fig. 3. Differential cross-section for a diffractive process, showing the coherent and incoherent contributions. The dotted line represents a straight extrapolation of the large momentum transfer region, while the dashed line represents an optical model calculation.

Fig. 4. The nuclear radius as a function of A, as determined by Alvensleben, et al.[17].

Fig. 5. The differential cross-section and mass distribution for a diffractive process. The dotted line represents the mass spectrum after weighting by the momentum transfer distribution.

Fig. 6. The total photon cross section as a function of photon energy[21]. The solid line is 1/200th of the mean of the π^+p and π^-p total cross sections.

Fig. 7. The ratio of the real to imaginary part of the Compton scattering amplitude as a function of energy. (The Thomson term e^2/m, has been subtracted from the calculated value.)

Fig. 8. Vector dominance model graph for the process $e^+e^- \rightarrow \pi^+\pi^-$.

Fig. 9. Vector dominance model graphs for the decays a) $\omega \rightarrow \pi\gamma$ and b) $\omega \rightarrow \pi^+\pi^-\pi^o$.

Fig. 10. The three regions of momentum transfer in which rho photoproduction may be studied.

Fig. 11. (a) The energy spectrum from the monochromatic beam at 9 GeV,
(b) the thin target bremsstrahlung spectrum for 16 GeV,
(c) schematic representation of the photon beam energy spectra from various runs. The shaded areas show energy cuts at corresponding points on the spectra, allowing checks to be made on the possible contribution from inelastic processes. Note that the low energy cutoff of the above spectra is due to the energy acceptance of the spectrometer.

Fig. 12. The spectrometer system, showing the arrangement of the counters, the magneto-strictive read-out wire chambers and the two photon monitors, a pair spectrometer and a shower counter inside the tungsten beam

Fig. 12. (Continued)
stopper. Periodically, for calibrating the 2D4 pair spectrometer, the beam stopper was removed and the spark chamber system converted into an electron-positron pair spectrometer. For full description see ref. 36.

Fig. 13. The observed decay distribution of rho mesons from Be, at 9 GeV, evaluated in the helicity system. The data includes the forward coherent peak (i.e., $t \lesssim .05$ $(GeV/c)^2$).

Fig. 14. The mass distribution of the pion pairs produced from Be by photons from the 5 GeV monochromatic peak. The solid line is the best fit to the data using a coherent mixture of resonant and diffractive background amplitudes, as described in text.

Fig. 15. Schematic descriptions of the Söding model.

Fig. 16. The dipion mass distribution from 9 GeV photon interactions on hydrogen. The solid line is the best fit to the data using a coherent mixture of resonant and diffractive background amplitudes.

Fig. 17. The spin density matrix elements for rho decay evaluated in (a) the helicity frame, and (b) the Jackson frame. The data is from the SLAC wire spark chamber experiment at 9 GeV, the SLAC HBC group at 5 GeV and the Weizmann HBC group at 4.3. GeV.

Fig. 18. The differential cross section for rho production on (a) hydrogen and deuterium, and (b) complex nucleii, at 9 GeV.

Fig. 19. Schematic diagram representing rho photoproduction.

Fig. 20. The energy dependence of the forward rho cross section for Be, Cu, and Pb as measured by the SLAC wire chamber group. The forward hydrogen cross section is shown for comparison.

Fig. 21. The energy dependence of the extrapolated, $t = 0$, differential cross section for rho production.

Fig. 22. Schematic of the Cornell Spectrometer system.

Fig. 23. Dipion mass spectra from copper target at 8.8 GeV photon energy.

Fig. 24. The differential cross section for rho production on hydrogen and deuterium at 7.34 GeV photon energy.

Fig. 25. The ratio R_{DH} = ($d\sigma/dt$) Deuterium/($d\sigma/dt$) Hydrogen at t = 0 for various energies. The straight line at R_{DH} = 3.77 represents the prediction for pure diffractive photoproduction. The dashed curve represents an arbitrary S^{-1} fit, where $S \simeq 2kM_p$ = total c.m. energy squared.

Fig. 26. The forward rho cross section for hydrogen as a function of photon energy.

Fig. 27. Schematic of the DESY-MIT spectrometer.

Fig. 28. (a) Experimentally measured $\pi^+\pi^-$ cross sections $d\sigma/d\Omega dm$ in $\mu b/sr \cdot MeV/c^2$ for hydrogen as a function of the variables m and p. The curves are best fits to eq. [II - 6](the background is not shown). (b) Projection of Fig. 28a onto the (p, $d\sigma/d\Omega dm$) plane for fixed values of m. The curves are best fits to $d\sigma/d\Omega dm = p^2 (1 + M/p)^2$. This shows explicitly that the data for fixed m increase more slowly than $p^2 (M > 0)$.

Fig. 29. (a) The cross section Z = $d\sigma/d\Omega dm$($\mu b/sr$ MeV/c^2 . nucleon) as a function of m (MeV/c^2) and t in units of -0.001 GeV$^2/c^2$ for p = 6.2 $\pm$ 0.2 GeV/c^2. The curves are the best fits to eq. [II - 6] . The background is not drawn. This figure shows about 2% of the data. (b) Mass spectra after removal of production mechanism. (Note that in the absence of background, all spectra would be identical.)

Fig. 30. (a) Distribution of the effective mass of the $\pi^+\pi^-$ pair for Carbon summed between t = 0 and t = .1(GeV/c)^2. The curve is a fit Breit-Wigner plus polynomial background. The Breit-Wigner shape is corrected by the Ross-Stodolsky factor $(m/m_{\pi\pi})^4$. (b) Differential cross section $d\sigma/dt$ for Carbon. Theline represents the optical model calculation with harmonic-well density distribution and r = 2.35f.

Fig. 31. Summary of the various experimental determinations of $\sigma(\rho N)$ and $\gamma_\rho^2/4\pi$.

Fig. 32. Geometry of the apparatus used for detecting photoproduced ω mesons through their decay $\pi^+\pi^-\pi^o$.

Fig. 33. (a) Invariant mass distribution of the two detected γ rays.
(b) Invariant mass distribution of $\pi^+\pi^-\pi^o$, after a mass cut has been applied to the invariant 2γ mass.

Fig. 34. Differential cross sections for ω photoproduction in Be and Cu. The two dashed lines indicate the contributions given by the two terms in Eq. [III - 2] for Be. The solid lines are fits to the data given by Eq. [III - 3] .

Fig. 35. Experimental layout. The insert indicates the arrangement of counters in the spectrometer.

Fig. 36. Time spectrum of particles arriving at the rear of the spectrometer. The pattern is cyclic with another proton spike beginning just above the deuteron spike.

Fig. 37. Yield curve of deuterons counted as the spectrometer angle was decreased. The smooth curve through the data is a least squares fit. It is the sum of a ρ-step and an empirical background, which are also shown.

Fig. 38. Measured cross sections at 6, 12, and 18 GeV. The smooth curves are theoretical, and are described in the text. The normalization at low $|t|$ is fixed by the cross sections for forward ρ-photoproduction from photons (given in Table XII). The fit at large $|t|$ is arranged by adjusting $\sigma_{\rho N}$. There are no other adjustable parameters.

Fig. 39. Schematic diagram of layout for the total photon cross section experiments

Fig. 40. Diagrmatic representation of the a) one-step and b) two-step processes contributing to forward compton scattering.

Fig. 41. Comparison of the A-dependence for $\sigma_{tot}(\gamma p)$ and $[\frac{d\sigma}{dt}(\gamma p \to \rho p)]^{1/2}$.

Fig. 42. The energy dependence of the total photon cross section for several nucleii. The curves show the calculated k-dependence for different values of the rho-nucleon total cross section, $\sigma(\rho N)$, using the total of Brodsky and Pumplin with $r_0 = 1.13f$.

Fig. 43. Experimental set-up to measure Compton scattering, by the Ritson group at SLAC.

Fig. 44. Compton yields (a) yield curves with shower counter in the Compton plane, $(\gamma + \pi^0)$ and out of the Compton plane, (π^0); (b) difference between the two curves in (a).

Fig. 45. The differential cross-section for Compton scattering at 5.5, 8.5, 11.5, and 17 GeV. The dashed curves are the prediction of the VDM.

Fig. 46. Forward differential cross-section for rho photoproduction on hydrogen.

Fig. 47. Ratio of single pion production, π^-/π^+, from deuterium.(2)

Fig. 48. Vector dominance comparison for single pions produced by unpolarised photons.(2)

Fig. 49. Single π^+ differential cross-section(2), multiplied by $(S-M^2)^2$, and plotted as a function of t.

Fig. 50. Vector dominance comparison for single pions produced by photons with linear polarization perpendicular to the production plane.[2]

Fig. 51. Schematic for the model hadronic interaction of the photon.

Fig. 52. The A-dependence of the total photon cross section. Also included is the square root of the t = 0 rho cross sections. These should be equal within the framework of VDM. The upper and lower lines represent the A-dependence expected from zero absorption and asymptotic strong absorption of the photon. The intermediate lines are the prediction of a simple model of photon interactions described in the text.

Fig. 53. The k-dependence of the total cross section, with the predictions of the simple model of photon interactions described in the text.

Fig. 54. Weighted events versus $|\cos\theta_{\pi\pi}|$ in the helicity system. $1.0 \leq M_{\pi\pi} \leq 2.0$ GeV/c^2, $|t-t_{min}| \leq 0.3$ (GeV/c)^2 and $E_{\pi\pi} \geq 14.0$ GeV.

Fig. 55. Momentum transfer distributions for $E_{\pi\pi} \geq 14.0$ GeV, $|\cos\theta_{\pi\pi}| \leq 0.6$ and (a) $0.8 \leq M_{\pi\pi} \leq 1.0$ GeV/c^2 and (b) $1.0 \leq M_{\pi\pi} \leq 2.0$ GeV/c^2. Smooth curves are drawn only as a viewing aid.

Fig. 56. Variation with $M_{\pi\pi}$ of ratio of cross-sections at $t = t_{min}$ to that at $t-t_{min} = -0.12$ (GeV/c^2). $E_{\pi\pi} \geq 14.0$ GeV, $|\cos\theta_{\pi\pi}| \leq 0.6$. Curves explained in text.

Fig. 57. Variation of yield versus $M_{\pi\pi}$ for $|t-t_{min}| \leq 0.046$ (GeV/c)^2, $|\cos\theta_{\pi\pi}| \leq 0.6$ and $E_{\pi\pi} \geq 14.0$ GeV. (Data for $M_{\pi\pi} \leq 0.9$ GeV/c^2 acquired from our study of rho photoproduction at 16 GeV.) Dashed curve is the calculated acceptance and the solid curves are explained in text.

Fig. 58. Dipion mass plot from CORNELL high mass search.

Fig. 59. Two pion mass spectra from all SLACK HBC experiments. Private communication G. B. Chadwick.

Fig. 60. Subtracted yield curve in missing-mass search by Ritson group.

Fig. 61. (a) The ratio of experimental yield to that expected from BH production as a function of muon-pair invariant mass.

TABLE I

	$\frac{\gamma_\rho^2}{4\pi}$	$\frac{\gamma_\omega^2}{4\pi}$	$\frac{\gamma_\phi^2}{4\pi}$
Colliding Beam Experiment	0.50 ± 0.03	3.7 ± 0.7	2.9 ± 0.2

TABLE II

SYSTEMATIC STUDY OF RHO MESON PHOTOPRODUCTION
USING A WIRE SPARK CHAMBER SPECTROMETER AT SLAC

TARGET \ ENERGY (GeV)	MONOCHROMATIC γ's			BREMSSTRAHLUNG		
	5	7	9	10	13	16
H_2	×		×	×	×	×
D_2			×	×		×
B_e	×	×	×	×		×
C	×	×	×			
Aℓ	×	×	×			
Cu	×	×	×			
Ag			×			
Pb	×	×	×			×

Table III

E_ρ GeV	Nuclear Parameters	$\alpha_{\rho\rho}$	$\gamma_\rho^2/4\pi$	$\sigma_{\rho N}$ mb	$\lvert f_\rho \rvert^2$ ub/GeV^2
8.8	Best Fit	-.24	.68 ± .04	26.8 ± 1.2	105 ± 11
	E-S	-.24	.63 ± .04	25.9 ± 1.0	106 ± 11
6.5	Best Fit	-.27	.74 ± .05	30.1 ± 1.5	124 ± 15
	E-S	-.27	.65 ± .05	27.9 ± 1.3	120 ± 15
6.1	Best Fit	-.27	.58 ± .03	26.1 ± .9	117 ± 10
	E-S	-.27	.62 ± .04	27.5 ± 1.1	122 ± 13

TABLE IV

A	(MASS FIT 1) $\frac{d\sigma}{dt}(\gamma A \rightarrow \rho A)$	(MASS FIT 2)
Beryllium	627 ± 31	652 ± 50
Carbon	772 ± 52	800 ± 50
Aluminum	1322 ± 63	1279 ± 51
Titanium	1796 ± 78	1706 ± 66
Copper	2099 ± 115	2102 ± 68
Silver	2591 ± 79	2585 ± 73
Cadmium	2656 ± 93	2583 ± 74
Indium	2696 ± 90	2634 ± 74
Tantalum	2958 ± 154	2900 ± 151
Tungsten	2925 ± 140	2877 ± 75
Gold	2948 ± 128	2966 ± 147
Lead	3112 ± 93	3167 ± 76
Uranium	3070 ± 93	3035 ± 58
$\chi^2(A)/DF(A)$	~ 1.2	~ 1.2
$m_\rho (MeV/c^2)$	765 ± 10	775 ± 10
$\lvert f_o \rvert^2$ $\mu b/(GeV/c)^2$	118 ± 6	120 ± 7.4
$\sigma_{\rho N}$ (mb)	26.7 ± 2.0	27.7 ± 1.7
$\gamma_\rho^2/4\pi$	0.57 ± 0.10	0.59 ± 0.08

Table V

EXPERIMENT	$\sigma(\rho N)$ (mb)	$\gamma_\rho^2/4\pi$
DESY	27.7 ± 1.7	$0.59 \pm .08$
CORNELL	28 ± 1	$0.68 \pm .03$
SLAC	29 ± 2.5	$0.85 \pm .1$
ROCHESTER	29 ± 2.5	$0.71 \pm .12$

TABLE VI

	$\gamma\rho^2/4\pi$	$\gamma_\omega^2/4\pi$	$\gamma\phi^2/4\pi$
Colliding beam experiment	$0.5 \pm .05$	3.7 ± 0.7	2.9 ± 0.2
$\gamma A \to vA$	~ 0.75	~ 9	~ 8 (for $\alpha\phi N = 0$) ~ 6 (for $\alpha\phi N = -.2$)

TABLE VII

	$\frac{1}{\gamma_\rho^2}$	:	$\frac{1}{\gamma_\omega^2}$	:	$\frac{1}{\gamma_\phi^2}$
SU(3)	9	:	1	:	2
DMO	7.4	:	1	:	0.85
OS	13.8	:	1	:	2.1
Colliding beam	7.5 ± 1.5	:	1	:	$1.3 \pm .3$
$\gamma A \to vA$	12 ± 3	:	1	:	$1.1 \pm .4$ (for $\alpha\phi N = 0$) $1.3 \pm .4$ (for $\alpha\phi N = -.2$)

TABLE VIII

k	$\frac{d\sigma}{dt}(t=0,\ A=1)$ $\mu b/GeV^2$	$\gamma_\rho^2/4\pi$	$\sigma_{\rho N}$ mb
6	133 ± 13	.66 ± .14	30.2 ± 3.0
12	112 ± 7	.70 ± .14	28.6 ± 2.5
18	105 ± 6	.71 ± .14	27.8 ± 2.5

Table IX

(after Silverman[4])

Experimental Group	Decay Mode	Mass Range	
H. Hicks et al.	2π	1360-1780	
G. McClellan et al.	2π	1000-1800	$\frac{\gamma_\rho'^2}{\gamma_\rho^2} > 1\times10^3 \frac{\Gamma_\rho'(2\pi)\Gamma_\rho}{\Gamma_\rho'^2}$
F. Bulos et al.	2π	1000-2000	
Y. Eisberg et al.	2π	1000-2000	
J. Ballam et al.	2π	1000-2000	
D. Earles et al.	2μ	1100-1800	$(\frac{\gamma_\rho'}{\gamma_\rho})^2 > (5 \rightarrow 20) \frac{\Gamma_\rho^*}{\Gamma_\rho'}$
S. Hayes et al.	2μ	1250-1900	
B. Anderson et al.	ALL	1000-2000	$\frac{\frac{d\sigma}{dt}(\rho')}{\frac{d\sigma}{dt}(\rho)} < \frac{.025\ \Gamma_\rho'}{\Gamma_\rho}$

*The limit varies smoothly with mass; 5 corresponds to 1100 MeV whereas 20 corresponds to 1200 MeV.

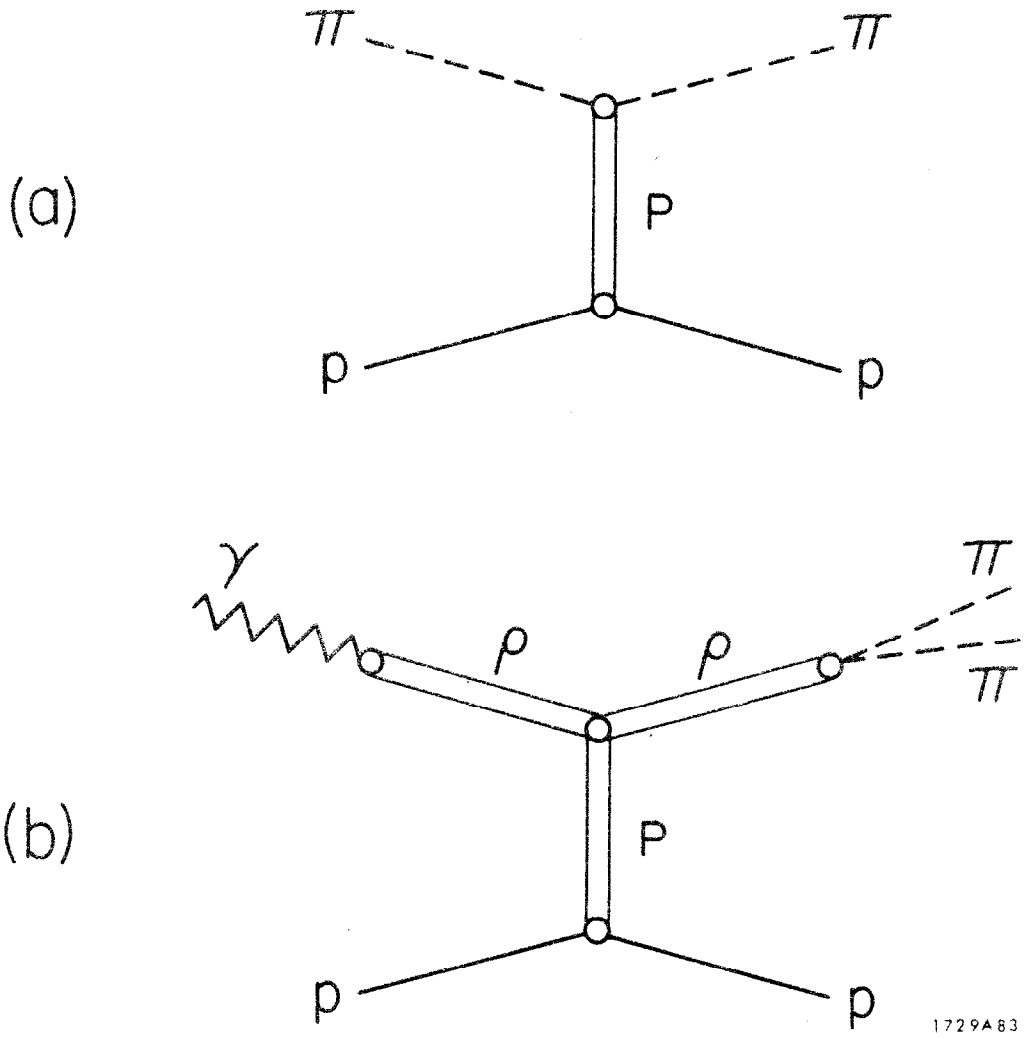

Fig. 1

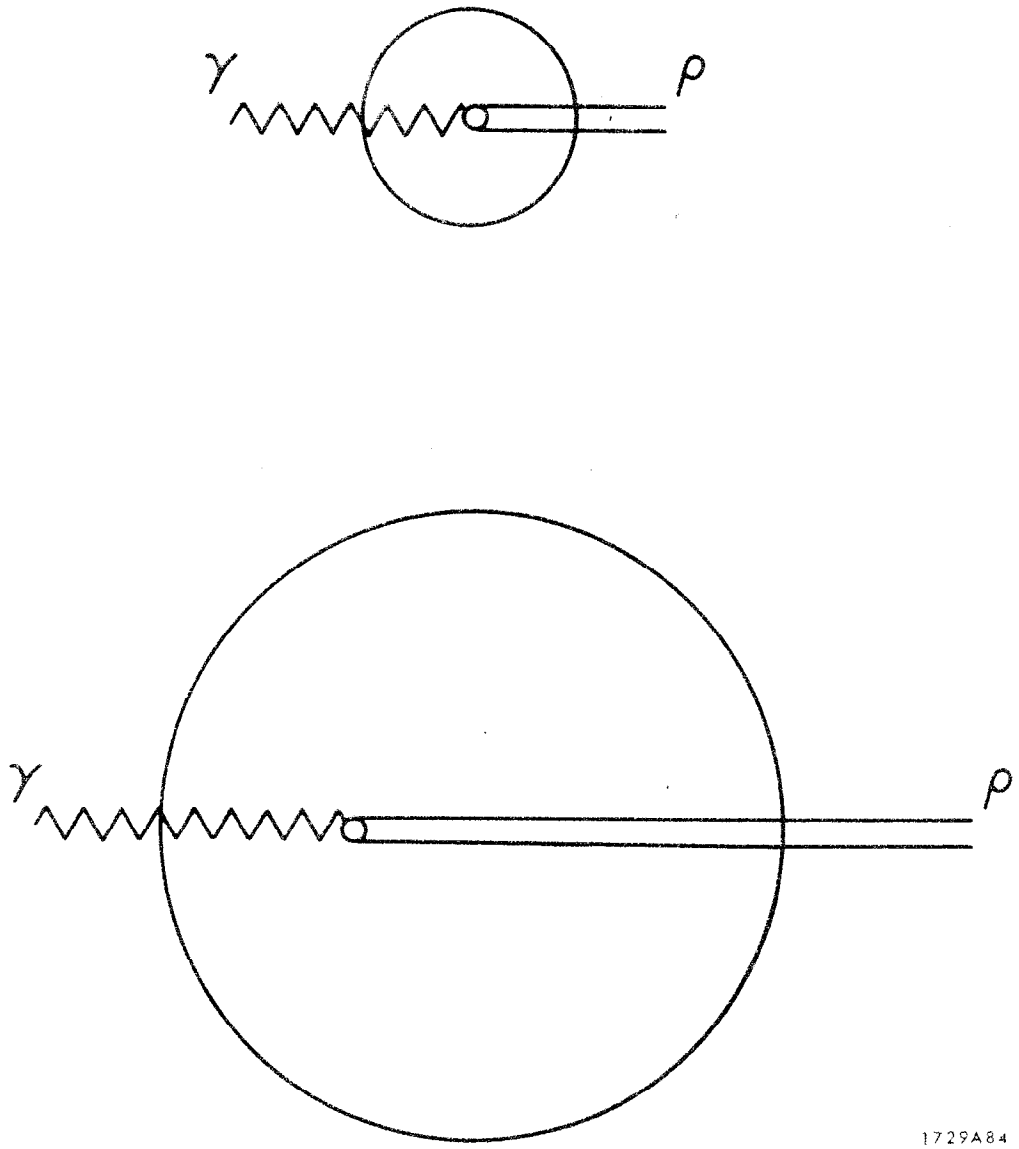

Fig. 2

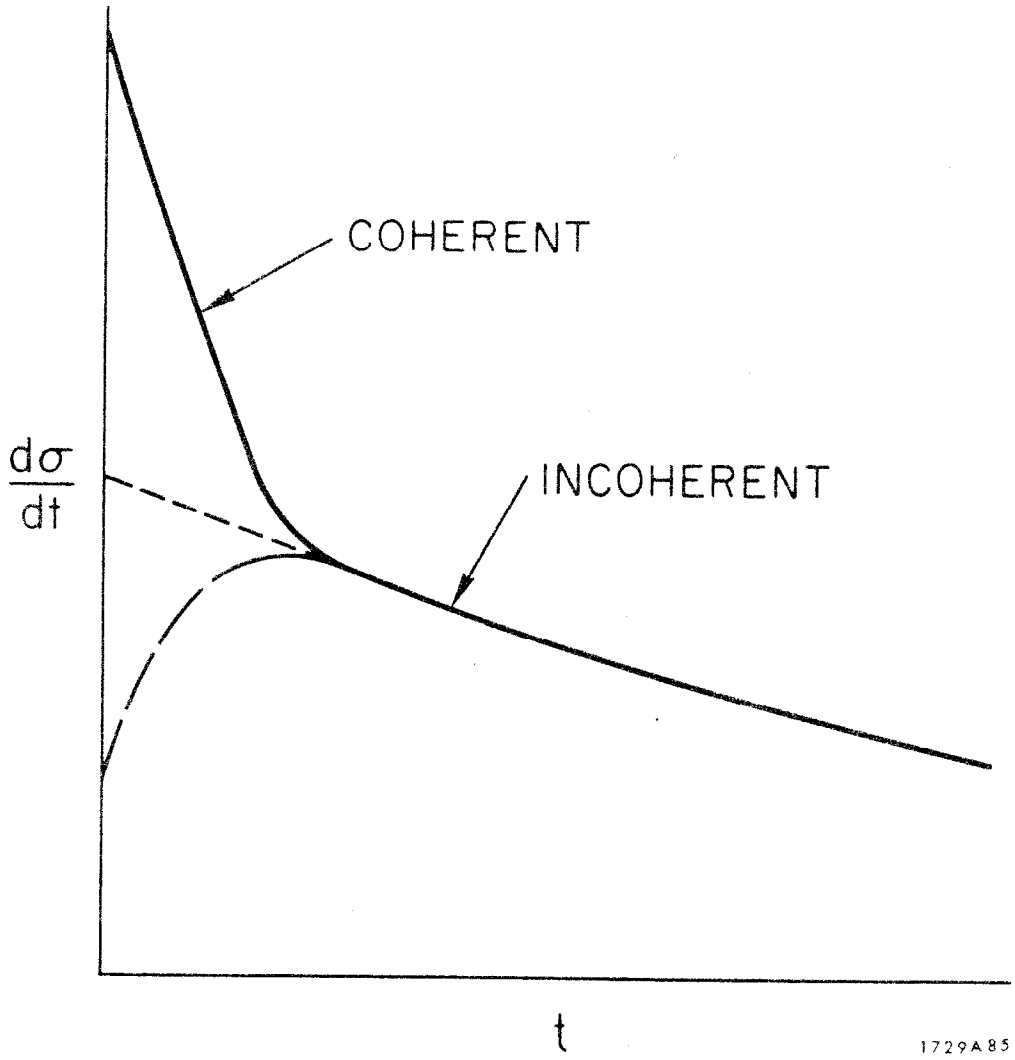

Fig. 3

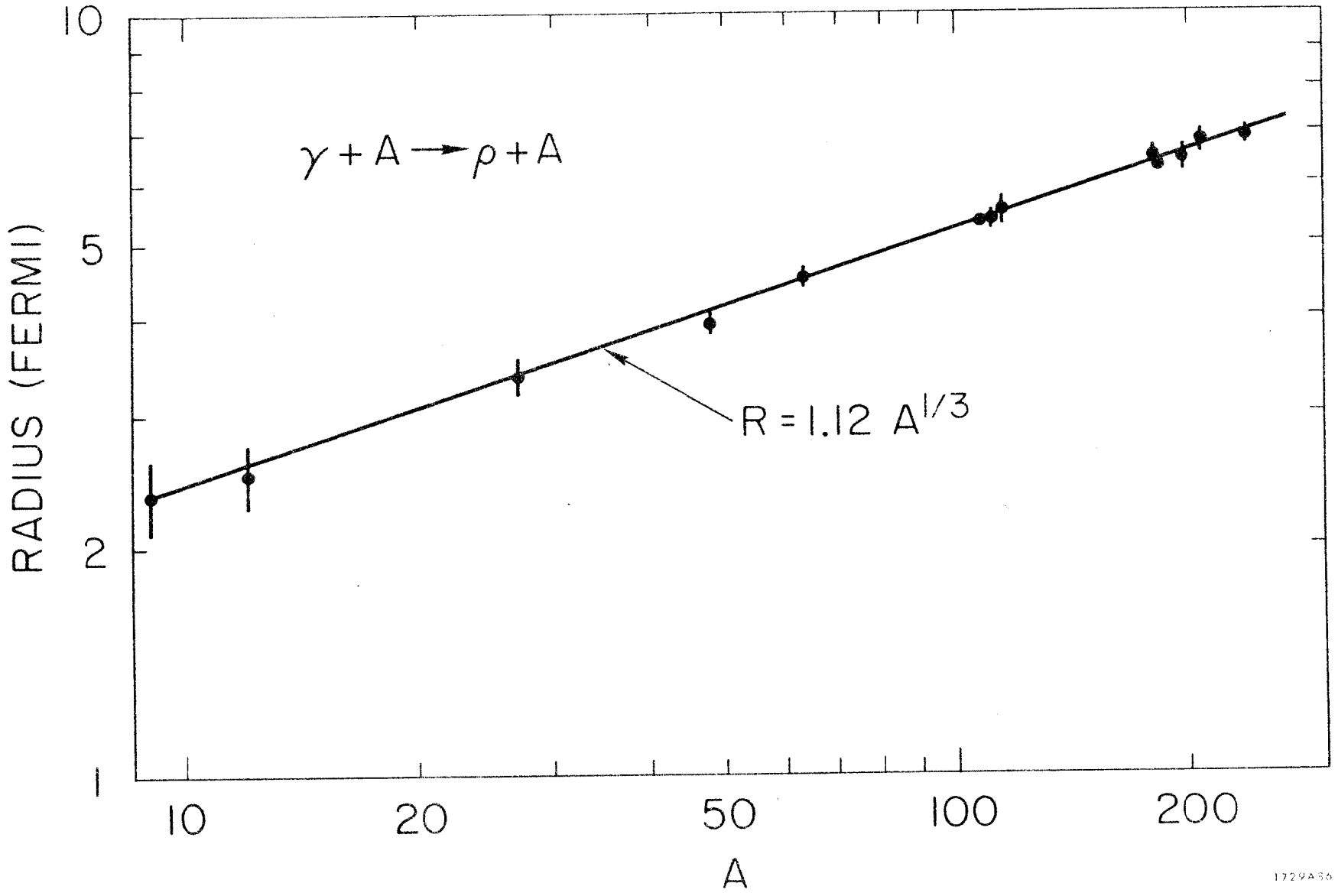
10
5
2
1
RADIUS (FERMI)
$\gamma + A \rightarrow \rho + A$
$R = 1.12\ A^{1/3}$
10
20
50
100
200
A
1729A56

Fig. 4

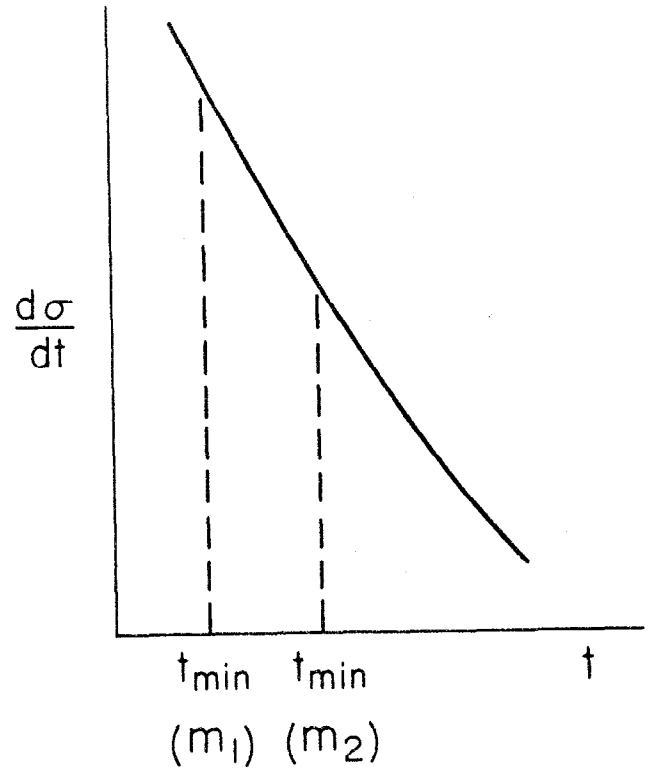

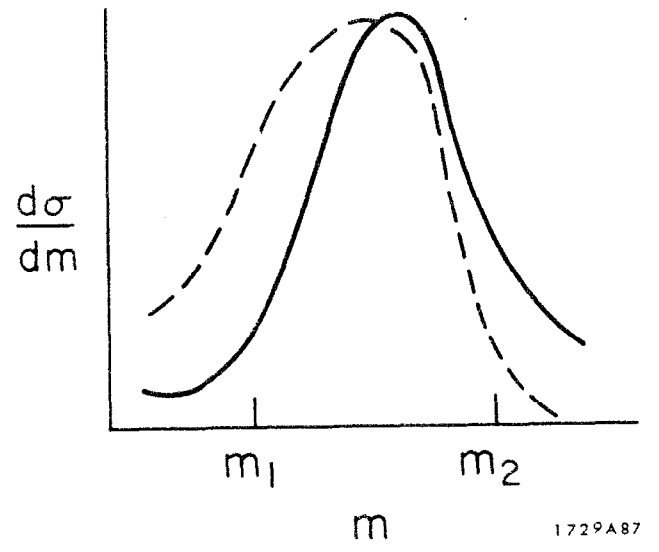

Fig. 5

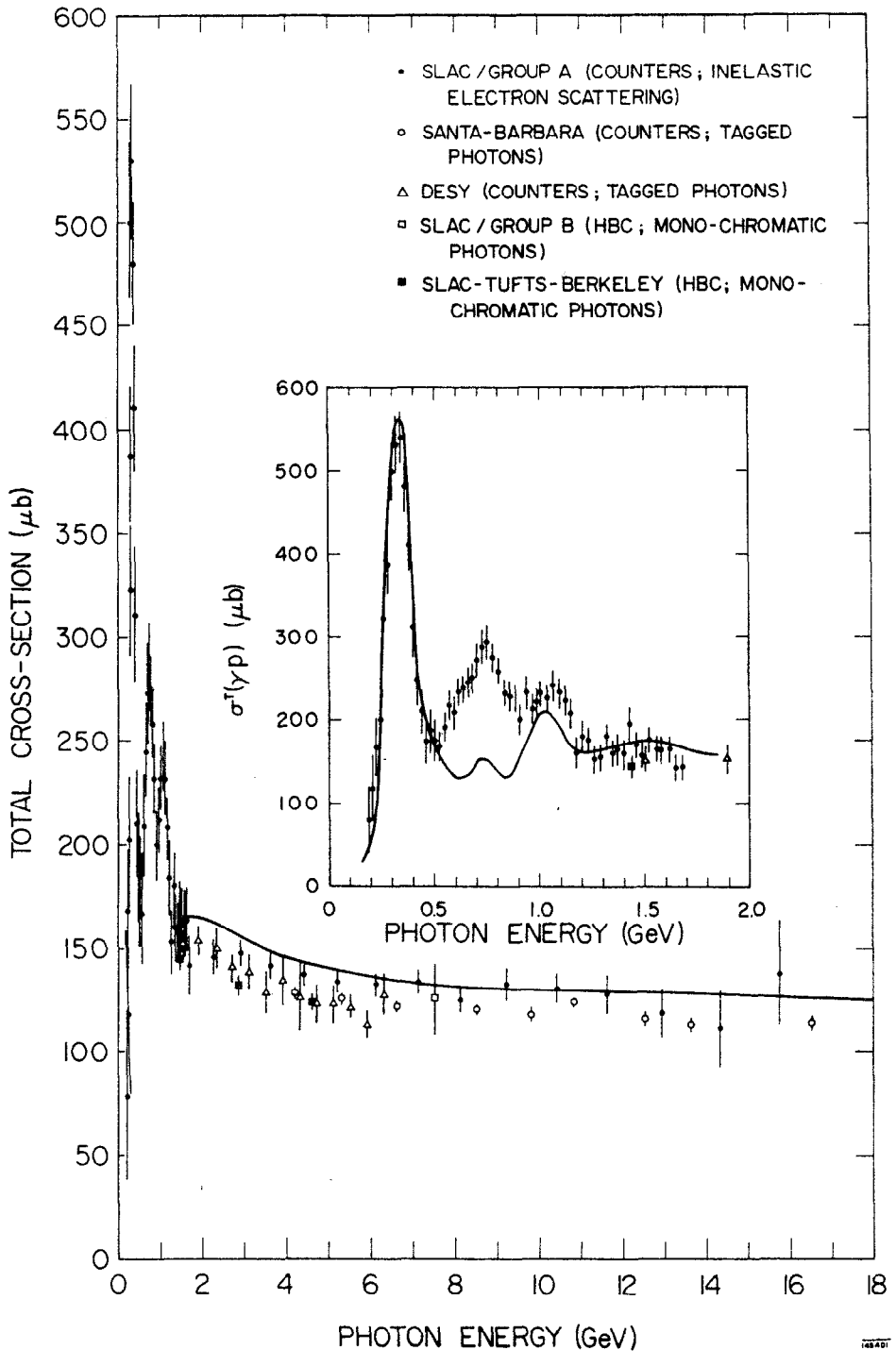
• SLAC / GROUP A (COUNTERS; INELASTIC ELECTRON SCATTERING)
○ SANTA-BARBARA (COUNTERS; TAGGED PHOTONS)
△ DESY (COUNTERS; TAGGED PHOTONS)
□ SLAC / GROUP B (HBC; MONO-CHROMATIC PHOTONS)
■ SLAC-TUFTS-BERKELEY (HBC; MONO-CHROMATIC PHOTONS)
TOTAL CROSS-SECTION (μb)
PHOTON ENERGY (GeV)
σ^T(γp) (μb)
PHOTON ENERGY (GeV)

Fig. 6

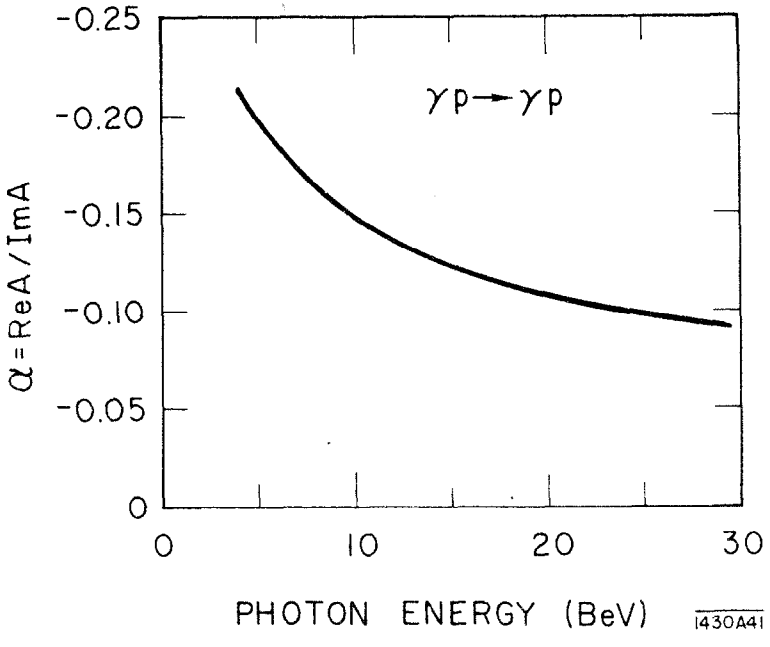
-0.25
-0.20
-0.15
-0.10
-0.05
0
0
10
20
30
α = ReA / ImA
γp → γp
PHOTON ENERGY (BeV)
1430A41

Fig. 7

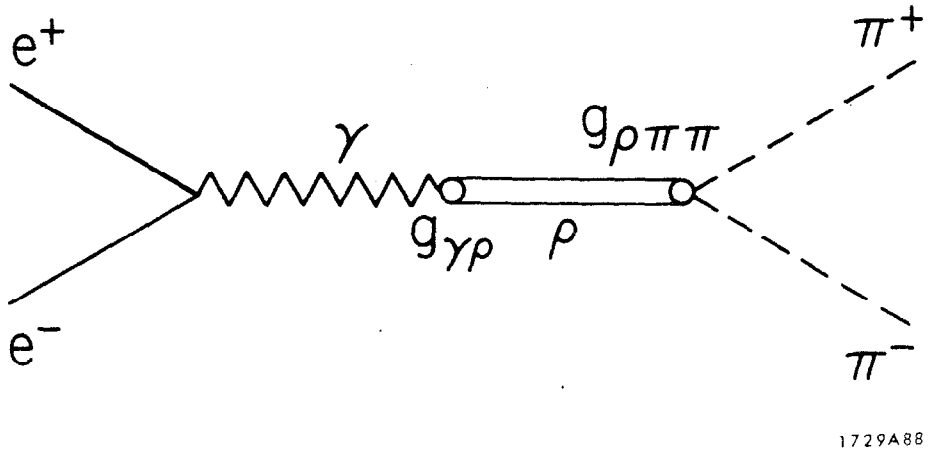

Fig. 8

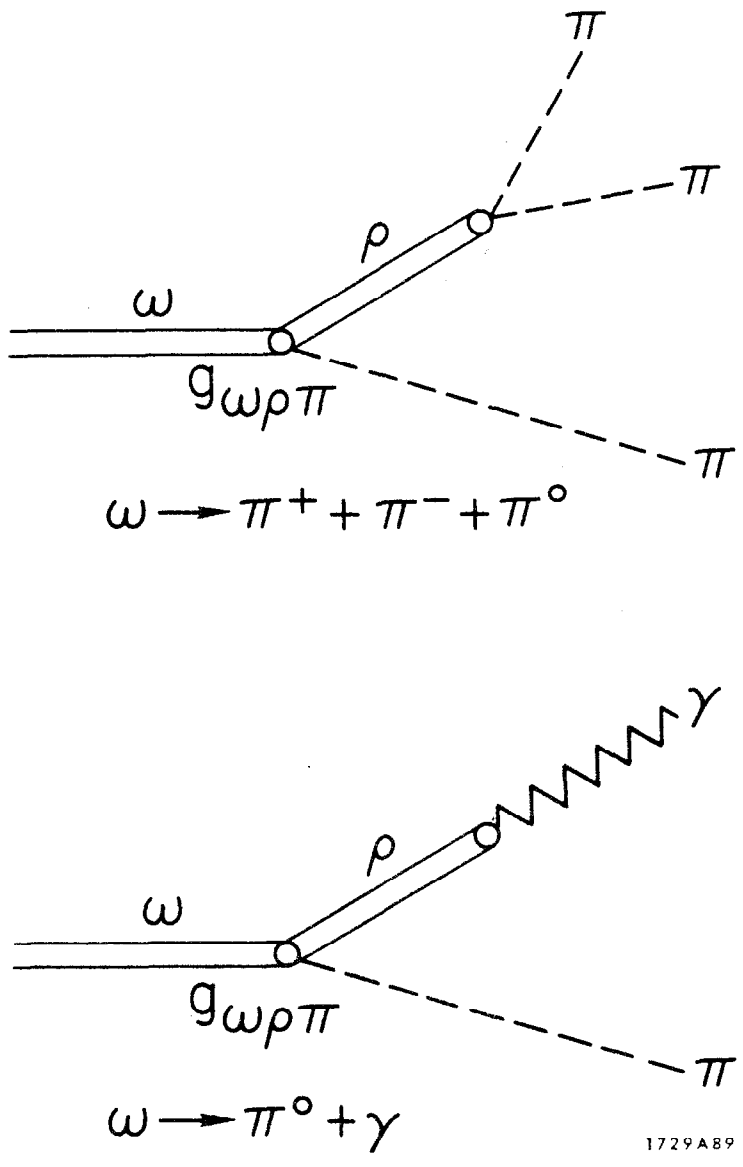
π
π
ρ
ω
$g_{\omega\rho\pi}$
π
$\omega \rightarrow \pi^+ + \pi^- + \pi^\circ$
γ
ρ
ω
$g_{\omega\rho\pi}$
π
$\omega \rightarrow \pi^\circ + \gamma$
1729A89

Fig. 9

(a) $q^2 < 0$

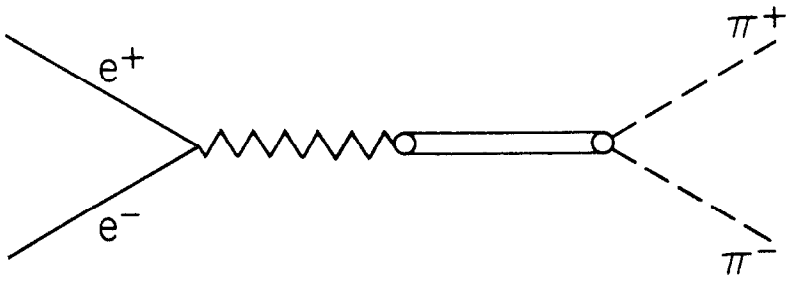

which may be studied in colliding beam experiments;

(b) $q^2 = 0$

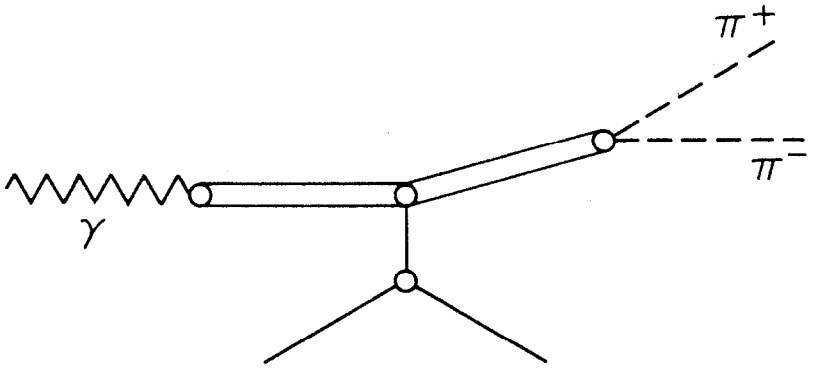

which may be studied in photoproduction reactions;

(c) $q^2 > 0$

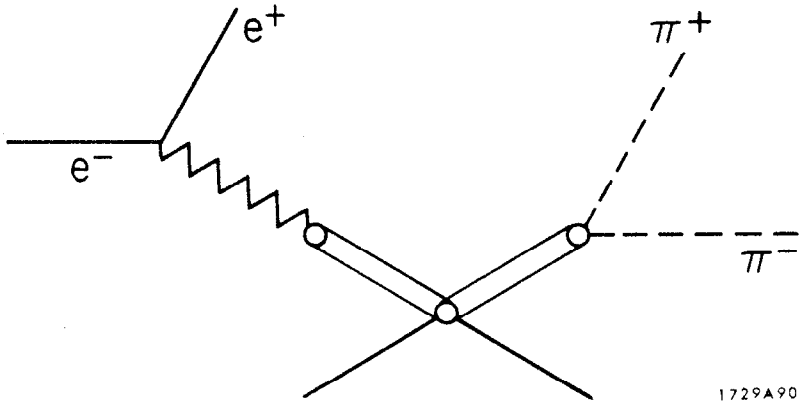

which may be studied in inelastic electron scattering.

Fig. 10

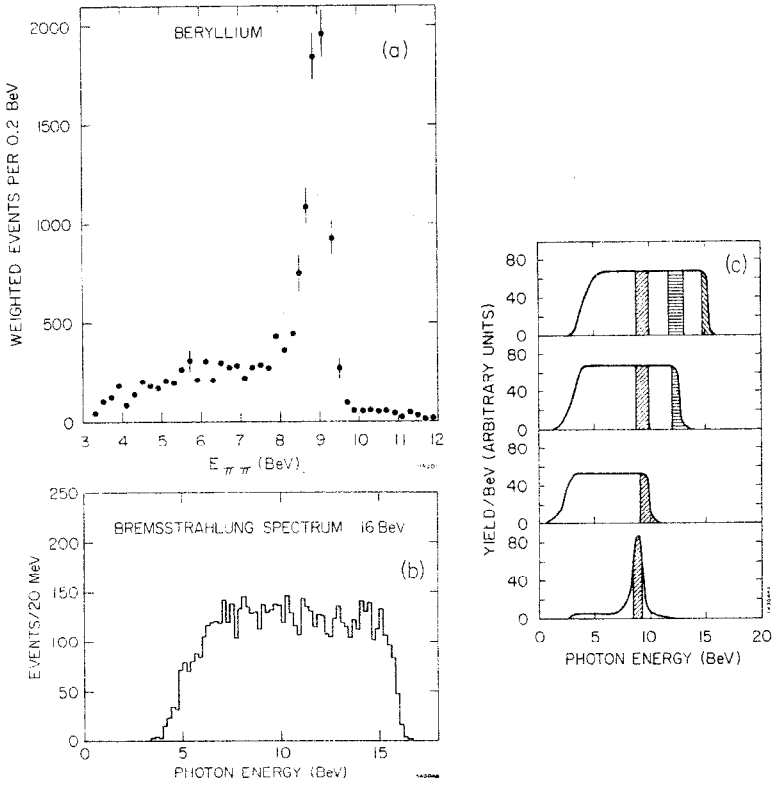
BERYLLIUM
(a)
WEIGHTED EVENTS PER 0.2 BeV
2000
1500
1000
500
0
3 4 5 6 7 8 9 10 11 12
$E_{\pi\pi}$ (BeV)
BREMSSTRAHLUNG SPECTRUM 16 BeV
(b)
EVENTS/20 MeV
250
200
150
100
50
0
0 5 10 15
PHOTON ENERGY (BeV)
(c)
YIELD/BeV (ARBITRARY UNITS)
80
40
0
0 5 10 15 20
PHOTON ENERGY (BeV)

Fig. 11

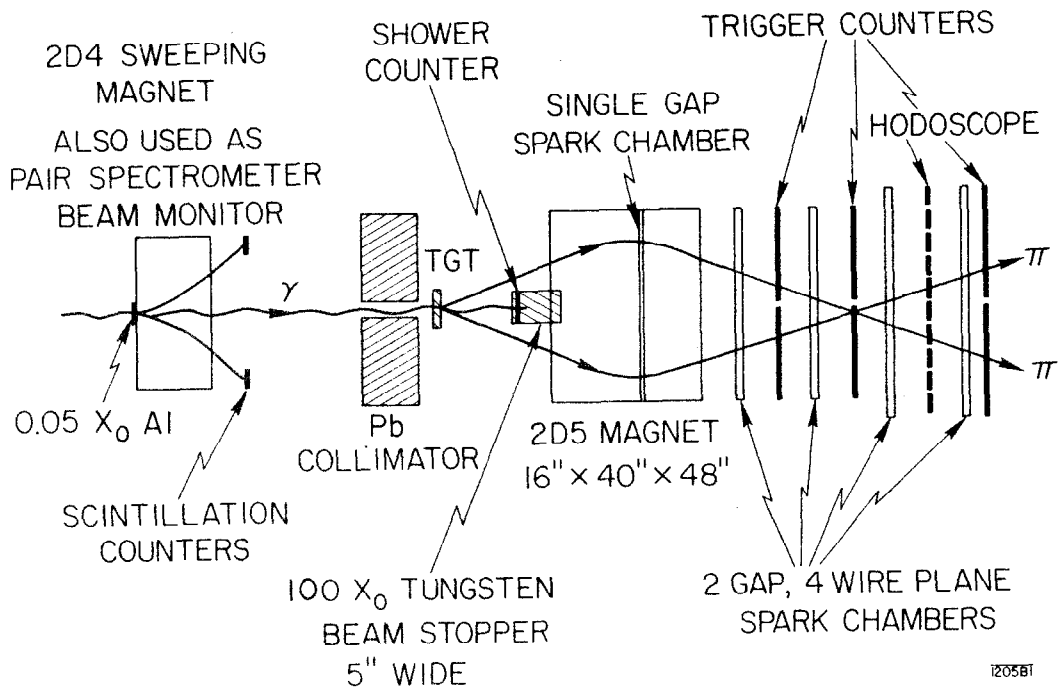
2D4 SWEEPING MAGNET
ALSO USED AS PAIR SPECTROMETER BEAM MONITOR
SHOWER COUNTER
SINGLE GAP SPARK CHAMBER
TRIGGER COUNTERS
HODOSCOPE
TGT
γ
π
π
0.05 X0 Al
Pb COLLIMATOR
2D5 MAGNET 16" × 40" × 48"
SCINTILLATION COUNTERS
100 X0 TUNGSTEN BEAM STOPPER 5" WIDE
2 GAP, 4 WIRE PLANE SPARK CHAMBERS
120581

Fig. 12

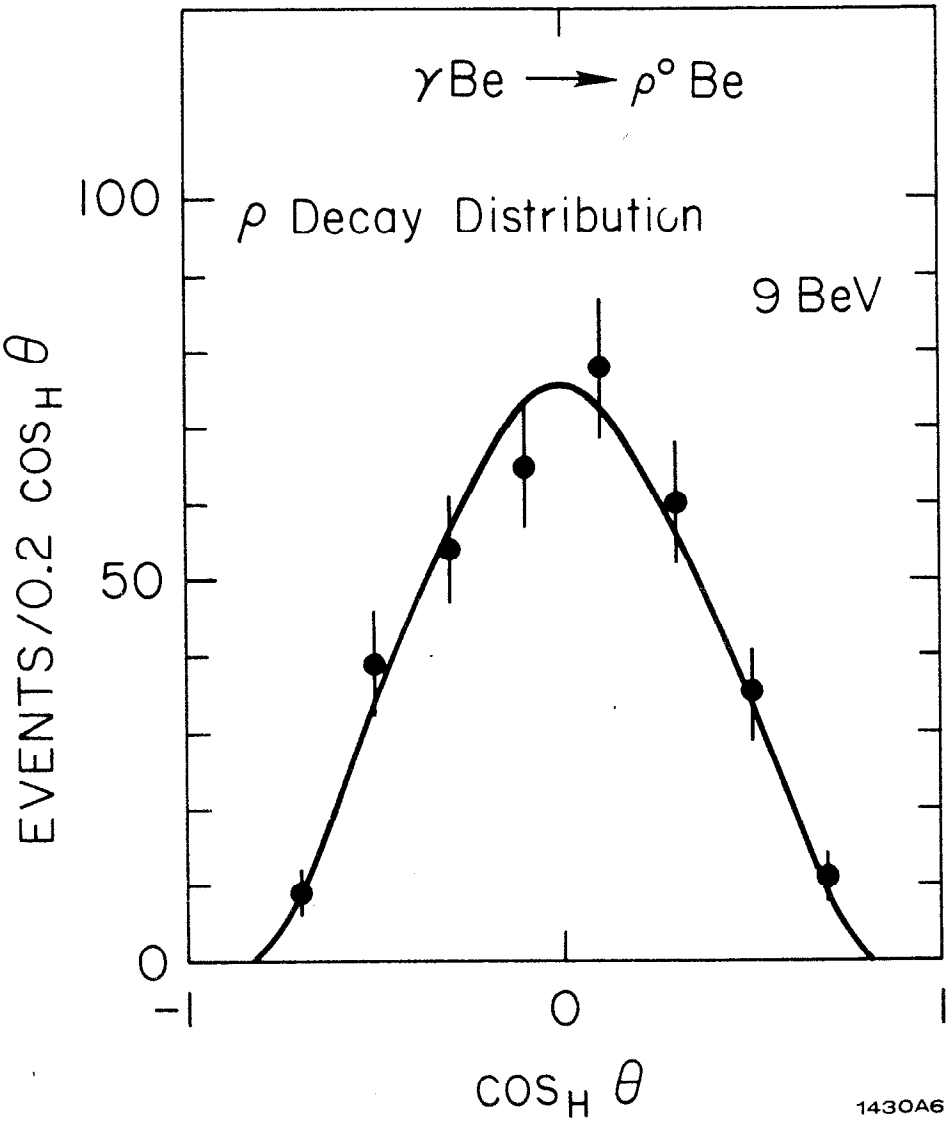
γ Be → ρ° Be
ρ Decay Distribution
9 BeV
100
50
0
EVENTS/0.2 cos_H θ
-1
0
1
cos_H θ
1430A6

Fig. 13

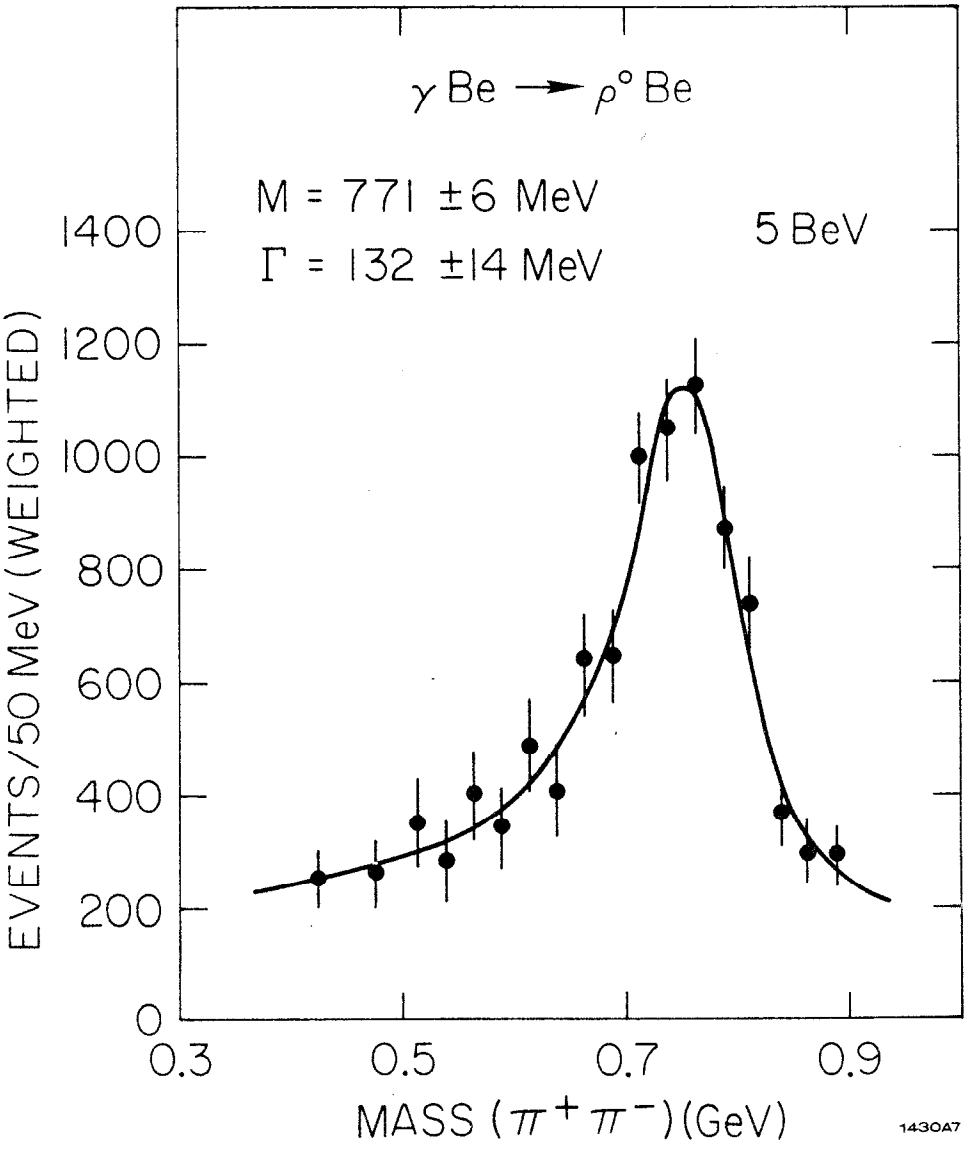
γ Be → ρ° Be
M = 771 ±6 MeV
Γ = 132 ±14 MeV
5 BeV
EVENTS/50 MeV (WEIGHTED)
1400
1200
1000
800
600
400
200
0
0.3
0.5
0.7
0.9
MASS (π⁺π⁻)(GeV)
1430A7

Fig. 14

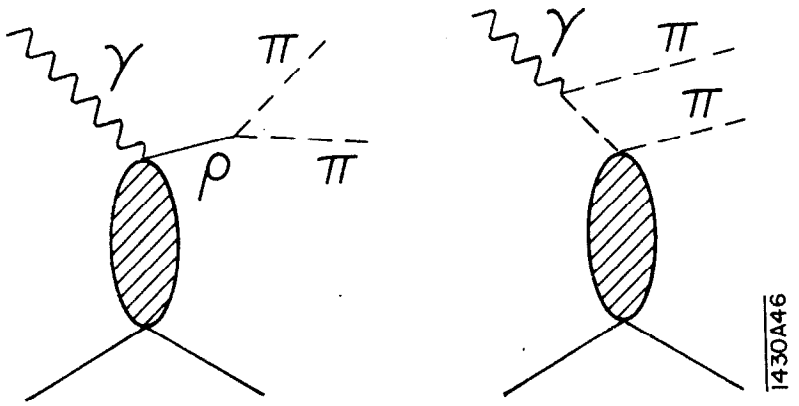

Fig. 15

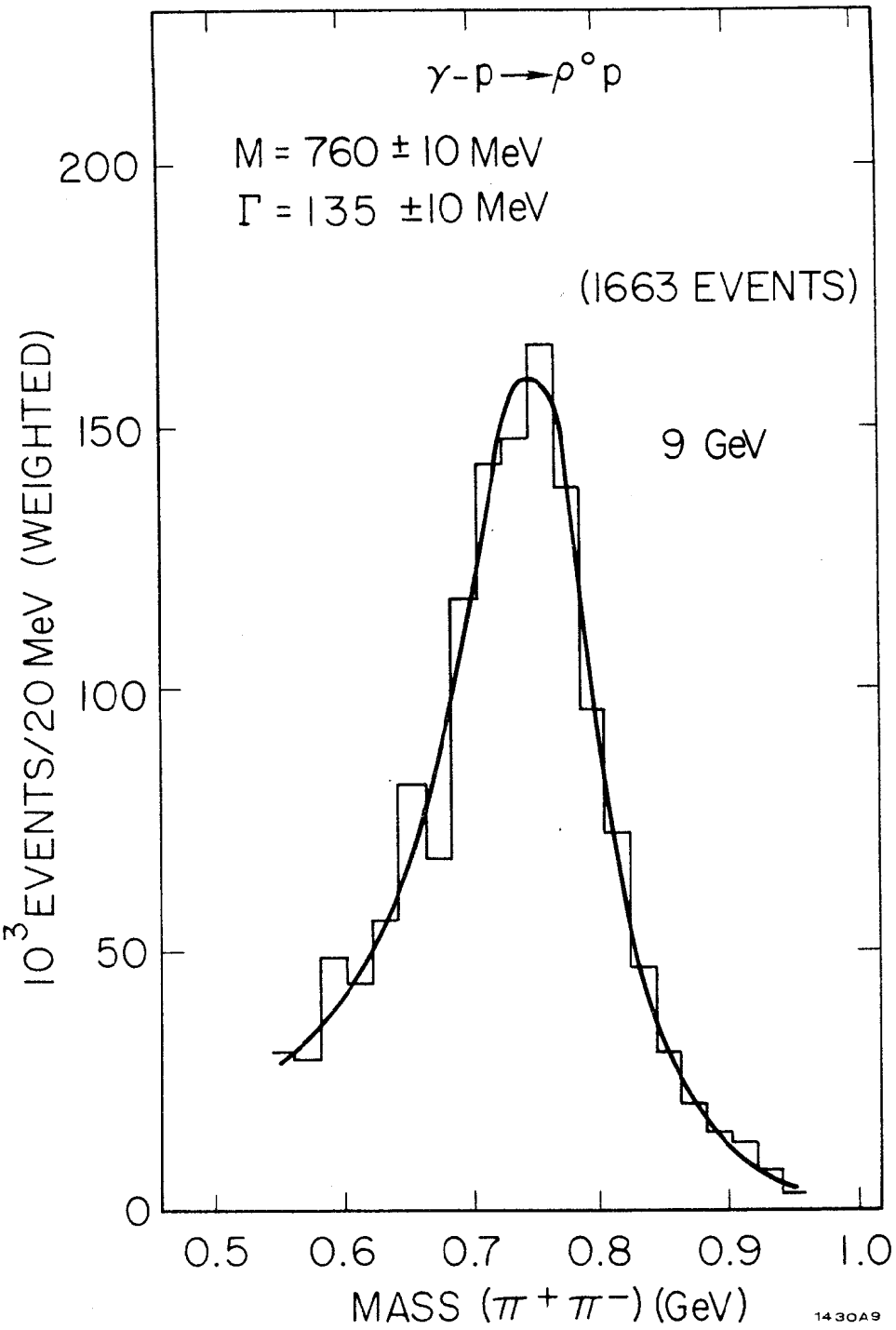
γ-p→ρ°p
M = 760 ± 10 MeV
Γ = 135 ±10 MeV
(1663 EVENTS)
9 GeV
200
150
100
50
0
10³ EVENTS/20 MeV (WEIGHTED)
0.5
0.6
0.7
0.8
0.9
1.0
MASS (π⁺π⁻) (GeV)
1430A9

Fig. 16

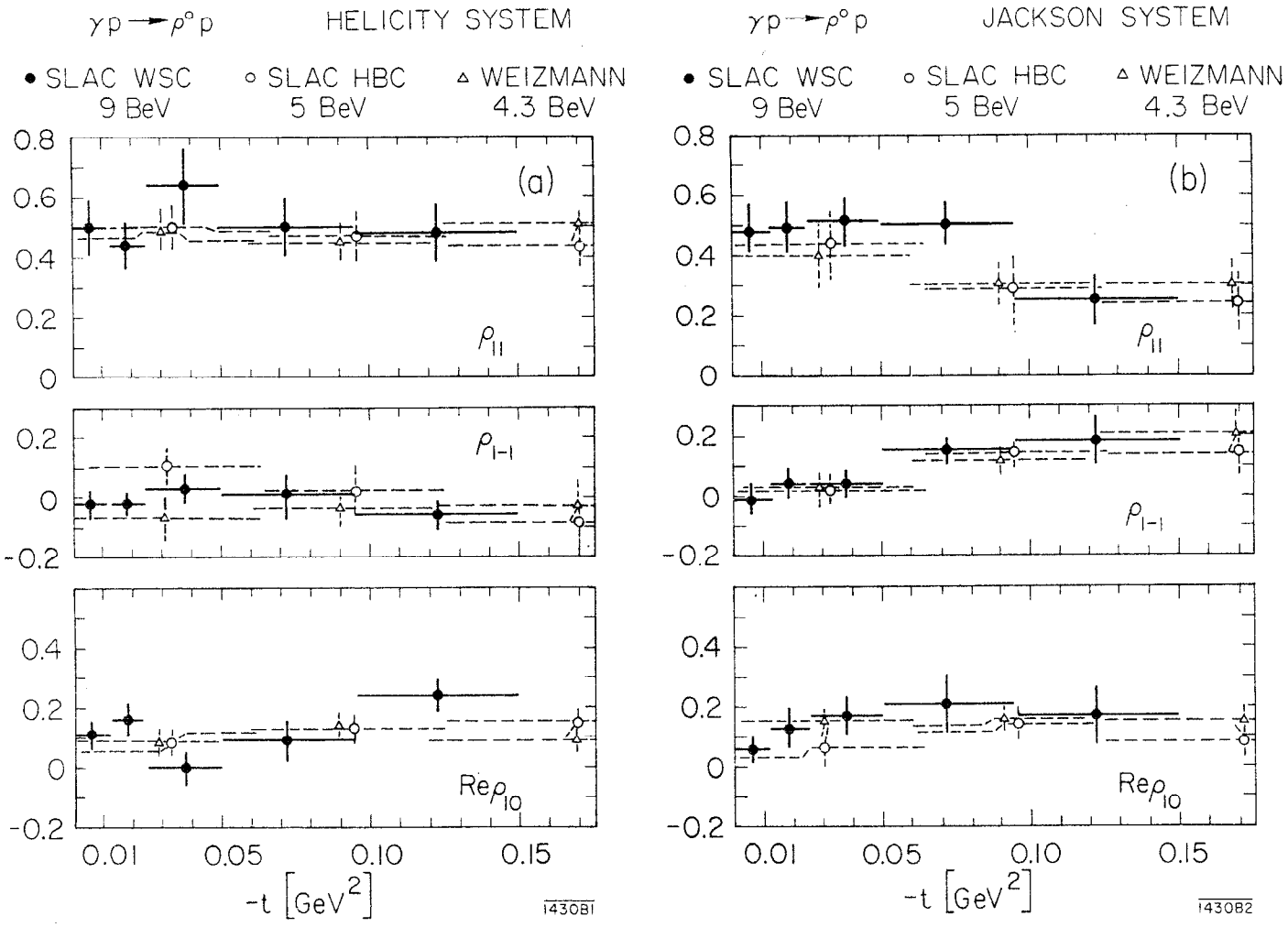
γp → ρ°p
HELICITY SYSTEM
• SLAC WSC 9 BeV
○ SLAC HBC 5 BeV
△ WEIZMANN 4.3 BeV
(a)
ρ_{11}
ρ_{1-1}
$Re\rho_{10}$
-t [GeV²]
143081
γp → ρ°p
JACKSON SYSTEM
• SLAC WSC 9 BeV
○ SLAC HBC 5 BeV
△ WEIZMANN 4.3 BeV
(b)
ρ_{11}
ρ_{1-1}
$Re\rho_{10}$
-t [GeV²]
143082

Fig. 17

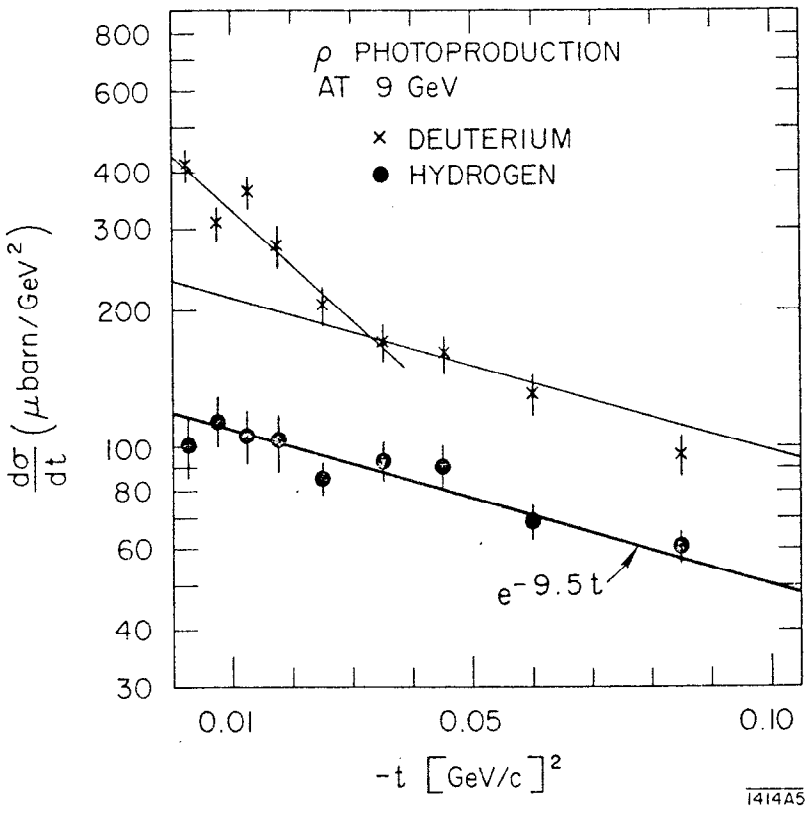
ρ PHOTOPRODUCTION
AT 9 GeV
× DEUTERIUM
● HYDROGEN
e^-9.5t
800
600
400
300
200
100
80
60
40
30
0.01
0.05
0.10
dσ/dt (μbarn/GeV²)
-t [GeV/c]²
1414A5

Fig. 18a

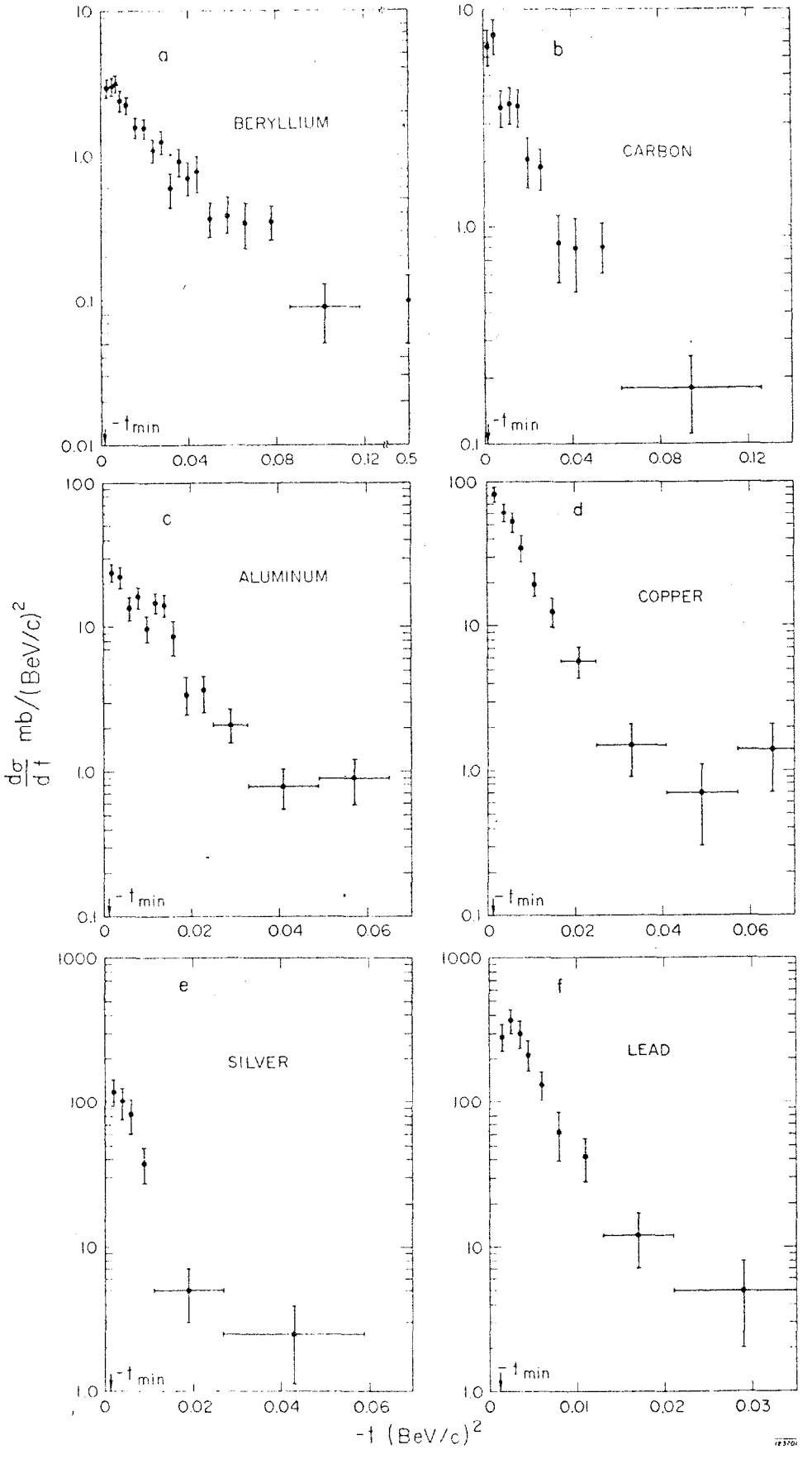
a
BERYLLIUM
b
CARBON
c
ALUMINUM
d
COPPER
e
SILVER
f
LEAD
$-t_{min}$
$\frac{d\sigma}{dt}$ mb/(BeV/c)^2
$-t$ (BeV/c)^2

Fig. 18b

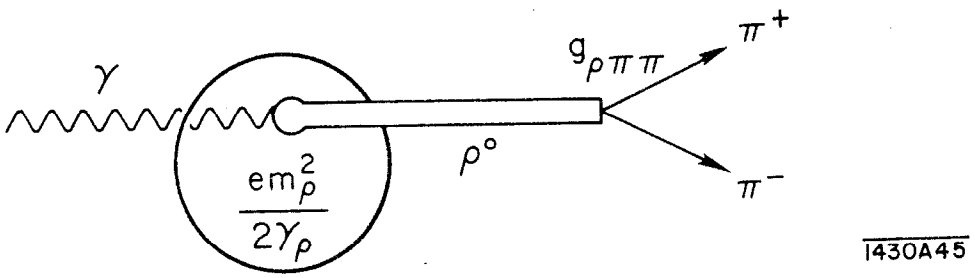

Fig. 19

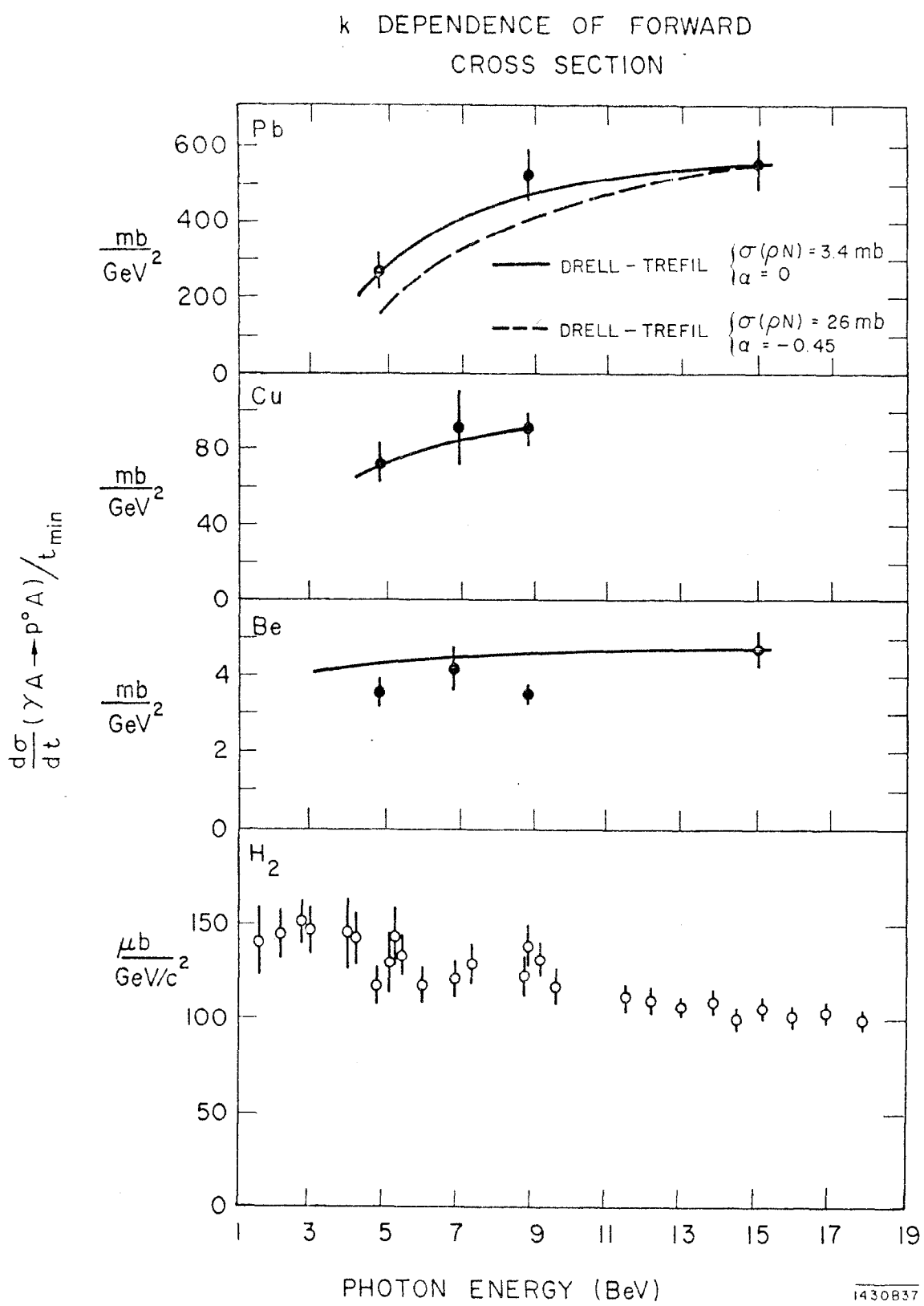
k DEPENDENCE OF FORWARD CROSS SECTION
Pb
Cu
Be
H_2
DRELL – TREFIL $\sigma(\rho N) = 3.4$ mb, $\alpha = 0$
DRELL – TREFIL $\sigma(\rho N) = 26$ mb, $\alpha = -0.45$
$\frac{d\sigma}{dt}(\gamma A \to p^\circ A)/t_{min}$
mb/GeV^2
μb/GeV/c^2
PHOTON ENERGY (BeV)
1430837

Fig. 20

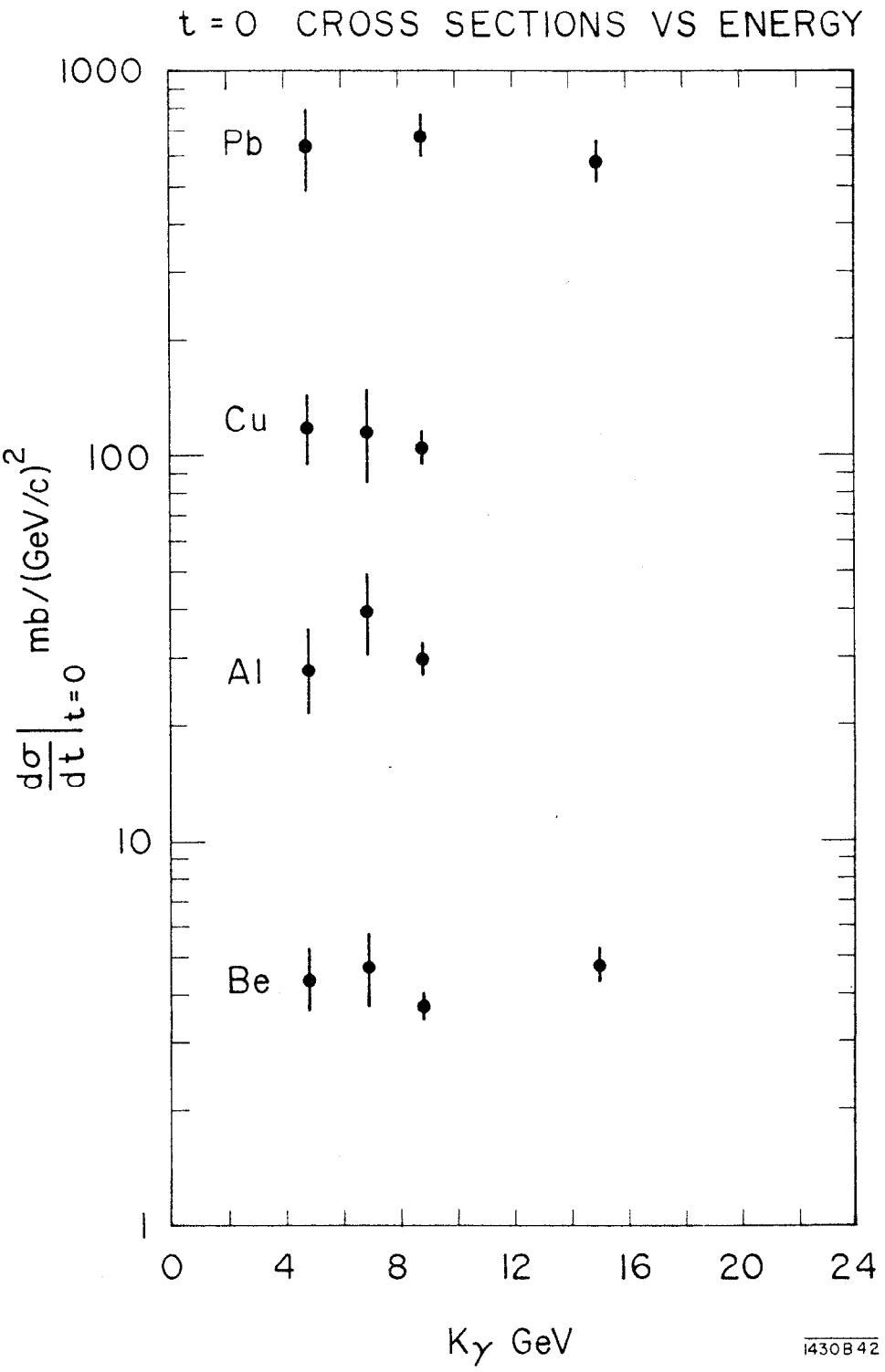
t = 0 CROSS SECTIONS VS ENERGY
1000
100
10
1
Pb
Cu
Al
Be
$\frac{d\sigma}{dt}\Big|_{t=0}$ mb/(GeV/c)^2
0
4
8
12
16
20
24
K_γ GeV
1430B42

Fig. 21

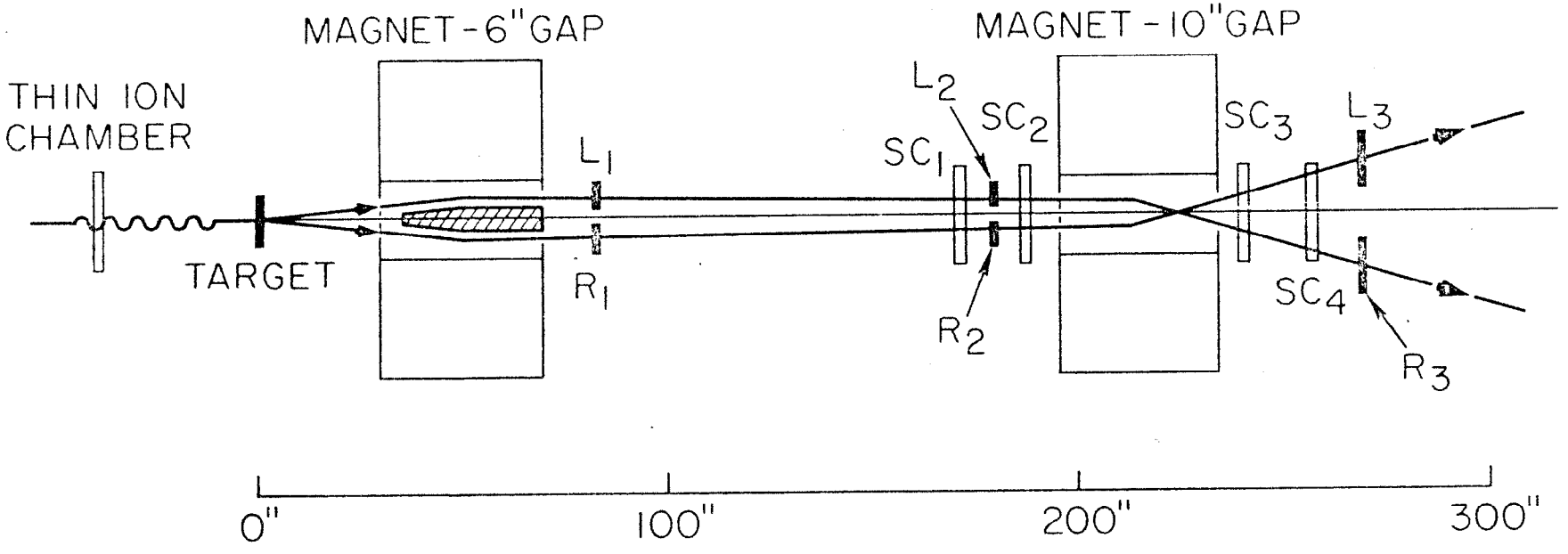

SC_1 THRU SC_4 ARE SPARK CHAMBERS
L_1 THRU L_3 AND R_1 THRU R_3 ARE SCINTILLATION COUNTERS

1729A2

Fig. 22

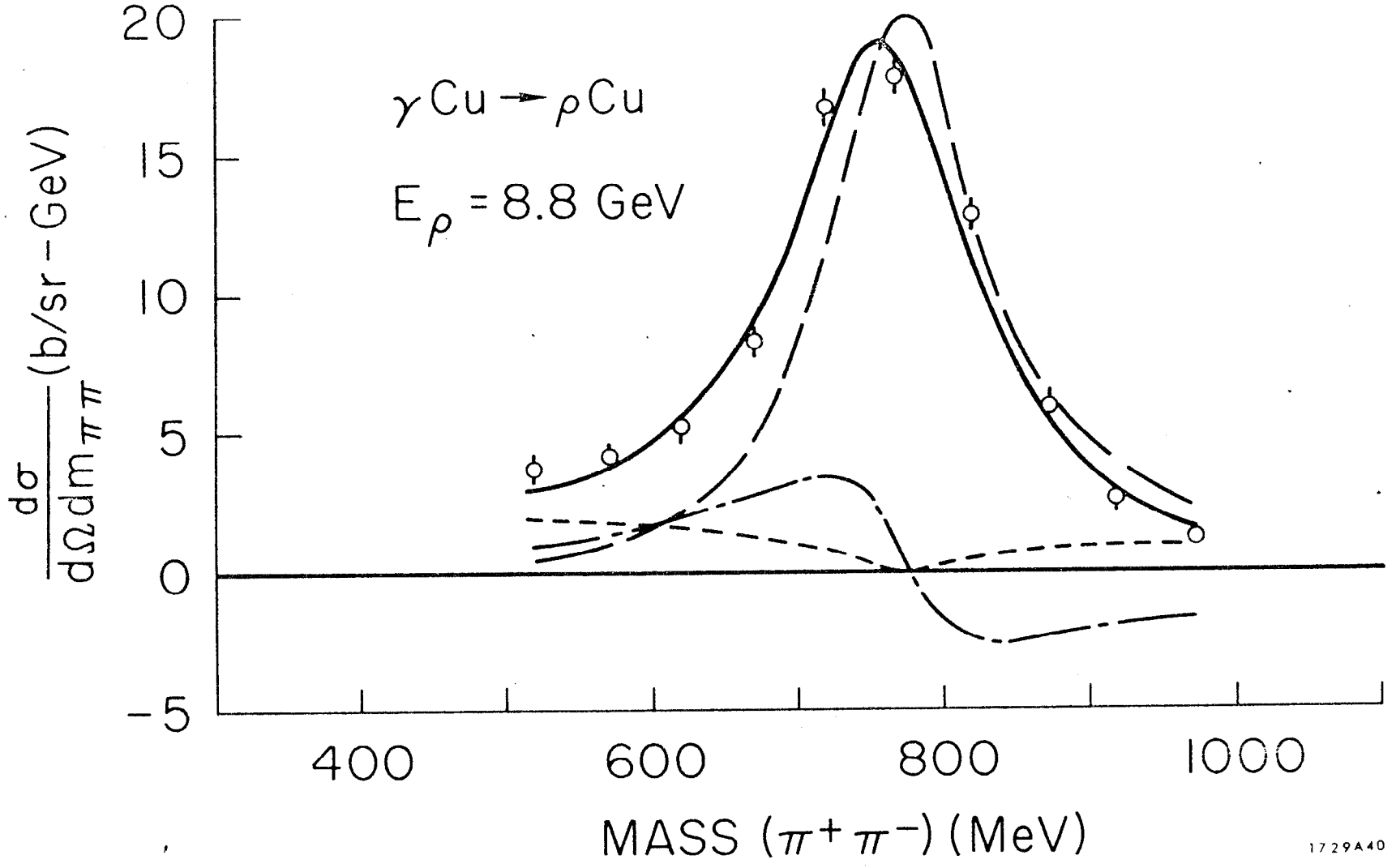
20
15
10
5
0
-5
400
600
800
1000
$\gamma Cu \rightarrow \rho Cu$
$E_\rho = 8.8$ GeV
$\frac{d\sigma}{d\Omega dm_{\pi\pi}}$ (b/sr-GeV)
MASS $(\pi^+\pi^-)$ (MeV)
1729A40

Fig. 23

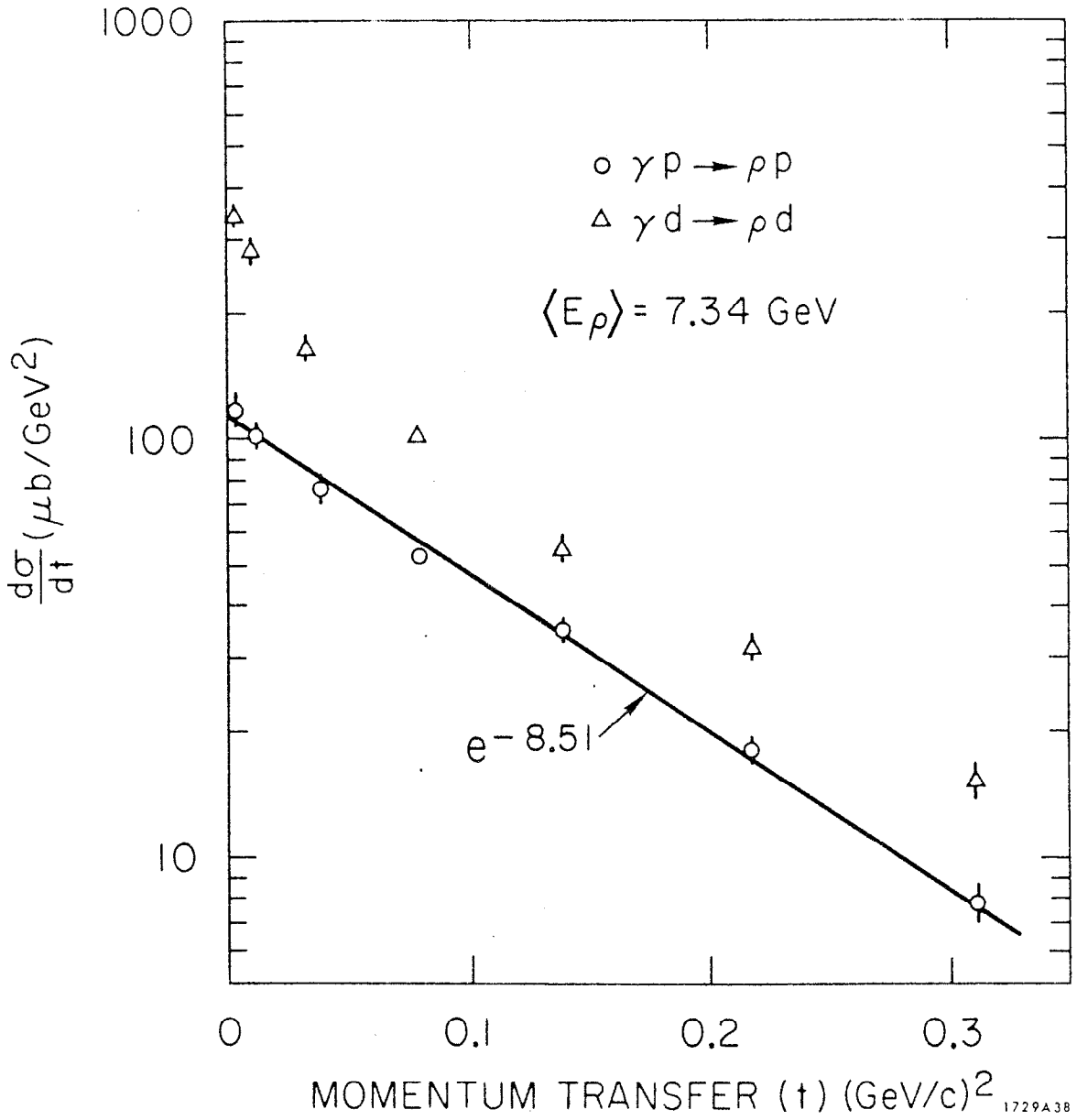
1000
100
10
$\frac{d\sigma}{dt}(\mu b/GeV^2)$
$\circ\ \gamma p \rightarrow \rho p$
$\triangle\ \gamma d \rightarrow \rho d$
$\langle E_\rho \rangle = 7.34$ GeV
$e^{-8.5t}$
0
0.1
0.2
0.3
MOMENTUM TRANSFER (t) $(GeV/c)^2$
1729A38

Fig. 24

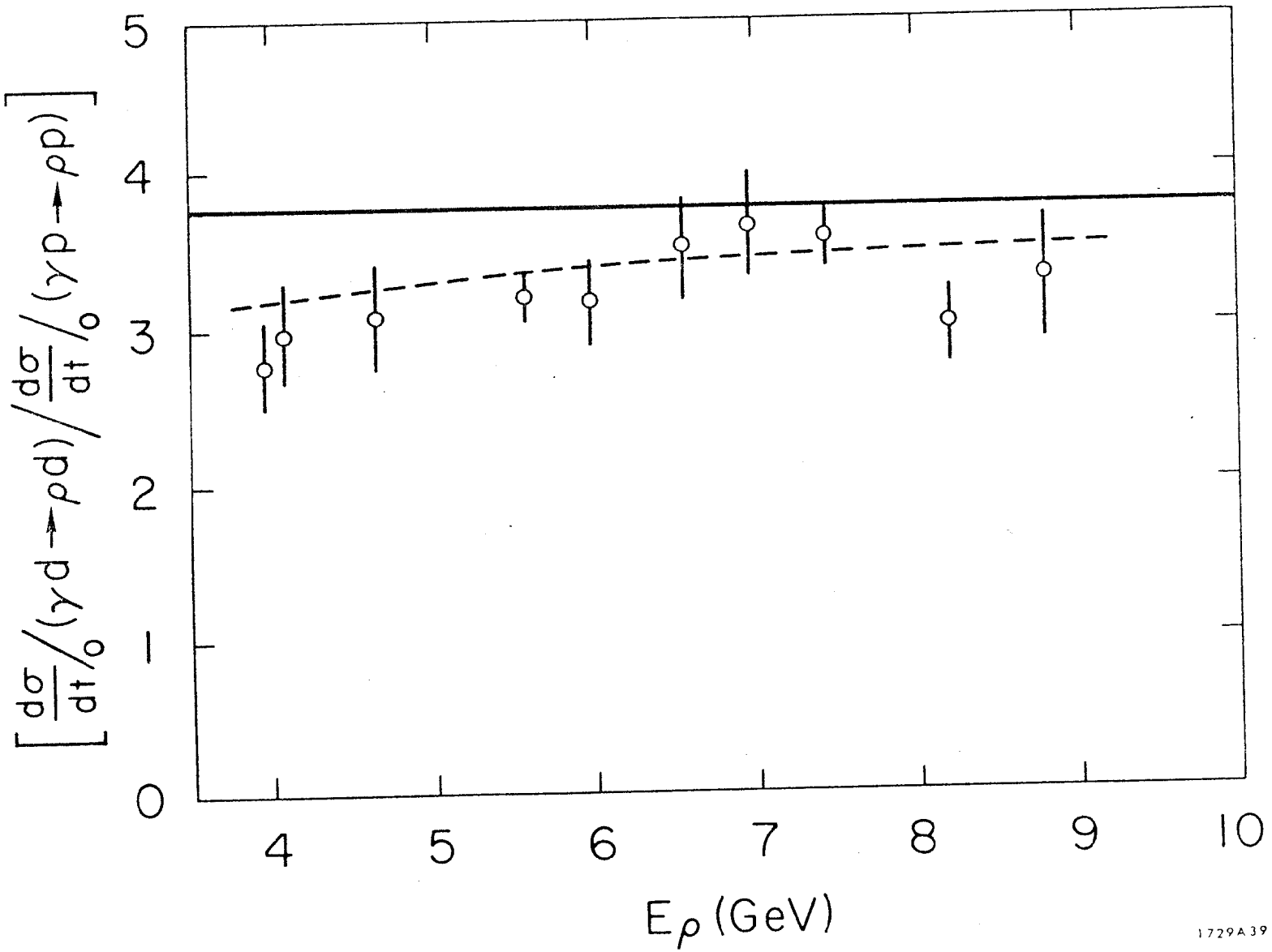
$\left[\frac{d\sigma}{dt}/_0(\gamma d \to \rho d)\right]/\frac{d\sigma}{dt}/_0(\gamma p \to \rho p)$
0
1
2
3
4
5
4
5
6
7
8
9
10
E_ρ (GeV)
1729A39

Fig. 25

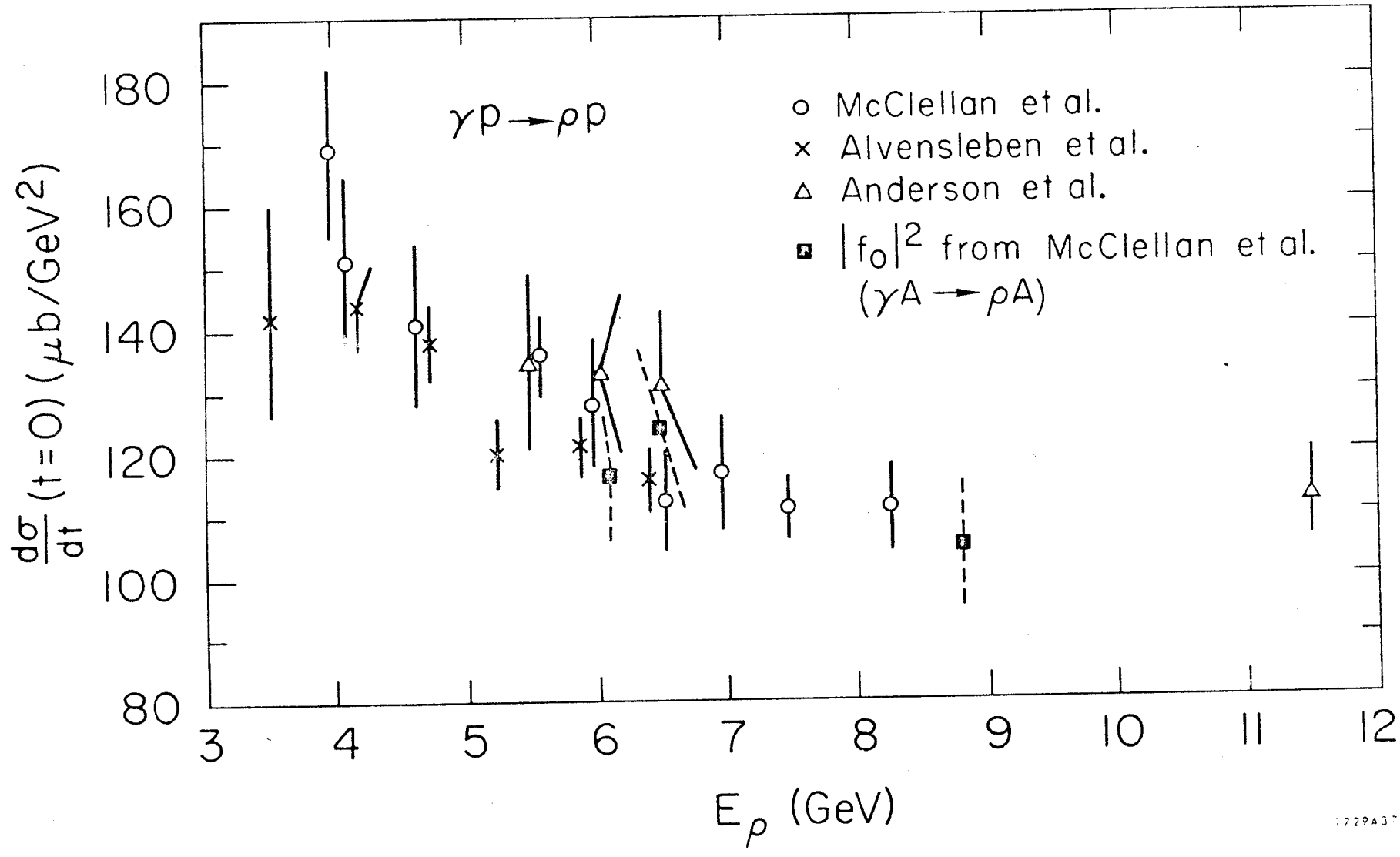
γp → ρp
o McClellan et al.
× Alvensleben et al.
△ Anderson et al.
■ |f0|² from McClellan et al. (γA → ρA)
dσ/dt (t=0) (μb/GeV²)
180
160
140
120
100
80
3
4
5
6
7
8
9
10
11
12
Eρ (GeV)
1729A37

Fig. 26

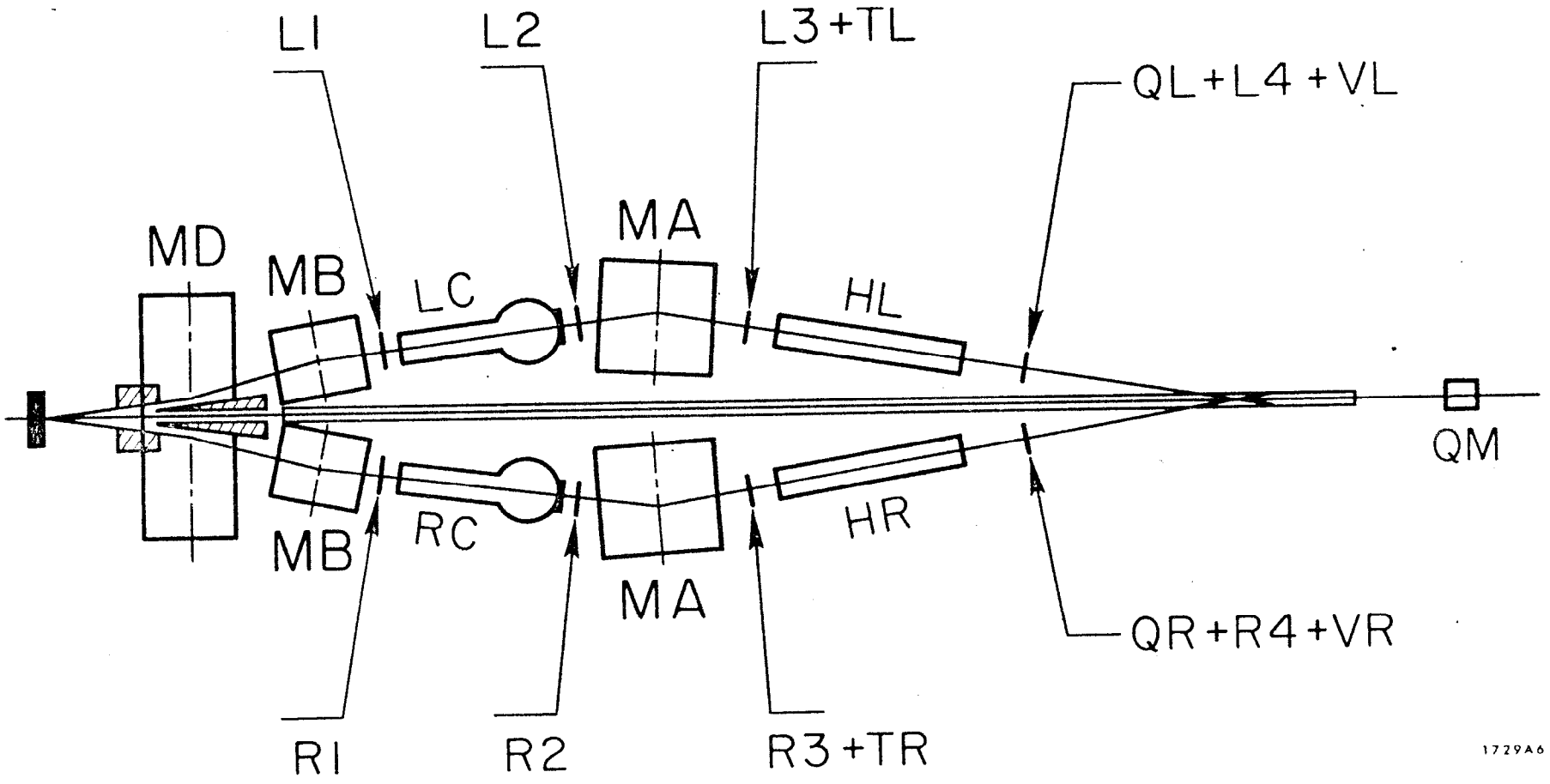
LI
L2
L3+TL
QL+L4+VL
MD
MB
LC
MA
HL
QM
MB
RC
MA
HR
QR+R4+VR
RI
R2
R3+TR
1729A6

Fig. 27

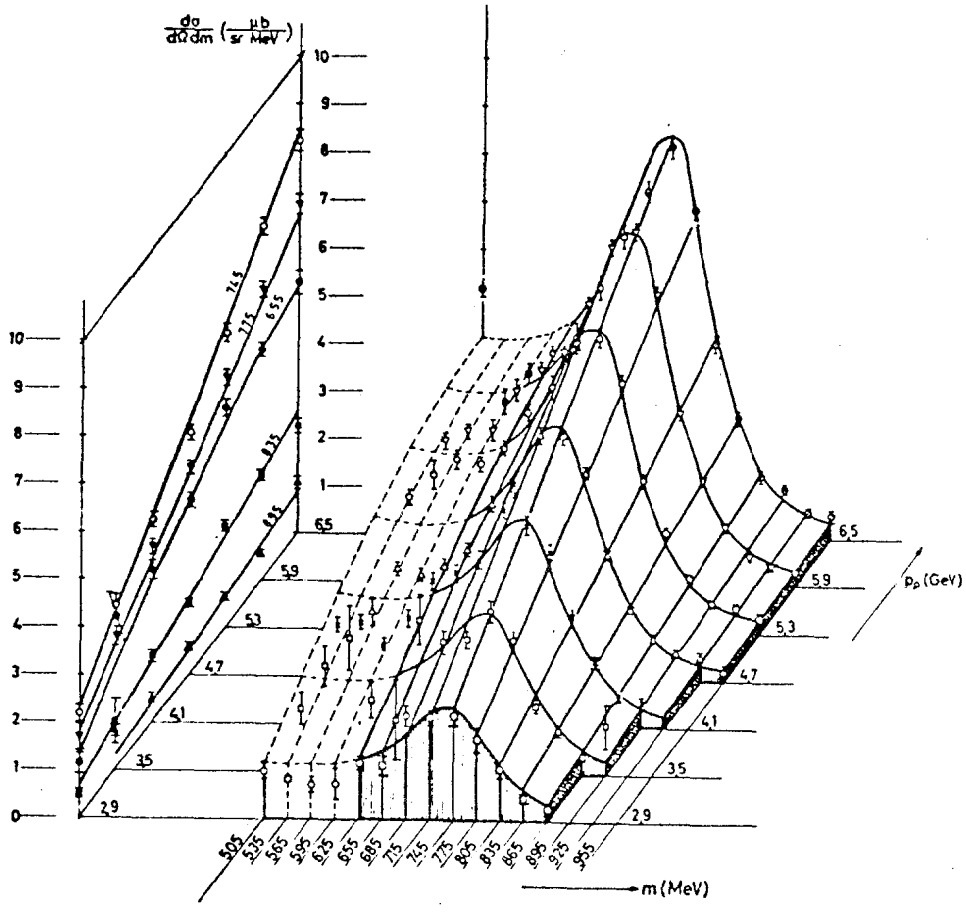

Fig. 28

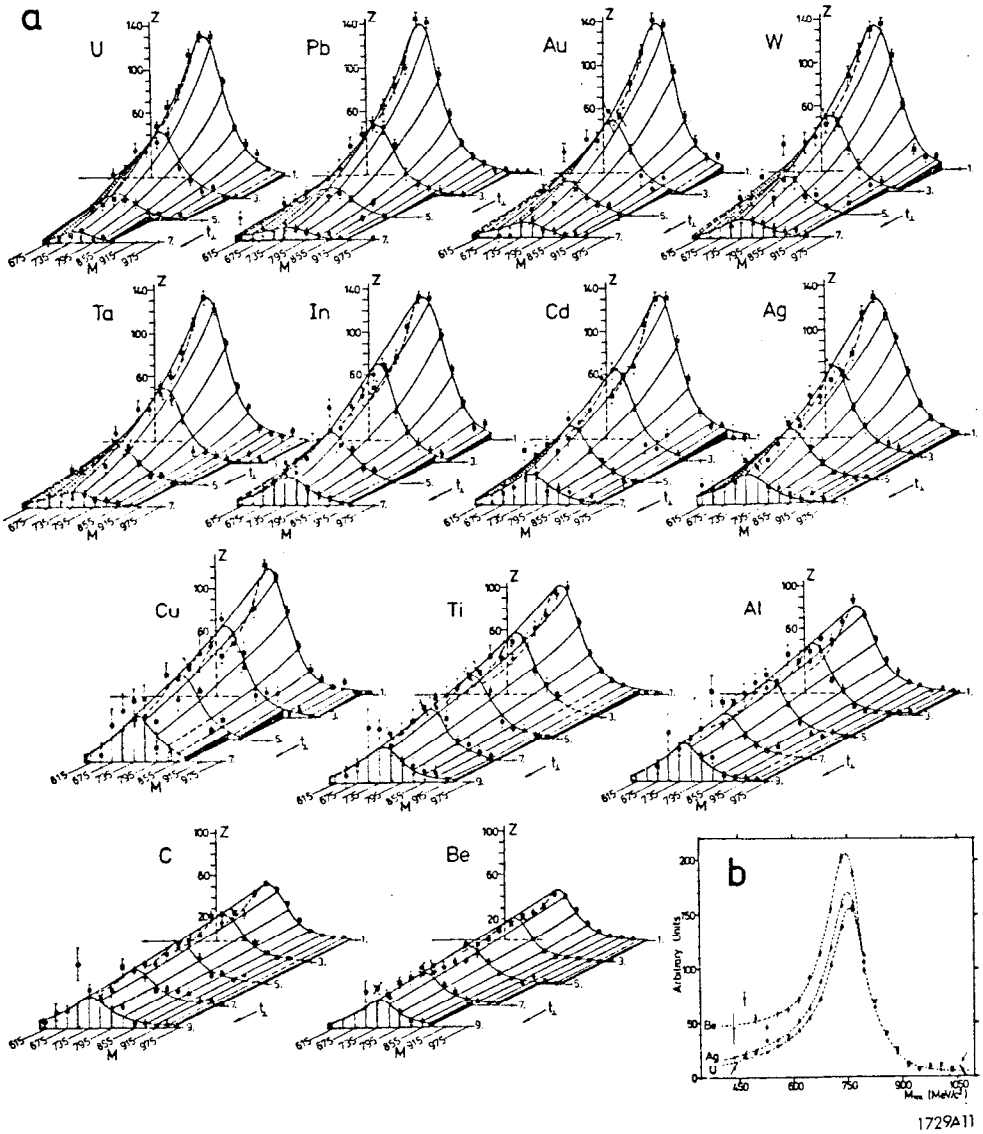
a
U
Pb
Au
W
Ta
In
Cd
Ag
Cu
Ti
Al
C
Be
b
Arbitrary Units
Be
Ag
U
1729A11

Fig. 29

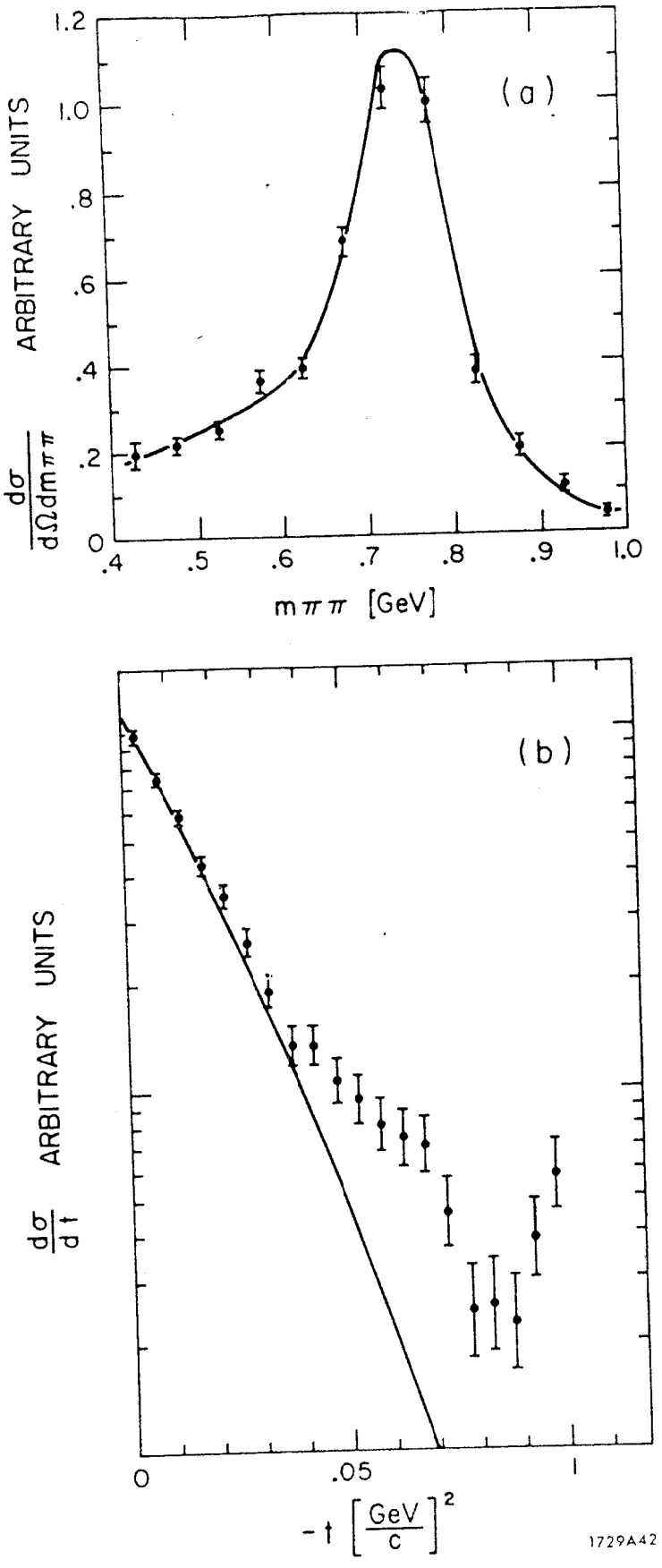
(a)
ARBITRARY UNITS
$\frac{d\sigma}{d\Omega dm_{\pi\pi}}$
1.2
1.0
.8
.6
.4
.2
0
.4
.5
.6
.7
.8
.9
1.0
$m_{\pi\pi}$ [GeV]
(b)
ARBITRARY UNITS
$\frac{d\sigma}{dt}$
0
.05
1
$-t\left[\frac{GeV}{c}\right]^2$
1729A42

Fig. 30

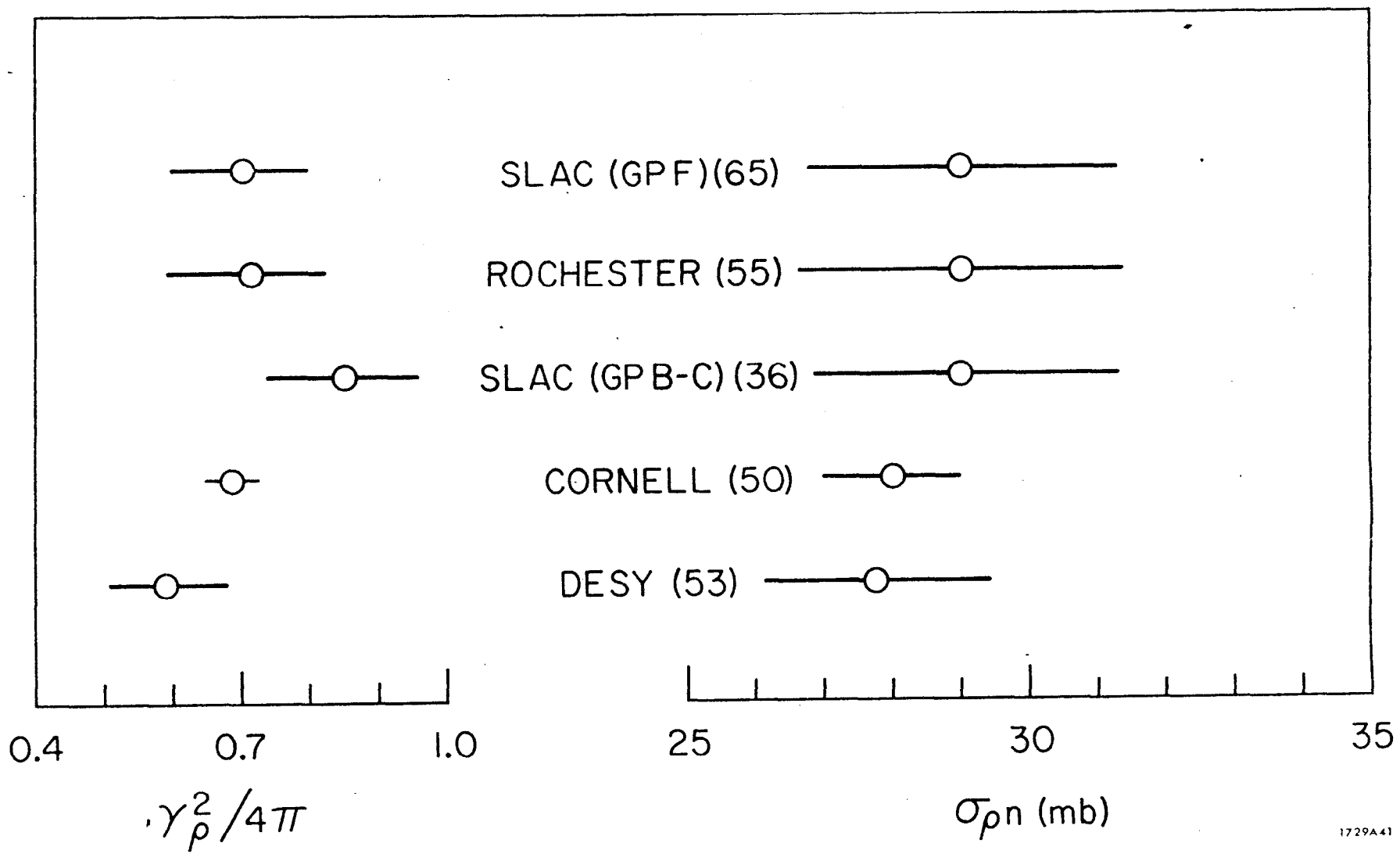
SLAC (GPF)(65)
ROCHESTER (55)
SLAC (GPB-C) (36)
CORNELL (50)
DESY (53)
0.4
0.7
1.0
$\gamma_\rho^2/4\pi$
25
30
35
$\sigma_{\rho n}$ (mb)
1729A41

Fig. 31

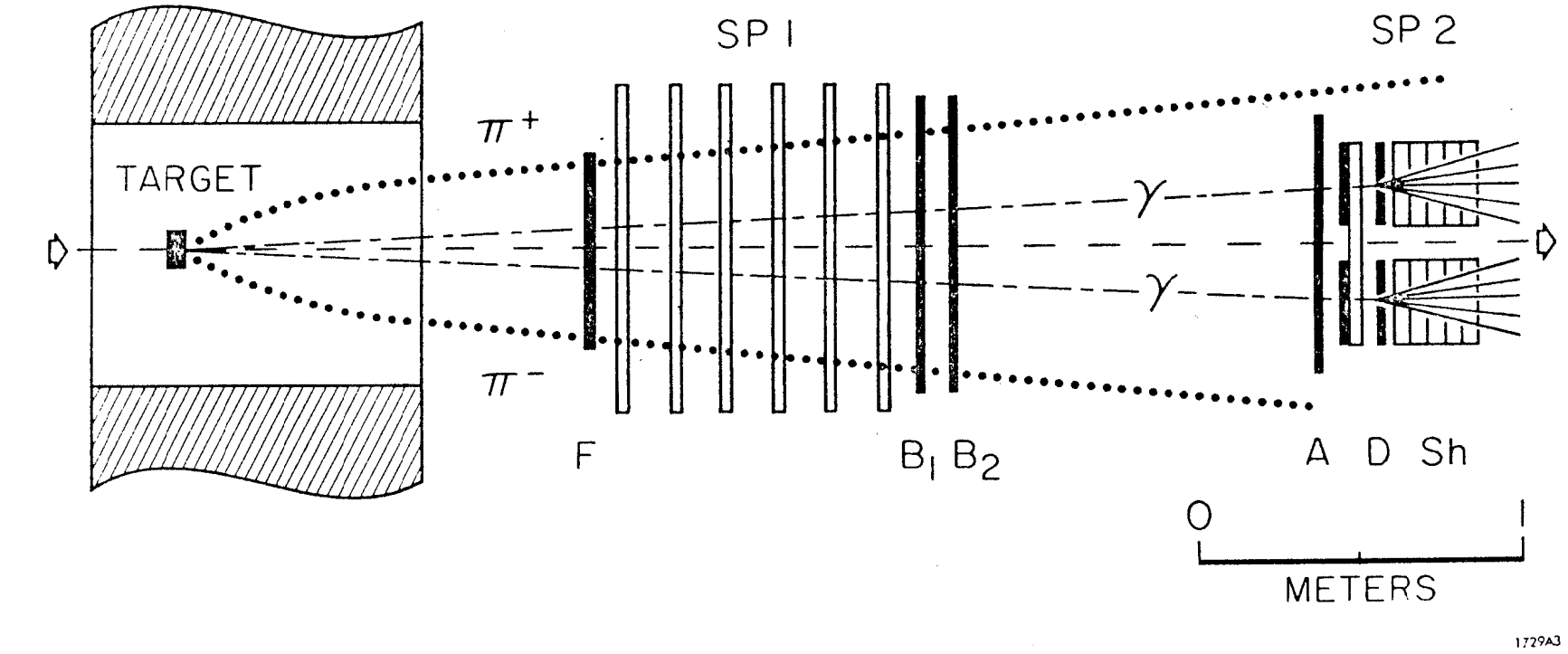
MAGNET (75 cm WIDE,
100 cm LONG, 25 cm GAP)
SP 1
SP 2
TARGET
π^+
π^-
γ
γ
F
B_1 B_2
A D Sh
0
1
METERS
1729A3

Fig. 32

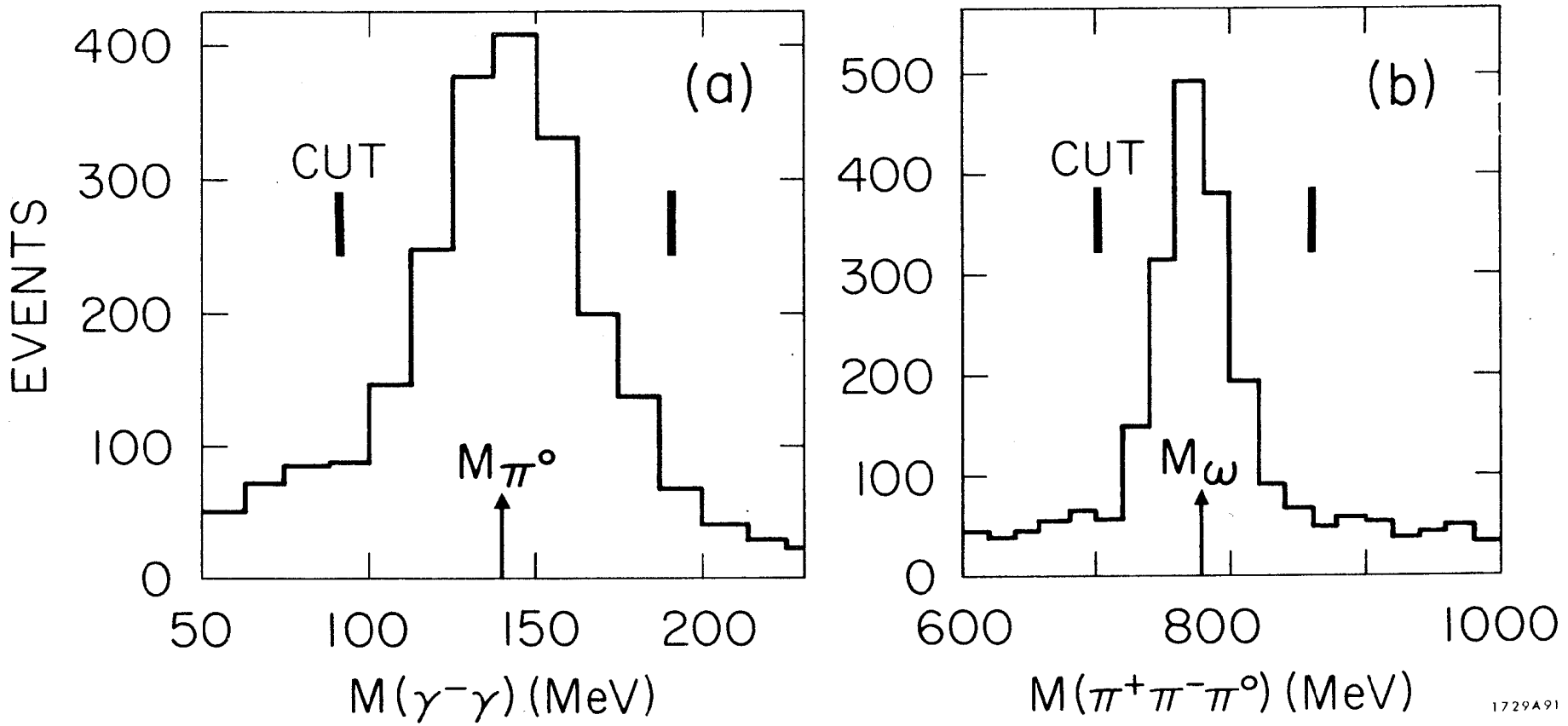
EVENTS
400
300
200
100
0
CUT
(a)
M_{π^0}
50
100
150
200
$M(\gamma^-\gamma)$ (MeV)
500
400
300
200
100
0
CUT
(b)
M_ω
600
800
1000
$M(\pi^+\pi^-\pi^0)$ (MeV)
1729A91

Fig. 33

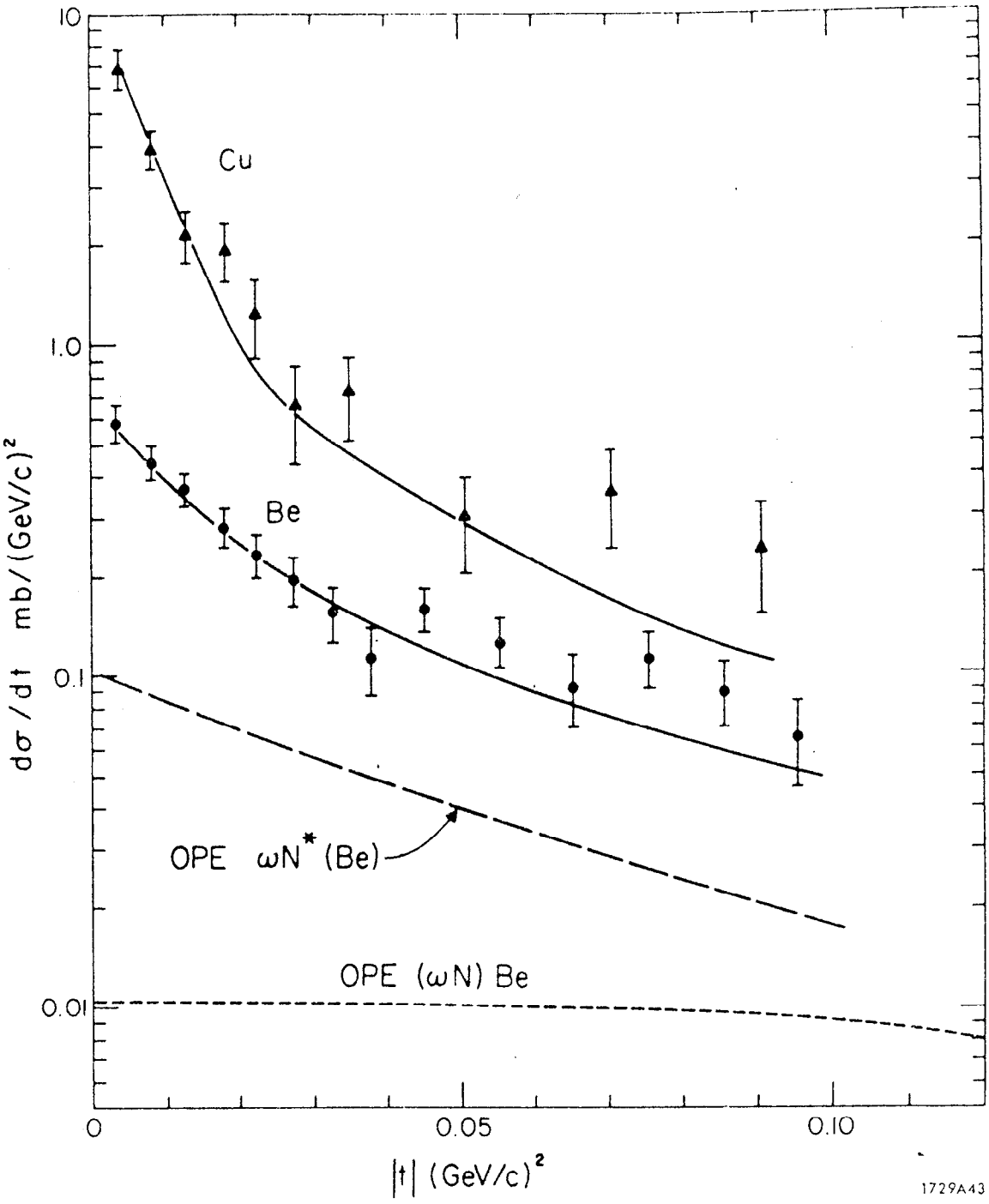
10
1.0
0.1
0.01
Cu
Be
OPE ωN* (Be)
OPE (ωN) Be
dσ/dt mb/(GeV/c)²
0
0.05
0.10
|t| (GeV/c)²
1729A43

Fig. 34

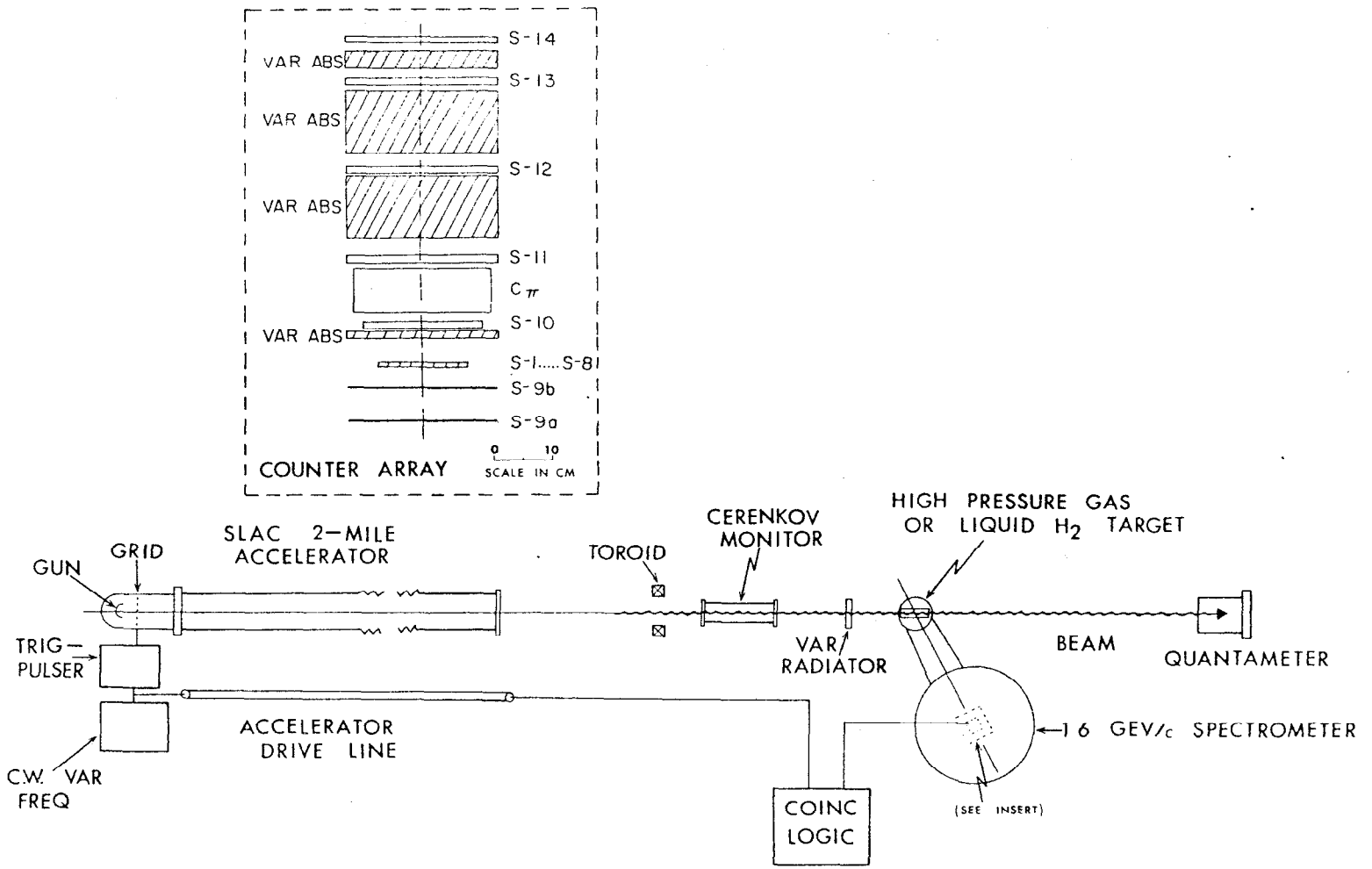

EXPERIMENTAL ARRANGEMENT FOR

$\gamma + D \longrightarrow \rho + D$

Fig. 35

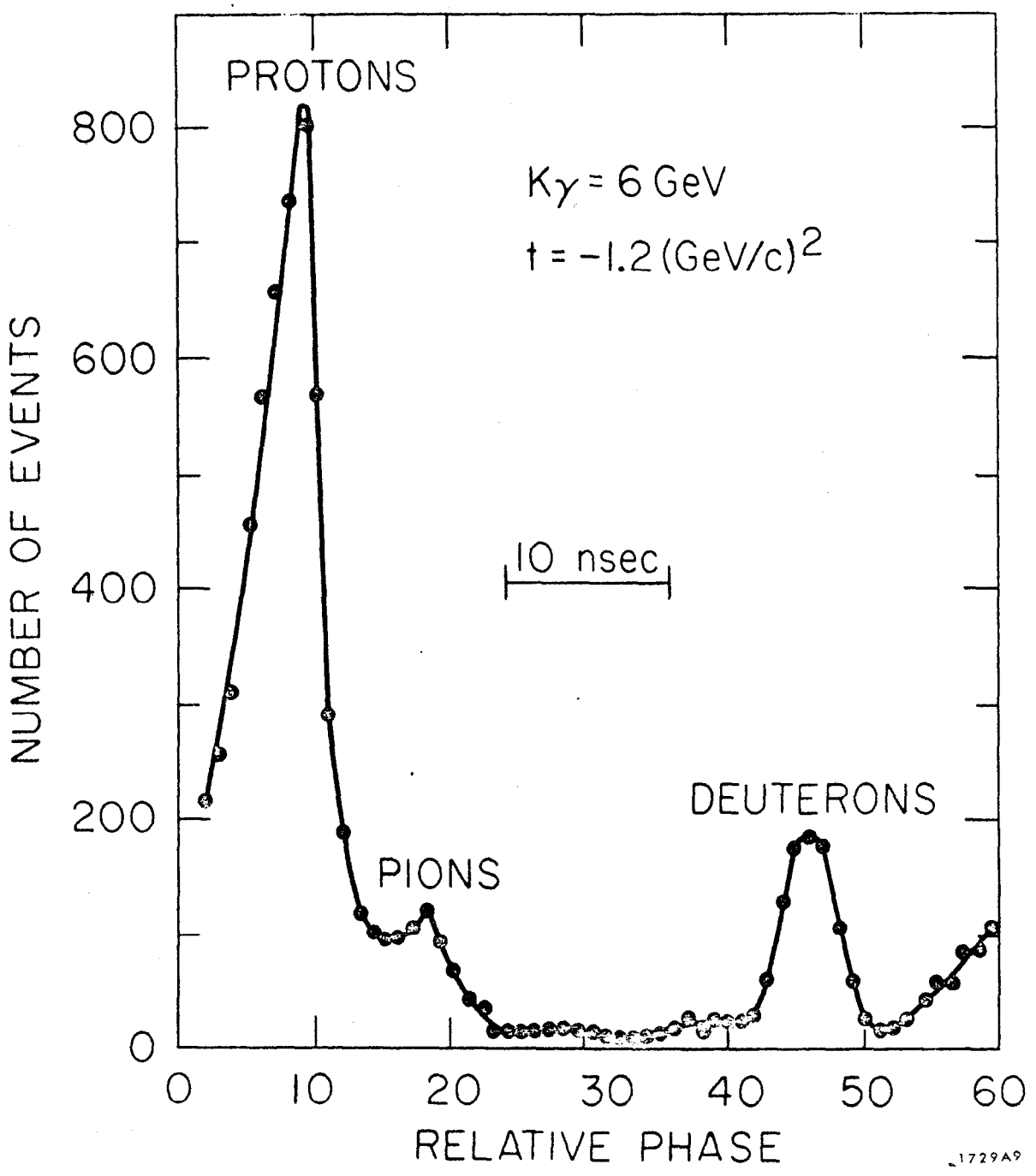
PROTONS
Kγ = 6 GeV
t = −1.2 (GeV/c)²
10 nsec
DEUTERONS
PIONS
NUMBER OF EVENTS
0
200
400
600
800
0
10
20
30
40
50
60
RELATIVE PHASE
1729A9

Fig. 36

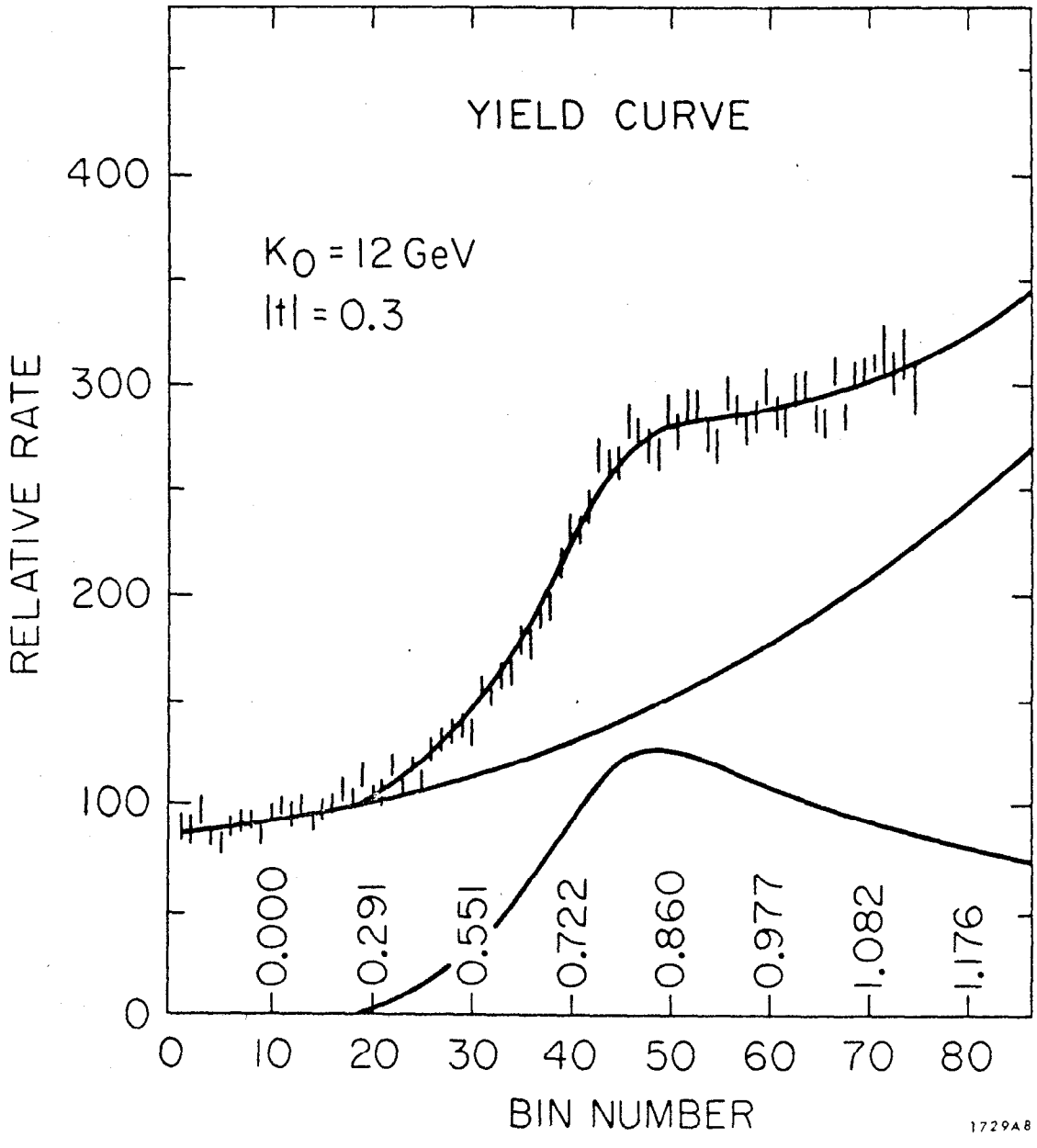
YIELD CURVE
K_0 = 12 GeV
|t| = 0.3
RELATIVE RATE
400
300
200
100
0
0.000
0.291
0.551
0.722
0.860
0.977
1.082
1.176
0
10
20
30
40
50
60
70
80
BIN NUMBER
1729A8

Fig. 37

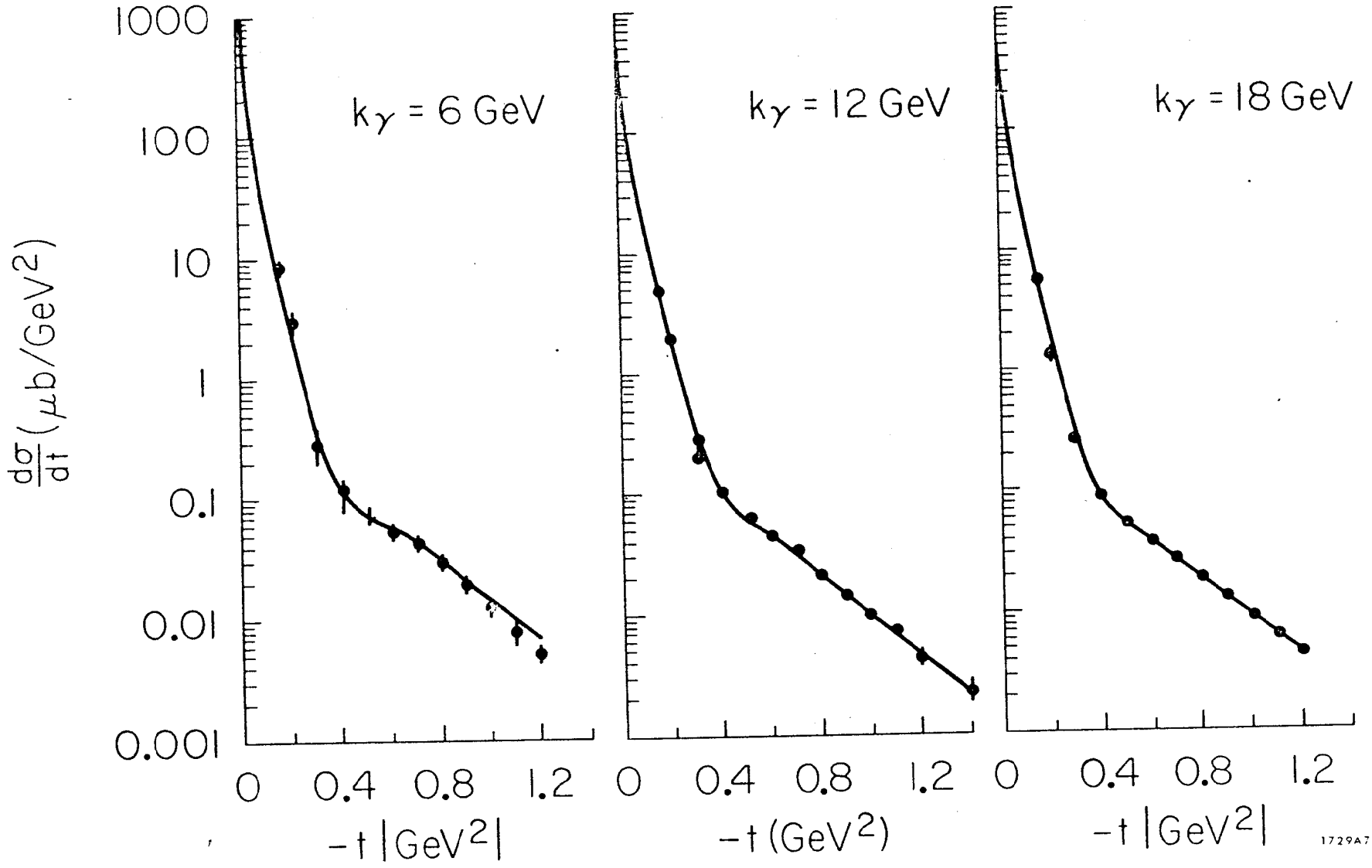
1000
100
10
1
0.1
0.01
0.001
dσ/dt (μb/GeV²)
kγ = 6 GeV
kγ = 12 GeV
kγ = 18 GeV
0
0.4
0.8
1.2
-t |GeV²|
-t (GeV²)
-t |GeV²|
1729A7

Fig. 38

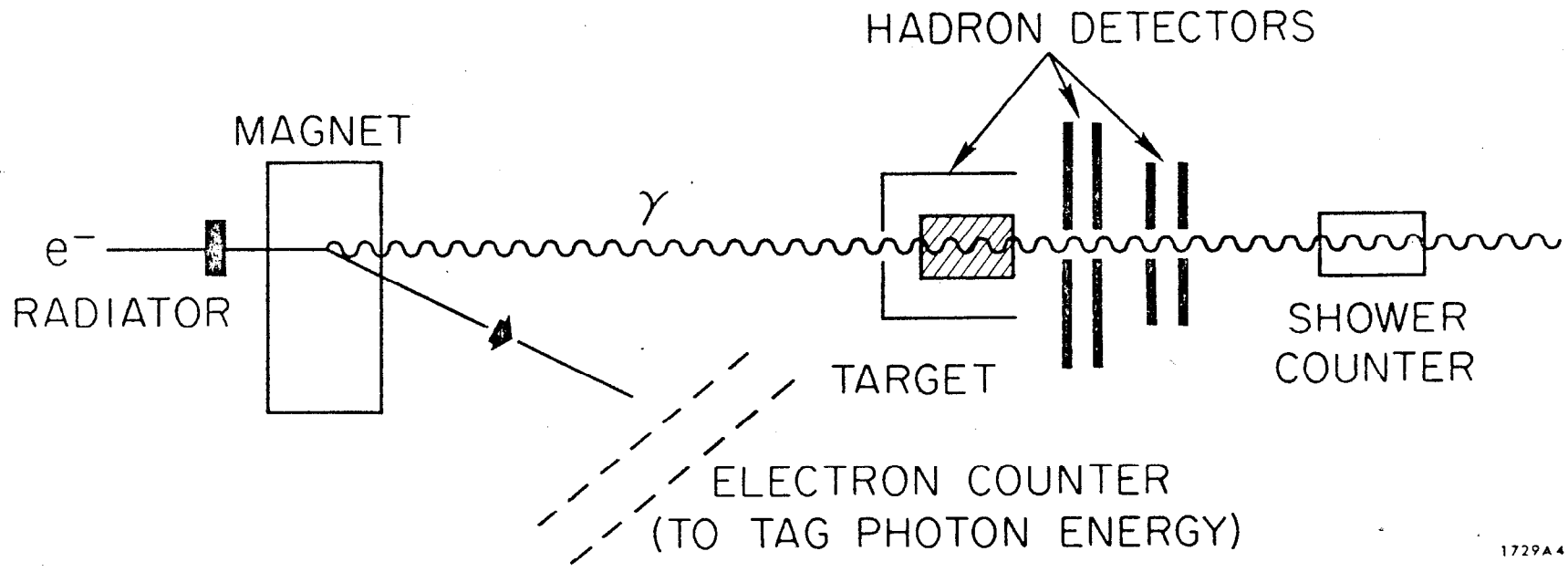
HADRON DETECTORS
MAGNET
γ
e^-
RADIATOR
TARGET
SHOWER
COUNTER
ELECTRON COUNTER
(TO TAG PHOTON ENERGY)
1729A4

Fig. 39

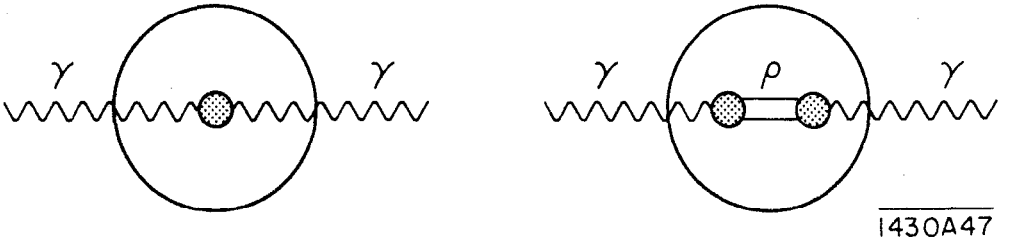

Fig. 40

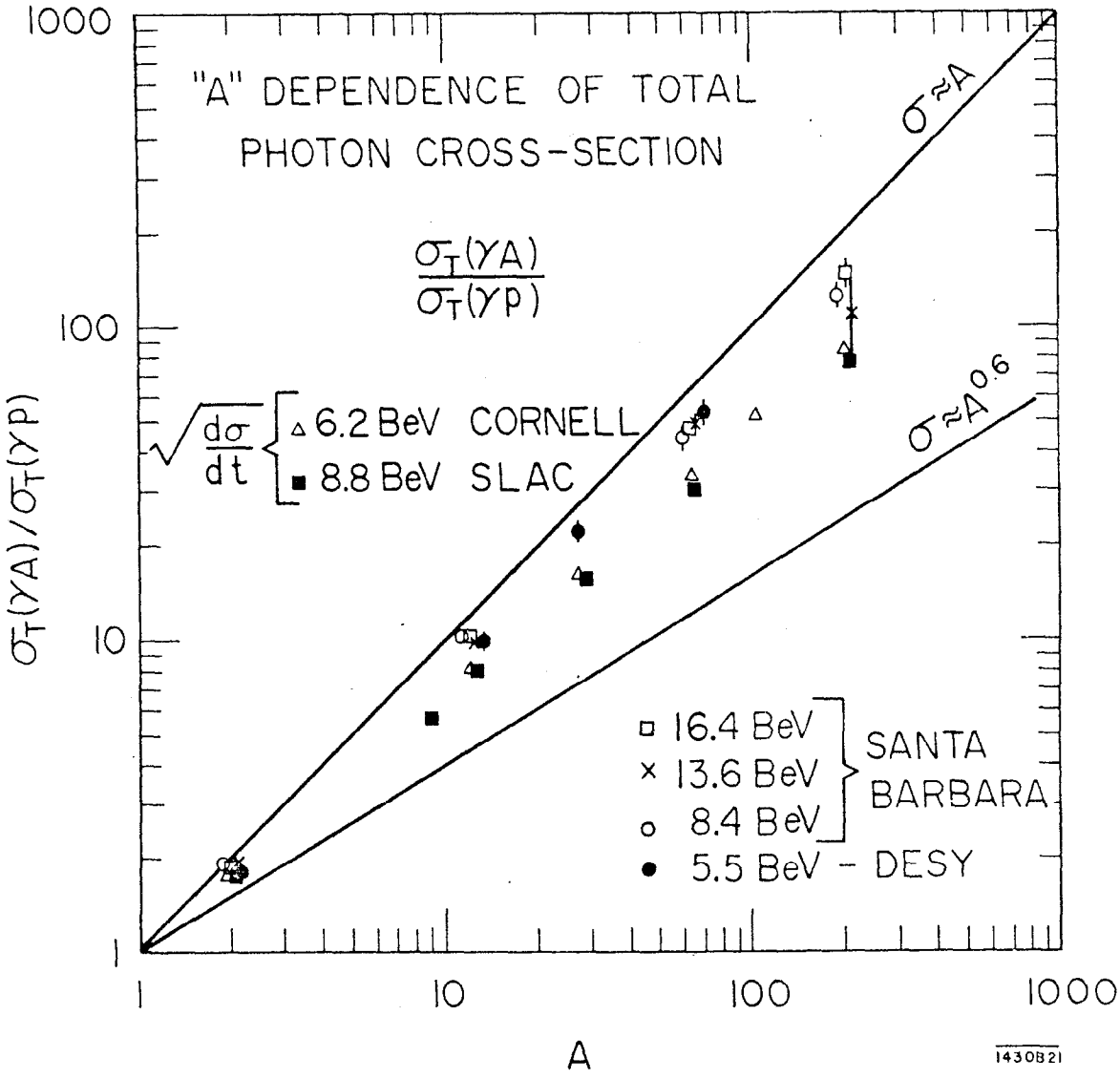
"A" DEPENDENCE OF TOTAL
PHOTON CROSS-SECTION
$\frac{\sigma_T(\gamma A)}{\sigma_T(\gamma p)}$
$\sqrt{\frac{d\sigma}{dt}}$
6.2 BeV CORNELL
8.8 BeV SLAC
16.4 BeV
13.6 BeV
8.4 BeV
SANTA BARBARA
5.5 BeV - DESY
$\sigma \approx A$
$\sigma \approx A^{0.6}$
$\sigma_T(\gamma A)/\sigma_T(\gamma p)$
A
1000
100
10
1
1
10
100
1000
1430821

Fig. 41

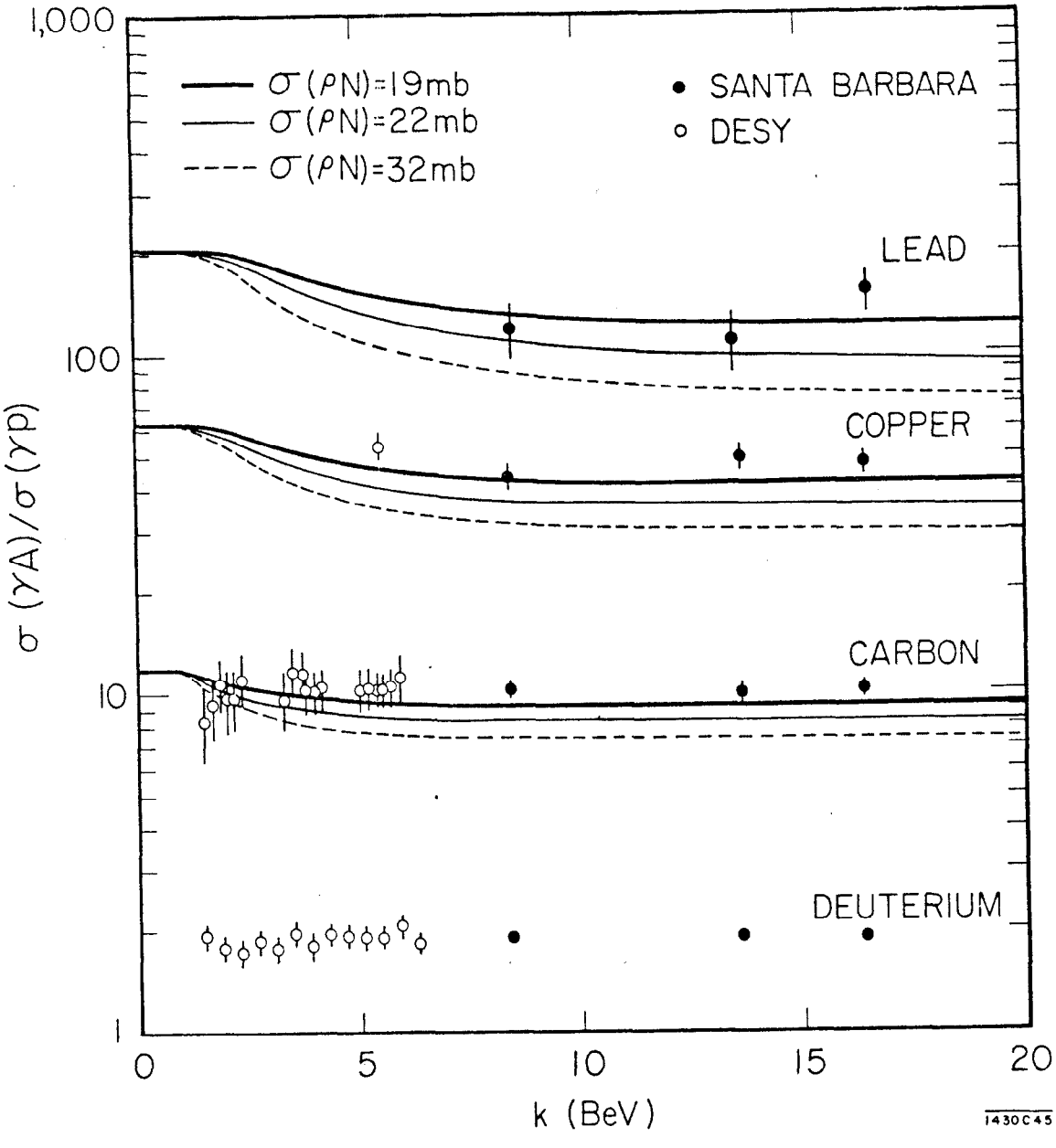
1,000
100
10
1
σ (γA)/σ (γp)
σ (ρN)=19mb
σ (ρN)=22mb
σ (ρN)=32mb
SANTA BARBARA
DESY
LEAD
COPPER
CARBON
DEUTERIUM
0
5
10
15
20
k (BeV)
1430C45

Fig. 42

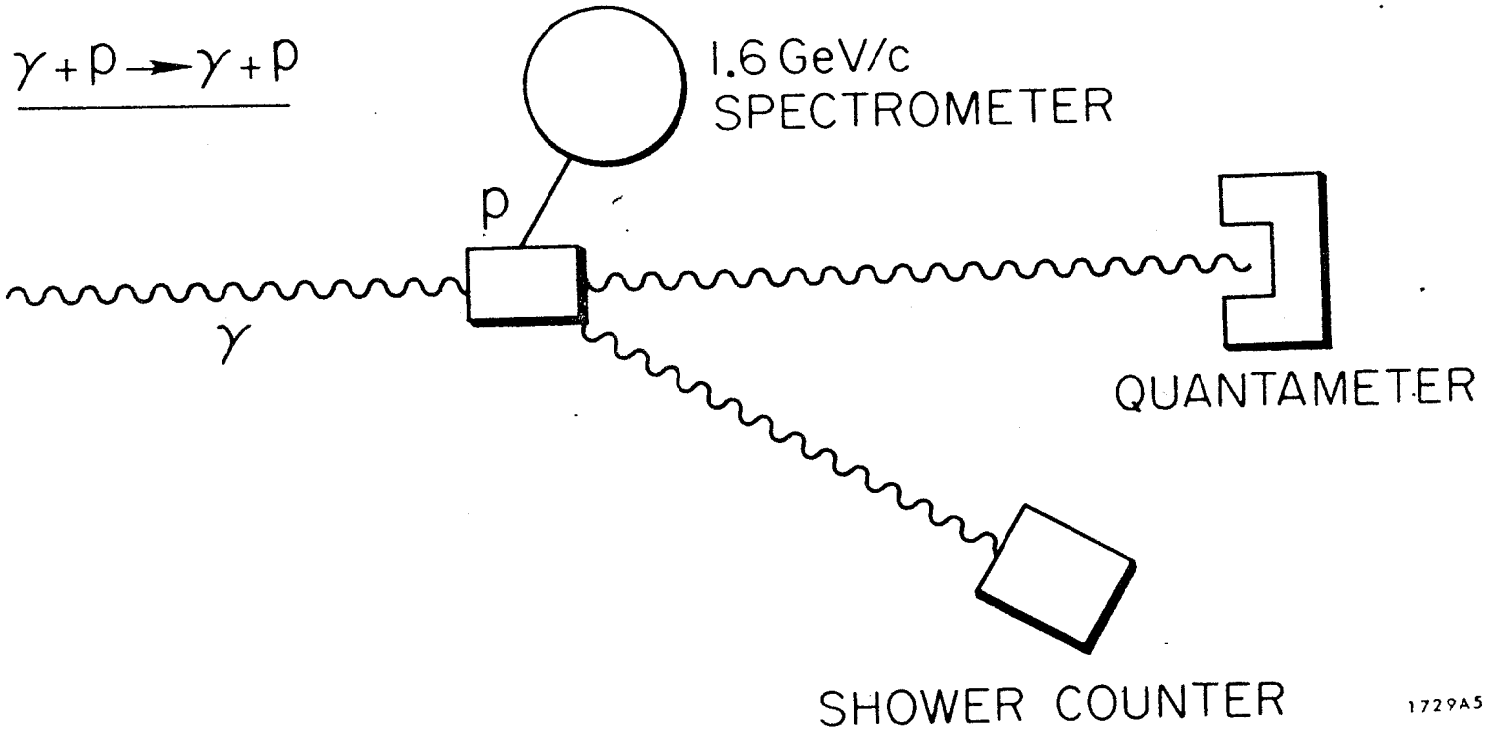
γ + p → γ + p
1.6 GeV/c
SPECTROMETER
p
γ
QUANTAMETER
SHOWER COUNTER
1729A5

Fig. 43

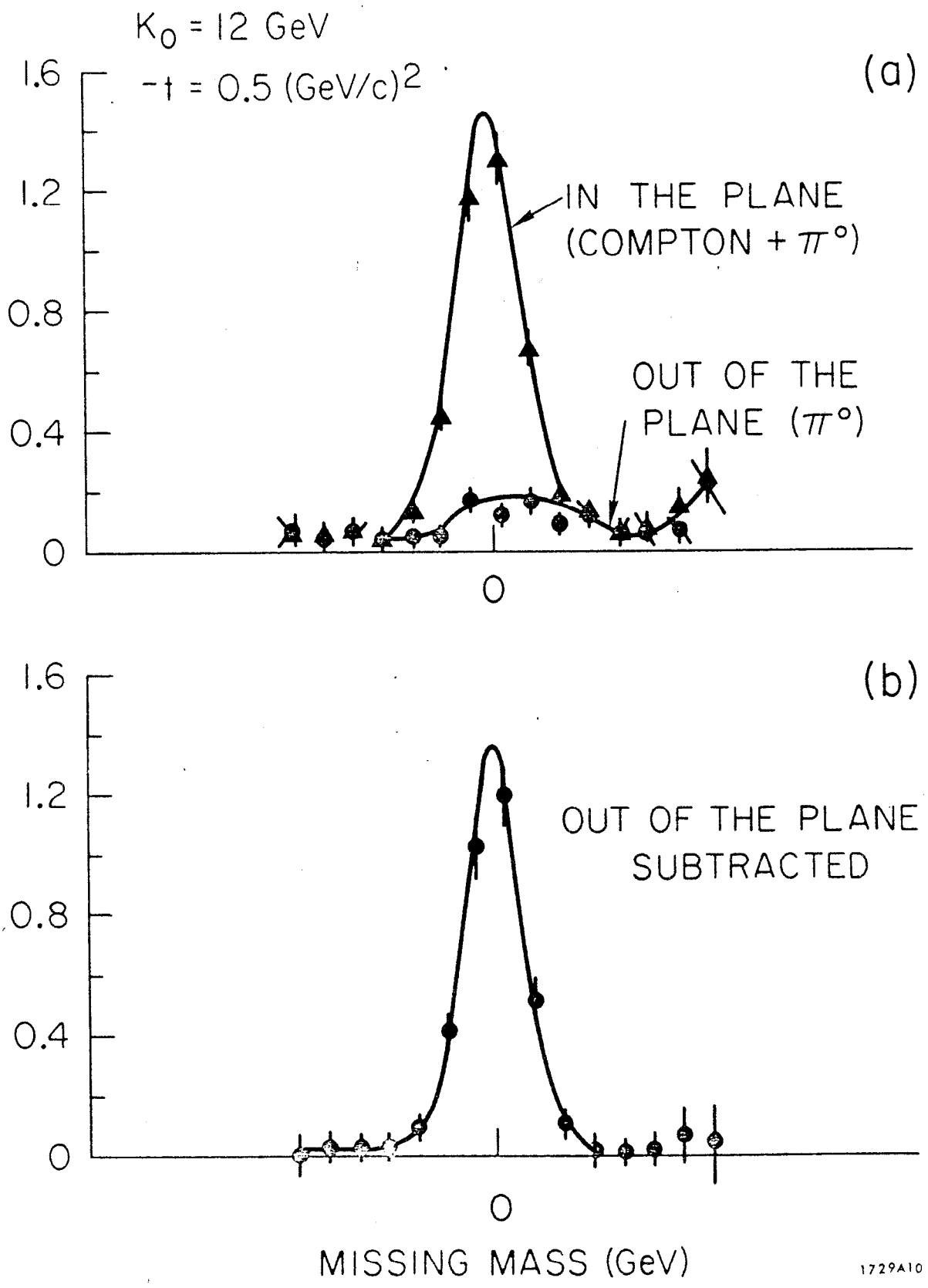
K_0 = 12 GeV
$-t$ = 0.5 (GeV/c)^2
(a)
1.6
1.2
0.8
0.4
0
IN THE PLANE
(COMPTON + π^0)
OUT OF THE
PLANE (π^0)
0
(b)
1.6
1.2
0.8
0.4
0
OUT OF THE PLANE
SUBTRACTED
0
MISSING MASS (GeV)
1729A10

Fig. 44

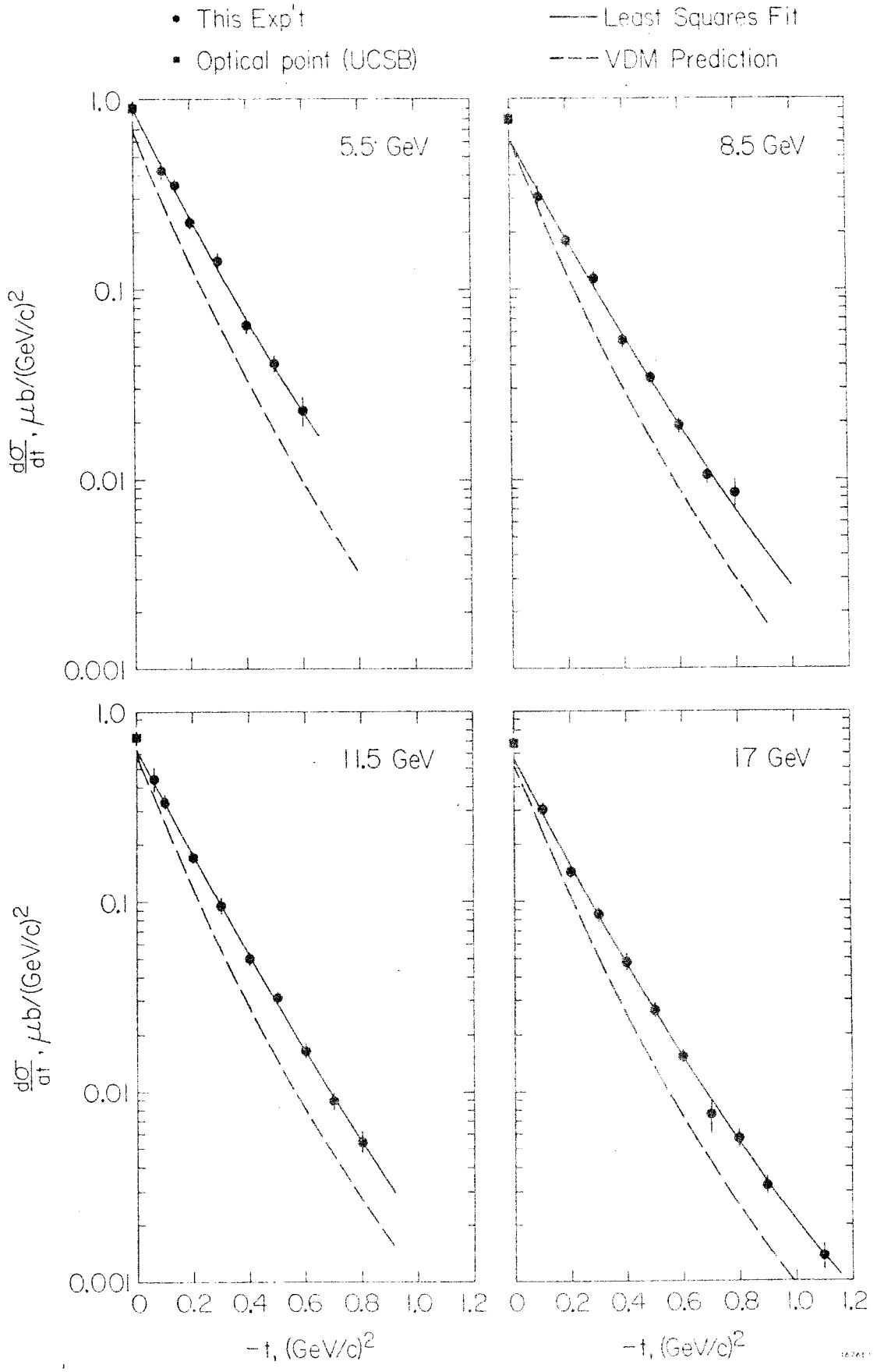
• This Exp't
• Optical point (UCSB)
—— Least Squares Fit
--- VDM Prediction
5.5 GeV
8.5 GeV
11.5 GeV
17 GeV
1.0
0.1
0.01
0.001
$\frac{d\sigma}{dt}$, μb/(GeV/c)^2
0
0.2
0.4
0.6
0.8
1.0
1.2
$-t$, (GeV/c)^2

Fig. 45

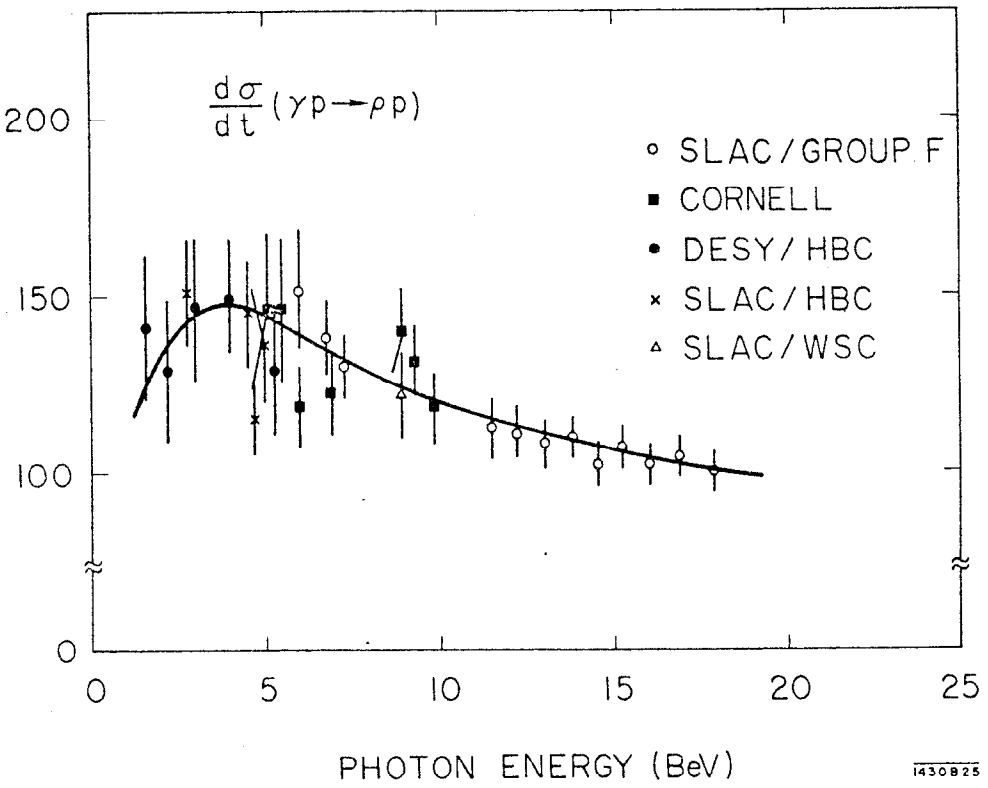
$\frac{d\sigma}{dt}(\gamma p \rightarrow \rho p)$
SLAC/GROUP F
CORNELL
DESY/HBC
SLAC/HBC
SLAC/WSC
200
150
100
0
0
5
10
15
20
25
PHOTON ENERGY (BeV)
1430B25

Fig. 46

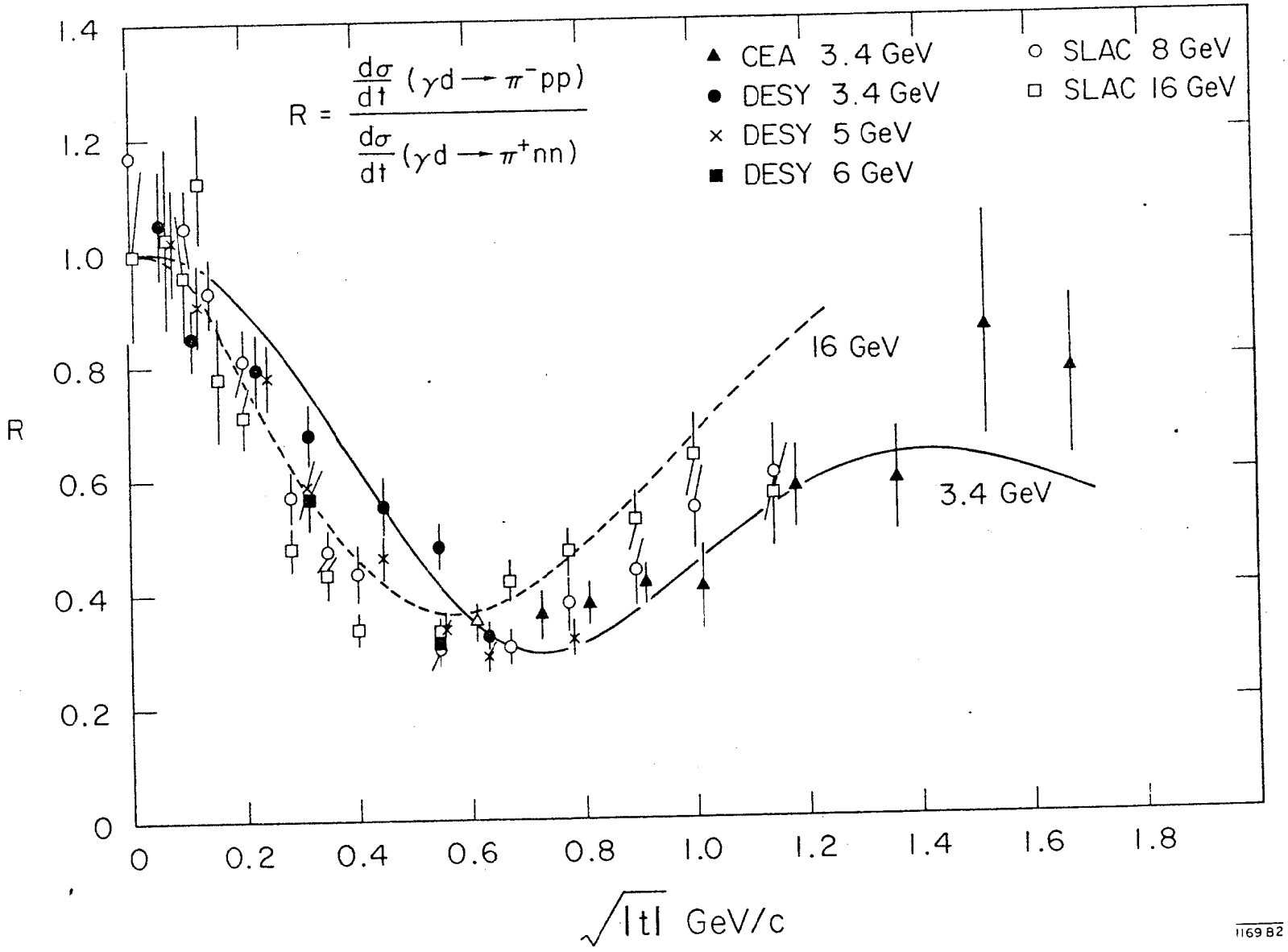
R = dσ/dt (γd → π⁻pp) / dσ/dt (γd → π⁺nn)
CEA 3.4 GeV
DESY 3.4 GeV
DESY 5 GeV
DESY 6 GeV
SLAC 8 GeV
SLAC 16 GeV
16 GeV
3.4 GeV
R
√|t| GeV/c
1169B2

Fig. 47

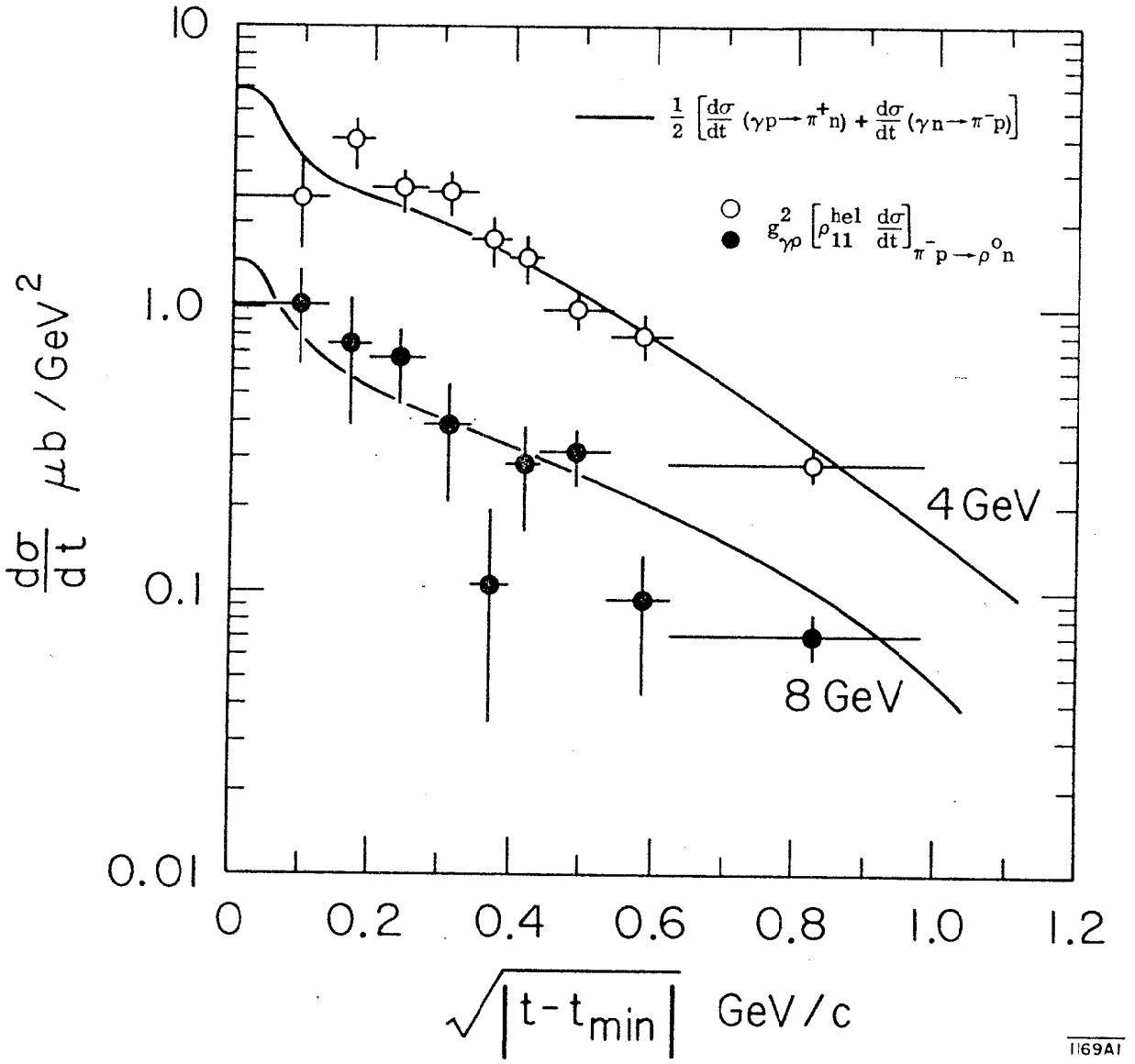
10
1.0
0.1
0.01
0
0.2
0.4
0.6
0.8
1.0
1.2
$\frac{d\sigma}{dt}$ μb / GeV^2
$\sqrt{|t-t_{min}|}$ GeV/c
$\frac{1}{2}\left[\frac{d\sigma}{dt}(\gamma p \to \pi^+ n) + \frac{d\sigma}{dt}(\gamma n \to \pi^- p)\right]$
$g^2_{\gamma\rho}\left[\rho^{hel}_{11}\ \frac{d\sigma}{dt}\right]_{\pi^- p \to \rho^0 n}$
4 GeV
8 GeV
1169A1

Fig. 48

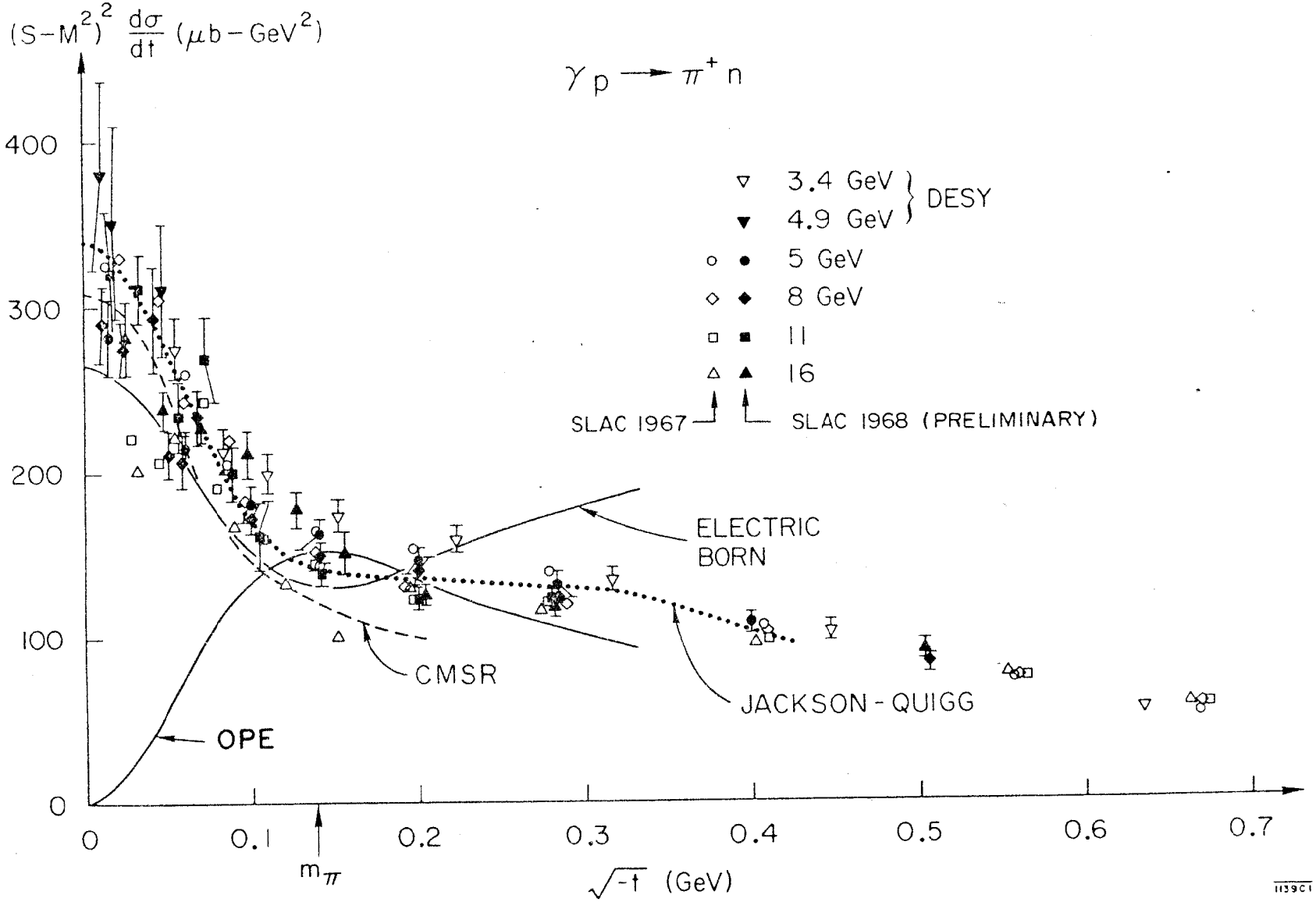
$(S-M^2)^2 \frac{d\sigma}{dt}$ ($\mu b - GeV^2$)
$\gamma p \rightarrow \pi^+ n$
400
300
200
100
0
3.4 GeV
4.9 GeV
DESY
5 GeV
8 GeV
11
16
SLAC 1967
SLAC 1968 (PRELIMINARY)
ELECTRIC BORN
CMSR
JACKSON - QUIGG
OPE
0
0.1
m_π
0.2
0.3
0.4
0.5
0.6
0.7
$\sqrt{-t}$ (GeV)
1139C1

Fig. 49

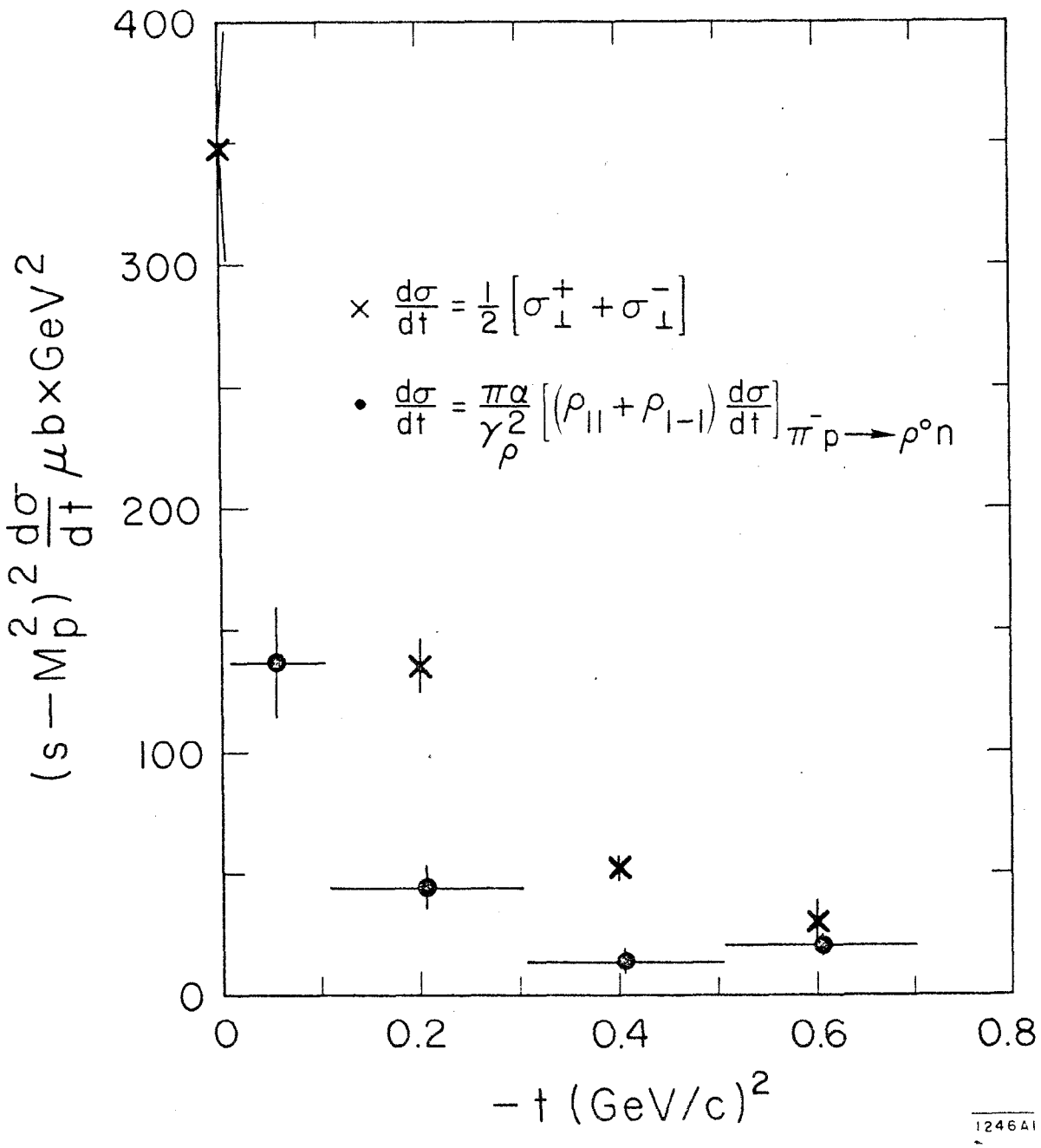
400
300
200
100
0
0
0.2
0.4
0.6
0.8
$(s-M_p^2)^2 \frac{d\sigma}{dt}\ \mu b \times GeV^2$
$-t\ (GeV/c)^2$
$\times\ \frac{d\sigma}{dt} = \frac{1}{2}\left[\sigma_\perp^+ + \sigma_\perp^-\right]$
$\bullet\ \frac{d\sigma}{dt} = \frac{\pi\alpha}{\gamma_\rho^2}\left[(\rho_{11}+\rho_{1-1})\frac{d\sigma}{dt}\right]_{\pi^- p \to \rho^0 n}$
124641

Fig. 50

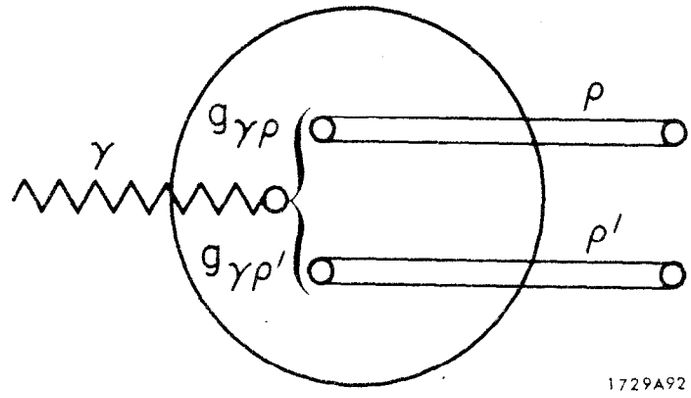

Fig. 51

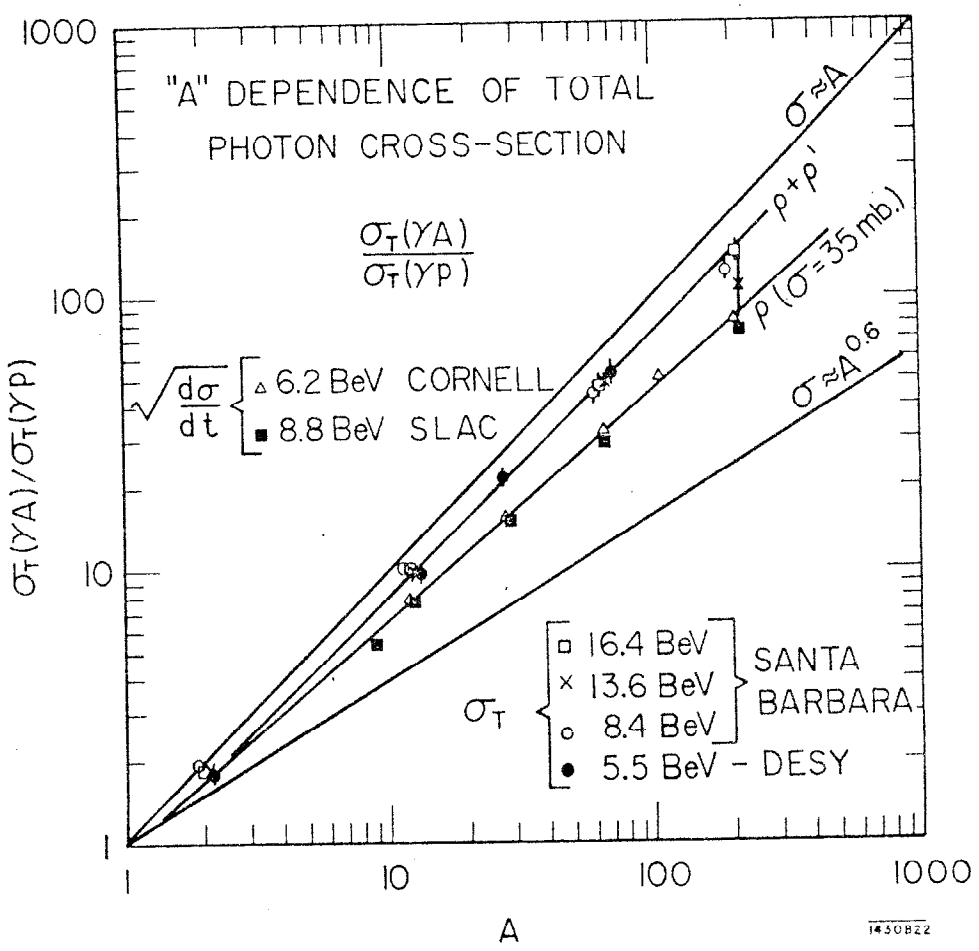
"A" DEPENDENCE OF TOTAL
PHOTON CROSS-SECTION
$\frac{\sigma_T(\gamma A)}{\sigma_T(\gamma p)}$
$\sigma_T(\gamma A)/\sigma_T(\gamma p)$
A
1000
100
10
1
1
10
100
1000
$\sigma \approx A$
$\rho + \rho'$
$\rho\ (\sigma = 35 mb.)$
$\sigma \approx A^{0.6}$
$\frac{d\sigma}{dt}$
6.2 BeV CORNELL
8.8 BeV SLAC
σ_T
16.4 BeV
13.6 BeV
8.4 BeV
SANTA BARBARA
5.5 BeV - DESY
1450B22

Fig. 52

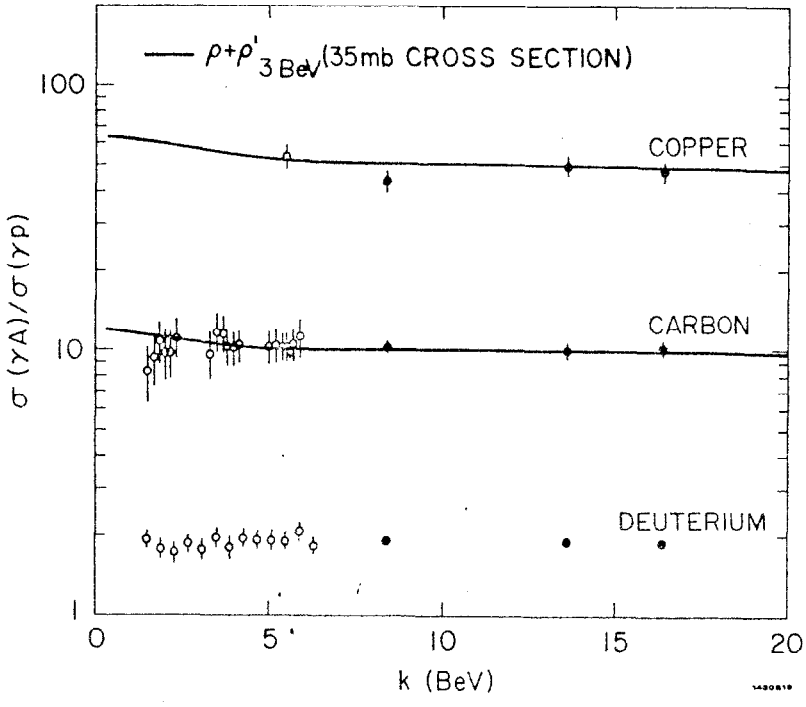
$\rho+\rho'_{3\,BeV}$ (35mb CROSS SECTION)
COPPER
CARBON
DEUTERIUM
100
10
1
0
5
10
15
20
k (BeV)
σ (γA)/σ (γp)

Fig. 53

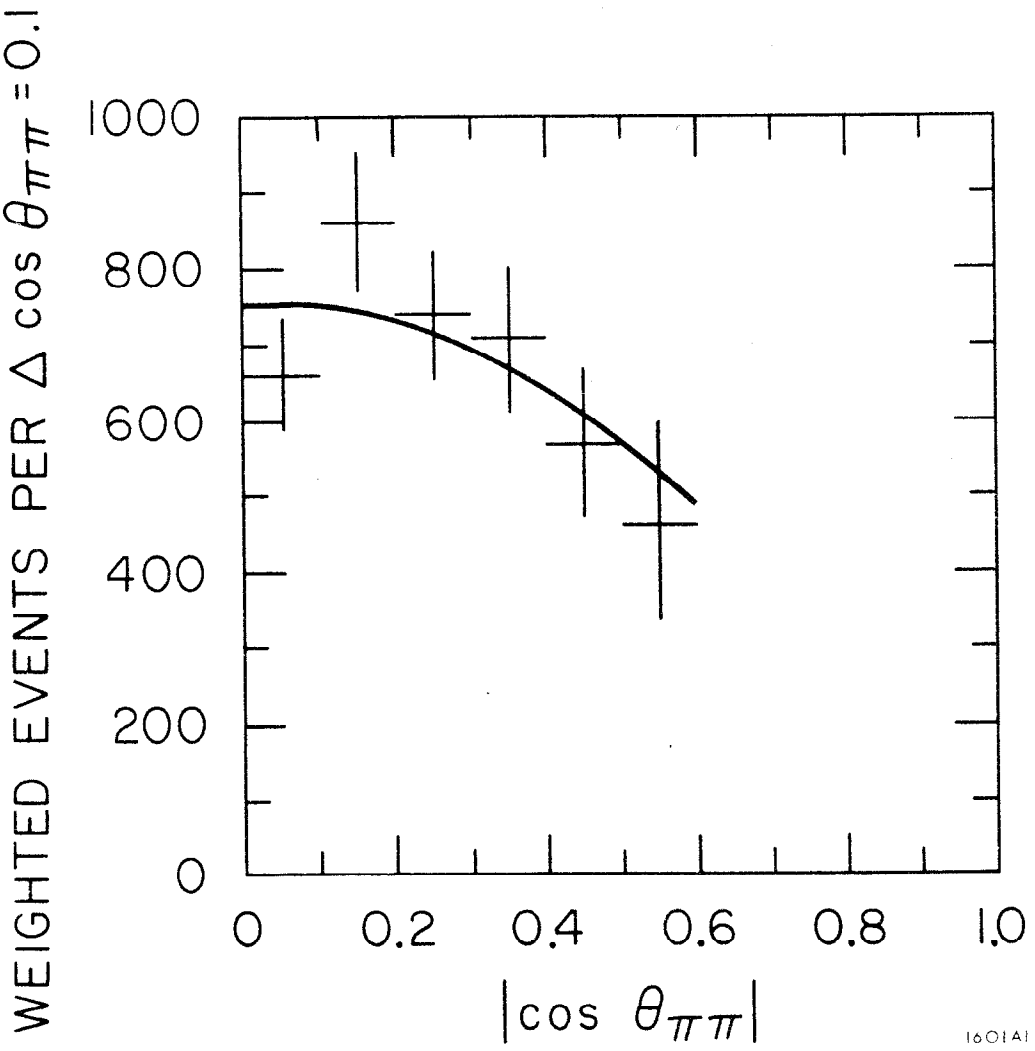
WEIGHTED EVENTS PER Δ cos θππ = 0.1
1000
800
600
400
200
0
0
0.2
0.4
0.6
0.8
1.0
|cos θππ|
1601A1

Fig. 54

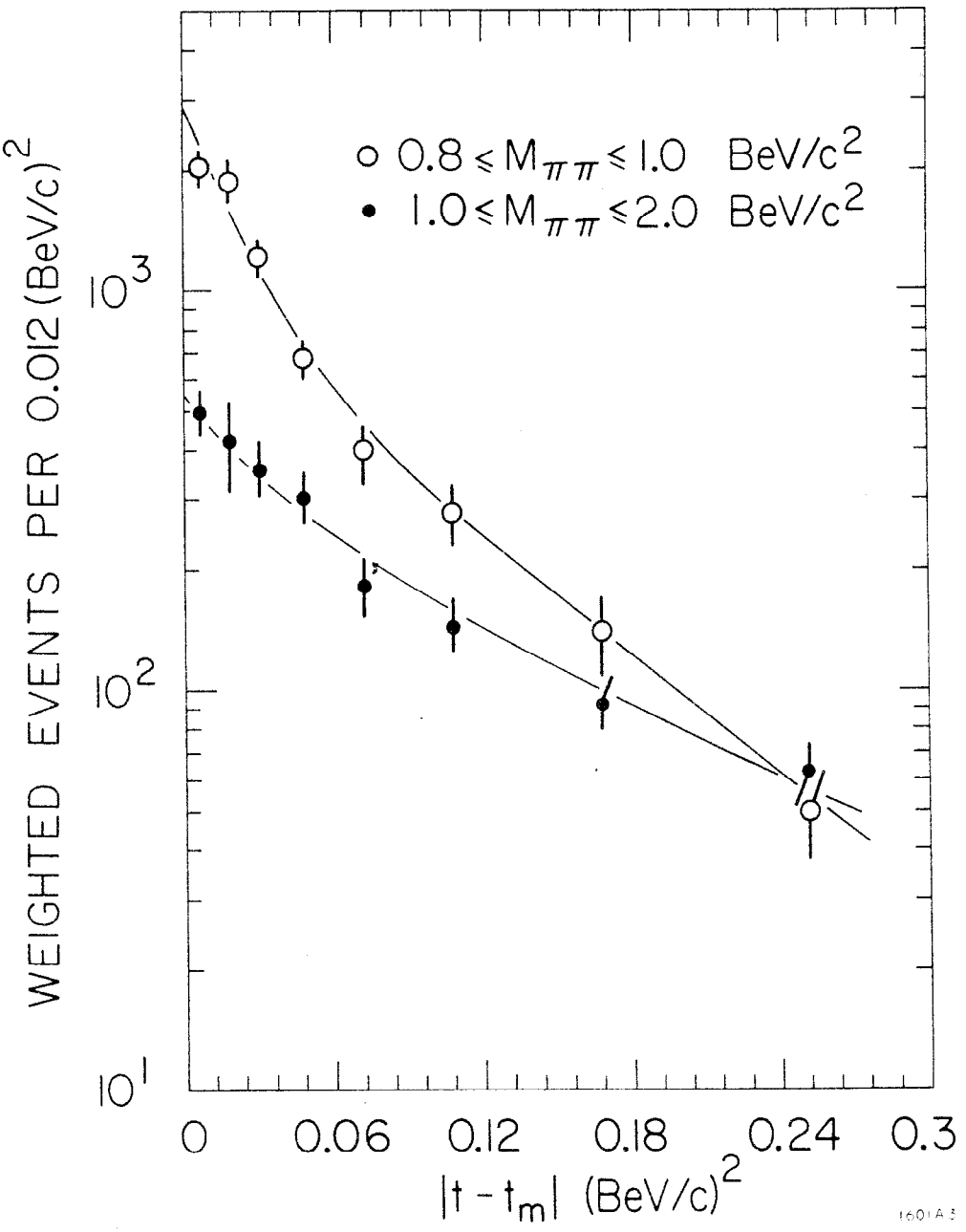
WEIGHTED EVENTS PER 0.012 (BeV/c)^2
10^3
10^2
10^1
○ $0.8 \leq M_{\pi\pi} \leq 1.0$ BeV/c^2
● $1.0 \leq M_{\pi\pi} \leq 2.0$ BeV/c^2
0
0.06
0.12
0.18
0.24
0.3
$|t - t_m|$ (BeV/c)^2
1601A3

Fig. 55

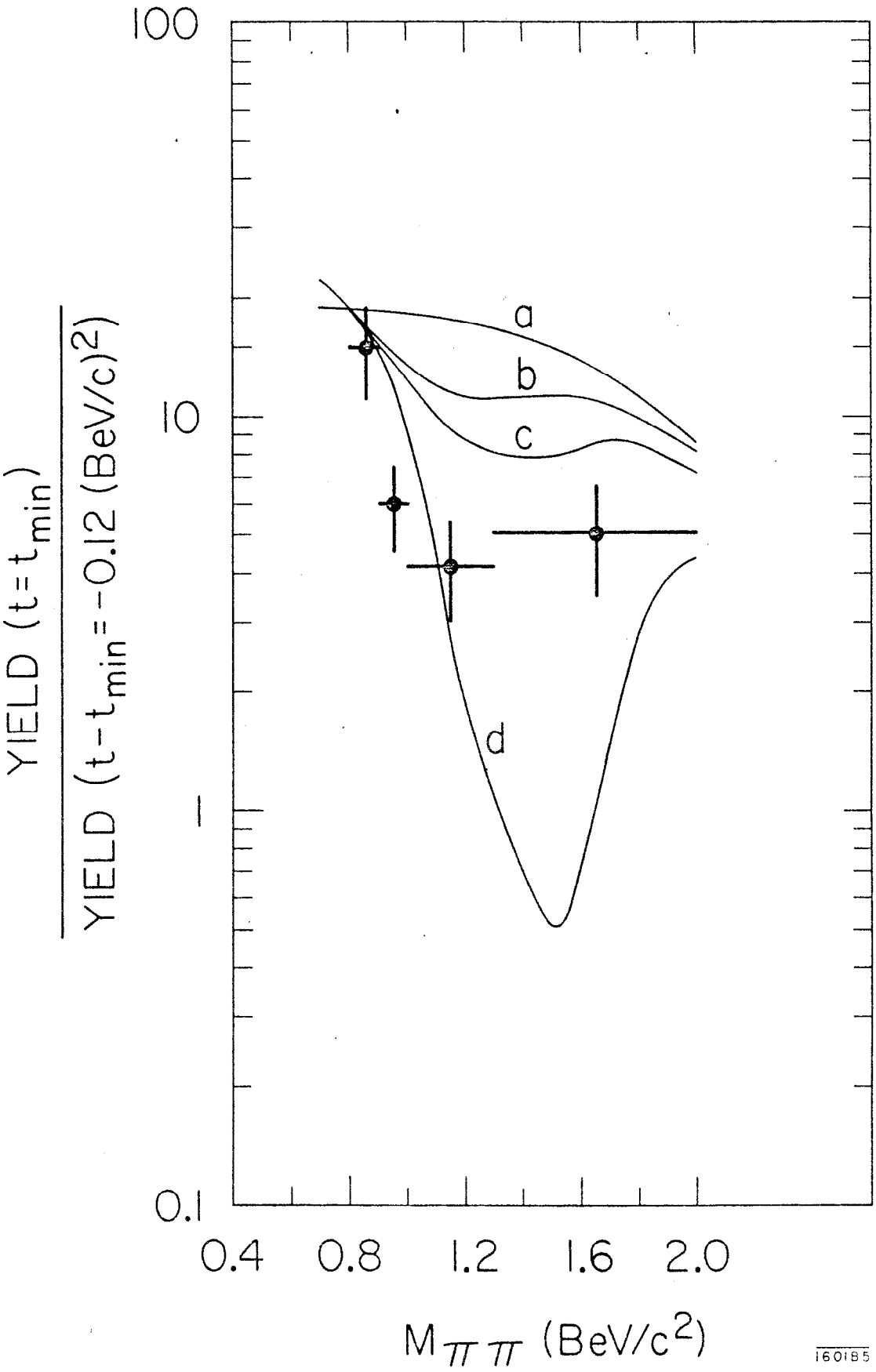
100
10
1
0.1
0.4
0.8
1.2
1.6
2.0
a
b
c
d
YIELD (t=t_min) / YIELD (t-t_min=-0.12 (BeV/c)^2)
M_ππ (BeV/c^2)
160185

Fig. 56

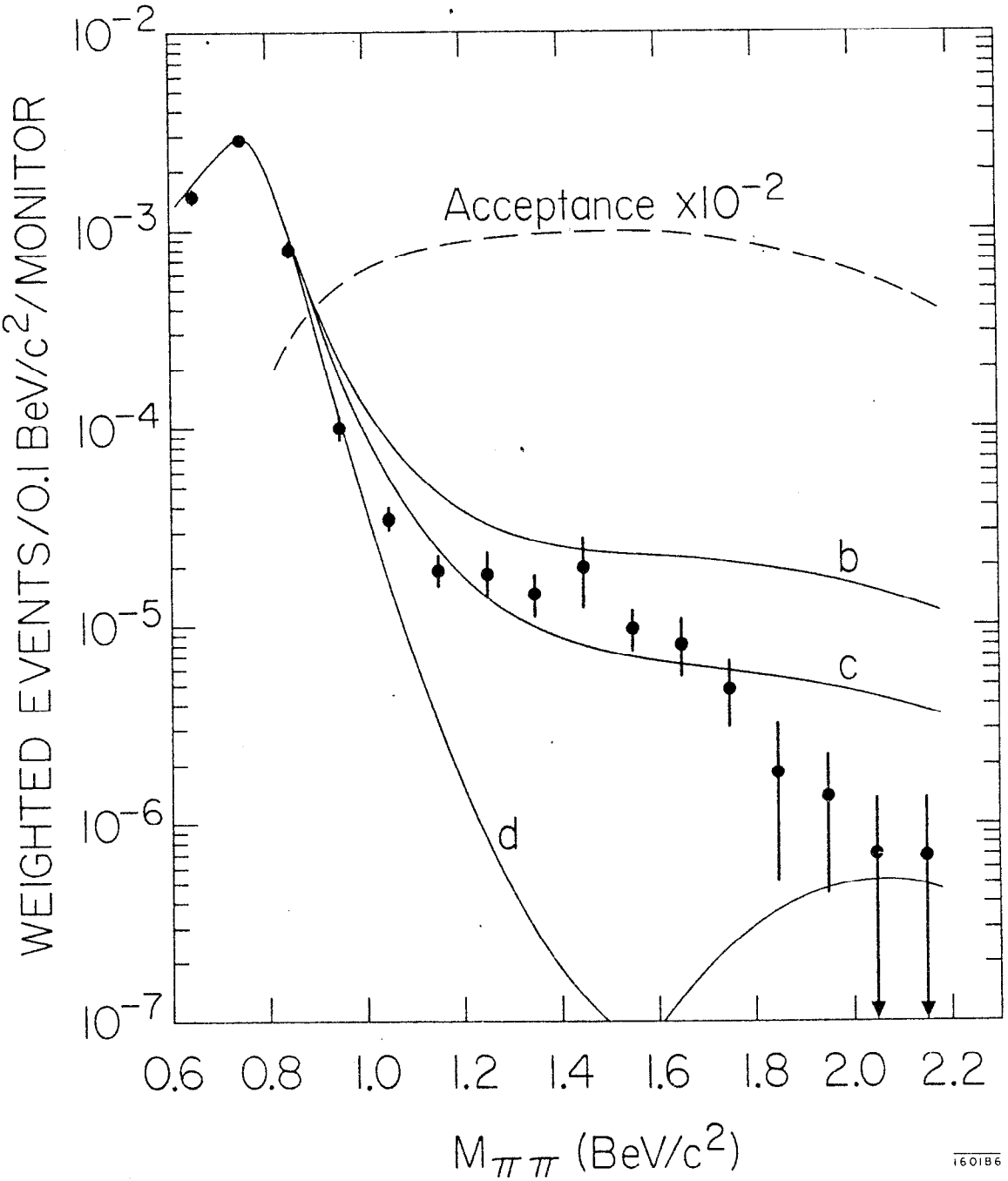
WEIGHTED EVENTS/0.1 BeV/c²/MONITOR
10⁻²
10⁻³
10⁻⁴
10⁻⁵
10⁻⁶
10⁻⁷
Acceptance x10⁻²
b
c
d
0.6
0.8
1.0
1.2
1.4
1.6
1.8
2.0
2.2
Mππ (BeV/c²)
160186

Fig. 57

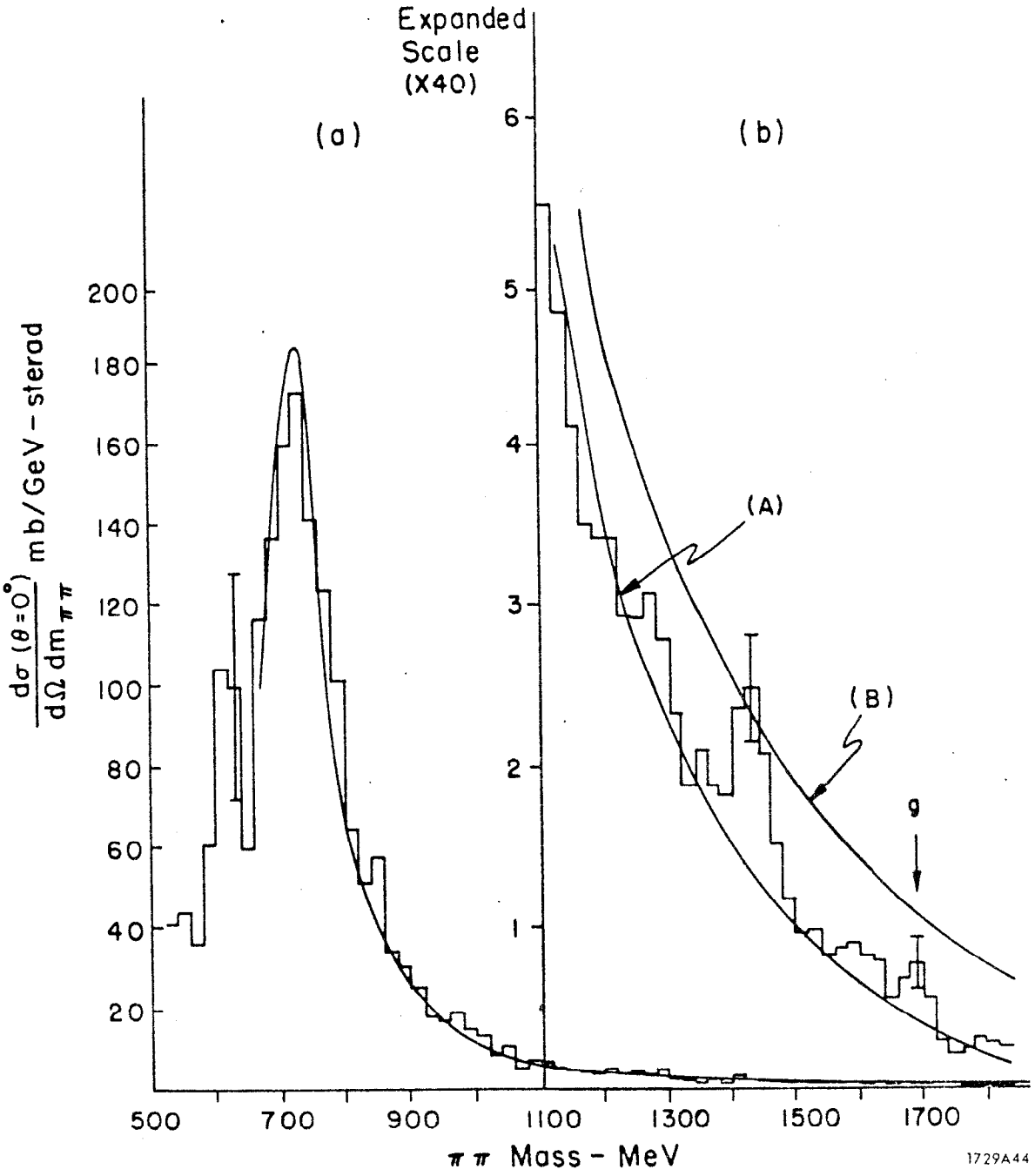
Expanded
Scale
(X40)
(a)
(b)
(A)
(B)
g
200
180
160
140
120
100
80
60
40
20
6
5
4
3
2
1
500
700
900
1100
1300
1500
1700
$\frac{d\sigma(\theta=0^\circ)}{d\Omega\, dm_{\pi\pi}}$ mb/GeV - sterad
$\pi\pi$ Mass - MeV
1729A44

Fig. 58

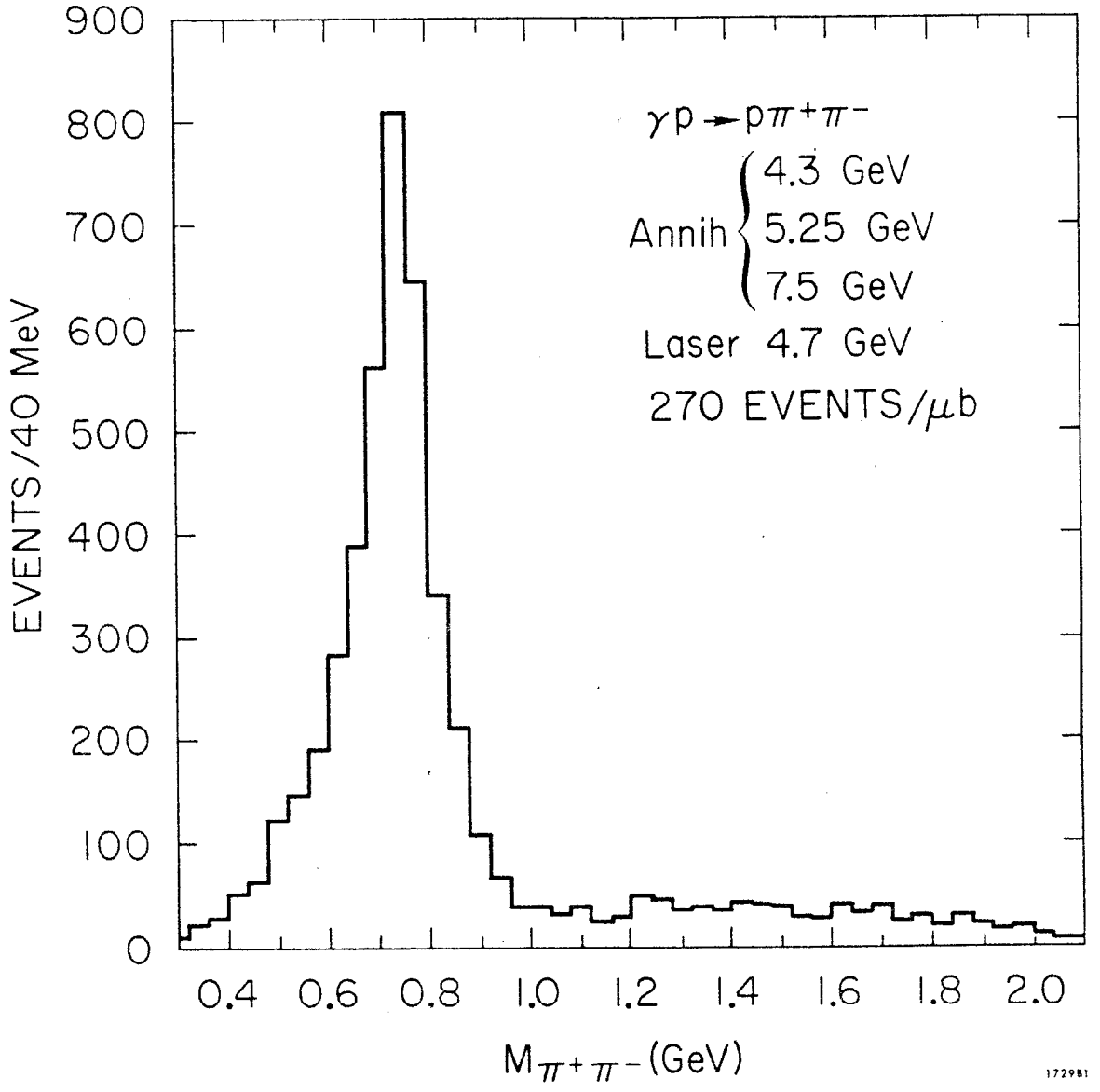
900
800
700
600
500
400
300
200
100
0
EVENTS/40 MeV
$\gamma p \to p\pi^+\pi^-$
Annih { 4.3 GeV
5.25 GeV
7.5 GeV
Laser 4.7 GeV
270 EVENTS/μb
0.4
0.6
0.8
1.0
1.2
1.4
1.6
1.8
2.0
$M_{\pi^+\pi^-}$ (GeV)
172981

Fig. 59

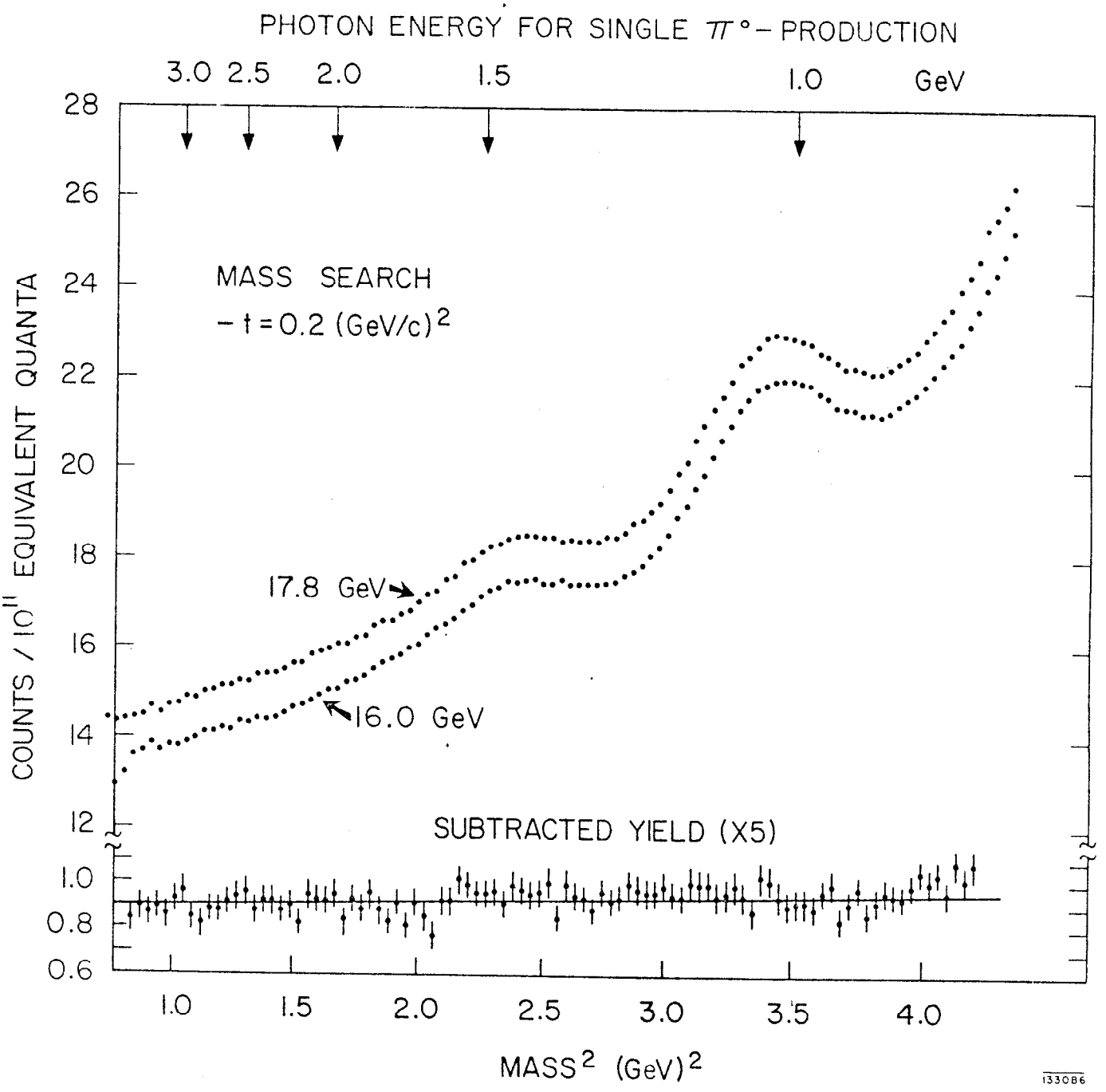
PHOTON ENERGY FOR SINGLE π°-PRODUCTION
3.0 2.5 2.0 1.5 1.0 GeV
MASS SEARCH
-t = 0.2 (GeV/c)²
17.8 GeV
16.0 GeV
SUBTRACTED YIELD (X5)
COUNTS / 10¹¹ EQUIVALENT QUANTA
MASS² (GeV)²
133086

Fig. 60

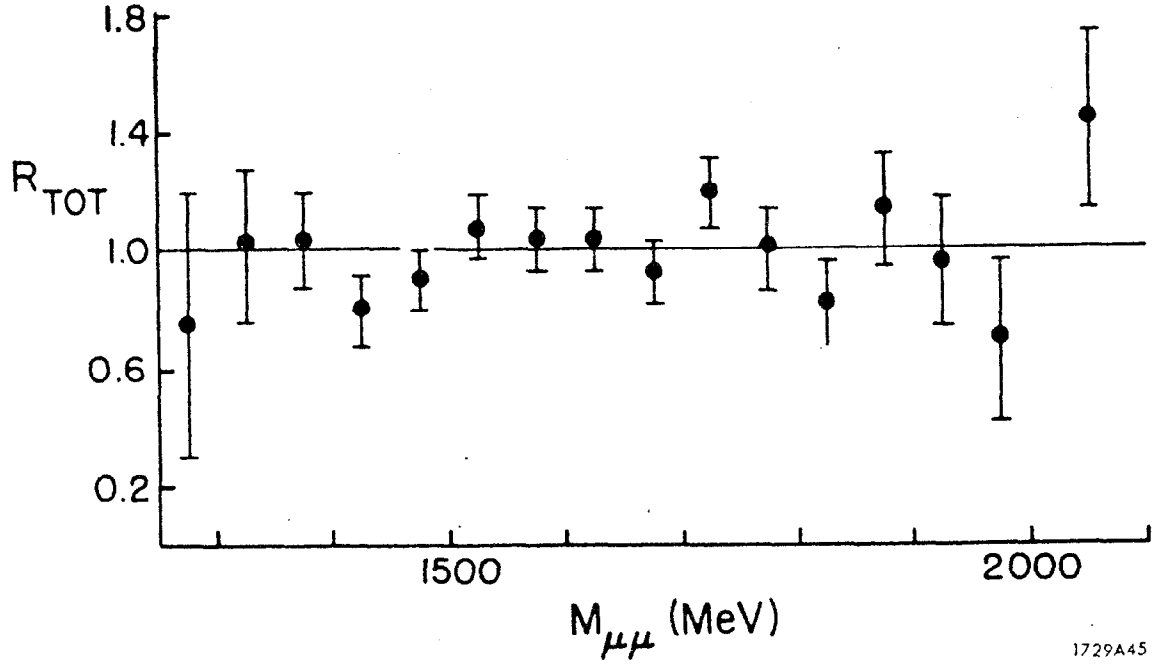

Fig. 61

PART B. Review of Photoproduction Experiments

In this section we will review new, and often quite preliminary, results from recent photoproduction experiments. For more complete coverage of the "recent past", the excellent reviews of Diebold[1] and Lubelsmeyer[2] are highly recommended.

CHAPTER I. Neutral Pion Photoproduction from Hydrogen

About one year ago, the experimental situation seemed to be very clear for the process

$$\gamma + p \rightarrow \pi^{o} + p \qquad [I\text{-}1]$$

There were experiments up to 6 GeV from CEA[3] and from DESY[4], and from (6-16) GeV from SLAC.[5] Two quite different techniques were employed at DESY and at SLAC, the former detecting only the photons from the π^{o} decay, while the latter detected only the recoil proton and isolated reaction [I-1] by missing mass analysis. Despite these differences, the data was in good agreement where it overlapped, as shown in Fig. 1.

The angular distribution around 6 GeV can be characterized by the following features (see Fig. 2):

(a) At large t the cross section falls off with the canonical e^{-3t} of most photoproduction processes,

(b) around $t \sim 0.6$ GeV^2 there is a broad dip,

(c) the cross section rises fairly sharply, (e.g. e^{-6t}), from this dip reaches a maximum at $t \sim 0.1$ GeV^2 and then turns over creating a forward dip,

(d) a very sharp forward peak is observed at essentially zero momentum transfer.

The energy dependence of the differential cross section is fitted by

$$\frac{d\sigma}{dt} = f(t)\ (S\text{-}M^2)^{2\alpha-2}$$

where α is an "effective slope" and not specific to some particular Regge exchange. The data was fitted with α small, $(-0.2 \leq \alpha \leq .2)$, but not as surely zero as for the charged pion photoproduction case. The data, as it existed at the time of the Daresbury Conference, is summarized in Fig. 3. Notice that the secondary dip around $t \sim 0.6$ GeV^2 seems to disappear at the highest energies.

The basic features of the data can be qualitatively explained from simple exchange arguments, but beyond that the trouble starts. The π^o photoproduction process (shown below in Fig. 4) involves the exchange of an object with C = -1. The possible candidates for such an exchange are the photon, the vector mesons, (ρ,ω), and the B-meson. (We will neglect the ϕ meson, since it couples weakly to nucleons.) In our naive picture they will all contribute. The photon exchange (or interaction with the Coulomb field) is responsible for the sharp forward spike -- the so-called Primakof effect.[6] From SU(3) we expect the vector meson contribution to come mainly from the ω. We then expect two dips in the differential cross section -- one in the forward direction since the π^o photoproduction process involves helicity-flip, and a second at $t \sim 0.5$ GeV^2 where the ω (and ρ) trajectories have a nonsense zero[7] in the helicity flip amplitudes.

Thus, the simple picture would expect the large, very sharp forward peak, the accompanying dip in the almost forward direction, and the

secondary dip around $t \sim 0.5\text{-}0.6$ GeV^2 as observed in the data. The B-exchange would be expected to fill in this secondary dip to some extent.

However, several experimental observations gave this picture a hard time. As the energy increased the contributions from the low-lying B-exchange should decrease faster than the ω-exchange contributions, resulting in the dip at $t \sim 0.5$ GeV^2 getting deeper. This is certainly not what is seen in Fig. 3. Further, the ω exchange contributes to the unnatural parity exchange. If indeed the above model were correct, the unnatural parity contribution should dominate in the region of $t \sim 0.5$ GeV^2. A CEA group[8] has studied this reaction using polarized photons, and their measured asymmetry parameter is shown in Fig. 5. For B dominance, we should expect the asymmetry parameter to be -1, whereas the data is positive (and nearly 1) for all values of t. Finally, the ratio between the reactions

$$\gamma + p \rightarrow \pi^o + p$$

$$\gamma + n \rightarrow \pi^o + n$$

should be unity within this simple model, since the B and ω exchanges should not interfere. However, studies from CEA[9] show quite substantial departures from unity. (See Fig. 6.)

Despite these problems the model was patched up by including cuts (or absorption effects, if you prefer) and finally made a fair attempt at fitting all the data.

Now, there is new information on the high energy differential cross sections. The SLAC group[10] has improved their experiment in two respects: (a) taken new data with a hydrogen gas target, and (b) reanalyzed all their data in the light of the Compton scattering measurements. The first enables

them to measure to even small t values, since they only detect the recoil proton and the limitation to the technique is multiple scattering to the proton as it comes out of the target. The new data now extends down to $t \sim 0.05$ GeV^2. The second effect turns out to be very important for the angular distribution at larger t. In Section A (VI, 1) above, we discussed the elegant experiment measuring Compton scattering from 6-16 GeV. There we remarked that the differential cross section had a substantial quadratic term in t, causing a flattening out of the cross section at large t values. Now Compton scattering is a serious background in the measurement of π^o photoproduction, since they cannot be separated by missing mass techniques. Initially the background had been estimated using $\gamma p \rightarrow \rho p$ data and assuming Vector Dominance Model was good. However, the quadratic term in the cross section, together with the fact that the total Compton cross section is essentially flat with energy while the total π^o cross section is falling fast, implies drastic changes in the angular distribution at high energies. This effect is shown clearly in Fig. 7.

The experiment uses the SLAC 1-6 GeV spectrometer to detect the recoil protons, and a typical missing mass plot is shown in Fig. 8. The Compton background is subtracted out at each momentum transfer and energy.

At each value of t, the differential cross section versus photon energy on a log-log scale may be fitted to a straight line with a good chi-square. An example is shown in Fig. 9 for $t = -0.3$ (GeV/c)^2. The effective Regge α has been obtained by setting the slope of the straight line equal to $2\alpha-2$. To provide angular distributions at standard energies, and as an average

over the numerous individual points, values of $d\sigma/dt$ were taken from these straight-line fits at fixed values of E_o = 6, 9, 12, and 15 GeV. The results are plotted in Fig. 10. The distributions show a "dip" around $t = -0.5(GeV/c)^2$, not changing much with energy. Notice that the dip appears at all energies now that the Compton scattering background can be properly dealt with, although it does not get deeper with energy. A comparison of this experiment with the lower energy data from DESY is shown in Fig. 11.

The effective trajectory $\alpha(t)$ is plotted in Fig. 12. A least-squares fit to a straight line gives $\alpha(t) = 0.18 + 0.26\ t$, although from pure ω-exchange we would expect $\alpha(t) = 0.45 + 0.9\ t$. The measured values of α seem to indicate that the cross section falls off somewhat slower than s^{-2} for small t-values.

It will be interesting to watch the double-take in the theory now that this new high energy data is available.

II. Study of the Reactions $\gamma N \rightarrow \pi\Delta$

(a) Photoproduction of $\Delta(1236)$ from Hydrogen and Deuterium at 16 GeV

Using the SLAC 20 GeV/c spectrometer, the differential cross sections for $\pi^{\pm}\Delta$ photoproduction off hydrogen and deuterium have been measured at a photon energy of 16 GeV and for t's of 0 to -0.2 GeV^2.(11) By subtraction of the proton data from the deutrons, they obtain cross sections on the following reactions:

$$\gamma + p \rightarrow \pi^- + \Delta^{++} \qquad [II\text{-}1]$$

$$\gamma + p \rightarrow \pi^+ + \Delta^{+} \qquad [II\text{-}2]$$

$$\gamma + n \rightarrow \pi^- + \Delta^{+} \qquad [II\text{-}3]$$

$$\gamma + n \rightarrow \pi^+ + \Delta^{-} \qquad [II\text{-}4]$$

Missing mass plots are shown in Fig. 13 for each of the reactions. Clear steps are seen in all charge states at the mass of the Δ (i.e, N*(1236)). The curves through the data represent the sum of contributions from $\gamma N \rightarrow \pi N$, $\gamma N \rightarrow \pi\Delta$, $\gamma N \rightarrow \rho N$ and the Drell process $\gamma N \rightarrow \pi$ + (anything). All processes were folded with a bremsstrahlung photon energy spectrum and smearing due to Fermi momentum was included for the deuterium reactions using the Hulthen momentum distribution.

Comparison of deuterium and hydrogen cross sections involve several possible systematic problems, such as Glauber shadowing of one nucleon by the oth in the deuterium processes. To get a feeling for these effects they compared their measured cross sections for $\gamma p \rightarrow \pi^+ n$ from free protons and from those bound in deuterium. (Only data for $t \gtrsim -0.2$ GeV^2 were used to avoid exclusion - principle effects.) This comparison gave a deuterium-to-hydrogen ratio of 1.02 ± 0.02. Comparison of their $K^+\Lambda$ production from deuterium to hydrogen

for $t \sim 0$ to -2 GeV^2 gave a ratio of 1.02 ± 0.04. The product of the systematic effects is thus consistent with unity and they took the neutron cross sections to be simply the difference between deuterium and hydrogen cross sections. The results are shown in Fig. 14.

These measurements are of particular interest because of the sensitivity of these cross sections to the possible exchange of particles with isospin > 1 (exotic exchanges). The Δ cross section can have a large contribution from the interference of a small exotic exchange amplitude with the I = 1 amplitudes while cross sections for processes involving double charge exchange ($\pi^- p \rightarrow \pi^+ \Delta^-$ for example) are only sensitive to the square of the I > 1 amplitude.

Comparisons of different charge states allow sensitive tests for amplitudes which are usually assumed to be small. In terms of t channel quantum numbers the four cross sections can be written as

$$\frac{d\sigma}{dt}\left[\gamma\binom{p}{n}\rightarrow\pi^{\mp}\Delta^{\pm+}\right] = 3\sum_{i=1}^{8}\left|A^i_{1-} \mp A^i_{1+} - \frac{1}{3}A^i_{2-}\right|^2 \qquad \text{[II-5]}$$

$$\frac{d\sigma}{dt}\left[\gamma\binom{n}{p}\rightarrow\pi^{\mp}\Delta^{+}_{0}\right] = \sum_{i=1}^{8}\left|A^i_{1-} \mp A^i_{1+} + A^i_{2-}\right|^2 \qquad \text{[II-6]}$$

where the summation is over the eight helicity amplitudes and the subscripts 1 and 2 refer to the t channel isotopic spin; the + and - subscripts denote the G parity of the t channel and correspond to isoscalar and isovector photons, respectively. Figure 15 shows the ratios of the charge-symmetric cross sections; in general, the cross sections are not equal and interference terms between exchanges of opposite G parity are required, as observed in single pion photoproduction.[12]

If I = 2 exchange is negligible, the cross sections are uniquely predicted to be in the ratio

$$\frac{\gamma p \to \pi^- \Delta^{++}}{\gamma n \to \pi^- \Delta^+} = \frac{\gamma n \to \pi^+ \Delta^-}{\gamma p \to \pi^+ \Delta^0} = 3 \qquad \text{[II-7]}$$

The deuterium-to-hydrogen ratios should then be 4/3 for π^- and 4 for π^+. These ratios are shown in Fig. 16 as a function of $\sqrt{-t}$. The π^+ ratio shows clear deviations from the prediction over most of the t range studied, a typical value being 3, in which case the I = 2 exchange amplitude must be at least 16% of the I = 1 exchange amplitude. Although this result can be interpreted in terms of exotic meson exchange, it could also be explained by double Regge pole exchange, giving Regge cuts. The measured π^- ratio is not as sensitive a test for I = 2 exchange since the errors are large in comparison to the smaller ratio.

The vector dominance model suggests the relation

$$\frac{1}{2}\left[\frac{d\sigma}{dt}(\gamma p \to \pi^- \Delta^{++}) + \frac{d\sigma}{dt}(\gamma n \to \pi^+ \Delta^-)\right] = g_\gamma^2 \rho \left(\rho_{11}^{\text{hel}} \frac{d\sigma}{dt}\right)_{\pi^+ p \to \rho^0 \Delta^{++}} + g_{\gamma\omega}^2 \left(\rho_{11}^{\text{hel}} \frac{d\sigma}{dt}\right)_{\pi^+ p \to \omega \Delta^{++}} \qquad \text{[II-8]}$$

where the two photoproduction cross sections are averaged to eliminate $\rho\omega$ interference terms. In addition to the usual vector dominance assumptions the derivation assumes line-reversal invariance. Using the $\pi^+ p \to \rho^0 \Delta^{++}$ data from the ABC collaboration,[13] the two sides of Eq. II-8 are plotted in Fig. 17 for 8 GeV, assuming the ratio of Δ^- to Δ^{++} cross sections to be independent of energy. The 10% ω contribution has been ignored and $\gamma_\rho^2/4\pi = 0.52$ was used. The figure shows a factor of 5 discrepancy i.

vector dominance relation, which also disagrees with the calculations of Dar[14] and of Gotsman.[15] Three possible sources can be found for the factor-of-5 discrepancy: (a) the vector dominance model which has had troubles elsewhere,[16] (b) the line-reversal assumption which will not be valid if interferences exist between amplitudes corresponding to t channel exchanges of opposite signature,[17] (c) difficulty in the cross section determination for $\rho^{\circ}\ \Delta^{++}$ since both the ρ and the Δ have large widths.[18]

(b) Δ Production by Linearly Polarized Photons:

This process has also been studied at 2.8 and 4.7 GeV using polarized photons in the SLAC 82" HBC.[19] The photon beam is obtained by backscattering ruby laser light from the SLAC electron beam. The 180° scattered photons have multi-GeV energies, are fairly monoenergetic and maintain the polarization of the incident visible light. For more details of this technique see reference (20).

The effective mass spectra for the $p\pi^{+}$ and $p\pi^{-}$ systems are shown in Fig. 18. At both energies a clear Δ^{++} signal is found, but not much sign of Δ°.

The solid curves in Fig. 18 were obtained from a maximum likelihood fit to the entire Dalitz plot assuming Δ^{++}, Δ°, ρ° production, and a phase space background. The ρ° mesons were assumed to have their spin aligned along their direction of motion in the overall c.m.s. In order to determine the total Δ cross section, $\sigma(\Delta\pi)$, they chose a form of T_{Δ} which agrees with the results for the (3,3) πN phase shift, δ_{33}, even at many half widths above the resonance,[21] viz:

$$|T_{\Delta}|^2 \propto \frac{\sin^2\delta_{33}}{\Gamma(M)} \propto \frac{1}{\Gamma(M)}\ \frac{\left(M_{\Delta}\Gamma(M)\right)^2}{\left(M_{\Delta}^2 - M^2\right)^2 + \left(M_{\Delta}\Gamma(M)\right)^2} \qquad \text{[II-9]}$$

where $\Gamma(M)$ follows from $\tan \delta_{33} = M_\Delta \Gamma(M)/(M_\Delta^2 - M^2)$ and $M_\Delta = 1.236$ GeV. The values of δ_{33} have been taken from a phase shift analysis.[22] If instead the second part of the above equation is used together with a conventional parameterization for $\Gamma(M)$ (as was done, e.g., by Boyarski et al.,[11]) one finds a value of $\sigma(\Delta\pi)$ larger by ~ 20%. Notice that this would give good agreement between these two experiments.

Figure 19 shows the differential cross sections $d\sigma/dt$ for Δ^{++} production obtained from an independent maximum likelihood fit as described above for each t-interval. Also shown are the measurements of Boyarski, et al.[11] at $E_\gamma = 5.0$ GeV. Measurements in the backward direction have been made by Anderson, et al.[23]

The Δ^{++} angular distributions are analyzed in terms of the Δ spin density matrix in the Gottfried-Jackson frame. The z axis is taken as the direction of the incident proton in the Δ rest frame; the y axis is defined as the normal to the production plane ($\hat{y} \propto \hat{\gamma} \times \hat{\pi}^-$). The electric vector ϵ of the photon makes an angle Φ with the production plane: $\cos \Phi = \hat{\gamma} \cdot (\hat{\epsilon} \times \hat{y})$, $\sin \Phi = \hat{y} \cdot \hat{\epsilon}$. The decay angles θ and ϕ are the polar and azimuthal angles of the outgoing proton in the Δ rest system: $\cos \theta = \hat{p} \cdot \hat{z}$, $\cos \phi = \hat{y} \cdot (\hat{z} \times \hat{p})/|\hat{z} \times \hat{p}|$, $\sin \phi = -(\hat{y} \times \hat{z}) \cdot (\hat{z} \times \hat{p})/|\hat{z} \times \hat{p}|$. The decay angular distribution is then given by:[24]

$$
\begin{aligned}
W(\cos\theta, \phi, \Phi) = \frac{3}{4\pi} \Big\{ & \rho^0_{33} \sin^2\theta + \left(1/2 - \rho^0_{33}\right)\left(1/3 + \cos^2\theta\right) \\
& - 2/\sqrt{3}\ \mathrm{Re}\ \rho^0_{31} \cos\phi \sin 2\theta - 2/\sqrt{3}\ \mathrm{Re}\ \rho^0_{3-1} \cos 2\phi \sin^2\theta \\
& - P_\gamma \cos 2\Phi \left[\rho^1_{33} \sin^2\theta + \rho^1_{11} \left(1/3 + \cos^2\theta\right) \right. \\
& \left. - 2/\sqrt{3}\ \mathrm{Re}\ \rho^1_{31} \cos\phi \sin 2\theta - 2/\sqrt{3}\ \mathrm{Re}\ \rho^1_{3-1} \cos 2\phi \sin^2\theta \right] \\
& - P_\gamma \sin 2\Phi \left[2/\sqrt{3}\ \mathrm{Im}\ \rho^2_{31} \sin\phi \sin 2\theta + 2/\sqrt{3}\ \mathrm{Im}\ \rho^2_{3-1} \sin 2\phi \sin^2\theta \right] \Big\}
\end{aligned}
$$

where P_γ is the degree of linear polarization; P_γ = 94% at 2.8 GeV and P_γ = 92% at 4.7 GeV. We define the polarization asymmetry Σ by

$$\Sigma = \frac{1}{P_\gamma} \frac{W(\Phi=0) - W(\Phi=\pi/2)}{W(\Phi=0) + W(\Phi=\pi/2)} \qquad [II\text{-}11]$$
$$= -2\left(\rho^1_{33} + \rho^1_{11}\right)$$

where $W(\Phi)$ is the Φ distribution integrated over θ and ϕ. A related quantity is the parity asymmetry, P_σ, defined in terms of the cross sections for natural and unnatural parity exchange in the t-channel, σ^N and σ^U:

$$P_\sigma = \frac{\sigma^N - \sigma^U}{\sigma^N + \sigma^U} \qquad [II\text{-}12]$$

At high energies $P_\sigma = 2(\rho^1_{33} + \rho^1_{11}) = -\Sigma$.[25]

To obtain the nine measurable density matrix parameters, events were selected with $M_{p\pi^+} < 1.32$ GeV and the method of moments was used with the Eberhard-Pripstein procedure[26] to remove the ρ^o reflection: only events with $\cos\theta_H < 0.3$ (0.7) at 2.8 GeV (4.7 GeV) were used, where θ_H is the angle in the c.m.s. of the Δ between the decay proton and the Δ line of flight in the total c.m.s. Figure 20 shows the ρ^α_{ik} and P_σ obtained this way. It is clear that OPE alone cannot explain the data since it would require $P_\sigma = -1$.

The solid lines in Fig. 19 and 20 are the predictions of gauge invariant OPE model, and are in fair agreement with the data. It is clear from the behaviour of the forward cross section and the spin density matrix elements, that simple OPE bears no resemblance to the data.

This group also made a VDM comparison to the reaction $\pi p \rightarrow \Delta V$. They use OPE calculations for the hadronic process to predict the cross sections at 5 GeV, (the energy of the HBC γp experiment), whereas the spectrometer group (described IIa above) extrapolated their photon data to the same energy as the πp experiment using the invariance of $d\sigma/dt\ (S-M^2)^2$ in photon processes. The HBC experiment claims that VDM works moderately well.

III. Measurement of the Energy Dependence of $\rho\Delta$ Photoproduction:

The reaction $\gamma p \rightarrow \rho\Delta$ has been studied by the DESY[27] and CEA[28] HBC groups for photon energies up to 4.5 GeV. The most likely production mechanism for the reaction is OPE (one pion exchange), as indicated in Fig. 21, with the only unknown the $\rho\pi\gamma$ coupling at the upper vertex. The early studies derived a value for this coupling of 0.1 MeV $\leq \Gamma(\rho \rightarrow \pi\gamma) \leq$ 0.25 MeV, in excellent agreement with the SU(3) prediction of $\Gamma(\rho \rightarrow \pi\gamma) = 1/9\Gamma(\omega \rightarrow \pi\gamma) = 0.13$ MeV. However, there were some hints that all was not well, in that the spin density matrix elements for the ρ and Δ decays were not in good agreement with OPE predictions.

Two new pieces of information are available on this process.

First the Weizmann HBC group[29] have recently measured the process

$$\gamma + n \rightarrow \omega^{o}\Delta^{o} \rightarrow \omega^{o} p\, \pi^{-}$$

at 4.3 GeV.

If this reaction is dominated by OPE then we can relate the cross section to that for $\gamma p \rightarrow \rho\Delta$:

$$\left(\begin{array}{l} \text{viz. } \sigma\ \omega^{o}\Delta^{o} \longrightarrow \sigma(\rho^{o}\Delta^{o}) \longrightarrow \sigma(\rho^{-}\Delta^{++}) \\ \text{by} \quad \xleftarrow{(SU(3))}\ (OPE)\ \xrightarrow{(SU(2))} \end{array} \right)$$

One finds that $\omega\Delta^{o}$ is expected to be twice, (x 2), the observed cross section for $\rho^{-}\Delta^{++}$, whereas the experimental data gives an upper limit of $1/3\ \rho^{-}\Delta^{+}$.

i.e.,

$$(OPE) + SU(3) \Rightarrow \sigma(\omega\,\Delta^{o}) = 2\sigma(\rho^{-}\Delta^{++}).$$

$$\text{Expt.} \quad \Rightarrow \sigma(\omega\,\Delta^{o}) \leq \tfrac{1}{3}\,\sigma\,(\rho^{-}\Delta^{++}). \qquad \text{[III-1]}$$

This implies that there are other contributions to the $\rho^{-}\Delta^{++}$ process. It will be interesting to see what the data on $\gamma p \rightarrow \rho^{o}\Delta^{+}$ looks like, to get an indication of what these other processes might be.

Secondly, the energy dependence of the reaction

$$\gamma p \rightarrow \rho^{-}\Delta^{++}$$

has been measured by the SLAC-Weizmann-Tel-Aviv HBC collaboration[30] in the energy region (2-8) GeV. The data is shown in Fig. 22. OPE would predict that the cross section should fall at E^{-2}, while the data show a fall-off more like $E^{-0.6}$, although E^{-1} gives quite an acceptable fit.

This is an interesting puzzle -- clearly OPE is not dominating the reaction yet the estimate for the coupling constant $\rho\pi\gamma$, obtained under this assumption, is quite reasonable.

IV. Photoproduction of ω-mesons:

(a) Production of ω-mesons by Polarized Photons:

The SLAC-LRL-Tufts HBC collaboration have measured the reaction

$$\gamma p \rightarrow p\pi^+\pi^-\pi^o$$

at 2.8 and 4.7 GeV, using linearly polarized photons in the SLAC 82-inch HBC.

The effective mass distribution of the $(\pi^+\pi^-\pi^o)$ system is shown in Fig. 23. Spectacular ω^o peaks are observed at both energies. The total ω^o production cross section is shown in Fig. 24, together with previous measurements.[27, 28, 31, 32, 33] The differential cross section is also shown in Fig. 25. The decay angular distribution of the ω is analyzed in the helicity frame,[34] where it may be expressed as

$$\rho_{ik} = \rho^o_{ik} - P_\gamma \cos 2\phi \rho^1_{ik} - P_\gamma \sin 2\phi \rho^2_{ik} \text{ is}$$

$$W(\cos\theta, \phi, \varphi) = \frac{3}{4\pi}\left\{\frac{1}{2}(1-\rho^o_{00}) + \frac{1}{2}(3\rho^o_{00}-1)\cos^2\theta - \sqrt{2}\,\mathrm{Re}\,\rho^o_{10}\sin 2\theta\cos\phi\right.$$

$$-\rho^o_{1-1}\sin^2\theta\cos 2\phi$$

$$-P_\gamma\cos 2\phi\left[\rho^1_{11}\sin^2\theta + \rho^1_{00}\cos^2\theta - \sqrt{2}\,\mathrm{Re}\,\rho^1_{10}\sin 2\theta\cos\phi - \rho^1_{1-1}\sin^2\theta\cos 2\phi\right]$$

$$\left.-P_\gamma\sin 2\phi\left[\sqrt{2}\,\mathrm{Im}\,\rho^2_{10}\sin 2\theta\sin\phi + \mathrm{Im}\,\rho^2_{1-1}\sin^2\theta\sin 2\phi\right]\right\} \qquad \text{[IV-1]}$$

where P_γ is the degree of linear polarization. The nine independent measurable density matrix parameters, which were determined by a moment analysis, are shown in Fig. 26 as a function of t. In contrast to ρ photoproduction, they find considerable helicity flip amplitude for ω production.

From the density matrix parameters one can deduce the parity asymmetry, P_σ, which measures the cross section contributions σ^N, σ^U from natural parity and unnatural parity exchange in the t-channel:

$$P_\sigma = \frac{\sigma^N - \sigma^U}{\sigma^N + \sigma^U} \quad \text{or} \quad \sigma^{(N)}_{(U)} = \frac{1}{2}(2 \pm P_\sigma)\,\sigma \qquad [IV\text{-}2]$$

where $\sigma = \sigma^N + \sigma^U$. In the high energy limit P_σ is given by

$$P_\sigma = 2\rho^1_{1-1} - \rho^1_{00} \qquad [IV\text{-}3]$$

σ^N, σ^U, and P_σ are plotted in Fig. 24 and 26 respectively; natural and unnatural parity exchanges contribute in approximately equal amounts. The unnatural cross section, σ^U, decreases from 2.8 to 4.7 GeV whereas σ^N does not change significantly. The natural differential cross section, $d\sigma^N/dt$, for $0.02 \leq |t| \leq 0.4$ GeV^2, is shown in Fig. 25. Assuming that σ^U is accounted for by OPE, they find that $d\sigma^N/dt = 12.1\, e^{(5.6 \pm 1)t}$ μb/GeV^2. This value of the slope is in good agreement with that obtained for Compton scattering[35] and for rho photoproduction[36] (when analyzed using the Söding-Drell mechanism).

One can compare σ^N_ω to the corresponding quantity, σ^N_ρ, for ρ^o production in the reaction $\gamma p \to p\rho^o$.[37] For $|t| < 1$ GeV^2, they found the ratio $\sigma^N_\rho/\sigma^N_\omega$ to be between 6 and 9 depending on the models used to determine the ρ^o cross section. In Section (A,I-3) above, we had shown that this ratio should be 9 for pure diffractive production of the vector meson. However, there could be a large positive contribution ($\sim 40\%$) from A_2 exchange to σ^N_ω which would reduce the value of this ratio[36] (the A_2 exchange contribution to σ^N_ρ is expected to be small).

The fall off in σ^U agrees well with the OPE predictions which give a factor 2.5 between 2.8 and 4.7 GeV, while the data gives 2.2 $\pm$ 0.6. The magnitude of the OPE cross section is proportional to the radiative decay width of the ω, $\Gamma_{\omega\pi\gamma}$. From the values of σ_ω^U at 2.8 and 4.7 GeV in the interval $|t| < 1$ GeV^2 and using the parametrization of Benecke and Dürr[37] they obtained $\Gamma_{\omega\pi\gamma} = 0.98 \pm 0.12$ MeV, in good agreement with the value obtained from the ω width and branching ratio.[38]

Finally, we calculate the predictions for the ω density matrix elements assuming that the natural parity exchange contributions conserve helicity in the total c.m. system and that the contributions from unnatural parity exchange are due to OPE. As a function of t the ω density matrix is then given by

$$\rho_{ik} = \frac{d\sigma^N/dt\ \rho_{ik}^{(N)} + d\sigma^{OPE}/dt\ \rho_{ik}^{(ope)}}{d\sigma^N/dt + d\sigma^{OPE}/dt} \quad . \qquad [IV-4]$$

The solid line in Fig. 26 shows the predictions of this model.

(b) Energy Dependence of the ω^o Photo-Cross Sections:

Another experiment studying ω^o photoproduction has been reported by the SLAC-Weizmann HBC collaboration.[39] They have presented data on

$$\gamma p \rightarrow \omega p$$

in the energy region (1.2 - 8)GeV, from three monochromatic photon beam experiments at 4.3, 5.3, and 7.5 GeV, and bremsstrahlung data from (1-4) GeV.

Examples of the three pion mass plot are shown at various energies in Fig. 27. The ω signal is clear at all energies, although it is naturally sharper for the monochromatic beam experiments.

The energy dependence of the total ω production cross section is shown in Fig. 28. The authors fit this data to the following form

$$\sigma(\omega) = C_{OPE}\, p^{-\alpha_1} + C_{DIFF}\, p^{-\alpha_2}$$

where p is the photon laboratory momentum in GeV. The diffractive term one would expect to be almost constant with energy and the OPE term should fall like p^{-2}.

They find a best fit, within the energy region of the experiment, to be

$$\sigma(\omega) = (20\ E_\gamma^{-1.8} + 1.6\ E_\gamma^{-0.04})\ \mu b.$$

The diffractive and OPE contributions are shown separately in Fig. 28. For comparison, they plot the unnatural exchange cross section for this reaction as determined for the polarized photon experiment discussed above in Section B, IV. a. The agreement is very good.

V. Rho Photoproduction with Polarized Photons:

(a) Cross sections and the ρ^o Mass Shift:

The SLAC-LRL-Tufts HBC collaboration have used the linearly polarized photon beam to study the reaction

$$\gamma + p \rightarrow \pi^+ + \pi^- + p$$

in the SLAC 82-inch HBC at 2.8 and 4.7 GeV.[40] The average polarization is calculated to be 94% and 92% at each energy respectively.

The effective mass plots for $\pi^+\pi^-$ pairs are shown in Fig. 29, where the ρ is seen to dominate.

In order to test the Ross-Stodolsky factor[41] they multiplied the p-wave Breit-Wigner for the ρ by a factor of $(M_\rho/M_{\pi\pi})^{n(t)}$. Maximum likelihood fits have been made for each event allowing for ρ^o and $\Delta^{++}(1236)$ production and a phase space term and fitting these contributions together with the parameter n(t) as a function of t. The fits describe the $\pi^+\pi^-$ mass spectra well, as shown by the dashed curves in Fig. 29. The fitted values for n(t) are shown in Fig. 30c,d. In contrast to the prediction of Ross and Stodolsky, namely n(t=0) = 4, the parameter n is ~ 5 near t = 0; it drops to zero around t = 0.5 GeV^2.

From an analysis of the rho decay distribution, the authors were able to determine the intensity of the s-channel c.m. helicity-conserving p-wave π-π contribution, by isolating a characteristic moment of the ρ decay. The dots on the histogram of Fig. 29 show this contribution as a function of dipion mass for different t intervals. They remark that in the ρ region this contribution accounts for almost all the events, and shows the same skewing on the experimental mass distributions.

Further analysis of the $\pi\pi$ angular distribution was made by studying the $M_{\pi\pi}$ dependence of the $Y_L^M(\theta,\psi))$ moments. In Fig. 31 the moments Y_2^0 and Y_4^0 at 4.7 GeV are displayed. The Y_2^0 moment shows the behavior expected for the $\sin^2\theta$ decay of the ρ^0. The positive values of Y_2^0 above 1 GeV are due to the Δ^{++} reflection. The moment Y_4^0 shows a distinctive interference pattern in the ρ region which can be interpreted as an interference between the ρ^0 and a $\pi^+\pi^-$ state of spin $J \geq 3$. of the exponential slope of the t distribution on the $\pi^+\pi^-$ mass (see Fig. 30a,b). The shape of the interference pattern observed for Y_4^0 is also correctly predicted. (See Fig. 31.)

In Fig. 32 the differential cross sections are shown for the different methods of analysis. The helicity conserving p-wave, and modified Ross Stodolsky give essentially the same answers, while the ρ cross sections obtained from fitting the Soding model lead to smaller values of the forward cross section (by ~ 30%). This difference is very important for the Vector Dominance Model tests discussed quite fully in Section A, above.

(b) Conservation of s-channel Helicity in ρ^0 Photoproduction:

In the same experiment as reported above, the SLAC-LRL-Taft HBC collaboration investigated the rho decay distributions.[42] The analysis was carried out in three coordinate systems: the Gottfried-Jackson system, where the z-axis is chosen as the direction of the incident photon in the ρ^0 rest system; the helicity system where the z-axis is opposite to the direction of the outgoing proton in the ρ^0 rest system; and the Adair system where the z-axis is along the direction of the incident photon in the overall c.m. system. The y-axis is always normal to the production plane. Notice that for forward production all three coordinate systems coincide.

Taking Φ as the angle of the photon electron polarization vector with respect to the production plane, and θ and ϕ as the polar and azimuthal angles of the π^+ in the ρ^o rest system.

The decay angular distribution for rho mesons produced by linearly polarized photons can be expressed in terms of nine independent measurable spin density matrix parameters ρ^{α}_{ik}:(43)

$$W(\cos\theta, \phi, \Phi) = \frac{3}{4\pi}\left\{\frac{1}{2}\left(1-\rho^0_{00}\right) + \frac{1}{2}\left(3\rho^0_{00}-1\right)\cos^2\theta - \sqrt{2}\,\mathrm{Re}\,\rho^0_{10}\sin 2\theta\cos\phi\right.$$
$$- \rho^0_{1-1}\sin^2\theta\cos 2\phi - P_\gamma\cos 2\Phi\left[\rho^1_{11}\sin^2\theta + \rho^1_{00}\cos^2\theta\right.$$
$$\left.-\sqrt{2}\,\mathrm{Re}\,\rho^1_{10}\sin 2\theta\cos\phi - \rho^1_{1-1}\sin^2\theta\cos 2\phi\right]$$
$$\left. - P_\gamma\sin 2\Phi\left[\sqrt{2}\,\mathrm{Im}\,\rho^2_{10}\sin 2\theta\sin\phi + \mathrm{Im}\,\rho^2_{1-1}\sin^2\theta\sin 2\phi\right]\right\} \qquad [V\text{-}1]$$

Here, P_γ is the degree of linear polarization of the photon, which is calculated from the Compton scattering process to be 94% at 2.8 GeV and 92% at 4.7 GeV. The matrix elements ρ^0_{ik} describe the rho decay in the case of an unpolarized beam; the additional terms ρ^1_{ik} and ρ^2_{ik} result from the linear polarization of the photon.

Matters are simplified if we use the angle $\Psi = \phi - \Phi$, which in the forward direction is the angle between the photon-polarization and ρ^o decay planes. If the rho is transverse and linearly polarized like the photon then in the <u>helicity</u> system, $\rho^1_{1-1} = -\,\mathrm{Im}\,\rho^2_{1-1} = 1/2$ and all other ρ^{α}_{ik} in

in Eq. (2) are zero. In this case the decay angular distribution is proportional to $\sin^2\theta \cos^2\Psi$. Note that under these conditions Ψ becomes the azimuthal angle of the decay π^+ with respect to the rho polarization plane.

Figure 33 shows the distributions of the polar angle θ and the angle Ψ in the helicity system for events in the rho mass region with $|t| \leq 0.4$ GeV^2 where t is the square of the four-momentum transfer between incoming and outgoing proton.

The cos θ distributions are proportional to $\sin^2\theta$, i.e., the rho mesons are produced in reaction (1) with c.m.s. helicity ± 1. The Ψ distributions are $\sim \cos^2\Psi$ and show that the rho is almost completely linearly polarized.

The matrices ρ^0_{ik}, ρ^1_{ik} and ρ^2_{ik} can be used to examine the production mechanism; for example, the contributions σ^N, σ^U from natural parity ($P = (-1)^J$) and unnatural parity ($P = -(-1)^J$) exchanges in the t-channel can be obtained by measuring P_σ,

$$P_\sigma = \frac{\sigma^N - \sigma^U}{\sigma^N + \sigma^U} \qquad [V\text{-}2]$$

which to leading order in energy is given by

$$P_\sigma = 2\,\rho^1_{1-1} - \rho^1_{00} \qquad [V\text{-}3]$$

They studied the influence of possible background by determining the ρ^α_{ik} as a function of the $\pi^+\pi^-$ mass, $M_{\pi\pi}$, with the method of moments using all events in a given $\pi^+\pi^-$ mass interval. Figure 34 shows the $M_{\pi\pi}$ dependence of ρ^0_{00} and ρ^1_{1-1} in the helicity system and that of P_σ. There is a pronounced difference between their values inside and outside of the

rho region. The values $\rho^0_{00} \cong 0$, $\rho^1_{1-1} \cong 0.5$ and $P_\sigma \cong 1$ in the rho region are clearly associated with the production of the rho.

The polarization and asymmetry are shown in Fig. 35, as a function of t. It is clear that rho production is dominated by natural parity exchange out to $t \sim 1$ GeV^2. In fact, the contribution from unnatural parity, for $|t| < 1$ GeV^2, is estimated at $3.1 \pm 2.2\%$ for 2.8 GeV, and $-1.1 \pm 1.9\%$ for the 4.7 GeV experiment.

In Fig. 36 and 37 the density matrix elements are shown for 2.8 GeV and 4.7 GeV respectively, evaluated in the three different coordinate systems. They conclude from this data:

1. The density matrix parameters vary rapidly in the Gottfried-Jackson system. The t-channel helicity-flip amplitudes increase rapidly with increasing $|t|$. This behavior rules out t-channel helicity conservation and also excludes a zero spin particle exchange without absorption as the only contributor to rho production.

2. The ρ^α_{ik} in the Adair system also vary significantly with t (see also Fig. 38a). This excludes the hypothesis of spin independence in the total c.m. system for rho production.[44]

3. In the helicity system the helicity-flip contributions are zero within errors up to $|t| = 0.4$ GeV^2, i.e., the rho behaves like a photon with the spin aligned along its direction of motion. In other words, the rho production mechanism conserves s-channel c.m.s. helicity. The fact that the flip contributions are minimum in the helicity system is further demonstrated in Figs. 38b,c. The rho density matrix as calculated in the helicity frame was rotated by an angle β around the production normal and a least squares fit made to find that value of β for which the flip terms

become minimal, i.e., for which the rho density matrix is closest to that of the photon. Figs. 38b,c show β as a function of the rho c.m.s. production angle θ_{cm} together with lines indicating where the data points should fall if the flip terms were minimal in the Gottfried-Jackson (G.J.), helicity (H), or Adair system (A), respectively. For $\theta_{cm} \lesssim 25^{\circ}$, the helicity system is clearly preferred.

In summary, rho photoproduction via $\gamma p \rightarrow p\rho^{\circ}$ proceeds almost completely through natural parity exchange and conserves helicity in the s-channel c.m. system up to $|t| = 0.4$ GeV^2.

REFERENCES

1. R. Diebold, Proceedings of the Boulder Conference on High Energy Physics, Boulder, Colorado (1969).

2. K. Lubelsmeyer, Proceedings of the 4th International Conference on Photon and Electron Interactions, Liverpool, England (1969).

3. G. C. Bolon, et al., P.R.L. 18, 926 (1967).

4. M. Braunschweig, et al., P.L. 22, 705 (1966); P.L. 26B, 405 (1968).

5. R. Anderson, et al., P.R.L. 21, 384 (1968); P.R., D1, 27 (1970).

6. H. Primakoff, et al., P.R. 81, 899 (1951).

7. A dip in $d\sigma/dt$ is expected at values of $z \sim -0.6$ GeV/^{2}, from the vanishing of the ρ and ω spin-flip residues when γp or α_ω equals zero.

8. Z. Bar-Yuan, et al.,P.R.L. 19, 40 (1967).

9. G. C. Bolon, et al., Proceedings of the 4th International Conference on Photon and Electron Interactions, Liverpool, England (1969).

10. R. Anderson, et al., SLAC PUB 770

11. A. Boyarski, et al., SLAC PUB 744

12. A. Boyarski, et al., P.R.L. 21, 1767 (1968).

13. M. Aderholtz, et al., N.P. B8, 45 (1968).

14. A. Dar, N.P. B11, 634 (1969).

15. E. Gotsman, Letters to N.C. 2, 563 (1969).

16. D. Schildknecht, DESY Report 69/10;
W. Schmidt and D. R. Yennie, P.R.L. 23, 623 (1968).

17. F. Gilman, P.L. 29B, 673 (1969).

18. M. Walter, Deutsche Akademieder Wissenschaften zu Berlin-Zeuthen, Report No. PHE 69-1 (1969).

19. H. H. Bingham, et al., SLAC PUB 766 (to be published).

20. J. J. Murray and P. Klein, Report No. SLAC-TN-67-19, Stanford Linear Accelerator Center (1967); C. K. Sinclair, J. J. Murray, P. Klein, and M. Rabin, IEEE Trans. on Nucl. Sci. 16, 1065 (1969).

21. J. D. Jackson, N.C. 34, 1644 (1964).

22. A. Donnachie, R. G. Kirsopp, and C. Lovelace, CERN TH 838, (1967).

23. R. Anderson, et al., P.R.L. 23, 721 (1969).

24. D. S. Beder and P. Söding, UCRL-17867 (1967).

25. P. Stickel, Z. Physik, 180, 170 (1964).

26. P. Eberhard and M. Pripstein, PRL 10, 351 (1963).

27. Aachen-Berlin-Bonn-Hamburg-Heidelberg-Munchen Collaboration, P.R. 175, 1669 (1968).

28. Brown -Harvard-MIT-Padova-Weizmann Institute Bubble Chamber Group P.R. 155, 1468 (1967).

29. Y. Eisenberg, et al., P.R. 25, 764 (1970).

30. G. B. Chadwick, private communication.

31. M. Davier, et al., P.L. 28B, 619 (1969).

32. Y. Eisenberg, et al., P.R.L. 22, 669 (1969).

33. J. Ballam, et al., P.L. 30B, 421 (1969).

34. In this frame the z axis is given by the ω direction of flight in the total c.m. system. The angles θ and ϕ are defined as the polar and azimuthal angles of the normal to the ω-decay plane in the ω-rest system. The photon polarization plane in the total c.m.s. makes an angle Φ with the production plane. The y axis is the normal to the production plane, defined by the cross product $\hat{k} \times \hat{\omega}$ of the directions of the photon and the ω meson. The angle Φ between the electric vector of the photon, θ, and the production plane in the total c.m. system is defined by $\cos \Phi = \hat{\epsilon} \cdot (\hat{y} \times \hat{k})$, $\sin \Phi = \hat{y} \cdot \hat{\epsilon}$. The decay angles θ, ϕ are the polar and azimuthal angles of the normal $n = \pi^+ \times \pi^-$ to the ω decay plane in the ω rest system:

$$\cos \theta = \hat{n} \cdot \hat{z} \qquad \cos \phi = \hat{y} \cdot (\hat{z} \times \hat{n})/|\hat{z} \times \hat{n}|$$

$$\sin \phi = -\hat{x} \cdot (\hat{z} \times \hat{n})/|\hat{z} \times \hat{n}|$$

The x axis is given by $\hat{x} = \hat{y} \times \hat{z}$.

35. SLAC-Berkeley-Tufts Collaboration, Report No. SLAC PUB 727, Stanford Linear Accelerator Center (1970), submitted to Phys. Rev. Letters; SLAC-Berkeley-Tufts Collaboration, Report No. SLAC PUB 728, Stanford Linear Accelerator Center (1970), Submitted to Phys. Rev. Letters.

36. H. Harari, Proceedings of the 4th International Symposium on Electron and Photon Interactions at High Energies, Liverpool, England (1969).

37. J. Benecke and H. P. Dürr, Nuovo Cimento 56, 269 (1969); G. Wolf, Phys. Rev. 182, 1538 (1969). A value of 2.31 GeV^{-1} was used for the R parameter describing the $\omega\pi\gamma$ vertex, i.e., the same value obtained for the R parameter of the $\rho\pi\pi$ vertex.

38. Particle Data Group, Rev. Mod. Phys. 43, 87 (1970). A value of 0.87 was used for the branching ratio $\Gamma(\omega \rightarrow \pi^+\pi^-\pi^0)/\Gamma(\omega \rightarrow \text{all})$.

39. Private communication, G. B. Chadwick

40. H. H. Bingham, et al., P.R.L. 24, 955 (1970).

41. M. Ross and L. Stodolsky, P. R. 149, 1172 (1966).

42. SLAC-LRL-Tufts HBC Collaboration: SLAC PUB 728, 729, 730 (1970).

43. K. Schilling, P. Seyboth, and G. Wolf, SLAC PUB 683.

44. This assumption was made in the "strong absorption model - SAM". Y. Eisenberg, et al., P.L. 22, 217 (1966), 22, 223 (1966).

FIGURE CAPTIONS

1. Comparison of DESY and SLAC π^o photoproduction cross sections at time of Daresbury Conference.
2. Typical differential cross section for π^o photoproduction.
3. SLAC π^o photoproduction cross sections at time of Daresbury Conference.
4. Graph of π^o photoproduction process.
5. Asymmetry in π^o photoproduction.
6. Ratio $(\pi^o n / \pi^o p)$ for photoproduction of π^o from deuterium.
7. Comparison of π^o and Compton cross sections.
8. Typical π^o missing mass signal.
9. Cross section for process $\gamma p \rightarrow \pi^o p$, at a fixed t, as a function of energy.
10. π^o angular distributions.
11. Comparison of SLAC and DESY π^o cross sections.
12. Effective $\alpha(t)$ for $\gamma p \rightarrow \pi^o p$.
13. Fits to the π^+ and π^- data from hydrogen and deuterium for $d\sigma/d\Omega_{lab}$ vs MM^2 at 1.4^o. The curves show the single nucleon, the delta and the rho processes folded with a 0.03 X_0 bremsstrahlung spectrum including a Fermi smearing for the deuterium case as given by the Hulthen momentum distribution.
14. Measured cross sections for $\pi^{\pm}\Delta$ photoproduction vs momentum transfer $\sqrt{-t}$. The γn cross sections result from deuterium minus hydrogen subtractions. Fits made to missing mass spectra included the single nucleon process, the delta, background from $\gamma N \rightarrow \rho N$, and a correction for phase space $\gamma N \rightarrow \pi\pi N$. A Jackson type Breit-Wigner form was used to calculate the shape of the Δ contribution. Smooth curves are drawn to guide the eye.

15. The ratios $(\gamma p \to \pi^- \Delta^{++})/(\gamma n \to \pi^+ \Delta^-)$ and $(\gamma n \to \pi^- \Delta^+)/(\gamma p \to \pi^+ \Delta^0)$ vs $\sqrt{-t}$. These ratios, where different from one, indicate an interference between isoscalar (ω-like photon) and isovector (ρ^0-like photon) amplitudes. For comparison the curve shows the ratio for $(\gamma n \to \pi^- p)/(\gamma p \to \pi^+ n)$.

16. The deuterium-to-hydrogen ratios vs $\sqrt{-t}$. Neglecting absorption effects in deuterium, which were found to be negligible in our $\gamma d \to \pi^+ nn$ data, dominance of I-spin-one exchange implies R = 4 for π^+ and R = 4/3 for π^-. The π^+ data indicate that I-spin-one exchange alone does not fit the data for $|t| \gtrsim 0.15$ GeV^2.

17. Test of the vector dominance model. The average of Δ^{++} and Δ^- is compared to that predicted from the $\pi^+ p \to \rho^0 \Delta^{++}$ data at 8 GeV by vector dominance. There is disagreement by about a factor of 5. Smooth curves are drawn to guide the eye.

18. Reaction $\gamma p \to p\pi^+\pi^-$. Effective mass distributions for the $p\pi^+$ and $p\pi^-$ systems. The shaded histograms represent events with $|t| < 0.4$ GeV^2 and $M_{\pi^+\pi^-} > 1.0$ GeV.

19. Reaction $\gamma p \to \Delta^{++}\pi^-$. Differential cross sections $d\sigma/dt$ from this experiment ($\updownarrow$) and from Ref. 3 for $E_\gamma = 5$ GeV ($\updownarrow$). The shaded regions in (b), (d) are shown on an expanded scale in (a), (c). The curves are the predictions of the gauge invariant OPE model.

20. Reaction $\gamma p \to \Delta^{++}\pi^-$. Density matrix parameters and parity asymmetry P_σ. The solid curves are the predictions of the gauge-invariant OPE model. The dashed curves show the VDM predictions.

21. Graph of the process $\gamma p \to \rho^- \Delta^{++}$.

22. The cross section for $\gamma p \rightarrow \rho^- \Delta^{++}$ as a function of photon energy.

23. Three pion mass spectra for the reaction $\gamma p \rightarrow p\pi^+\pi^-\pi^o$.

24. The cross section for ω production as a function of photon energy.

25. Differential cross section for $\gamma p \rightarrow p\omega$.

26. Density matrix elements for ω decay.

27. Mass spectrum for $(\pi^+\pi^-\pi^o)$ as a function of photon energy.

28. Cross section for $\gamma p \rightarrow \omega p$ as a function of photon energy.

29. $\pi^+\pi^-$ mass distributions for events of the reaction $\gamma p \rightarrow p\pi^+\pi^-$. The helicity-conserving p-wave intensity is shown by the points o. The curves give the results of a maximum likelihood fit using the the ρ^o the parametrization $(M_\rho/M_{\pi\pi})^{n(t)}$(---) and the Soding model (——).

30. Reaction $\gamma p \rightarrow p\pi^+\pi^-$: (a),(b) The exponential slope of the t distribution as a function of the $\pi^+\pi^-$ mass taking all events in a given $\pi^+\pi^-$ mass bin and with $0.02 \leq |t| < .4$ GeV^2. The curves show the result of the Soding model. (c),(d) Fitted values for n(t) using the parametrization $(M_\rho/M_{\pi\pi})^{n(t)}$; (e),(f) Ratio of the fitted ρ^o production to Drell cross sections, $\sigma_\rho(t)/\sigma_D(t)$. The curves show the predictions of the Söding model.

31. Reaction $\gamma p \rightarrow p\pi^+\pi^-$: for moments $Y_2^0(\theta,\psi)$ and $Y_4^0(\theta,\psi)$ in the helicity frame as a function of $M_{\pi\pi}$ for $0.02 < |t| < 0.4$ GeV^2. The curves show the results of the Söding model.

32. Reaction $\gamma p \rightarrow p\pi^+\pi^-$: Differential cross sections as a function of t for the helicity-conserving p-wave contribution ($\triangle$), for ρ^o production as obtained from fits with the Soding model (ϕ) and using the parametrization $(M_\rho/M_{\pi\pi})^{n(t)}$($\phi$).

33. Reaction $\gamma p \rightarrow p\rho^{o}$. Rho decay angular distributions in the helicity system for $|t| < 0.4$ GeV^2 and $0.6 < M_{\pi\pi} < 0.85$ GeV without background subtraction. The curves for the cos θ distributions are proportional to $\sin^2\theta$.

34. Reaction $\gamma p \rightarrow p\pi^{+}\pi^{-}$. The density matrix elements ρ^{0}_{00} and ρ^{1}_{1-1} and the parity asymmetry, P_σ, as a function of $M_{\pi\pi}$.

35. Reaction $\gamma p \rightarrow p\rho^{o}$. The parity asymmetry, P_σ, and the asymmetry, Σ, as a function of t in the Gottfried-Jackson, helicity and Adair systems.

36. Reaction $\gamma p \rightarrow p\rho^{o}$. The spin density matrix parameters as a function of t in the Gottfried-Jackson, helicity and Adair systems, for 2.8 GeV.

37. Reaction $\gamma p \rightarrow p\rho^{o}$. The spin density matrix parameters as a function of t in the Gottfried-Jackson, helicity and Adair systems, for 4.7 GeV.

38. Reaction $\gamma p \rightarrow p\rho^{o}$. (a) Comparison of the spin density matrix parameters ρ^{0}_{00}, Re ρ^{0}_{10}, Im ρ^{2}_{10} in the helicity (ϕ) and Adair systems (ϕ) as a function of t (data of Fig. 36, 37). (b,c) The angle β for rotation into the "minimum flip" system as a function of the c.m.s. rho production angle θ_{cm}.

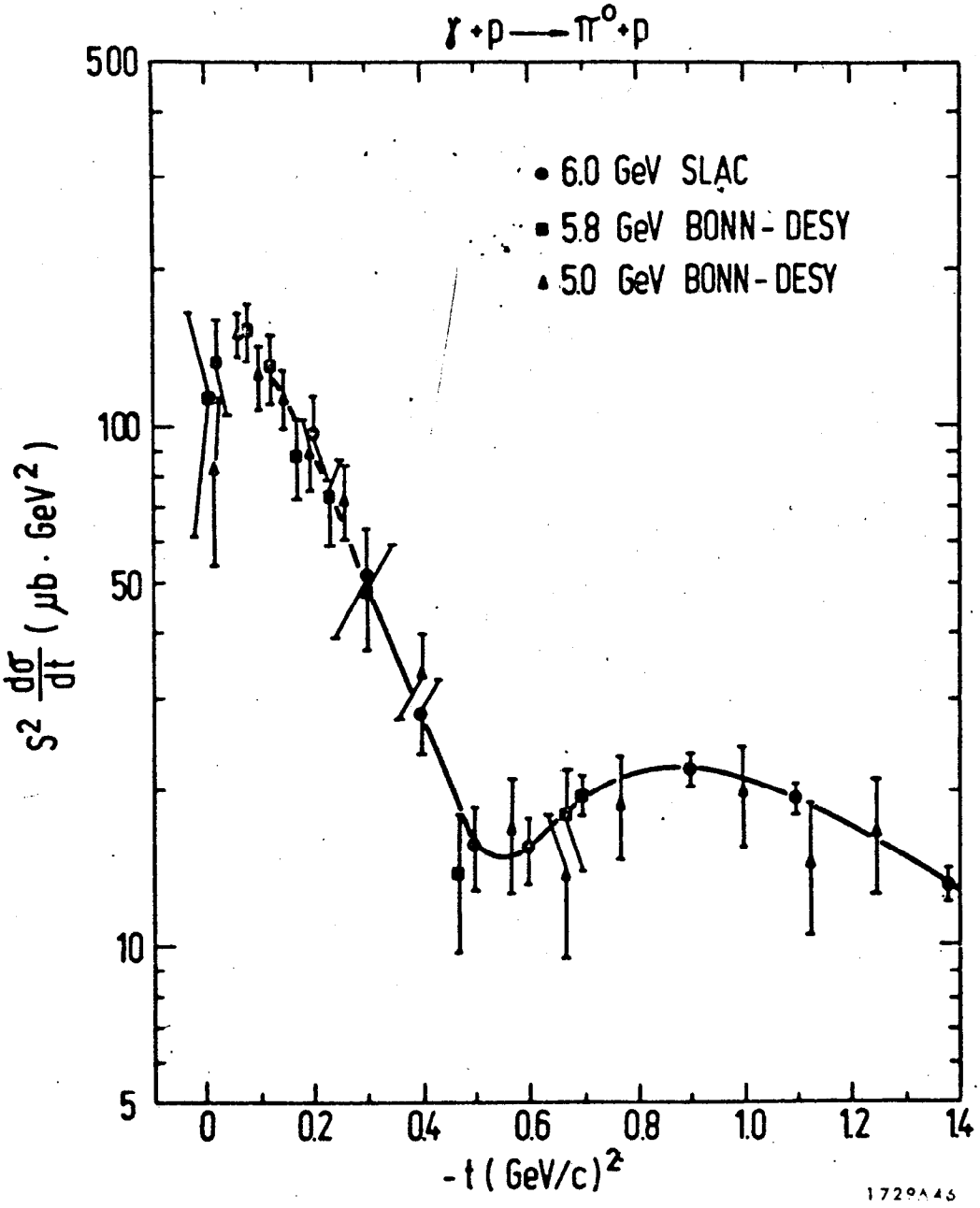
γ + p ——— π° + p
500
100
50
10
5
• 6.0 GeV SLAC
■ 5.8 GeV BONN - DESY
▲ 5.0 GeV BONN - DESY
$s^2 \frac{d\sigma}{dt}$ (μb · GeV²)
0
0.2
0.4
0.6
0.8
1.0
1.2
1.4
- t (GeV/c)²
1729A46

Fig. 1

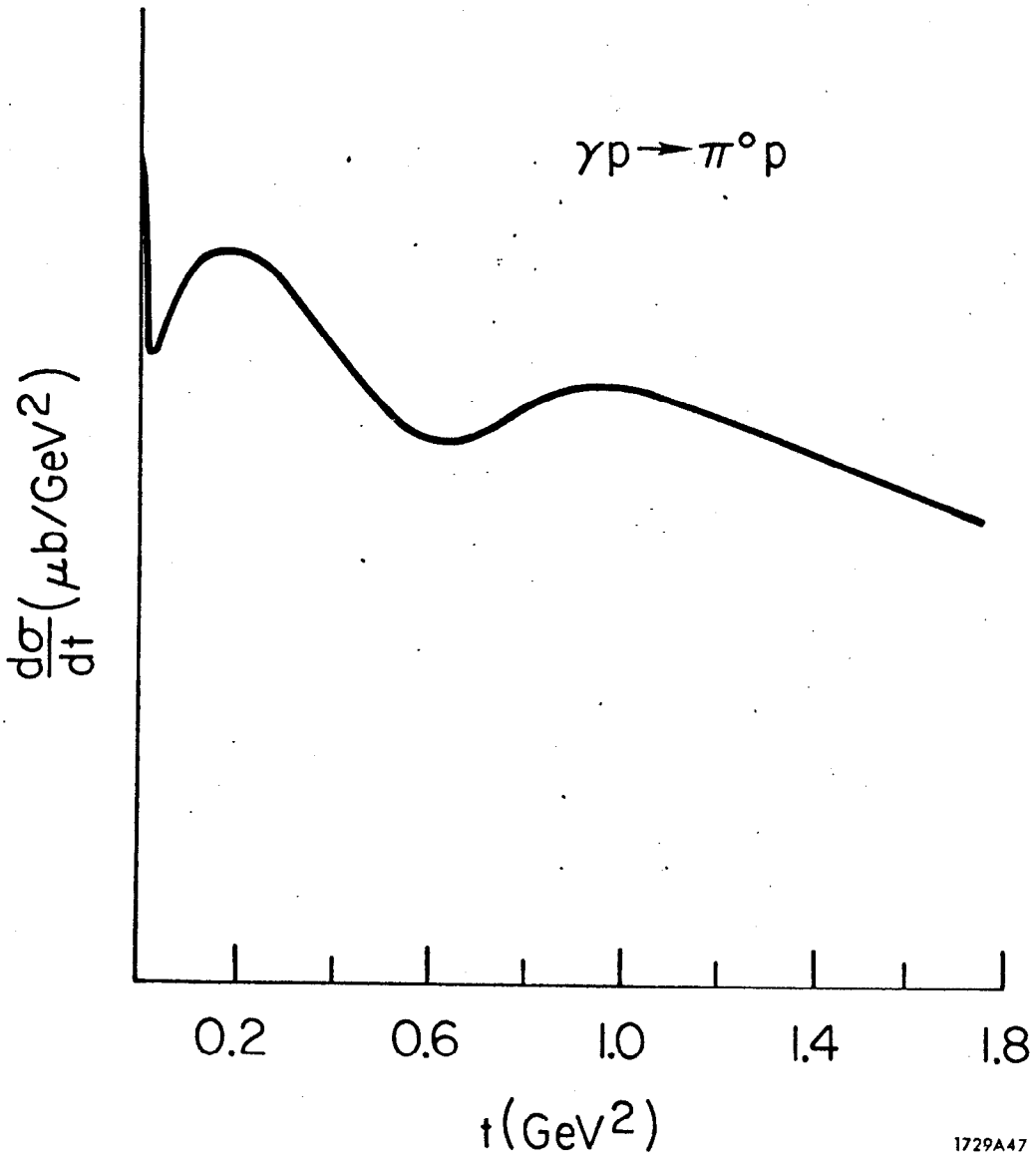

Fig. 2

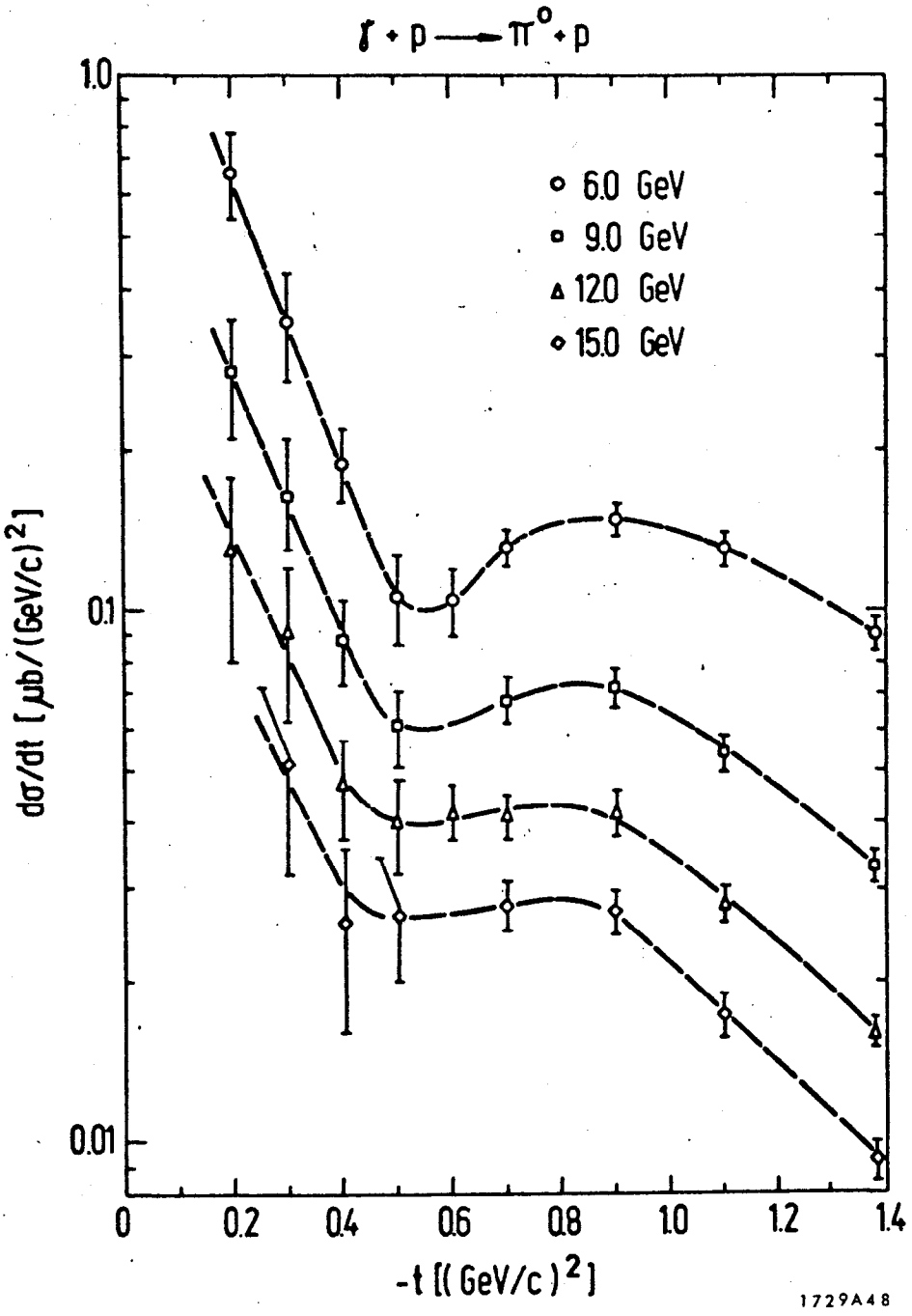
γ + p ⟶ π° + p
1.0
0.1
0.01
6.0 GeV
9.0 GeV
12.0 GeV
15.0 GeV
dσ/dt [μb/(GeV/c)²]
0
0.2
0.4
0.6
0.8
1.0
1.2
1.4
-t [(GeV/c)²]
1729A48

Fig. 3

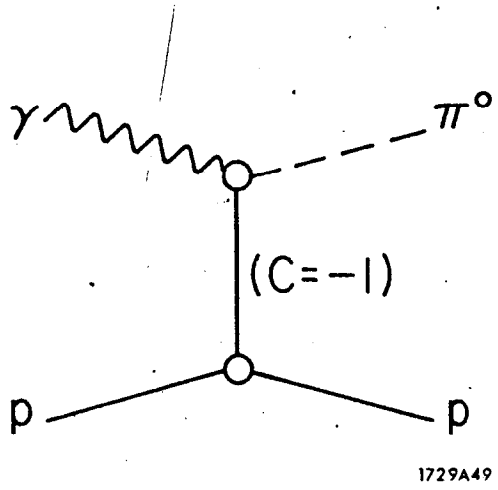

Fig. 4

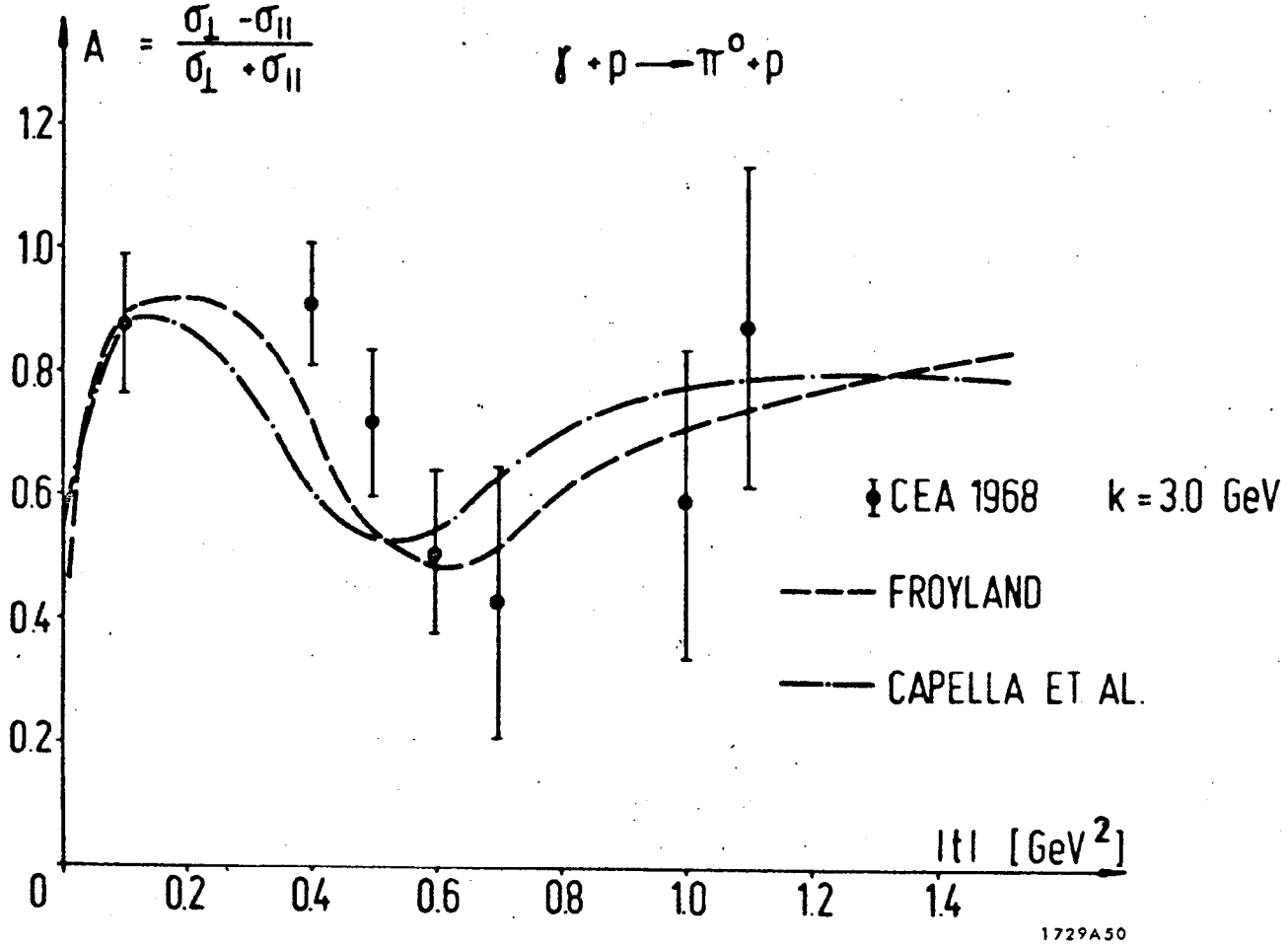
A = (σ⊥ - σ∥) / (σ⊥ + σ∥)
γ + p → π° + p
1.2
1.0
0.8
0.6
0.4
0.2
0
0.2
0.4
0.6
0.8
1.0
1.2
1.4
|t| [GeV²]
CEA 1968
k = 3.0 GeV
FROYLAND
CAPELLA ET AL.
1729A50

Fig. 5

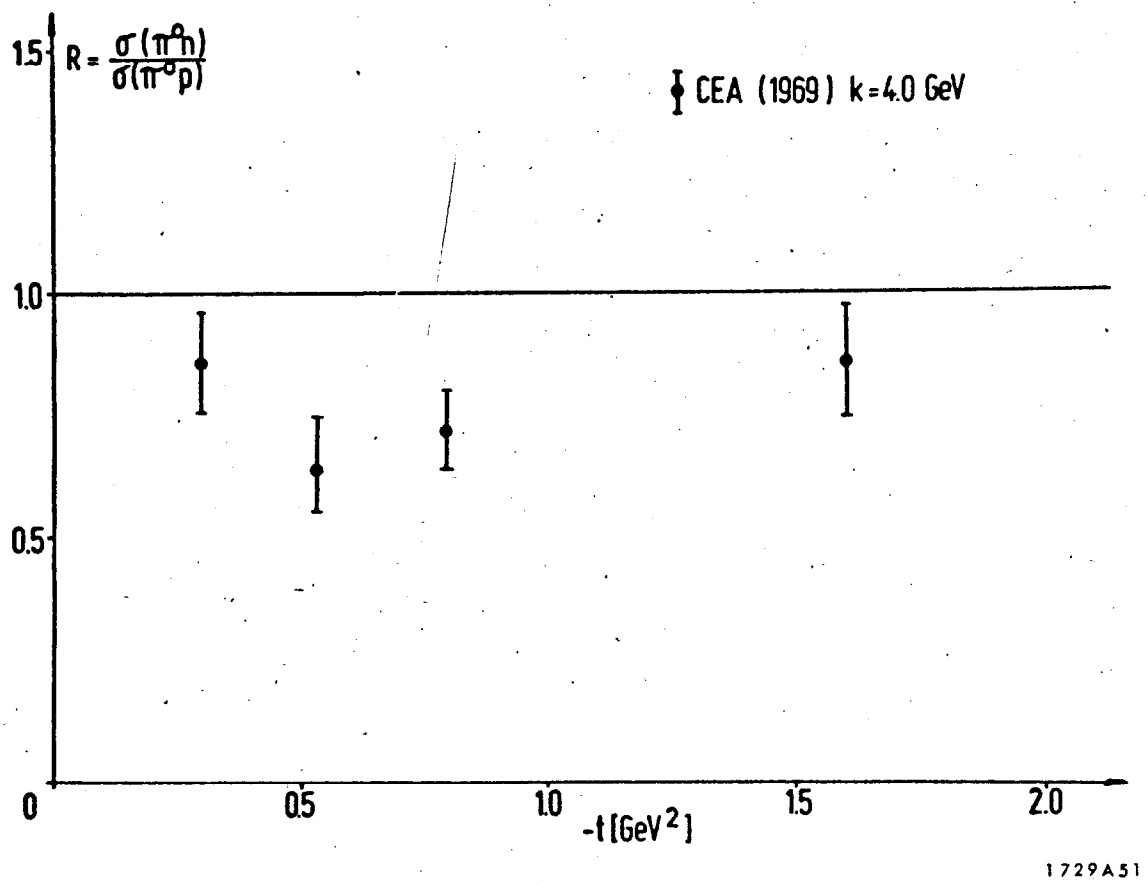

Fig. 6

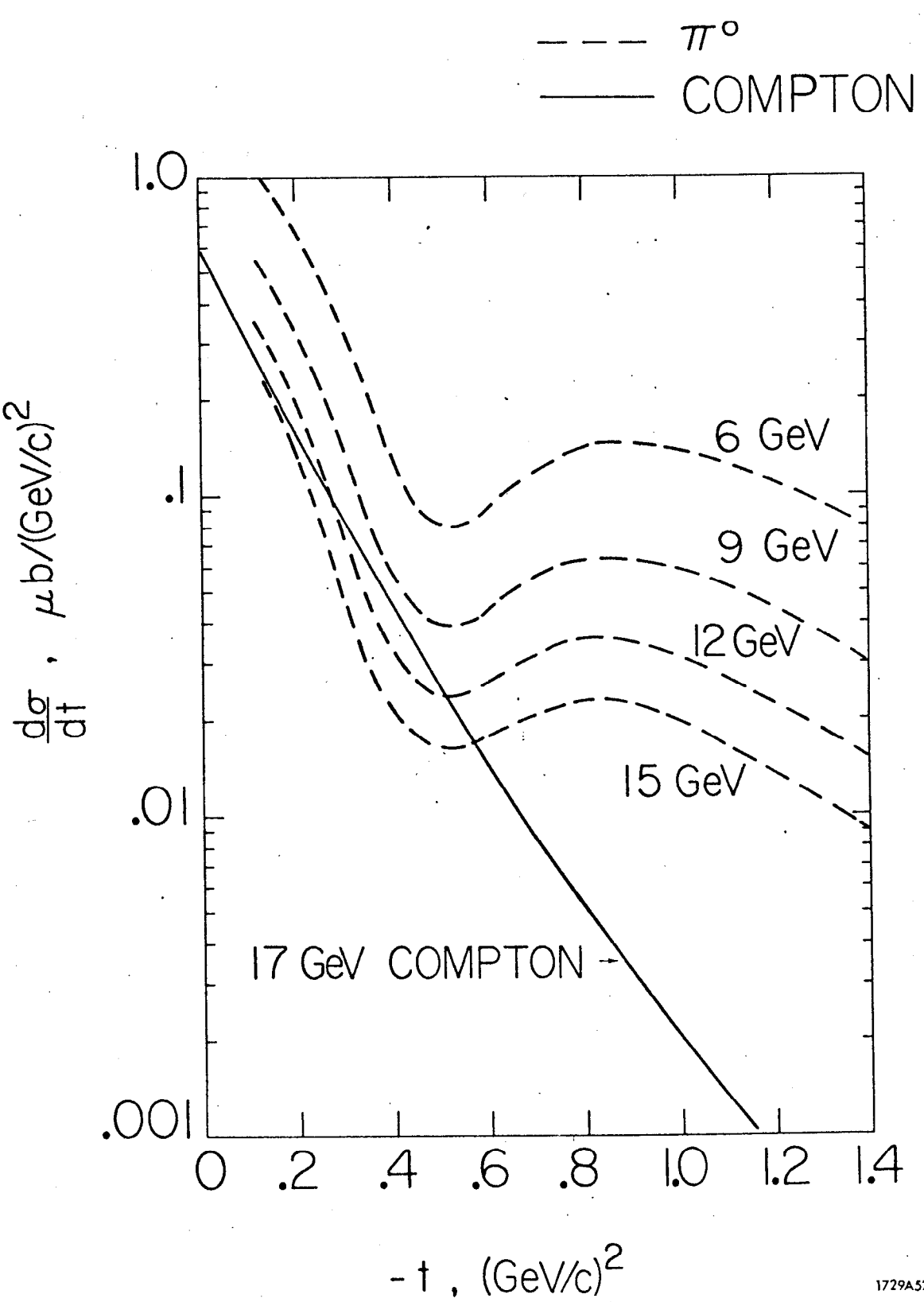
π°
COMPTON
1.0
.1
.01
.001
6 GeV
9 GeV
12 GeV
15 GeV
17 GeV COMPTON
0
.2
.4
.6
.8
1.0
1.2
1.4
dσ/dt , μb/(GeV/c)²
-t , (GeV/c)²
1729A52

Fig. 7

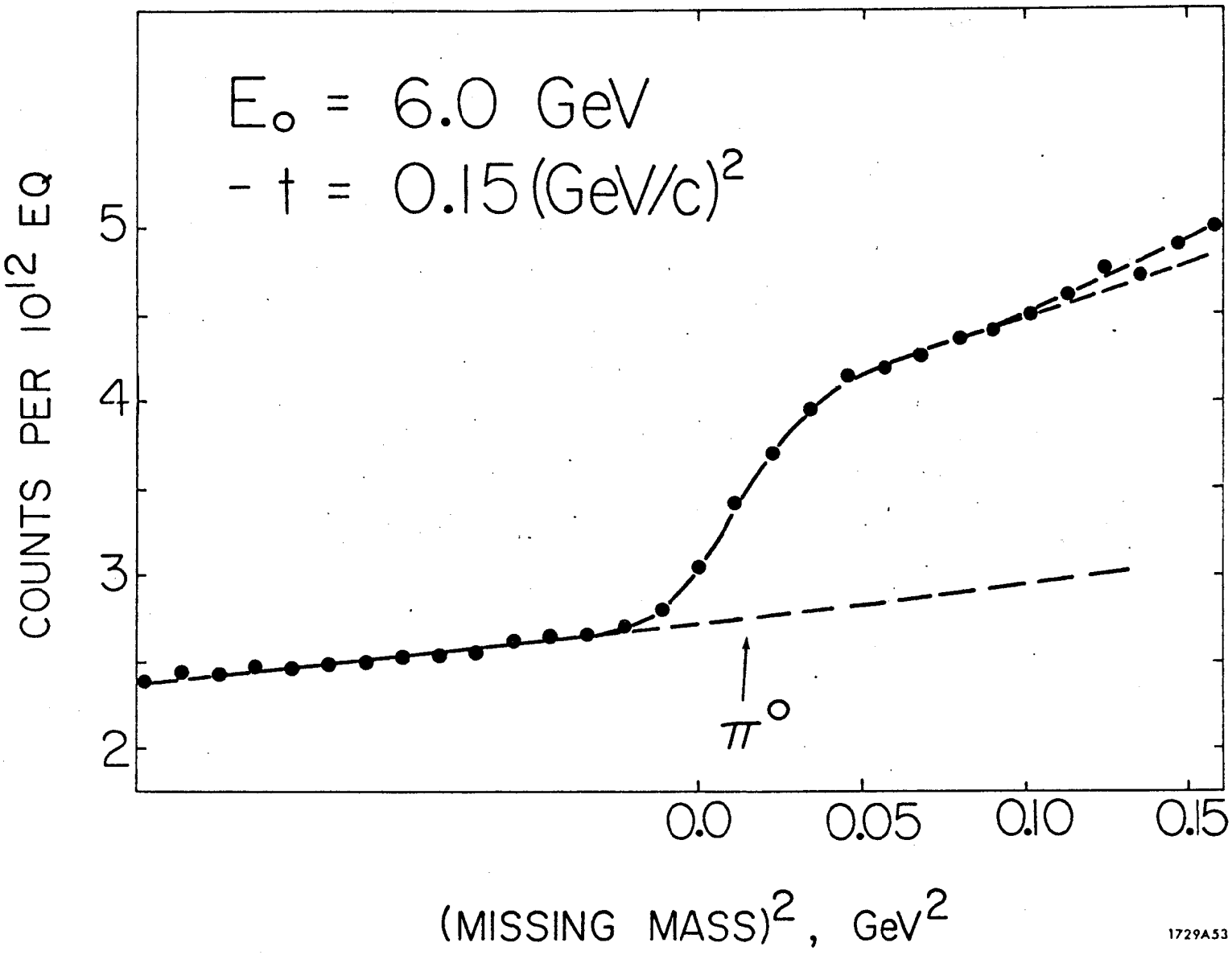
E_o = 6.0 GeV
- t = 0.15 (GeV/c)^2
COUNTS PER 10^{12} EQ
5
4
3
2
π^o
0.0
0.05
0.10
0.15
(MISSING MASS)^2, GeV^2
1729A53

Fig. 8

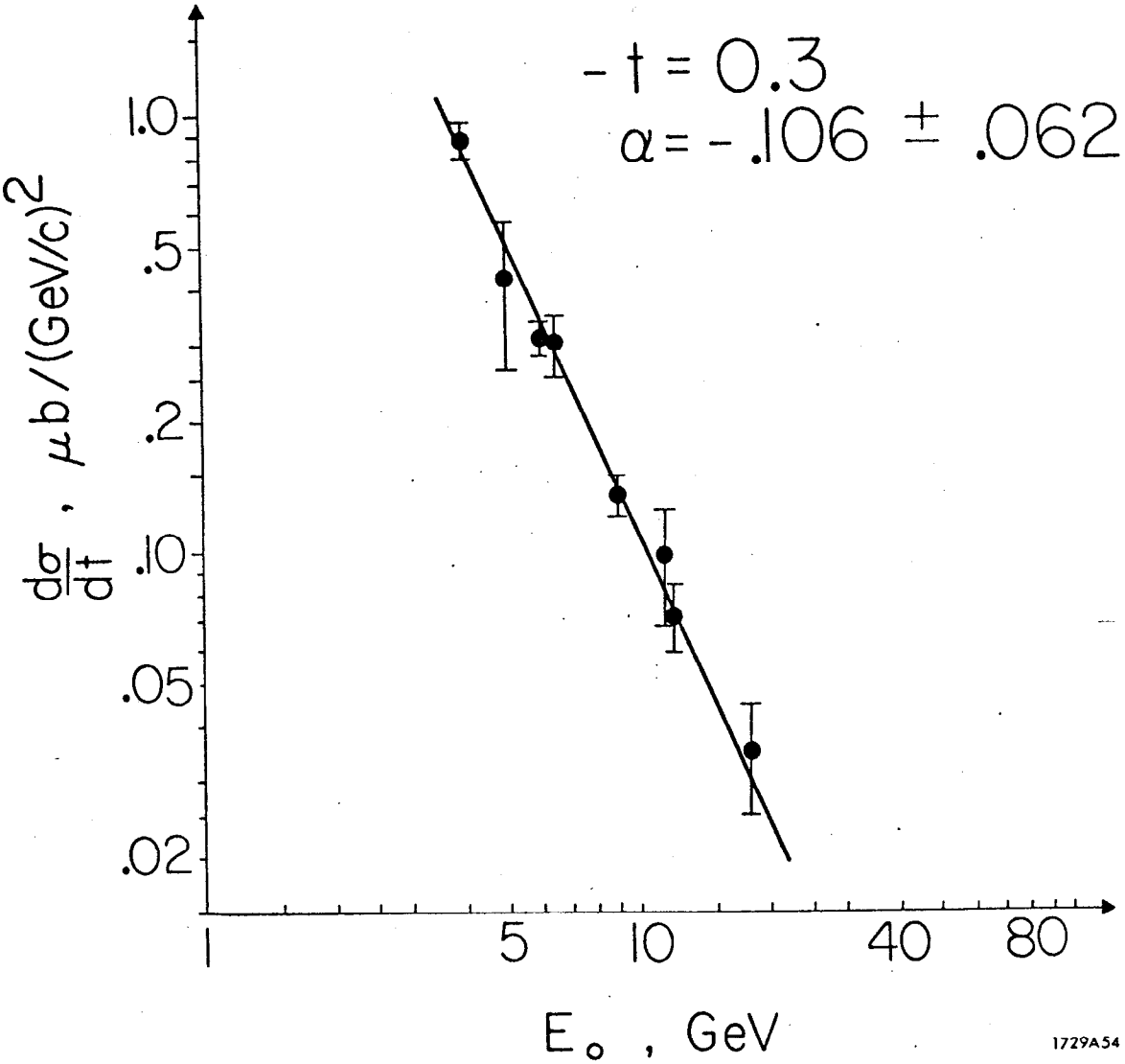
-t = 0.3
α = -.106 ± .062
dσ/dt , μb/(GeV/c)²
1.0
.5
.2
.10
.05
.02
1
5
10
40
80
E₀ , GeV
1729A54

Fig. 9

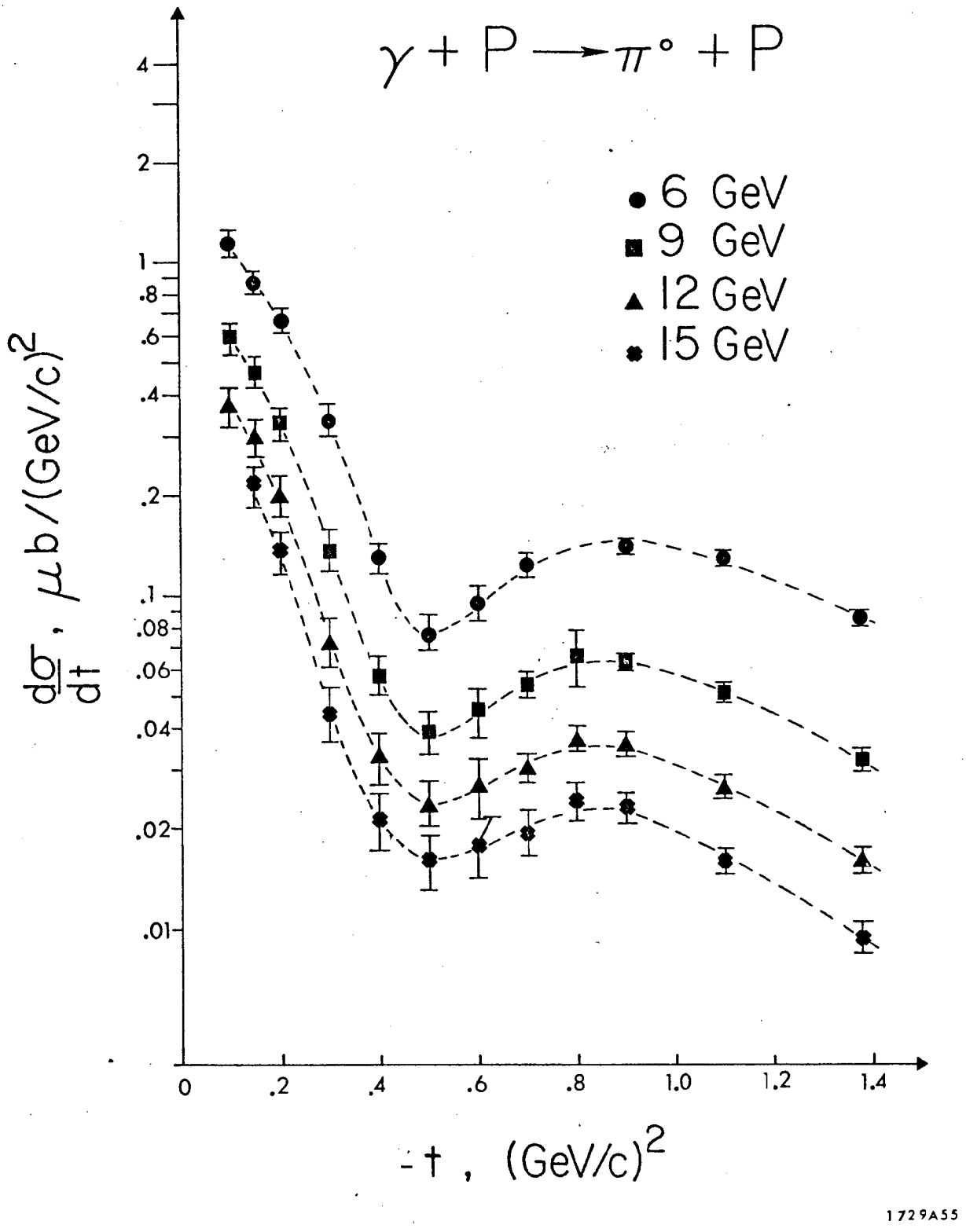
γ + P → π° + P
6 GeV
9 GeV
12 GeV
15 GeV
dσ/dt , μb/(GeV/c)²
4
2
1
.8
.6
.4
.2
.1
.08
.06
.04
.02
.01
0
.2
.4
.6
.8
1.0
1.2
1.4
-t , (GeV/c)²
1729A55

Fig. 10

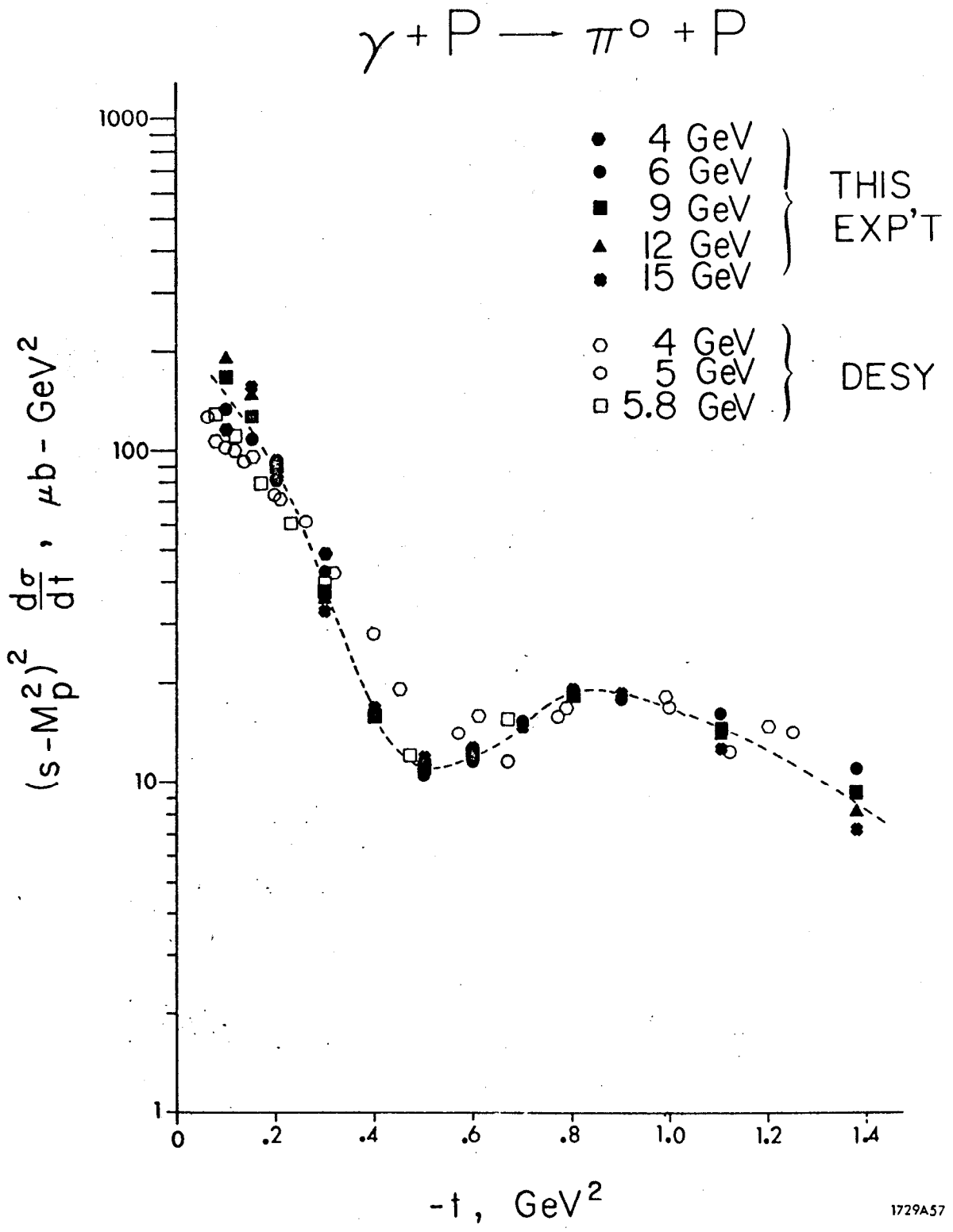
$\gamma + P \longrightarrow \pi^0 + P$
4 GeV
6 GeV
9 GeV
12 GeV
15 GeV
THIS EXP'T
4 GeV
5 GeV
5.8 GeV
DESY
$(s-M_p^2)^2 \frac{d\sigma}{dt}$, $\mu b - GeV^2$
1000
100
10
1
0
.2
.4
.6
.8
1.0
1.2
1.4
$-t$, GeV^2
1729A57

Fig. 11

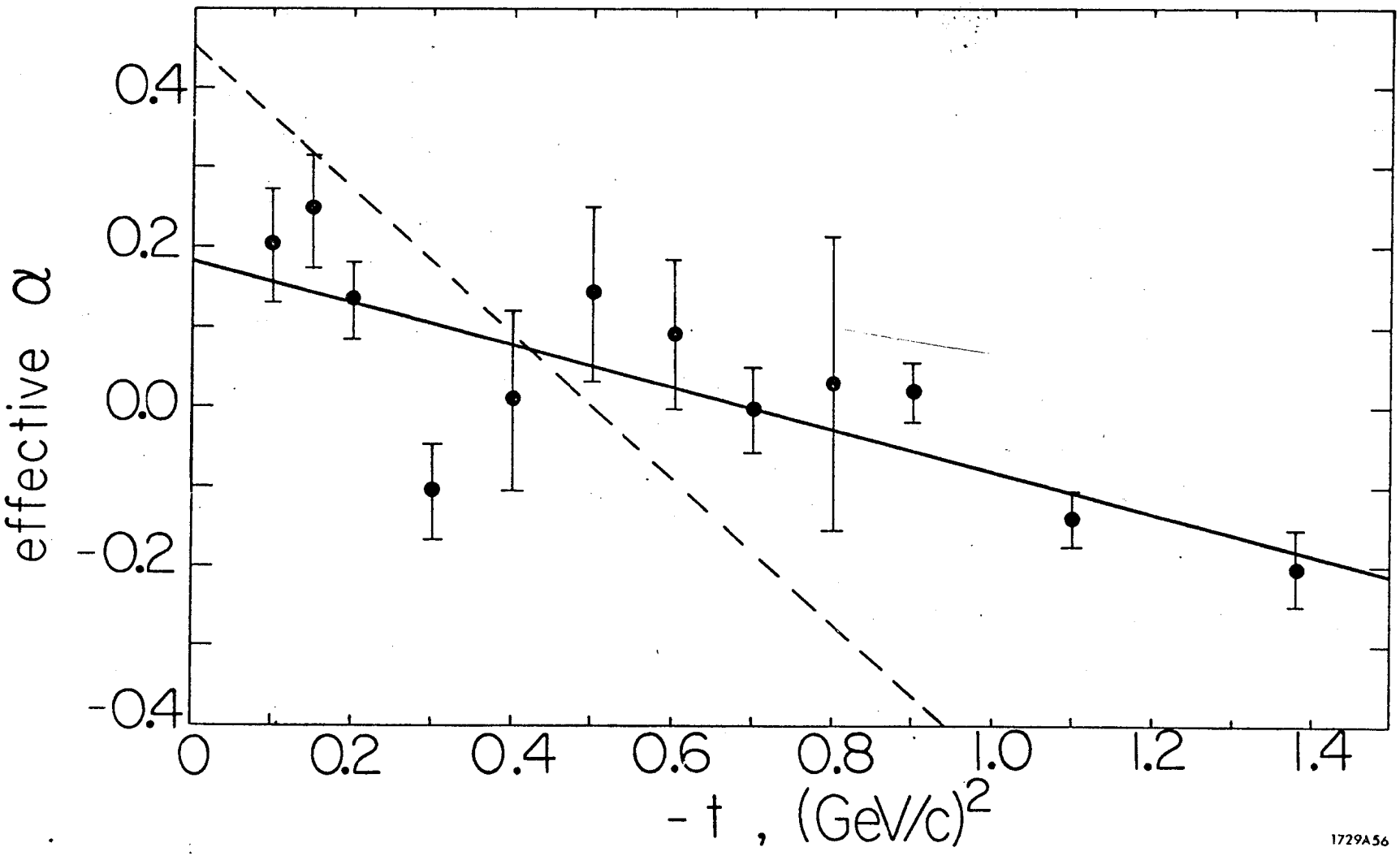

Fig. 12

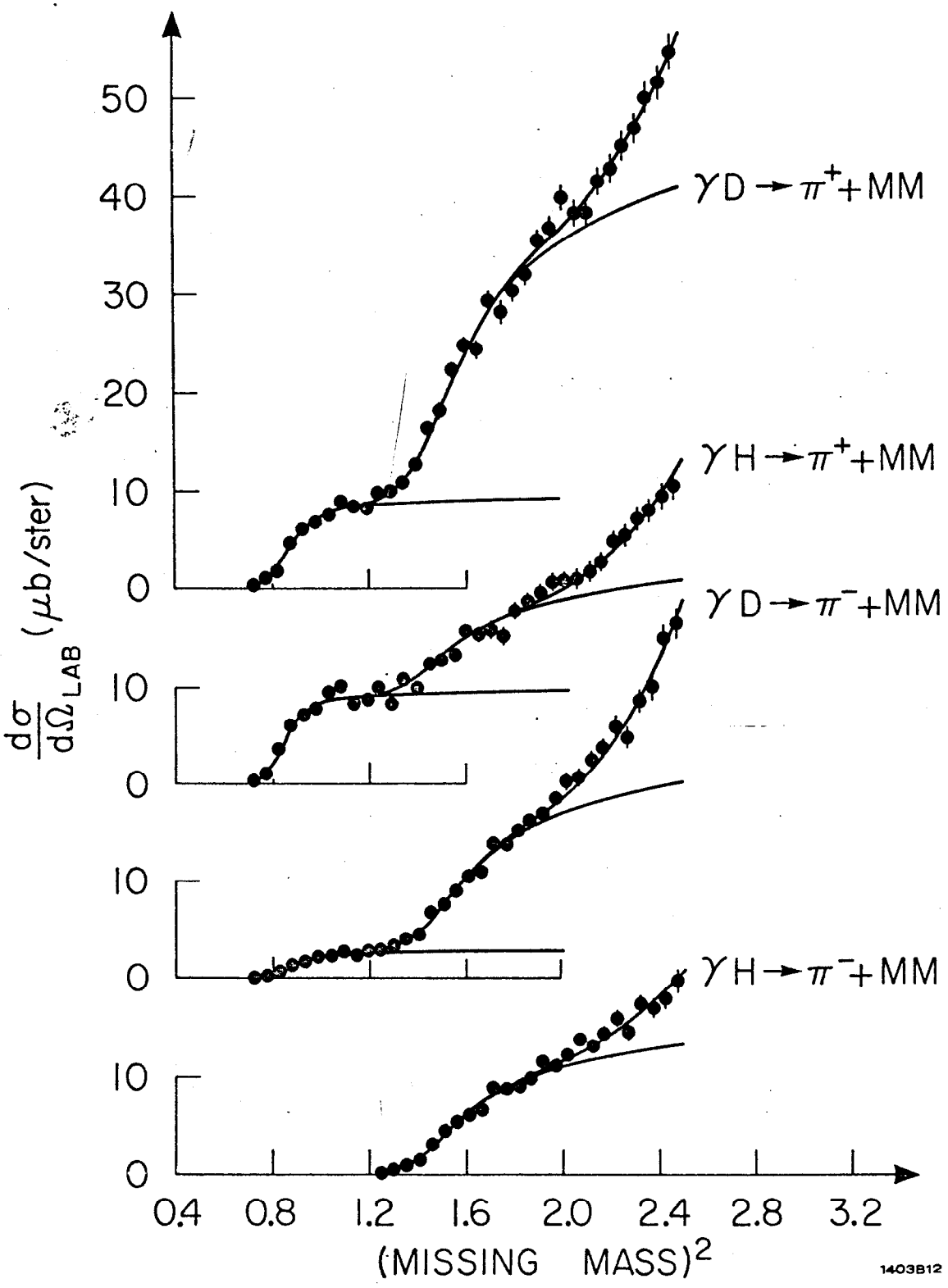
50
40
30
20
10
0
10
0
10
0
10
0
$\frac{d\sigma}{d\Omega_{LAB}}$ (μb/ster)
$\gamma D \rightarrow \pi^+ + MM$
$\gamma H \rightarrow \pi^+ + MM$
$\gamma D \rightarrow \pi^- + MM$
$\gamma H \rightarrow \pi^- + MM$
0.4
0.8
1.2
1.6
2.0
2.4
2.8
3.2
(MISSING MASS)^2
1403B12

Fig. 13

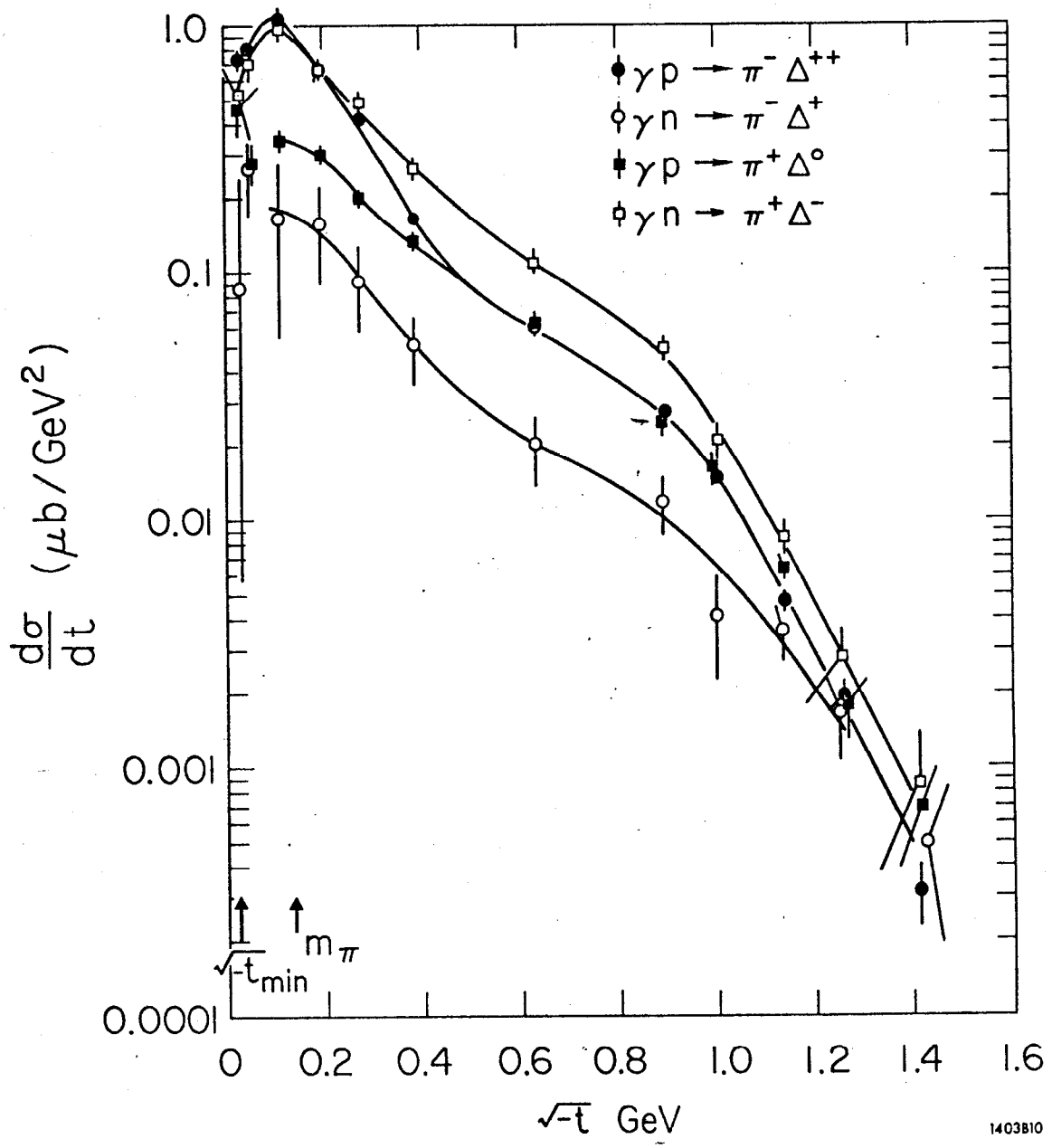
1.0
0.1
0.01
0.001
0.0001
$\frac{d\sigma}{dt}$ (μb/GeV^2)
$\gamma p \rightarrow \pi^- \Delta^{++}$
$\gamma n \rightarrow \pi^- \Delta^{+}$
$\gamma p \rightarrow \pi^+ \Delta^{\circ}$
$\gamma n \rightarrow \pi^+ \Delta^{-}$
m_π
$\sqrt{-t_{min}}$
0
0.2
0.4
0.6
0.8
1.0
1.2
1.4
1.6
$\sqrt{-t}$ GeV
1403810

Fig. 14

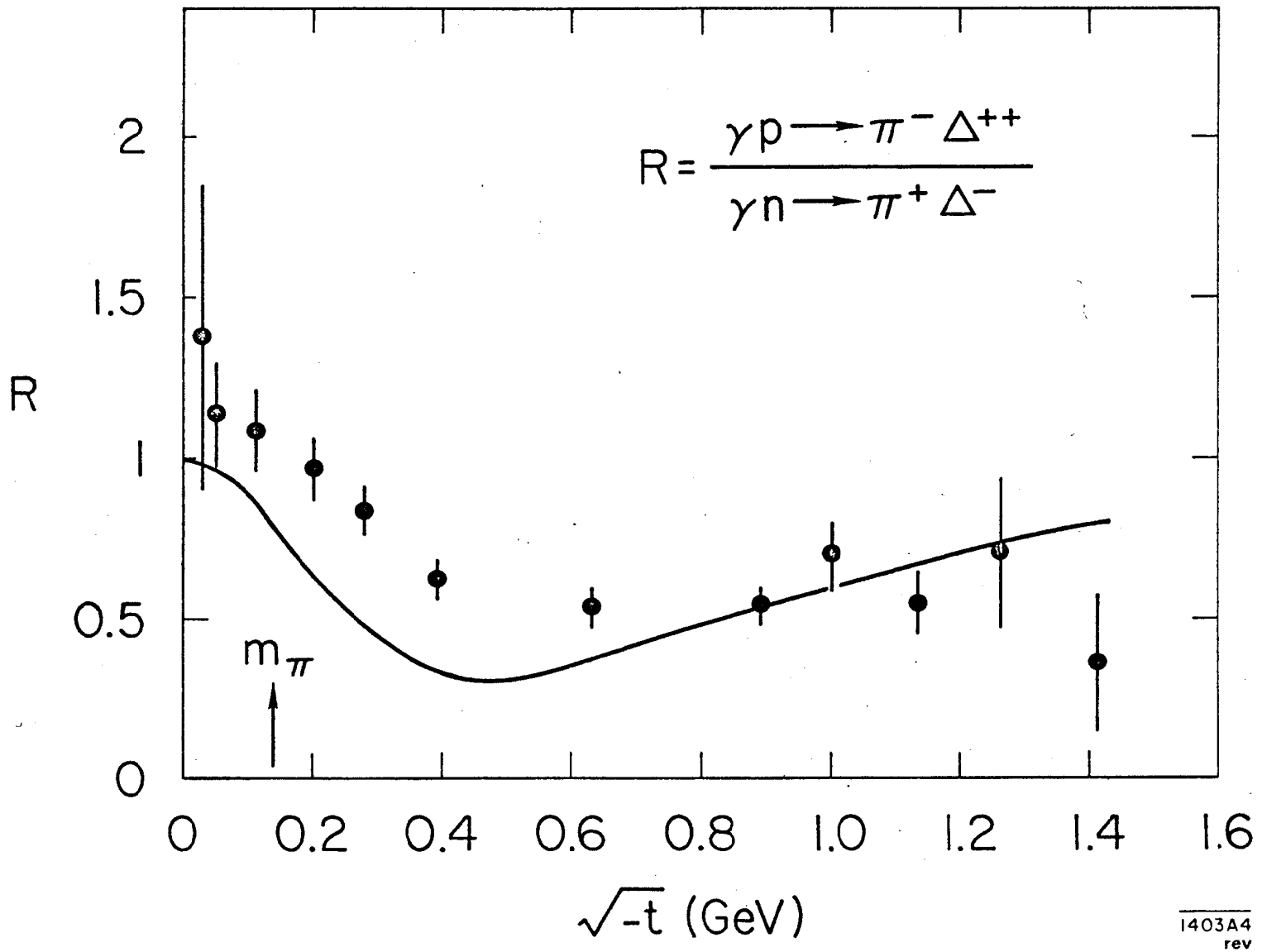

Fig. 15

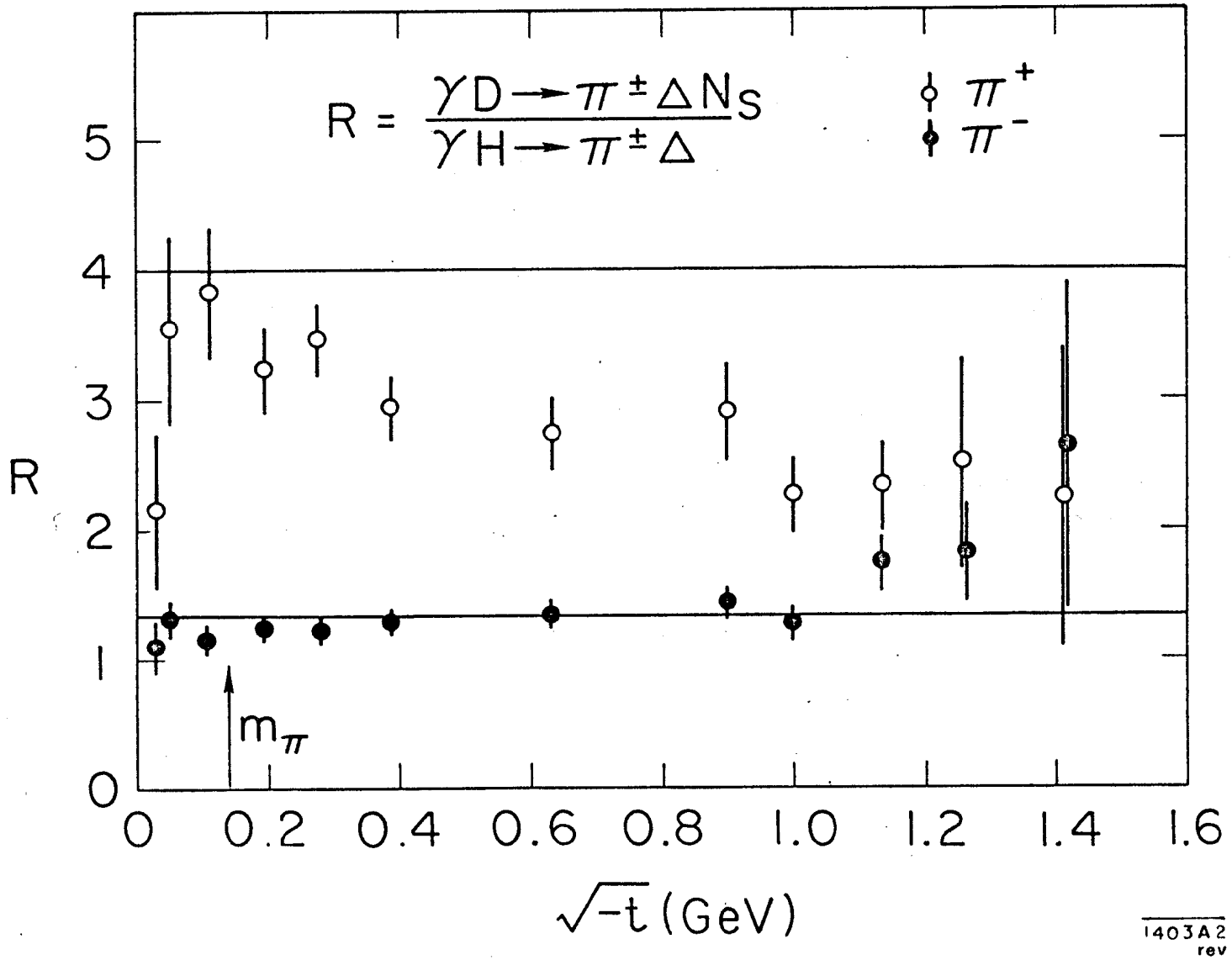
R = γD → π± ΔNs / γH → π± Δ
π+
π−
R
0
1
2
3
4
5
0
0.2
0.4
0.6
0.8
1.0
1.2
1.4
1.6
mπ
√−t (GeV)
1403A2
rev

Fig. 16

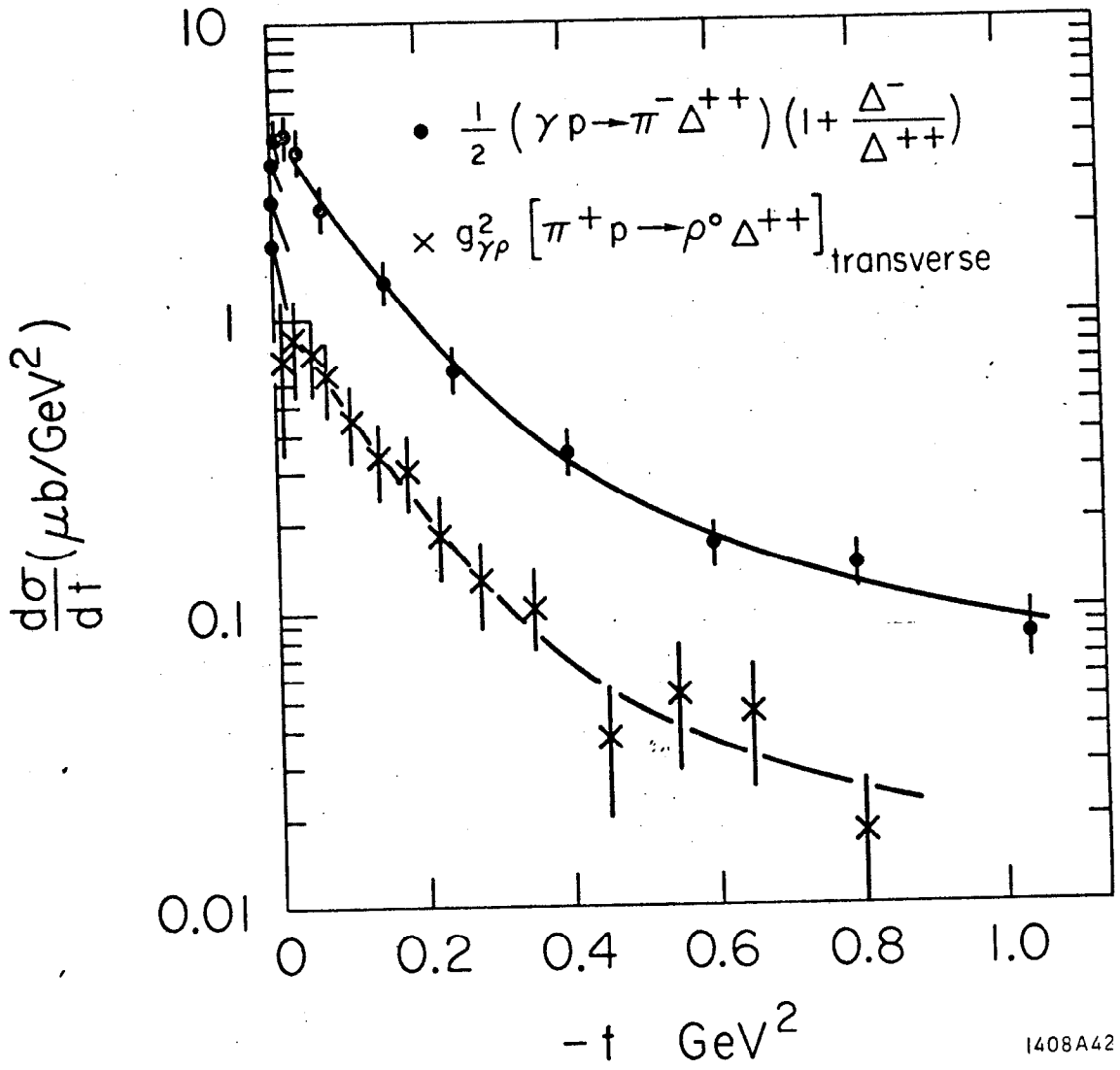
10
1
0.1
0.01
0
0.2
0.4
0.6
0.8
1.0
$\frac{d\sigma}{dt}(\mu b/GeV^2)$
$-t \quad GeV^2$
$\bullet \ \frac{1}{2}(\gamma p \to \pi^- \Delta^{++})(1+\frac{\Delta^-}{\Delta^{++}})$
$\times \ g^2_{\gamma\rho}[\pi^+ p \to \rho^0 \Delta^{++}]_{transverse}$
1408A42

Fig. 17

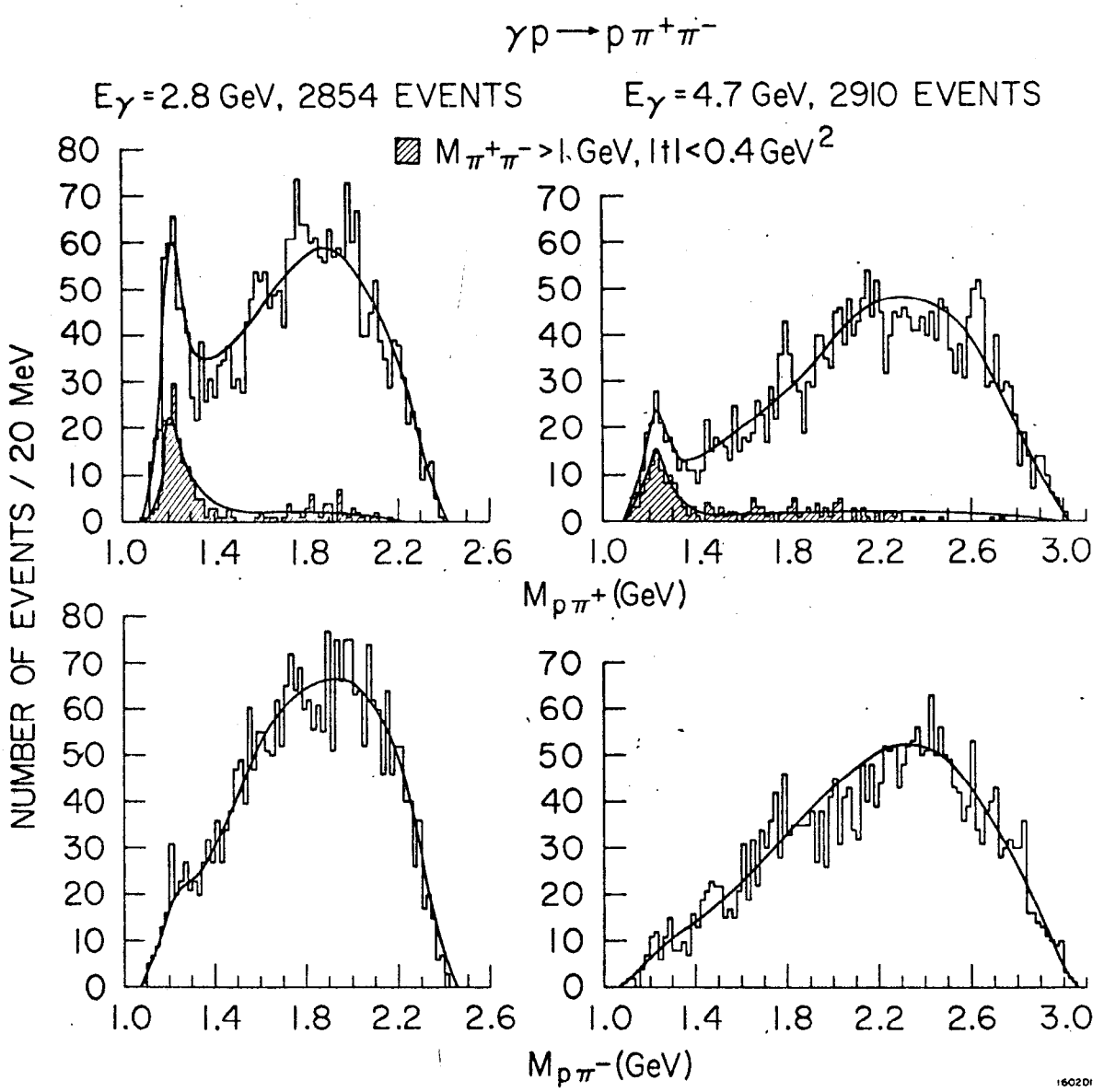
γp → pπ+π−
Eγ = 2.8 GeV, 2854 EVENTS
Eγ = 4.7 GeV, 2910 EVENTS
Mπ+π− > 1. GeV, |t| < 0.4 GeV2
NUMBER OF EVENTS / 20 MeV
Mpπ+ (GeV)
Mpπ− (GeV)
160201

Fig. 18

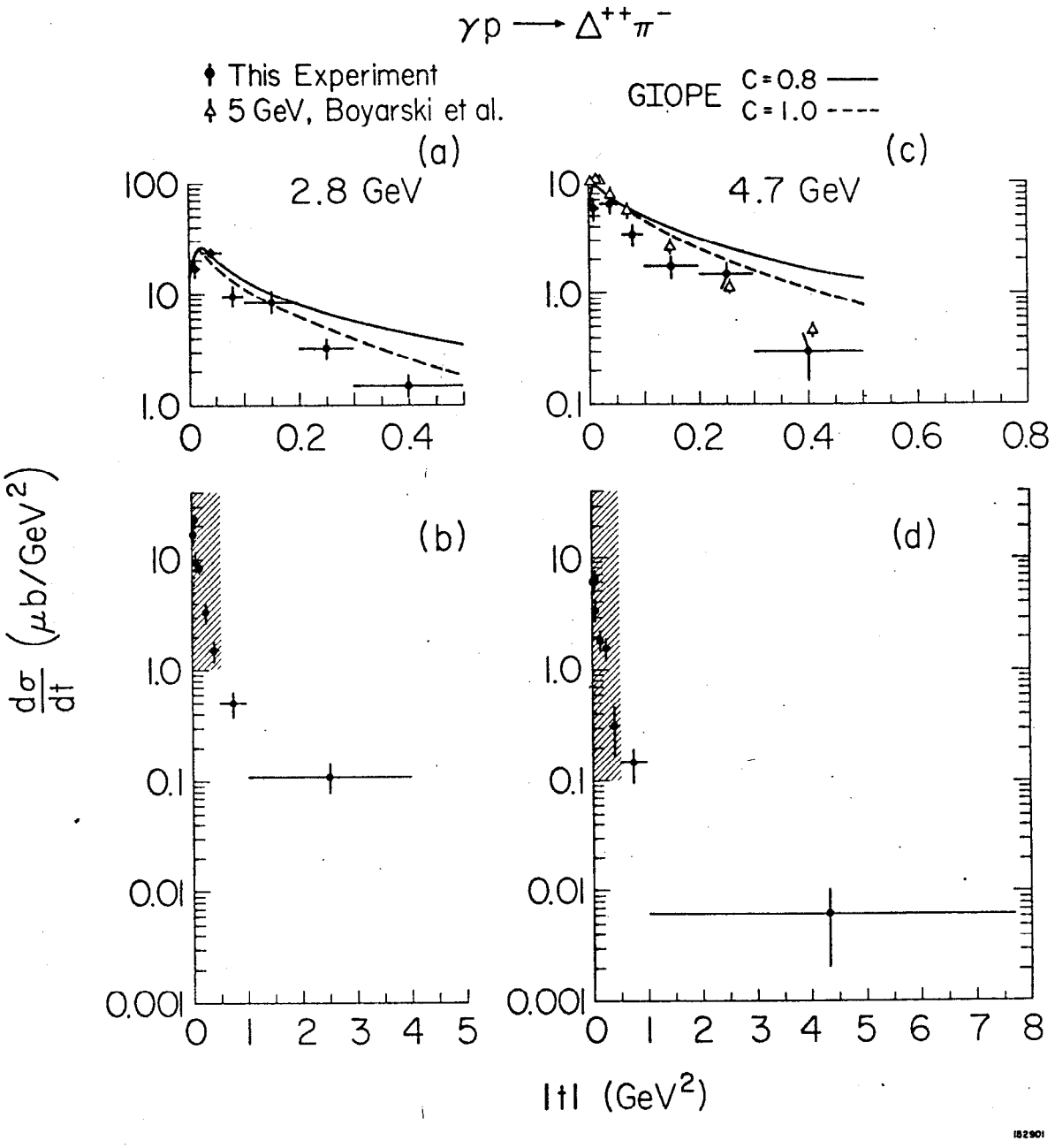
γp → Δ++π−
This Experiment
5 GeV, Boyarski et al.
GIOPE C=0.8
C=1.0
(a)
2.8 GeV
(b)
(c)
4.7 GeV
(d)
dσ/dt (μb/GeV²)
|t| (GeV²)
182901

Fig. 19

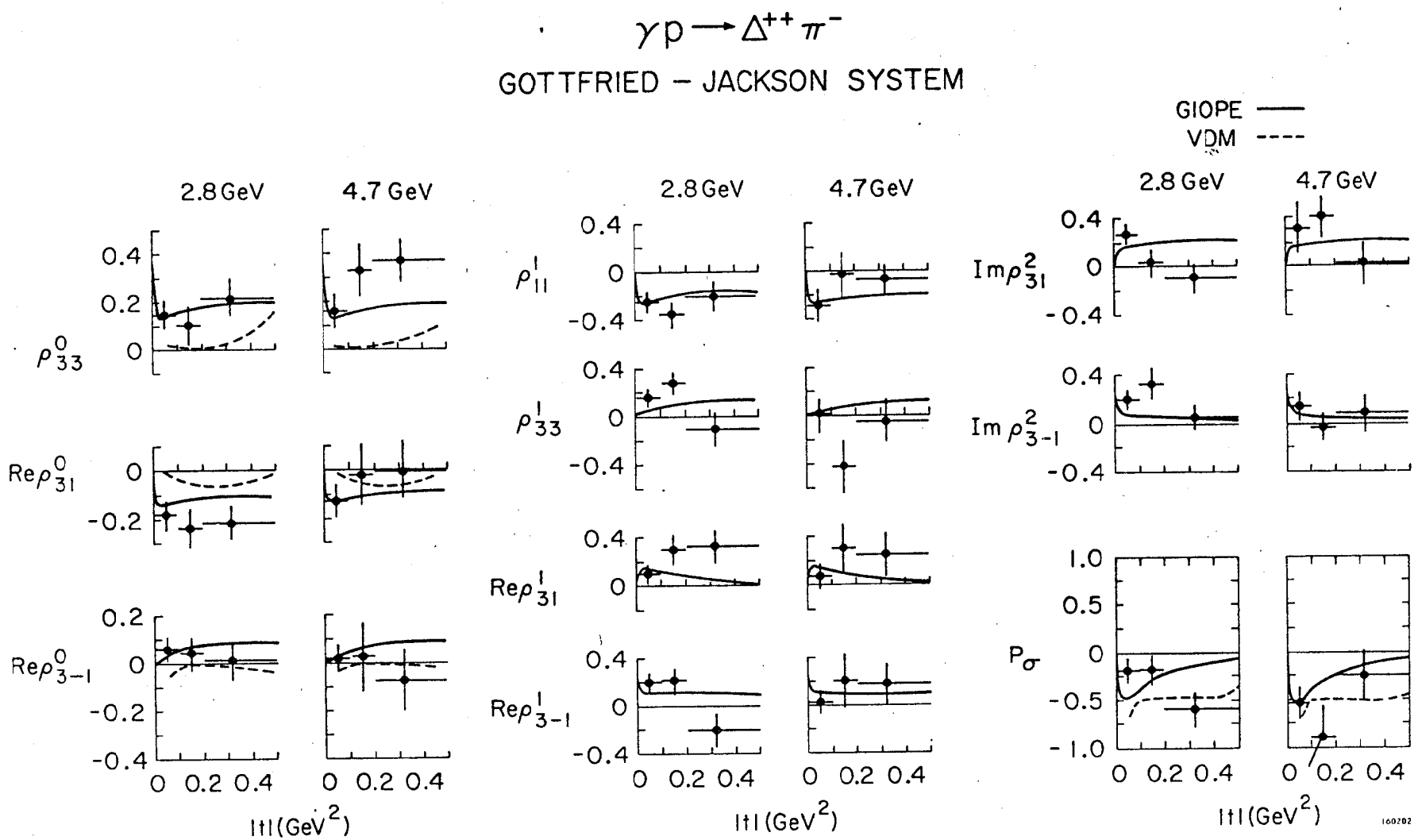
$\gamma p \rightarrow \Delta^{++}\pi^-$
GOTTFRIED – JACKSON SYSTEM
GIOPE
VDM
2.8 GeV
4.7 GeV
ρ^0_{33}
$\mathrm{Re}\rho^0_{31}$
$\mathrm{Re}\rho^0_{3-1}$
ρ^1_{11}
ρ^1_{33}
$\mathrm{Re}\rho^1_{31}$
$\mathrm{Re}\rho^1_{3-1}$
$\mathrm{Im}\rho^2_{31}$
$\mathrm{Im}\rho^2_{3-1}$
P_σ
$|t|(\mathrm{GeV}^2)$
160202

Fig. 20

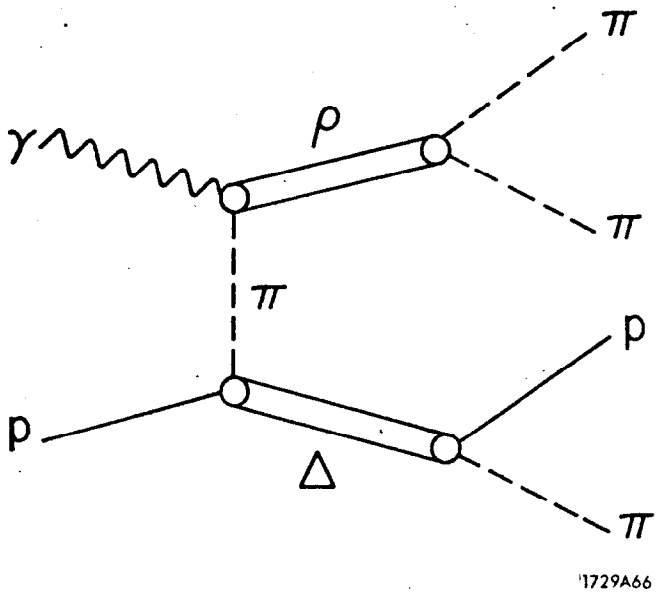

Fig. 21

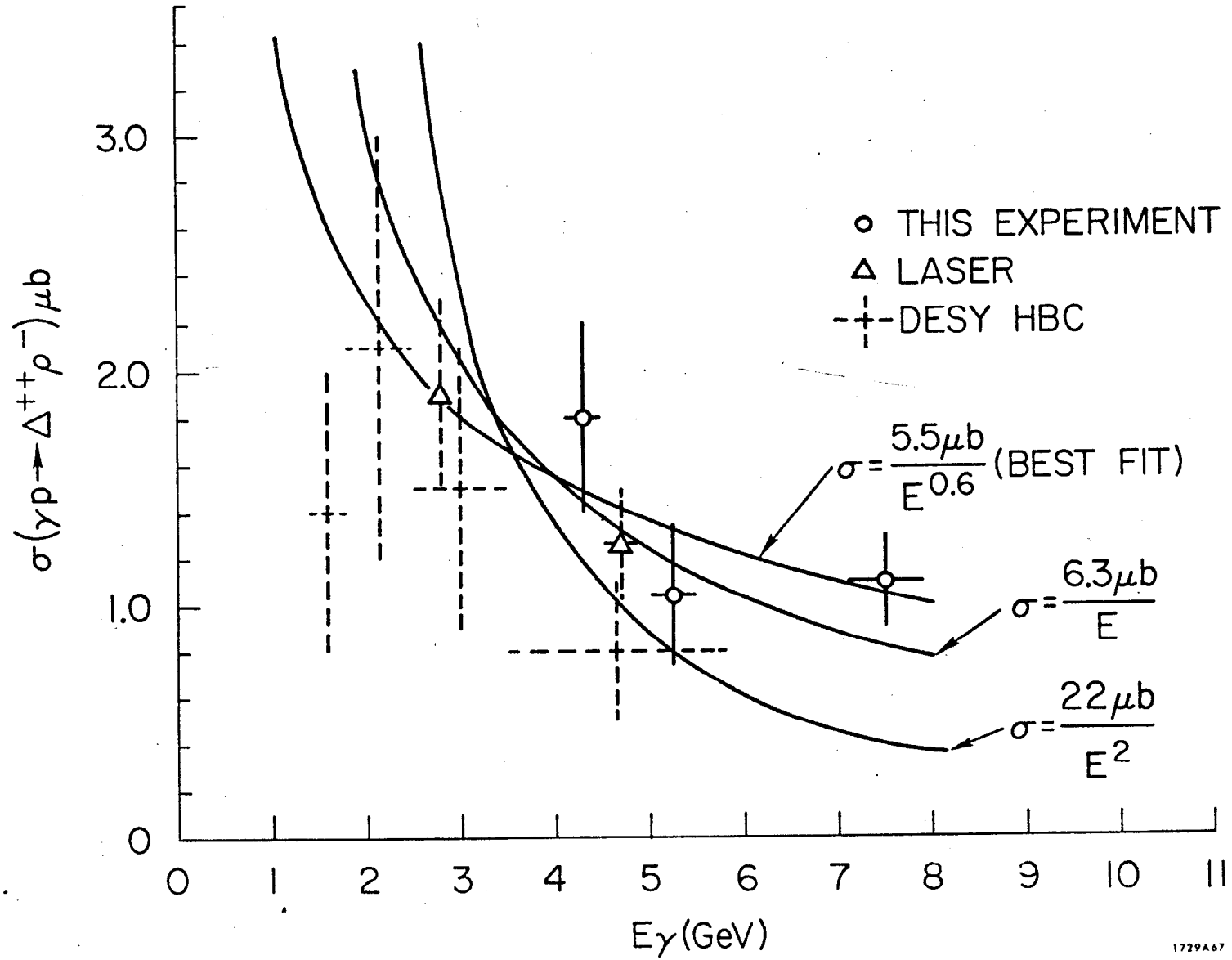
$\sigma(\gamma p \to \Delta^{++}\rho^-)\mu b$
3.0
2.0
1.0
0
0 1 2 3 4 5 6 7 8 9 10 11
$E\gamma$(GeV)
o THIS EXPERIMENT
Δ LASER
DESY HBC
$\sigma = \frac{5.5\mu b}{E^{0.6}}$ (BEST FIT)
$\sigma = \frac{6.3\mu b}{E}$
$\sigma = \frac{22\mu b}{E^2}$
1729A67

Fig. 22

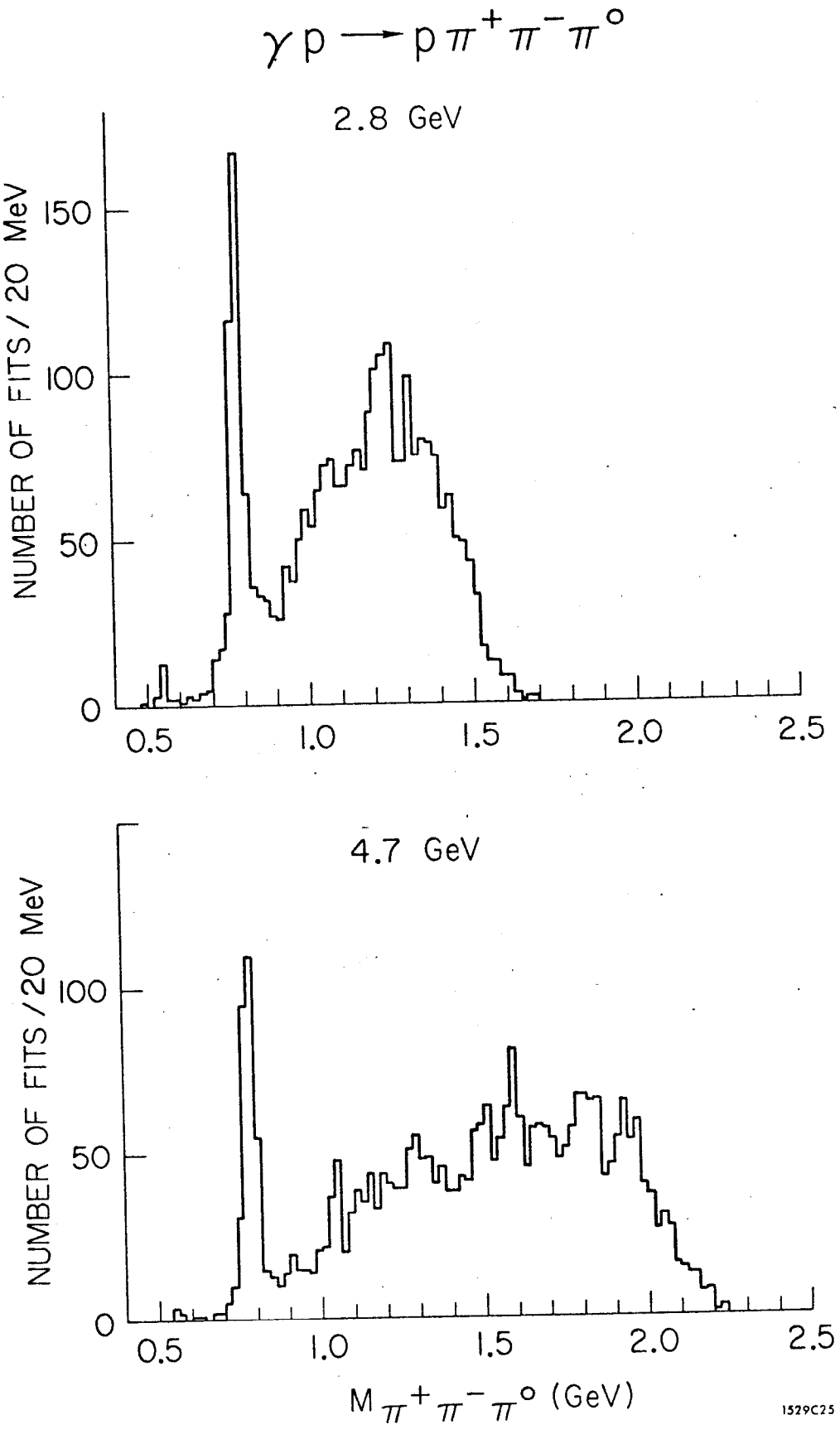
$\gamma p \rightarrow p\pi^+\pi^-\pi^\circ$
2.8 GeV
NUMBER OF FITS / 20 MeV
150
100
50
0
0.5
1.0
1.5
2.0
2.5
4.7 GeV
NUMBER OF FITS / 20 MeV
100
50
0
0.5
1.0
1.5
2.0
2.5
$M_{\pi^+\pi^-\pi^\circ}$ (GeV)
1529C25

Fig. 23

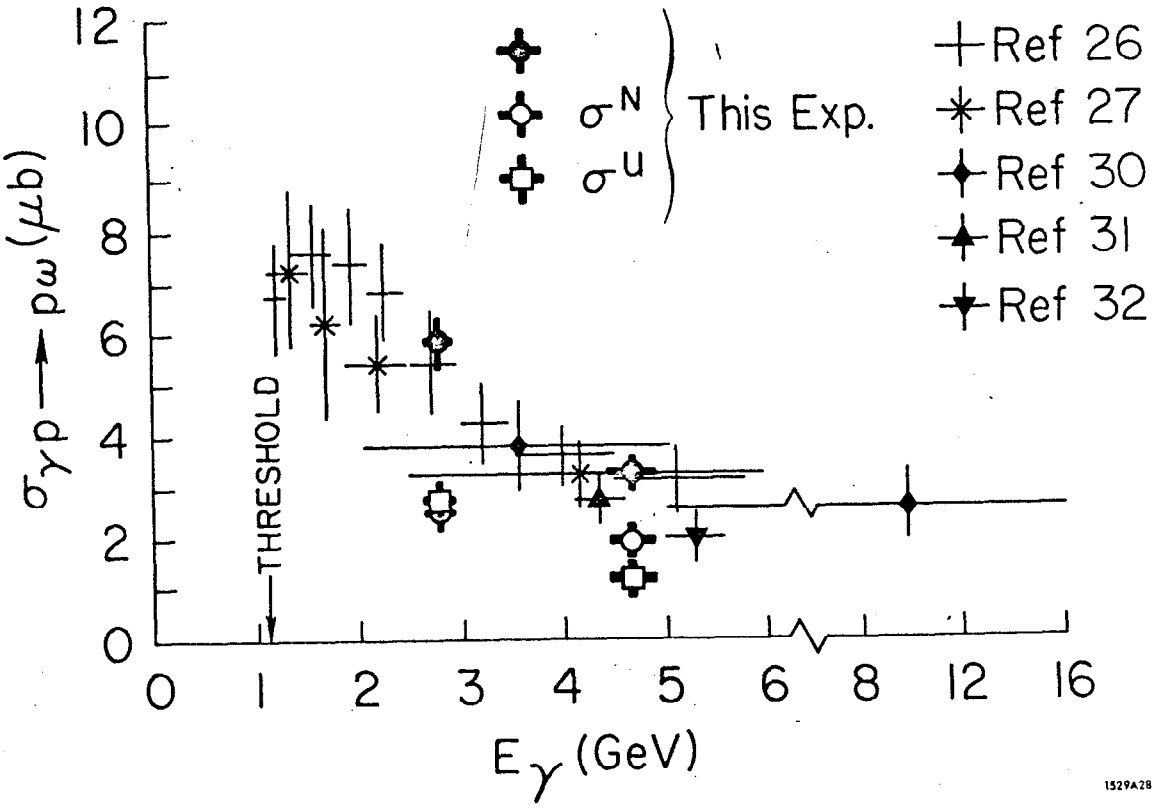
12
10
8
6
4
2
0
0
1
2
3
4
5
6
8
12
16
$\sigma_{\gamma p \to p\omega}$ (μb)
E_γ (GeV)
THRESHOLD
σ^N
σ^u
This Exp.
Ref 26
Ref 27
Ref 30
Ref 31
Ref 32
1529A28

Fig. 24

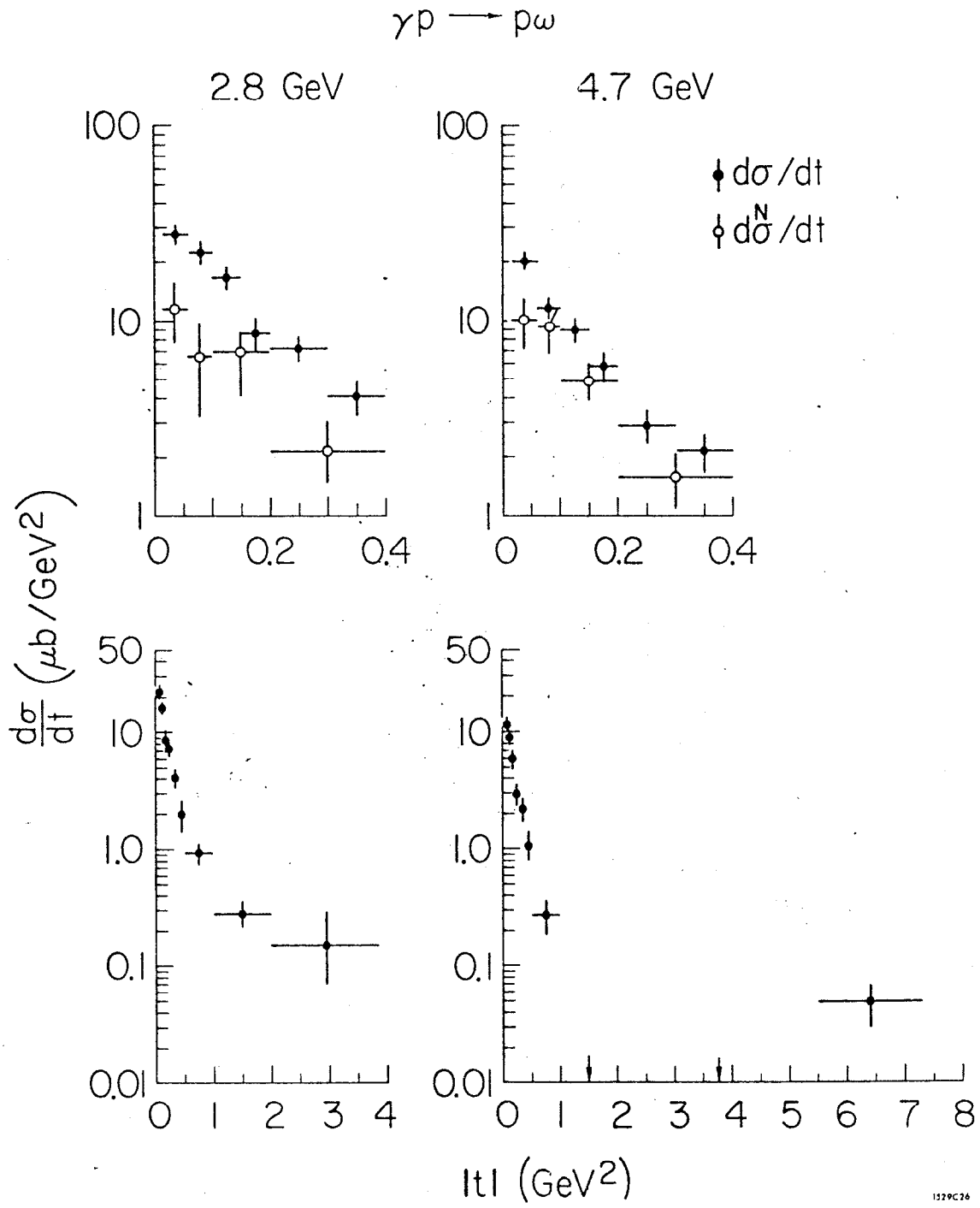

Fig. 25

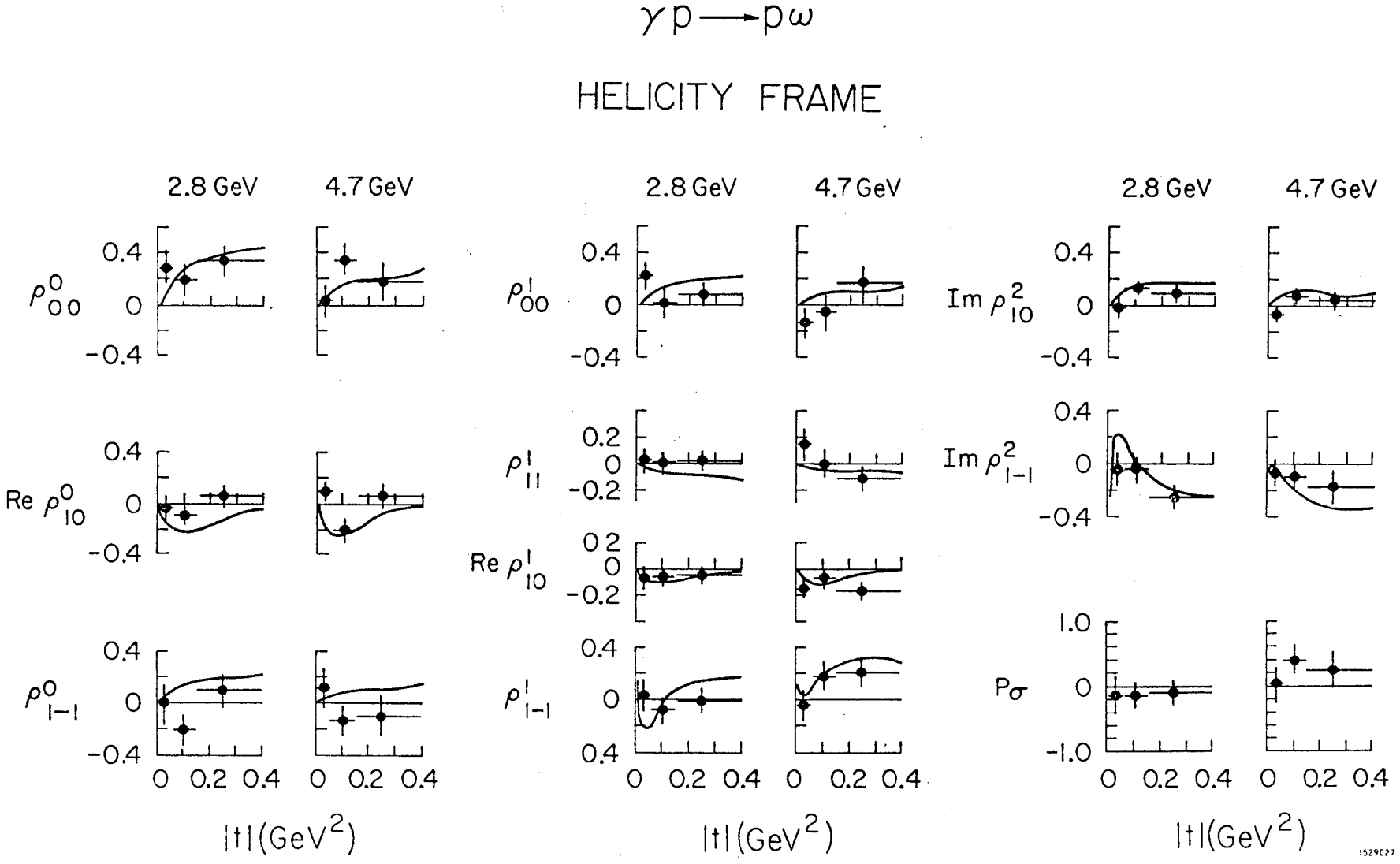
γp → pω
HELICITY FRAME
2.8 GeV
4.7 GeV
ρ^0_{00}
ρ^0_{10}
ρ^0_{1-1}
ρ^1_{00}
ρ^1_{11}
ρ^1_{10}
ρ^1_{1-1}
$\mathrm{Im}\,\rho^2_{10}$
$\mathrm{Im}\,\rho^2_{1-1}$
P_σ
0.4
0
-0.4
0.2
-0.2
1.0
-1.0
0 0.2 0.4
|t|(GeV²)
1529C27

Fig. 26

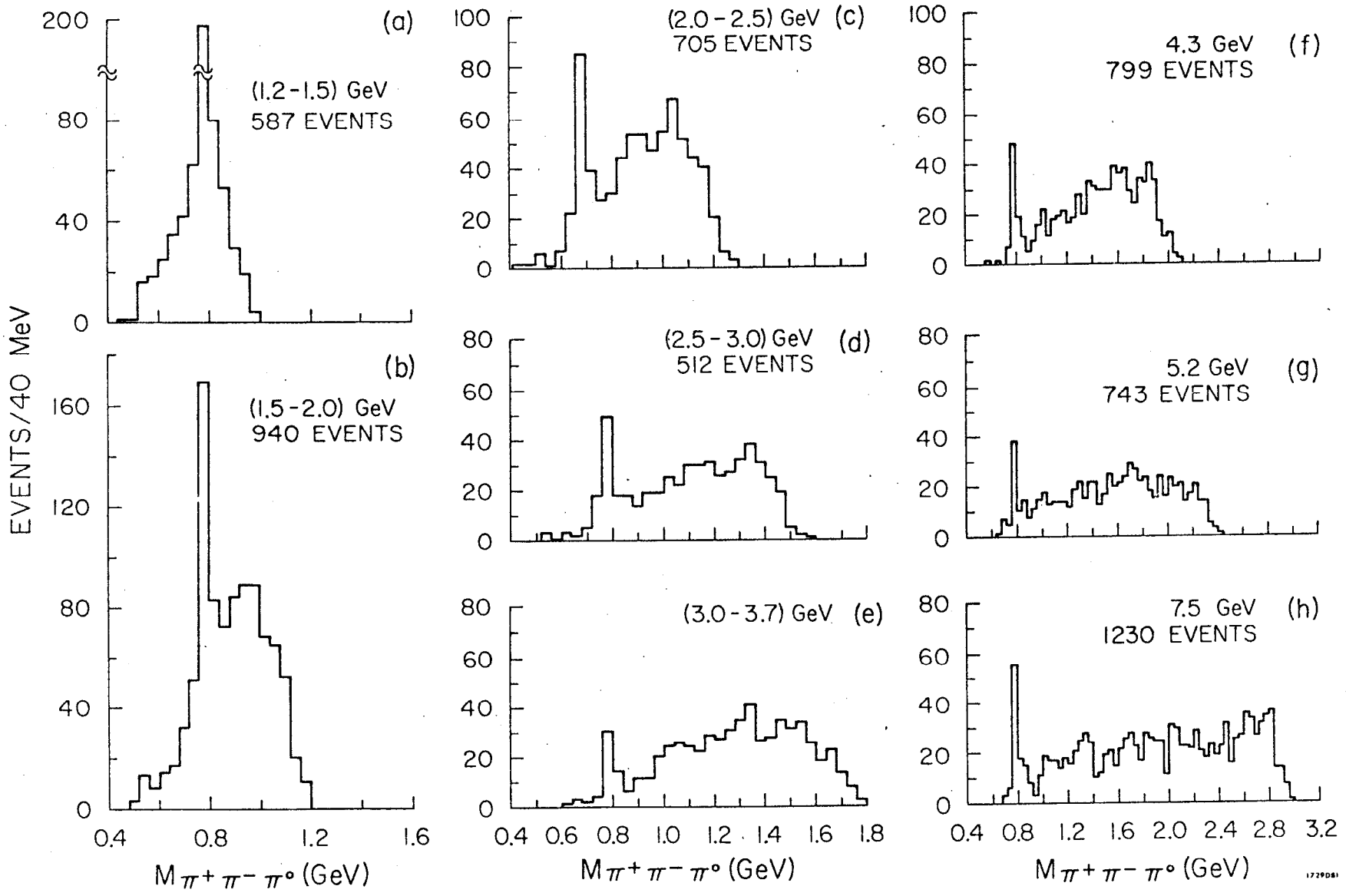
(a)
(1.2-1.5) GeV
587 EVENTS
(b)
(1.5-2.0) GeV
940 EVENTS
(c)
(2.0-2.5) GeV
705 EVENTS
(d)
(2.5-3.0) GeV
512 EVENTS
(e)
(3.0-3.7) GeV
(f)
4.3 GeV
799 EVENTS
(g)
5.2 GeV
743 EVENTS
(h)
7.5 GeV
1230 EVENTS
EVENTS/40 MeV
M π+ π− π° (GeV)
M π+ π− π° (GeV)
M π+ π− π° (GeV)

Fig. 27

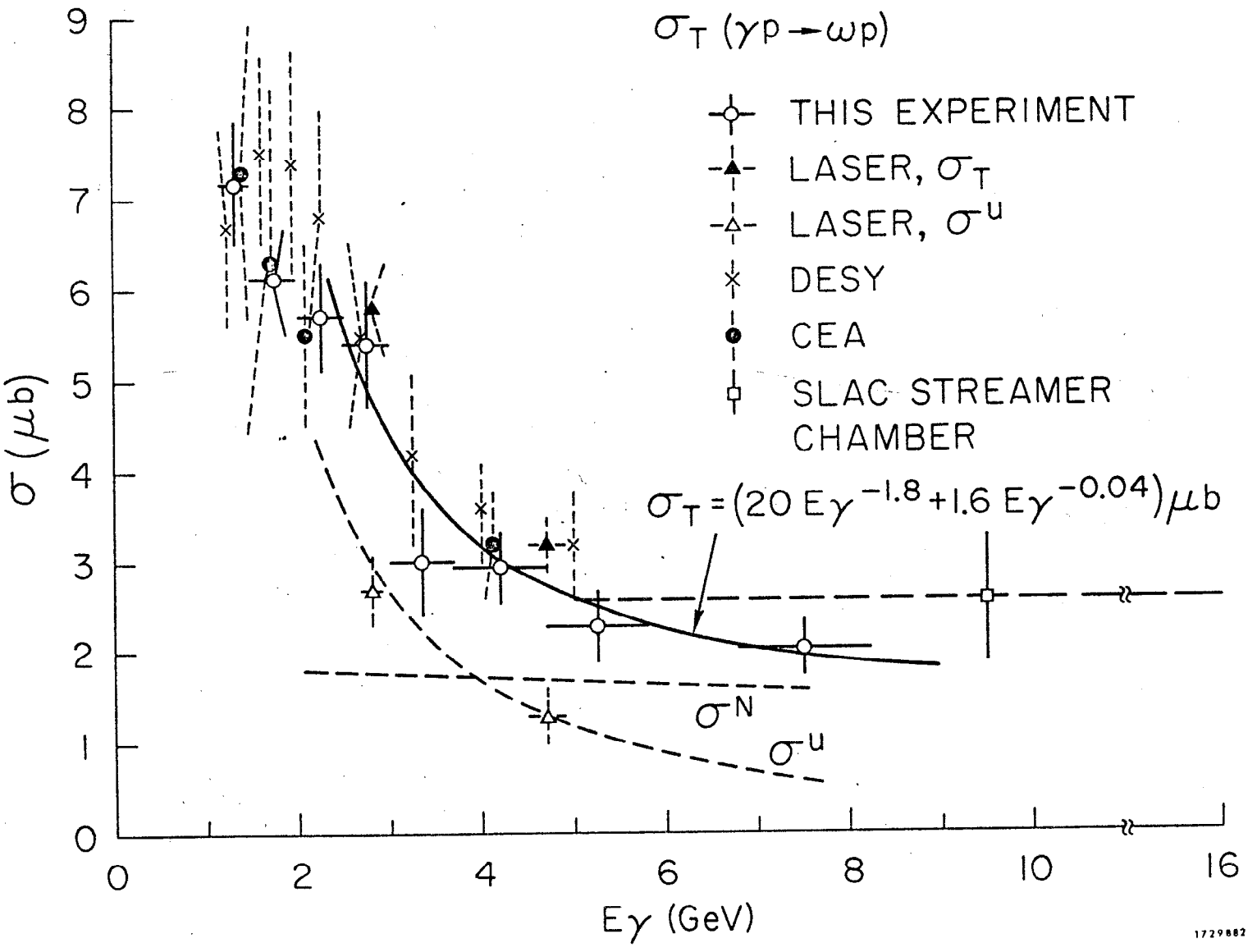
$\sigma_T(\gamma p \to \omega p)$
THIS EXPERIMENT
LASER, σ_T
LASER, σ^u
DESY
CEA
SLAC STREAMER CHAMBER
$\sigma_T = (20\, E\gamma^{-1.8} + 1.6\, E\gamma^{-0.04})\,\mu b$
σ^N
σ^u
$\sigma\ (\mu b)$
$E\gamma$ (GeV)
0
1
2
3
4
5
6
7
8
9
0
2
4
6
8
10
16
1729882

Fig. 28

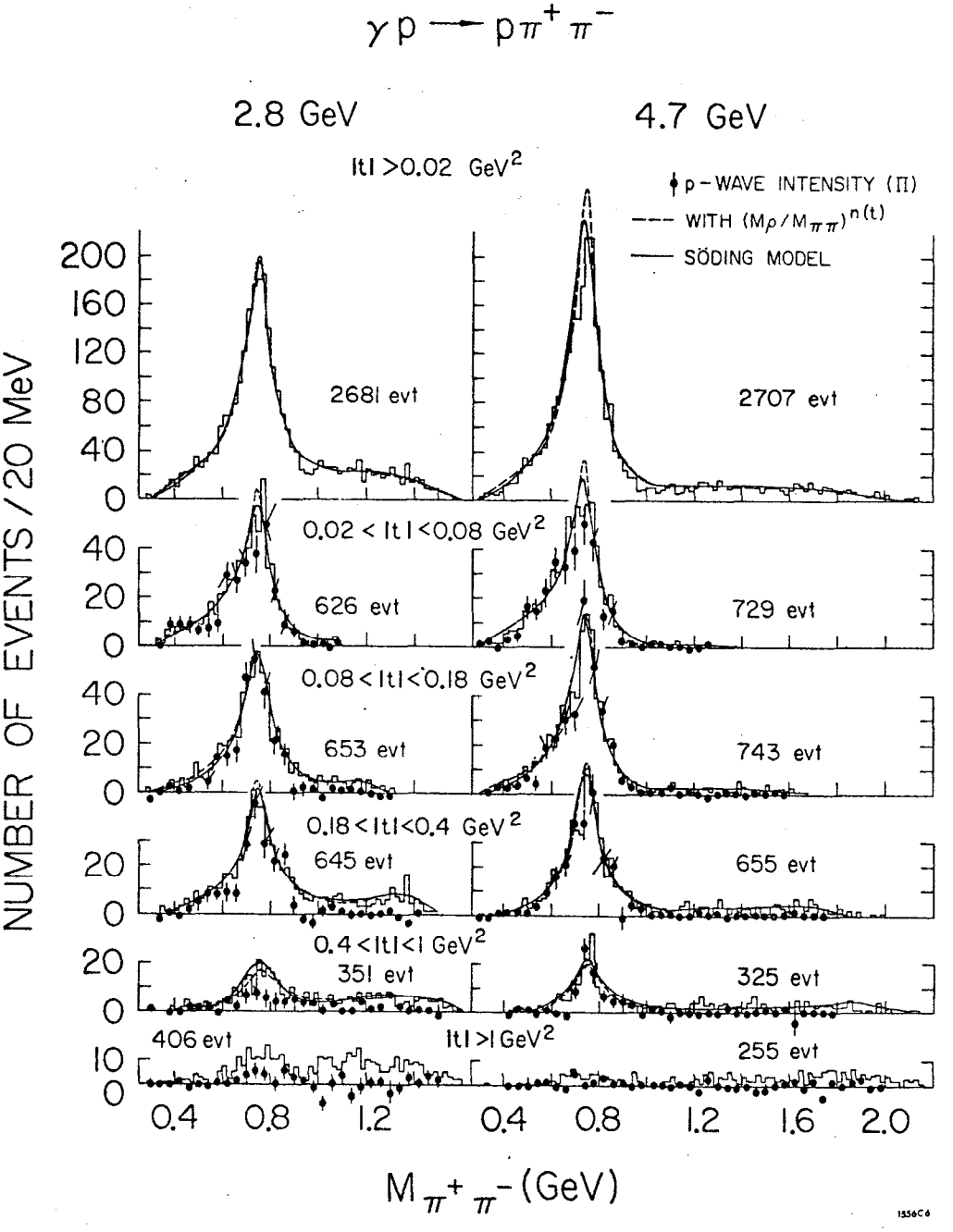
γ p → p π+ π−
2.8 GeV
4.7 GeV
|t| >0.02 GeV²
p-WAVE INTENSITY (Π)
WITH (Mρ/Mππ)^n(t)
SÖDING MODEL
NUMBER OF EVENTS / 20 MeV
2681 evt
2707 evt
0.02 < |t| <0.08 GeV²
626 evt
729 evt
0.08 < |t| <0.18 GeV²
653 evt
743 evt
0.18 < |t| <0.4 GeV²
645 evt
655 evt
0.4 < |t| <1 GeV²
351 evt
325 evt
406 evt
|t| >1 GeV²
255 evt
Mπ+π− (GeV)

Fig. 29

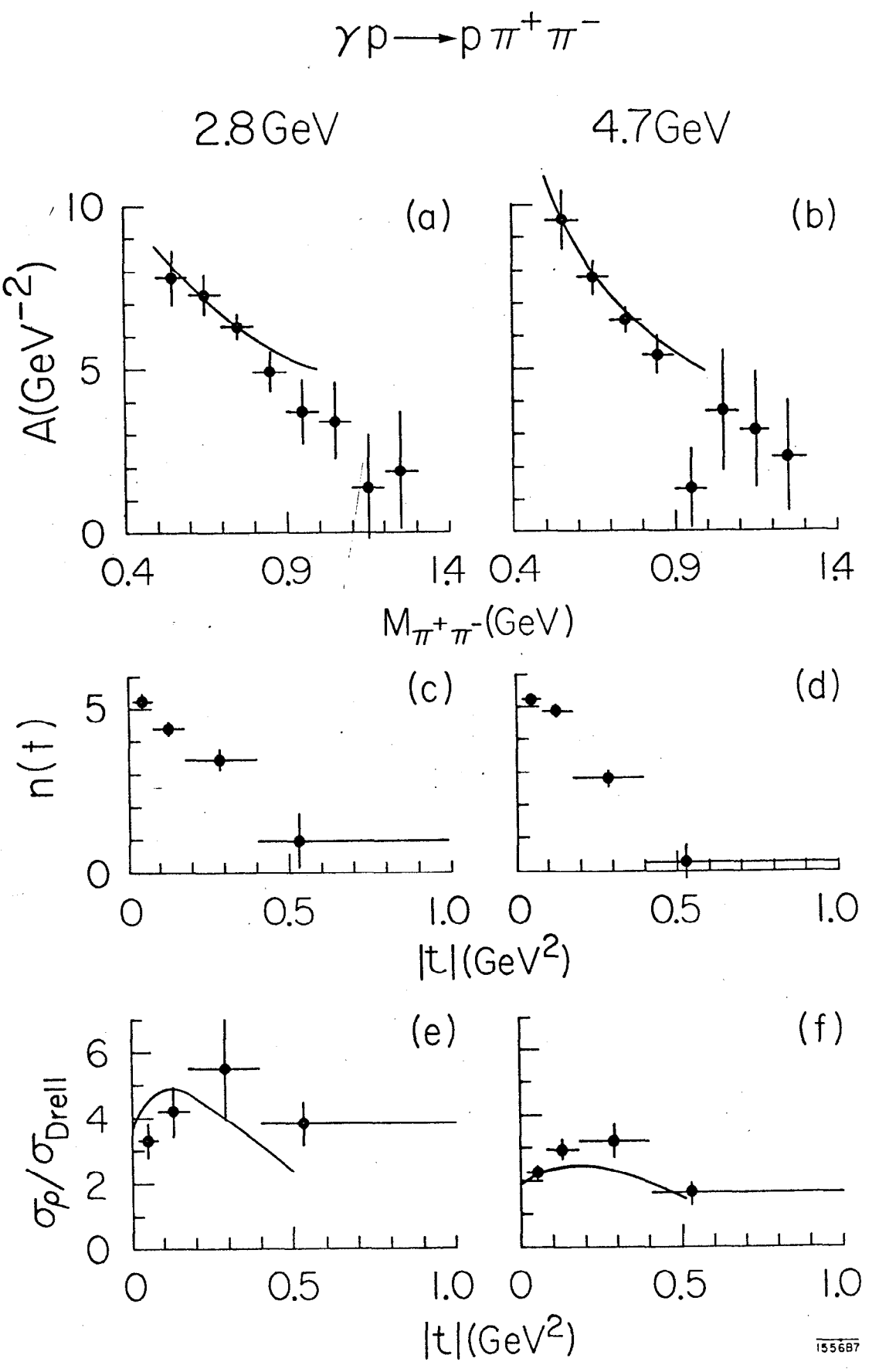
γp → pπ+π−
2.8GeV
4.7GeV
(a)
(b)
(c)
(d)
(e)
(f)
A(GeV−2)
10
5
0
0.4
0.9
1.4
Mπ+π−(GeV)
n(t)
5
0
0
0.5
1.0
|t|(GeV2)
σρ/σDrell
6
4
2
0
155687

Fig. 30

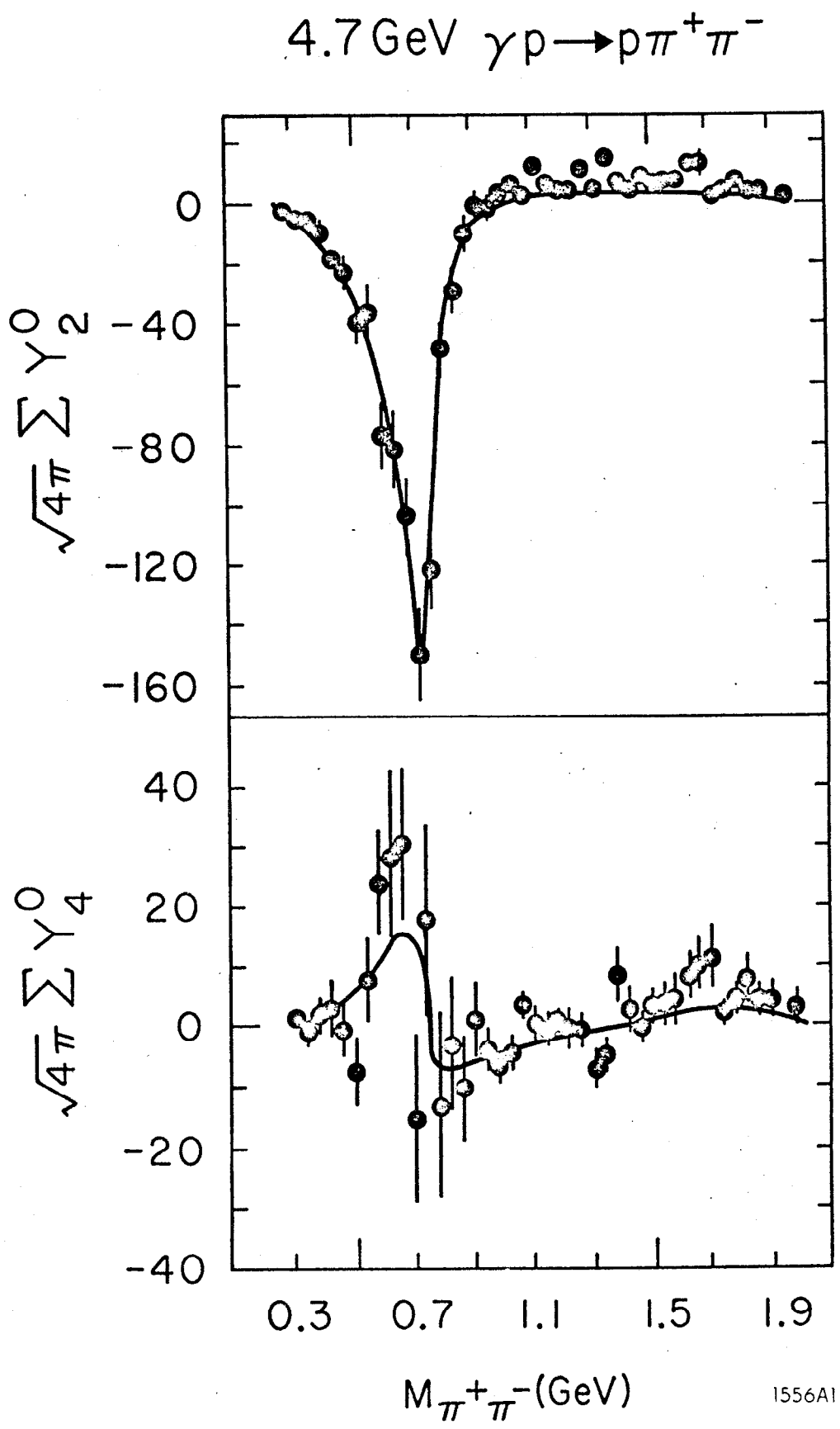
4.7 GeV γp → pπ⁺π⁻
0
-40
-80
-120
-160
√4π Σ Y⁰₂
40
20
0
-20
-40
√4π Σ Y⁰₄
0.3
0.7
1.1
1.5
1.9
Mπ⁺π⁻(GeV)
1556A1

Fig. 31

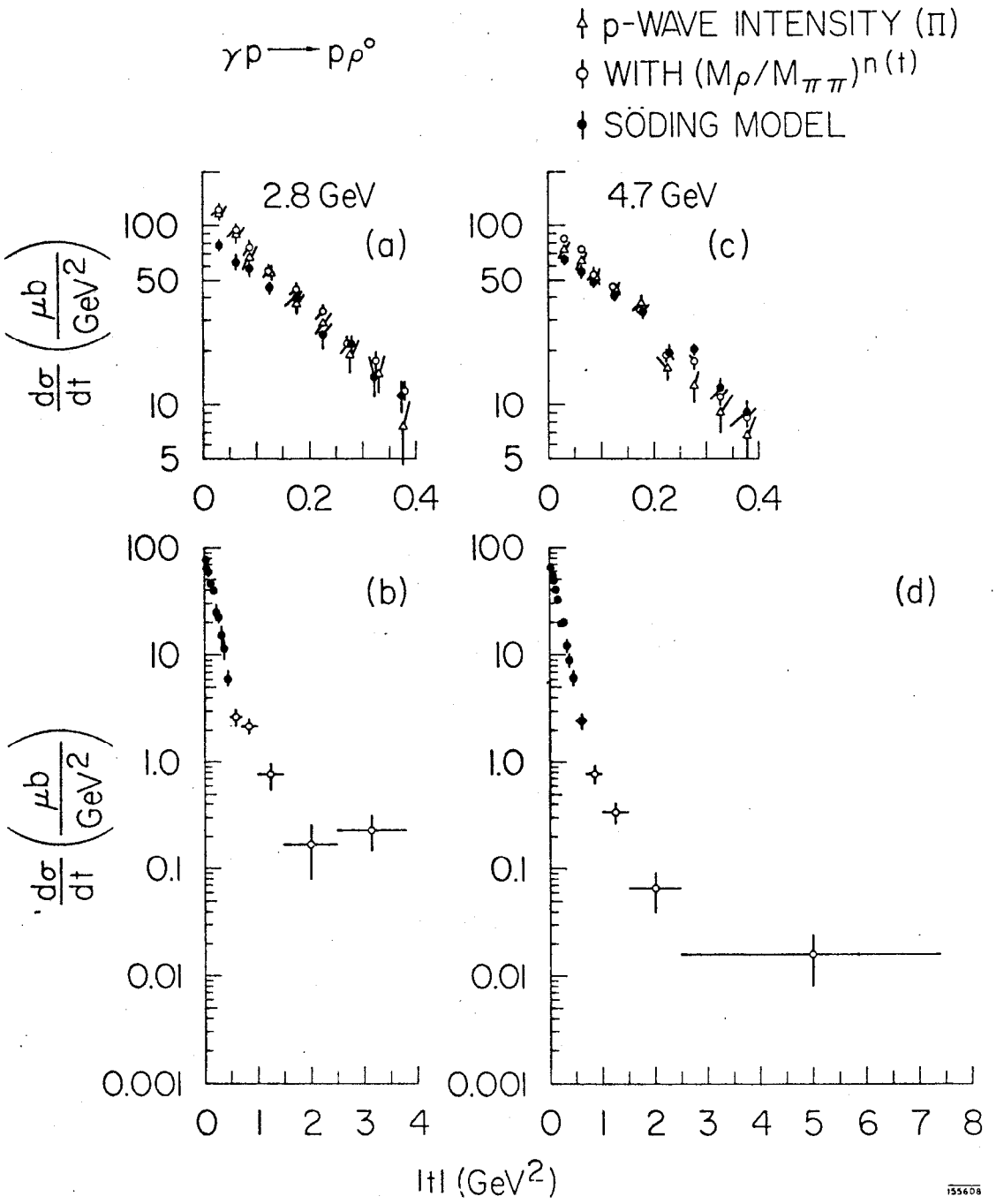
γp ⟶ pρ°
p-WAVE INTENSITY (Π)
WITH (Mρ/Mππ)^n(t)
SÖDING MODEL
2.8 GeV
(a)
4.7 GeV
(c)
(b)
(d)
dσ/dt (μb/GeV²)
|t| (GeV²)
155608

Fig. 32

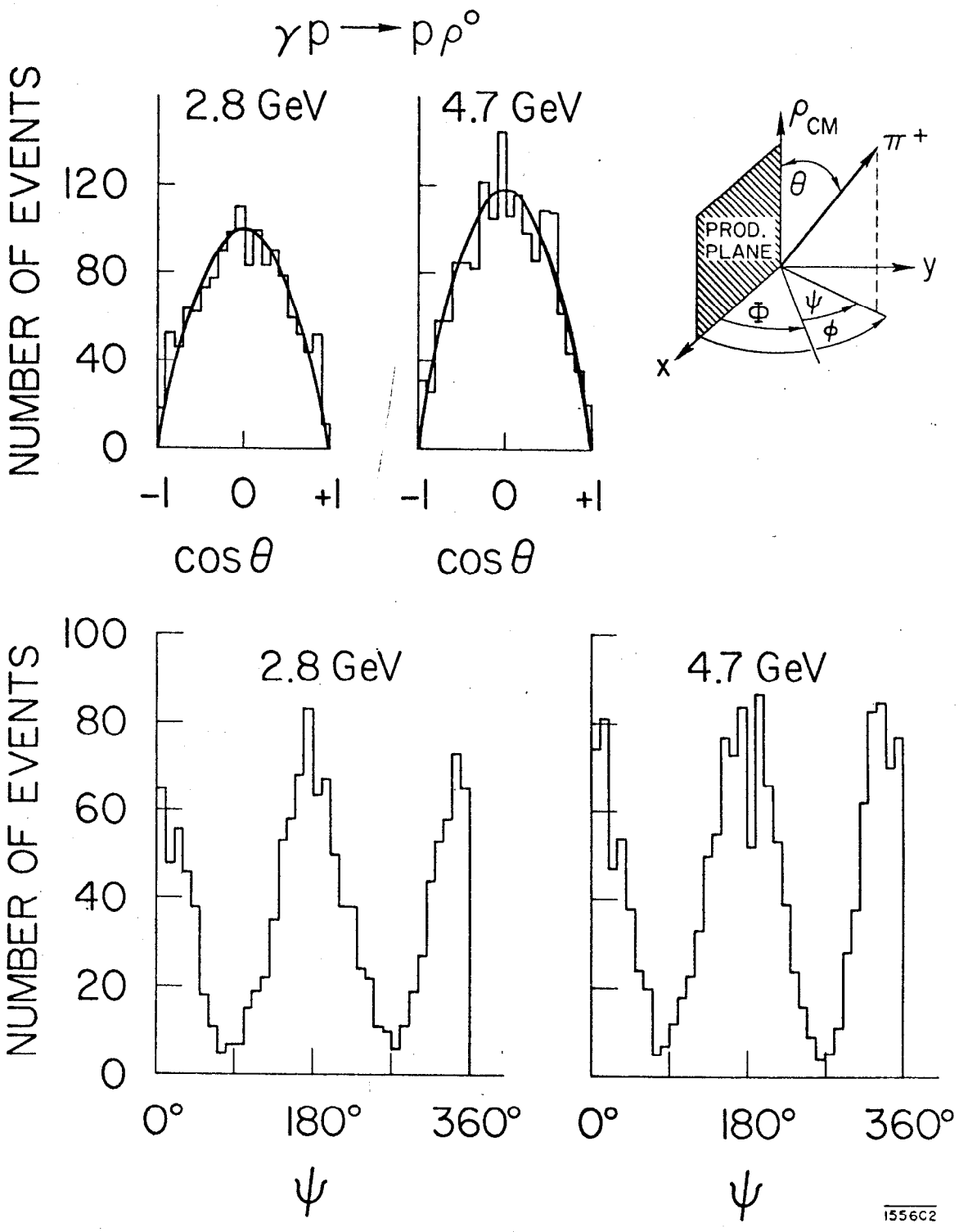
γp → pρ°
2.8 GeV
4.7 GeV
NUMBER OF EVENTS
120
80
40
0
-1
0
+1
cos θ
ρ CM
π +
θ
PROD. PLANE
y
x
Φ
ψ
φ
100
60
20
0°
180°
360°
ψ
1556C2

Fig. 33

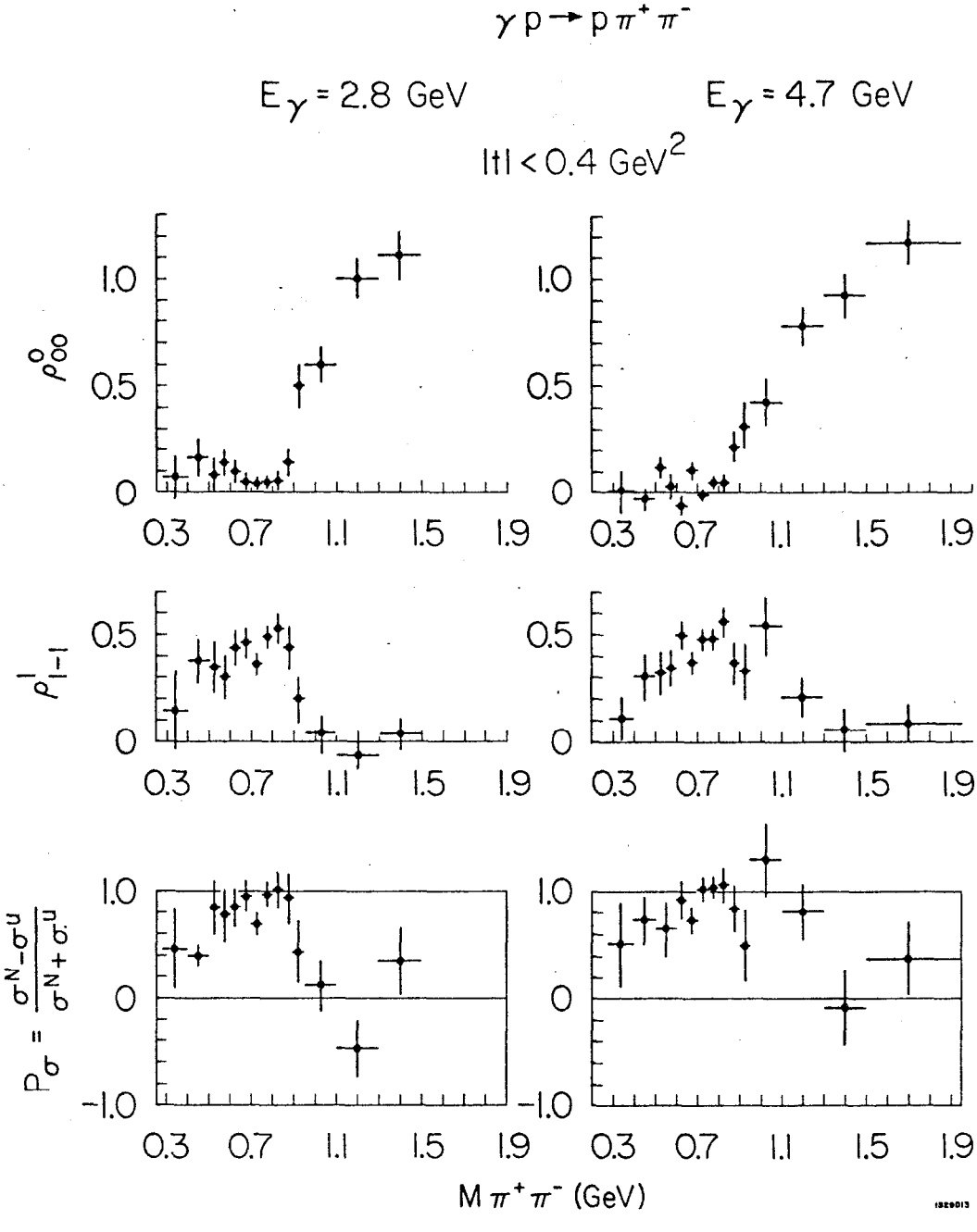
γ p → p π⁺ π⁻
E_γ = 2.8 GeV
E_γ = 4.7 GeV
|t| < 0.4 GeV²
ρ⁰₀₀
ρ¹₁₋₁
P_σ = (σ^N − σ^U)/(σ^N + σ^U)
1.0
0.5
0
−1.0
0.3
0.7
1.1
1.5
1.9
M π⁺ π⁻ (GeV)

Fig. 34

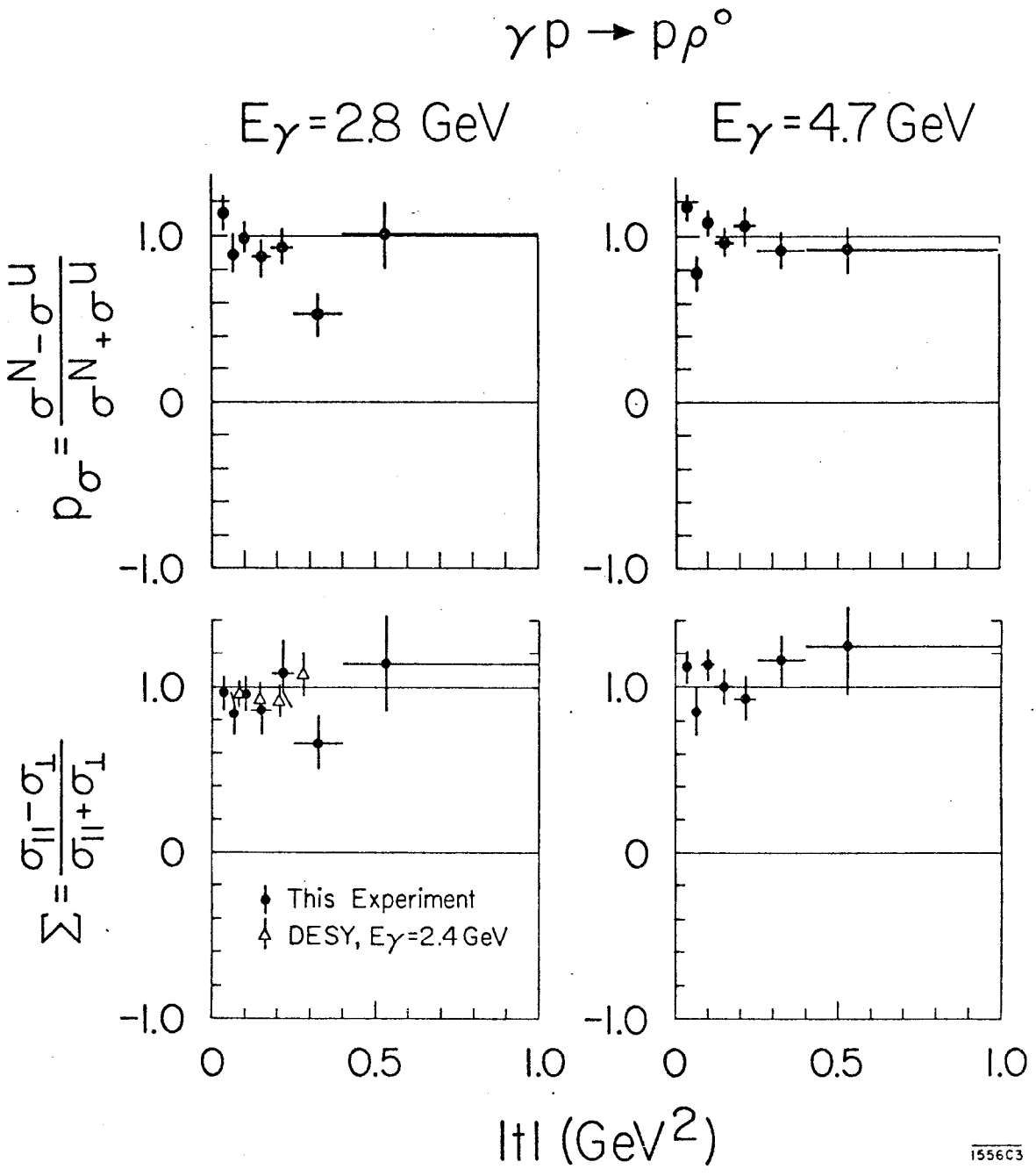
γp → pρ°
Eγ = 2.8 GeV
Eγ = 4.7 GeV
$\rho_b = \frac{N_\rho - \sigma_u}{N_\rho + \sigma_u}$
$\Sigma = \frac{\sigma_{\perp\rho} - \sigma_{\parallel\rho}}{\sigma_{\perp\rho} + \sigma_{\parallel\rho}}$
1.0
0
-1.0
This Experiment
DESY, Eγ = 2.4 GeV
0
0.5
1.0
|t| (GeV²)
1556C3

Fig. 35

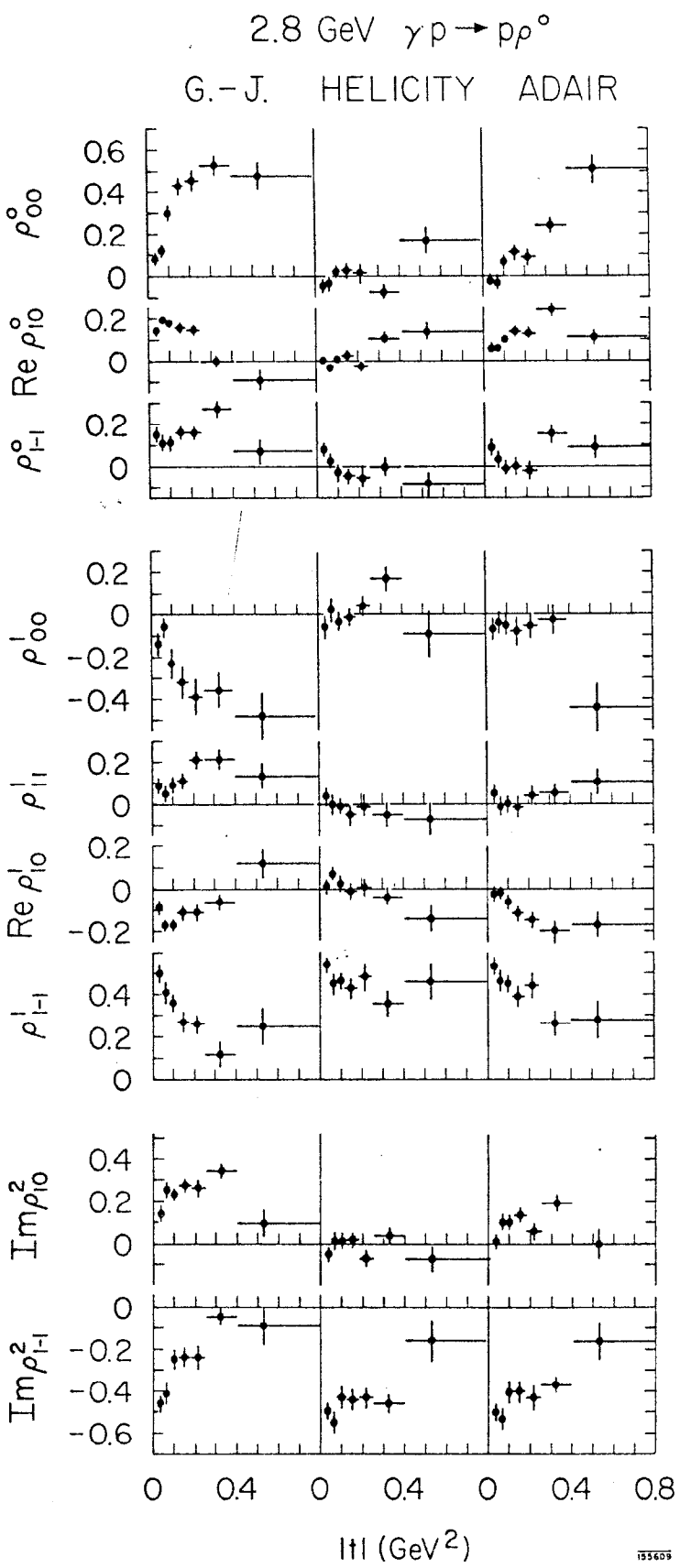
2.8 GeV γp → pρ°
G.-J. HELICITY ADAIR
ρ^0_{00}
$\mathrm{Re}\,\rho^0_{10}$
ρ^0_{1-1}
ρ^1_{00}
ρ^1_{11}
$\mathrm{Re}\,\rho^1_{10}$
ρ^1_{1-1}
$\mathrm{Im}\rho^2_{10}$
$\mathrm{Im}\rho^2_{1-1}$
|t| (GeV^2)
155609

Fig. 36

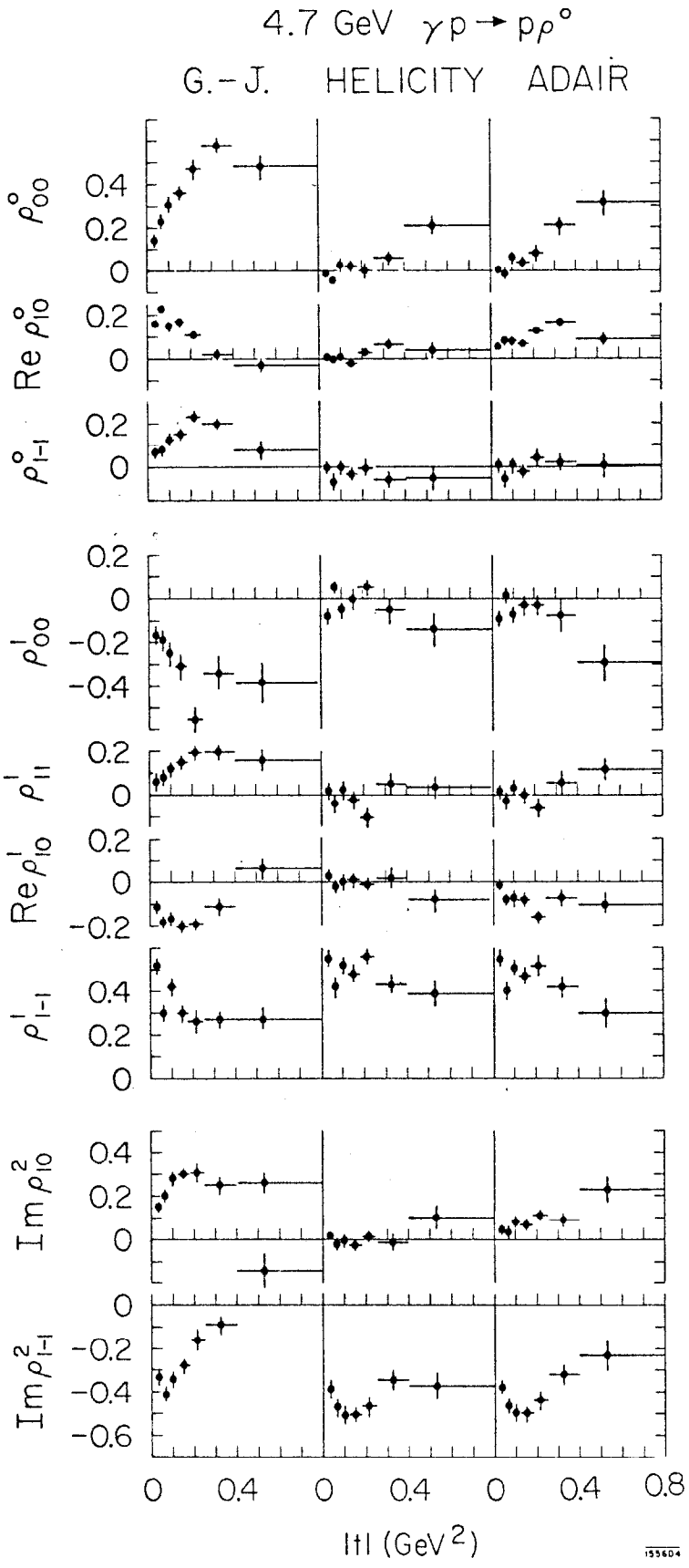
4.7 GeV γp → pρ°
G.-J. HELICITY ADAIR
ρ°00
Re ρ°10
ρ°1-1
ρ'00
ρ'11
Re ρ'10
ρ'1-1
Im ρ²10
Im ρ²1-1
0.4
0.2
0
-0.2
-0.4
-0.6
0.8
|t| (GeV²)
155604

Fig. 37

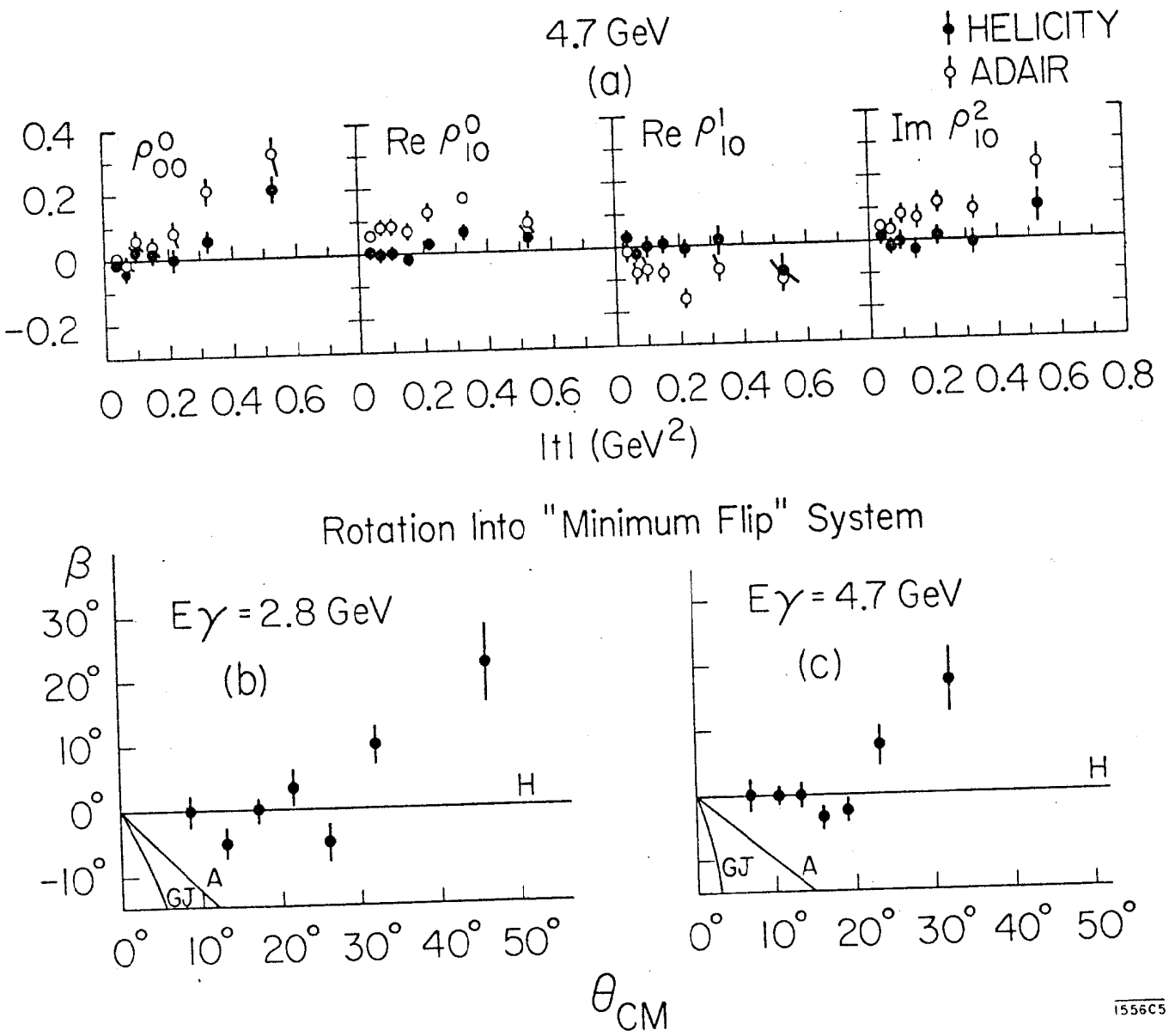
4.7 GeV
(a)
HELICITY
ADAIR
0.4
0.2
0
-0.2
ρ^0_{00}
Re ρ^0_{10}
Re ρ^1_{10}
Im ρ^2_{10}
0 0.2 0.4 0.6 0 0.2 0.4 0.6 0 0.2 0.4 0.6 0 0.2 0.4 0.6 0.8
|t| (GeV^2)
Rotation into "Minimum Flip" System
β
30°
20°
10°
0°
-10°
Eγ = 2.8 GeV
(b)
H
A
GJ
0° 10° 20° 30° 40° 50°
Eγ = 4.7 GeV
(c)
H
GJ
A
0° 10° 20° 30° 40° 50°
θ_{CM}
155605

Fig. 38